Turbulence Ingestion Noise of Open Rotors

Rosalyn A. V. Robison

Jesus College, Cambridge.

A Dissertation submitted for
the degree of Doctor of Philosophy
at the University of Cambridge
October 2011

Acknowledgements

Firstly, heartfelt thanks to my supervisor, Nigel Peake, who has always been generous with his time, helpful, and never dismissive of my thoughts or ideas. I am also grateful to Tony Parry, of Rolls-Royce, for our many useful conversations, and to Rolls-Royce and EPSRC for funding this Ph.D.

Secondly, thank you to all the people who have helped me push through the most difficult parts of the Ph.D. process, offering encouragement and advice. In particular, Katy Richardson, Helen Arnold, Dawn Lake, Alice Moncaster, Jane Cooper, Jill Shields, Susan Haines, Cally Roper and Pam Black. Also, huge thanks to all those who did a lot of proof-reading in a short space of time!: Tim Hughes, Clare Robison, Peter Foord, Brian Venner, Matthew Tinsley, Samantha Archetti and Hannah Dudley.

Thirdly, thanks to all the people at the Centre for Mathematical Sciences who have made this such a good workplace over the past four years: my fellow PhD students, the postdocs and academics who I've got to know, and also Mick Young, Zvezda Woodhouse and Beth Sweet-Rosborough, who keep everything running. Particular thanks also to my officemate, Hélène Posson, who read through drafts of Chapters 1 and 2 and gave very helpful comments.

Finally, thank you to all my family and other close friends, and especially Tim, for being such a source of support always.

Declaration

This dissertation is the result of my own work and includes nothing which is the outcome of work done in collaboration except where specifically indicated in the text. In particular, this work builds directly upon that of Majumdar (1996) and Cargill (1993).

All numerical calculations presented were computed using my own MATLAB code, with the exception of a LINSUB routine written by Dr V. Jurdic at the Institute of Sound and Vibration, University of Southampton. As indicated in the text, output from industry code was used in two plots and this was provided by Dr. M. J. Kingan (Institute of Sound and Vibration), Dr. P. J. G. Schwaller and Dr A. B. Parry (both at Rolls-Royce).

Some of the work presented in Chapter 4 has been published as Robison and Peake (2010), but is given here in more detail.

Rosalyn A. V. Robison
Cambridge, October 2011

SUMMARY OF THE DISSERTATION
'TURBULENCE INGESTION NOISE OF OPEN ROTORS'
BY ROSALYN A.V. ROBISON

Renewed interest in open rotor aeroengines, due to their fuel efficiency, has driven renewed interest in all aspects of the noise they generate. Noise due to the ingestion of distorted atmospheric turbulence, known as Unsteady Distortion Noise (UDN), is likely to be higher for open rotors than for conventional turbofan engines since the rotors are fully exposed to oncoming turbulence and lack ducting to attenuate the radiated sound. However, UDN has received less attention to date, particularly in wind-tunnel and flight testing programmes.

In this thesis a new prediction scheme for UDN is described, which allows inclusion of many key features of real open rotors which have not previously been investigated theoretically. Detailed features of the mean flow induced by the rotor, the form of atmospheric turbulence, asymmetries due to installation features, and the effect of rotor incidence are all considered. Parameter studies are conducted in each of these cases to investigate their effect upon UDN in typical static testing and flight conditions.

A thorough review of the technological issues of most relevance and previous theoretical work on all types of turbulence-blade interaction noise is first undertaken. The prediction scheme is then developed for the case in which the mean flow into the rotor is axisymmetric. This shows excellent qualitative agreement with previous findings, with increased streamtube contraction resulting in a more tonal noise spectrum. The theoretical framework involves using Rapid Distortion Theory to calculate the distortion of an isotropic turbulence field (such as given by the von Kármán spectrum) by the mean flow induced by the rotor (such as given by actuator disk theory), leading to an expression for the velocity incident upon the leading edge of the rotor blades. Strip theory is then used to calculate the pressure jumps across the blades, input as the forcing term in the far-field wave equation.

Models are derived for open rotor-induced flow which account for the variation of blade circulation with radius, and the presence of the rotor hub and rear blade row. An investigation of appropriate turbulence models and realistic turbulence parameters is also undertaken. A key finding is that the heights of the tonal peaks are determined by the overall magnitude of the induced streamtube contraction (dependent on the total thrust generated) whereas the precise form of distortion (affected by the detailed components of the mean flow and the form of atmospheric turbulence present) alters the resulting broadband level.

The prediction scheme is formulated in such a way as to facilitate extension to the asymmetric case, which is also fully derived. The model is applied in the first instance to the case of two adjacent rotors and then to the case of a single rotor at incidence. Under flight conditions, when distortion is reduced but UDN can still contribute a significant broadband component to overall noise levels, asymmetry is found to increase broadband levels around 1 Blade Passing Frequency but reduce levels elsewhere.

To Clare

Contents

Chapter 1

Introduction

1.1 Background

The underlying motivation for this work is the improvement of aviation efficiency. Optimisation of the very widely used turbofan engine has been ongoing since the 1960s, and has delivered both efficiency improvements and noise reduction within the commercial aircraft sector. There is now considerable interest in the future of another engine, the open rotor[1] (see Figure 1.1), predicted to deliver fuel savings of at least 30% compared to current turbofans (Smith, 1985), and 10-20% savings compared to next-generation turbofans. Open rotor driven aircraft can operate efficiently at speeds up to Mach 0.8, and are therefore suitable candidates for commercial short-haul flights[2]. However, the level of noise generated by the open rotor was a significant factor in commercial development being abandoned a decade after the technology first emerged in the 1980s. Research into many areas of open rotor aeroacoustics has now been resumed by manufacturers with the aim of meeting current and future noise certification criteria.

This Ph.D. project, in collaboration with Rolls-Royce, has involved analysing in detail one particular source of both broadband and tonal open rotor noise, termed *Unsteady Distortion Noise* (UDN). This arises from the interaction between unsteady perturbations to the mean flow (turbulent eddies) which are generated upstream of the engine and the large, unducted blades of the open rotor itself. As the turbulent eddies are drawn

---

[1] Also known as the Counter-Rotating Open Rotor (CROR), the Advanced Open Rotor (AOR), the advanced turboprop, the Counter-Rotating Propfan (CRP), or simply the propfan.

[2] Higher speeds would be desirable for long-haul flights. The conventional turboprop, a close relative of the open rotor, only delivers efficiency savings when travelling below Mach 0.6, although advanced turboprops do exceed this.

towards the engine they are stretched by the streamtube contraction which is induced as air is sucked into the engine. Such incoming eddies arise naturally due to atmospheric turbulence, but in addition any coherent fluid structures which are shed from parts of the aircraft several rotor diameters upstream of the rotors may also undergo significant distortion during their passage downstream. The subsequent interaction of the distorted eddies with the front row of rotating propeller blades leads to high tonal[3] noise at multiples of the Blade Passing Frequency[4] (BPF). Distortion is strongest at low flight speeds, and thus the tonal contribution of UDN may be particularly significant at take off and approach. These are also the situations in which strict noise certification criteria must be satisfied. For operating conditions where the distortion is weaker, UDN may still contribute a significant broadband component to the overall noise of the open rotor.

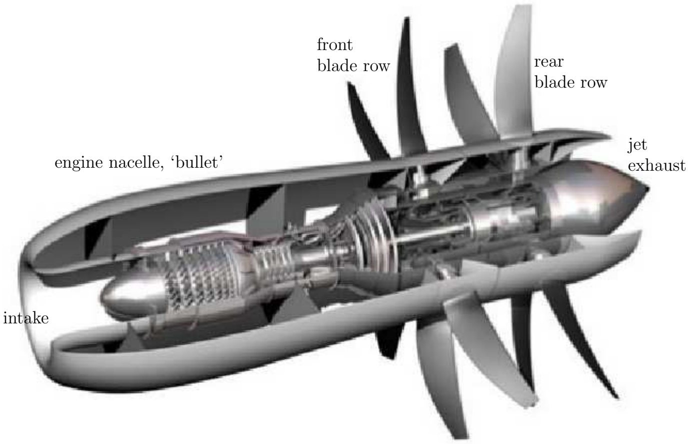

Figure 1.1: Illustration of a 'pusher' configuration of open rotor, with the blades toward the rear of the engine. Reproduced with permission from Rolls-Royce.

1.2 Technological context: *the open rotor design*

This work is strongly motivated by a real-world application within the rapidly expanding aviation sector. It is therefore desirable to be aware of the key technological issues which surround open rotor aeroacoustics research. Noise generated by the external rotors far outweighs noise from within the engine core, and is made up of many interacting com-

---

[3] Tonal noise is noise at a specific frequency, such as a note being played on an instrument, and arises from periodic variations in sound pressure. Broadband noise is noise at a wide range of frequencies, such as road noise heard when travelling in a car, and arises from more random variations in sound pressure.

[4] 1 BPF $= B\Omega$, where B is blade number and Ω is angular velocity of the rotor.

ponents. The aerodynamic and aeroacoustic performance of the open rotor's unducted blades are closely interlinked and it can be difficult to separate the optimisation of one from the other. The way in which experimental, computational and (ultimately) certification testing is carried out also affects which analytical results will be of most use.

1.2.1 Commercial development in the 1980s - the propfan

The current generation of open rotors are direct descendants of the propfan engine, first developed by NASA in the 1980s. The global nature of oil supply and demand has involved a number of 'oil shocks' in recent decades when oil prices have risen extremely rapidly. In 1973[5] fuel costs made up, on average, about 25% of the direct operating costs of aircraft, but this rose to 44% in 1978, (Lange, 1986). This was a key driver in the search for more efficient ways to fly and even led to the US Congress tasking NASA with identifying concepts which had major efficiency saving potential (Hager and Vrabel, 1988). As a result, the Advanced Turboprop Project ran at the NASA Lewis Research Center from 1976-1987 involving several large American manufacturers.

Much of the efficiency gains since the 1960s in aviation have been made by increasing the bypass ratio[6] of turbofan engines. This increases propulsive efficiency by reducing the energy wasted in high velocity wakes (Stuart, 1986). An added advantage of increasing the bypass ratio for turbofans is that noise is reduced. This is due to a combination of factors including the reduced jet velocity and a shielding effect from the air which has bypassed the core. However, for a turbofan engine, there is a bypass ratio limit beyond which fuel burn begins to increase due to drag along the interior of the engine nacelle. Today's high bypass ratio turbofans operate at ratios of around 10. As the external rotors of the open rotor are completely unducted, drag is no longer a limiting factor, and they can achieve 'Ultra High Bypass Ratios' of 30 and above. Ducting liners, which play a crucial role in specific tone reduction for turbofans, cannot of course be used to attenuate noise from these rotors.

General Electric (GE) in the US began an in-house 'UnDucted Fan' (UDF) research programme in 1983 and also collaborated with NASA. As the new engine design moved further from the starting point of the single-propeller turboprop, a significant increase

---

[5] The year the Organization of Arab Petroleum Exporting Countries (OAPEC) declared an oil embargo triggered by the Arab-Israeli conflict.

[6] Bypass ratio = mass flow rate of air drawn in by the engine which bypasses the engine core : mass flow rate of air which passes through the core.

in efficiency was made by adding a second counter-rotating blade row behind the first, see Figure 1.2. The rear rotor removes some of the swirl introduced by the front row, turning the flow back toward the axial direction and increasing the thrust generated very effectively. However, several new noise sources arise from the interaction of the wakes and tip vortices shed by the front blade row impinging upon the rear blade row (see recent work by Kingan and Self (2009)). Other features which distinguish the propfan from the turboprop include the distinctive blade shape (wide-chord and high-sweep[7]), and the use of variable rotor speeds. In order to achieve high speeds at cruise, the open rotor has a very large diameter and this leads to transonic tip speeds which are a source of significant tonal noise.


(a) (b) (c)

Figure 1.2: a) Propeller swirl recovery testing at the NASA Lewis Research Center in the 1980s, courtesy of nasaimages.org. The rear row of vanes are fixed. b) MacDonald Douglas test flight. Image reproduced with permission from Niels Sampath. One turbofan engine has been replaced by a propfan. c) Rolls-Royce Rig 140 testing in 1988. Image reproduced with permission from Rolls-Royce. Note the large hub protruding upstream of the rotors; due to its appearance this is called the 'bullet'.

In the UK, Rolls-Royce also began a propfan research programme in the late 1980s. Work was focused on Rig 140, a 1/5th scale 7x7 blade configuration which underwent low-speed testing in 1988 (Kirker, 1990), seen in Figure 1.2c. This was then reconfigured as a ducted version, Rig 141, which was tested in 1990 at the Aircraft Research Association's transonic wind tunnel in Bedford.

The noise spectra of 1980s propfans were dominated by very many close tones, concentrated toward the lower frequency range, see Figure 1.3. Both the front and rear blade rows of the propfan experience a range of fluctuating forces due the unsteadiness of the

---

[7] Sweep denotes the translation of each radial section of the blade in the chordwise direction relative to adjacent sections. Thus a blade whose leading edge curves back in the axial direction, as seen in Figure 1.4, has non-zero sweep.

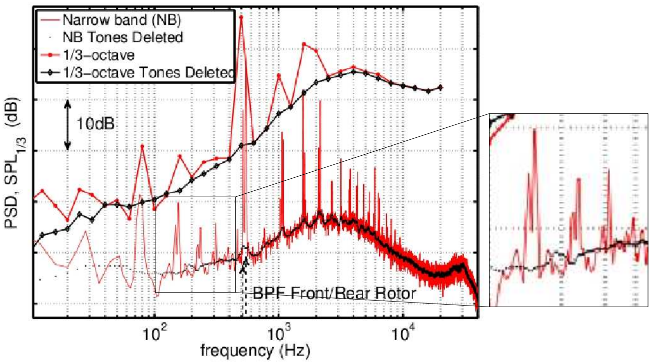

Figure 1.3: Example of Rig 140 noise results. Image reproduced with permission from Blandeau et al. (2009). Note there are the same number of blades in the front and rear rows, so tones are doubled up (shown in zoomed-in box).

flow in their reference frame, leading to noise at multiples of the front and rear BPF, $B_1\Omega_1$ and $B_2\Omega_2$. In addition, rotor-rotor interaction gives rise to tones at integer combinations of these two frequencies, $nB_1\Omega_1 + mB_2\Omega_2$. In contrast, turbofans generate fewer tones and produce relatively smooth spectra.

Much early propfan aeroacoustics work was therefore focussed on the most prominent tonal sources. As might be expected, propfan noise more closely resembled that of turboprops[8] than turbofans. Perhaps the most detailed publicly available propfan report from that period is that by Hoff (1990), which described testing programmes run in collaboration between GE and NASA from 1984-1987. The testing concentrated on three major sources of propfan tonal noise - steady loading noise, rotor-rotor interaction noise and pylon wake interaction noise - and included rig testing, flight testing and calibration of methods. Hoff included a diagram which illustrated the many different propfan noise sources, see Figure 1.4. There was also a recognition that distortion is an important factor in predicting the acoustics of propeller planes. Distortion is a broad term used by different authors to describe a whole range of effects which are not measured in rotor alone wind tunnel testing. It can therefore include both mean flow effects (such as the influence of installation features, the airframe and angle of attack), and also unsteady effects due to turbulence generated both in the atmosphere and by the aircraft itself. There was some evidence that distortion noise dominated over rotor alone noise for certain single unducted rotor configurations.

Another area of interest at the time was the potential response of the public to the

---

[8] Commercially active turboprops include Bombardier's Q400 and ATR's 72 series.

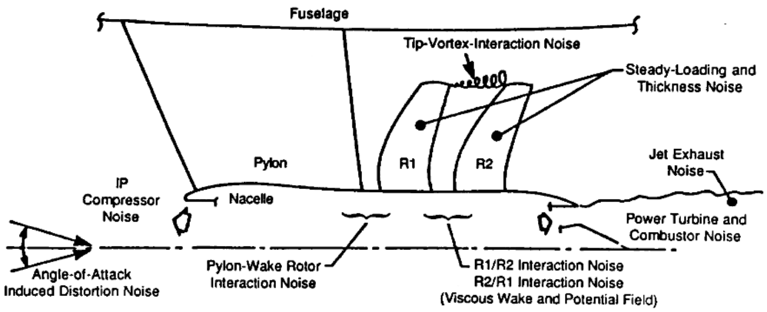

Noise-Source Mechanisms with Counterrotating Fan Engines.

Figure 1.4: Figure from Hoff (1990), detailing the major tonal noise source mechanisms. There are additional broadband sources and in particular Hoff noted that broadband levels would be related to inflow turbulence.

noise of the propfan. Studies have shown that changes in the tone-to-broadband ratio and fundamental frequency (both of which are different for the propfan and the turbofan) affect annoyance levels (McCurdy, 1990). Tonal noise is usually perceived as more irritating by the human ear than broadband, and frequencies within the range 2-6 kHz are perceived as louder (for a given Sound Pressure Level) than lower or higher frequencies. In addition, the 'noiseprints' (the area around take-off/landing location which experiences noise above a certain level) were predicted to change with the use of the propfan (Lange, 1986), with the noiseprint at some levels increasing in area, and at other levels decreasing. High levels of cabin noise were also identified as a potential problem.

Later studies found some evidence that people's annoyance response to propfan noise might not be significantly different to contemporary turbofan and turboprop noise (McCurdy, 1992). Certainly, in the mid-1980s, there was confidence that the propfan could meet the Chapter 3 noise regulations in place at that time if blade design, blade number and rotor spacing were chosen appropriately. The joint GE/NASA rig testing had produced configurations which would comfortably meet Chapter 3, see Figure 1.5, and they had also successfully calibrated between rig testing and flight testing results. As NASA's Advanced Turboprop Project progressed, test flights were carried out between 1986-1988 with a GE36 UDF engine replacing one of the turbofans on both a Boeing 727 (Harris and Cuthbertson, 1987) and a McDonnell Douglas MD-80, as seen in Figure 1.2b. Commercial production of a propfan-powered McDonnell Douglas, the MD-94X, was planned for 1994. However, a dramatic drop in oil prices had removed the major driving factor for the technology by 1988. Other commercial issues, such as the replacement of airport infrastructure and maintenance equipment which would be involved with any major transfer to a new technology, meant the balance of the argument fell on the side of continued use of the turbofan. Many manufacturers, including GE and Rolls-Royce, had pulled their research programmes by the early 1990s. However, work on the propfan did not stop completely; in particular, in the Ukraine development of the Antonov An-70 military transport aircraft has been ongoing.

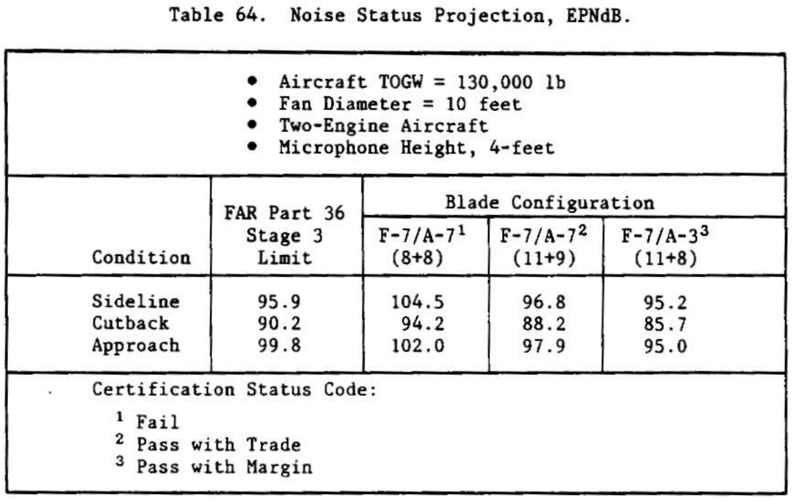

Table 64. Noise Status Projection, EPNdB.

- Aircraft TOGW = 130,000 lb
- Fan Diameter = 10 feet
- Two-Engine Aircraft
- Microphone Height, 4-feet

Condition	FAR Part 36 Stage 3 Limit	Blade Configuration		
		F-7/A-7[1] (8+8)	F-7/A-7[2] (11+9)	F-7/A-3[3] (11+8)
Sideline	95.9	104.5	96.8	95.2
Cutback	90.2	94.2	88.2	85.7
Approach	99.8	102.0	97.9	95.0

Certification Status Code:

[1] Fail
[2] Pass with Trade
[3] Pass with Margin

Figure 1.5: Table from Hoff's 1990 NASA report, showing predicted noise levels of the propfan at the three certification points, based on their rig testing results. Three blade configurations are shown, where F-7, A-7 etc. denote the particular blade models used for the front and rear (aft) rows. The A-3 model has a reduced diameter compared to the A-7. The results were obtained by scaling up the rig results to a 10-foot diameter engine, and then adjusting the dB level to account for the 2 engines, ground reflections during testing, core noise (at both cutback and approach) and airframe noise (at approach).

1.2.2 Commercial development since 2001 - the Advanced Open Rotor

Reduction of carbon emissions is a new driver for the development of more efficient technologies, as well as the return of oil price rises, and there is pressure on all industries to use less fossil fuels[9]. In addition, complaints over aircraft noise remain one of the most

---

[9] Any long term sustainable option for aviation, e.g. the use of biofuels, must be considered against a backdrop of ever-increasing aviation demand. Since 1960 there has been growth of nearly 9% per year of air passenger traffic, and the UK's Department for Transport predicts 500 million air passengers in 2030, almost 3 times as many as in 2002. Transporting cargo by air to the UK doubled between 1989

significant issues for airport operators and regulatory bodies. The Advisory Council for Aeronautics Research in Europe (ACARE), has established ambitious targets for new aircraft entering service in 2020, compared to those entering service in 2000, of a 50% reduction in fuel consumption and CO_2 emissions per passenger kilometre (of which 20%, that is just under half of the reduction, should come from engine technology) and a 50% reduction in Perceived Noise (Busquin et al., 2001). Although these are aspirational targets, they impose a tight timescale for manufacturers, and the expectation of some in the field is that open rotors will be seen on airliners by the end of the decade, (Spalart et al., 2010). For example, in 2007 easyJet announced plans to develop an 'easyJet ecoJet' by 2015 which would emit 50% less CO_2 than their current fleet, using open rotor technology.

Figure 1.6: Rig 145 testing, which took place between 2008-2010. Image reproduced with permission from Rolls-Royce.

There is general consensus that any future significant gains in efficiency must come from a major shift to a new technology. The two most promising designs are Geared Turbofans (Pratt & Whitney are now concentrating on this area with their PW1000G engine) and open rotors[10]. The former is likely to be quieter, but the open rotor will be better in terms of fuel efficiency. The huge financial investment needed to develop these designs from concept to production has led to several collaborative programmes between manufacturers, with significant government funding. These have included the New Aircraft Concept Research in Europe (NACRE) programme (2005-2009), the UK-led Omega project (2007-2009) which concentrated heavily on Advanced Open Rotor technology, the DREAM project which Rolls-Royce coordinates with funding from the European Commission, and the Clean Sky Joint Technology Initiative (2008-2013).

---

and 1999, Anderson et al. (2006). Efficiency savings must therefore play a crucial role in moving towards sustainability.

[10] A third option which has received less attention is the Ducted Contra-Fan, essentially an open rotor with casing. Rolls-Royce's Rig 141 was used to test this concept in 1990. The Counter-Rotating Integrated Shrouded Propeller (CRISP) is a separate, but related, concept which was investigated by MTU and Snecma in the mid-1980s.

Under DREAM, Rolls-Royce and Airbus have carried out three sets of modern open rotor testing. Rig 140, built for the first propfan tests in the late 1980s (and subsequently rebuilt as Rig 141), has again been rebuilt as Rig 145 for this new round of testing with different blade designs and blade number combinations, see Figure 1.6. Low-speed 0.2-0.25 Mach testing was undertaken in 2008, where different combinations of blade number, blade row gap and rotor speeds were trialled. High-speed 0.8 Mach testing took place in 2009, and further low-speed testing was carried out in 2010 using an optimised blade design, with increased blade chord and thickness and improved sweep for high performance. Throughout this thesis our primary interest is in predicting the impact of Unsteady Distortion Noise on community noise levels on the ground near airports and therefore we are particularly interested in the low-speed testing which is used to simulate take-off/approach conditions. High speed testing, simulating cruise, is more relevant to the assessment of cabin noise[11].

Testing results have shown that advances made since the 1980s have led to reductions in both the number of tones and the tone protrusion above broadband level seen in open rotor noise spectra. Although this is a commercially sensitive area, and therefore exact designs are not publicly available, broadly speaking noise reduction has been achieved through adjustments in blade design (sweep, chord, thickness, camber[12], tip shape), blade numbers and diameters (mismatched between the front and rear rows, see Parry and Vianello (2010)), adjustments in pitch[13] and tip speed (increased blade number allows a reduction in tip speed), and careful consideration of the installation, including using 'pylon blowing' to reduce peaks at harmonics of the front rotor BPF, see Figure 1.7. Thus tonal noise is still of primary concern, but broadband sources are becoming an increasingly important factor, Parry et al. (2011). There is confidence that noise regulations can be met but it is also likely the open rotor will not be as quiet as next-generation geared turbofans.

Little wind tunnel testing has been done to date specifically addressing Unsteady Distortion Noise, attempting to measure key turbulence parameters at the rotor face or the UDN contribution to overall noise levels. Wind tunnel operators aim to achieve very

---

[11] The relatively low fundamental frequencies of open rotor noise means 'active control' (cancelling noise out using loudspeakers) may be used within the cabin. Such systems have been used in Saab 340 and 2000 aircraft, Peake and Crighton (2000)

[12] When slicing through a blade at a particular radial station, high camber corresponds to a profile which is significantly curved.

[13] Pitch denotes the rotation of a blade about its pitch-change axis, which runs in the radial direction but whose axial position must be carefully chosen.

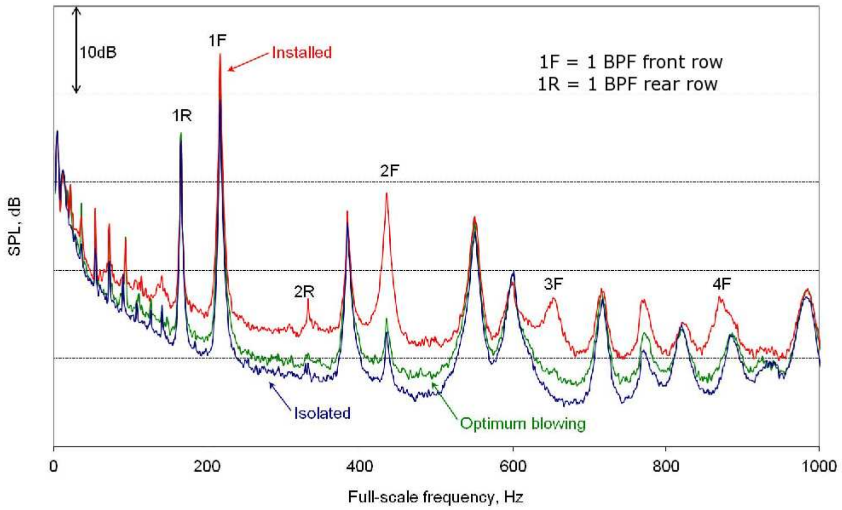

Figure 1.7: Figure reproduced from Ricouard et al. (2010). Installed = with the pylon in place, isolated = rotor alone. The large pylon, which connects the open rotor to the fuselage (shown in Figures 1.4 and 1.6), reduces the velocity of the air hitting the rotor in the region directly behind it. A system which blows air from the rear of the pylon can be effective in reversing this effect, thereby producing a more uniform flow onto the blades and reducing the level of certain tones.

low levels of natural turbulence and since atmospheric turbulence lengthscales do not scale with the rig, it may not be until full-scale outdoor testing takes place that atmospheric UDN will become an important factor (although the effect of distortion on turbulence generated by the airframe may appear in rig testing).

Wind tunnel testing is only one part of the current design phase of the advanced open rotor, there are also significant computational modelling programmes being run, and the development of better analytic models to predict noise levels is ongoing. In the second half of this introductory chapter we will review numerical, experimental and analytic work addressing noise specifically due to turbulence. Certain noise mechanisms are better understood than others, as they correspond to aspects of turbofan noise which have undergone decades of study. Distortion noise is expected to be more significant for the open rotor than the turbofan, due to the large rotor diameters (and therefore greater upstream streamtube radius), the lack of ducting, and the complex interaction between flow shed from structures upstream of the rotors and the rotor blades. It is therefore of interest to revisit past analytic work on UDN and extend it; this is the premise of this Ph.D.

As in the 1980s, key design questions for the open rotor include: blade number, rotor-

rotor spacing, rotor diameter, blade shape, position of pitch change axes and tip speed. Traditionally, propeller engines set one blade speed and then use pitch change to vary the thrust generated, whereas a key design feature of the open rotor is the ability to vary tip speed. There are two different configurations possible to achieve variable tip speed: Geared open rotors have greater tip-speed control, whereas Direct Drive open rotors avoid having a complex gearbox placed in the middle of the engine airflow. Besides the rotor itself, positioning of the engine and prediction of installation effects are crucial, and will affect noise directivities, (Ricouard et al., 2010). It is even possible for installation effects to be used to reduce noise in certain directions, for example careful positioning of engine ducts could help reduce cabin noise. Key installation design questions include: pusher vs. puller configuration (see Figure 1.8), blade-off/failure testing compliance, pylon position and shape, position of exhaust ducts, and the use of gearboxes.

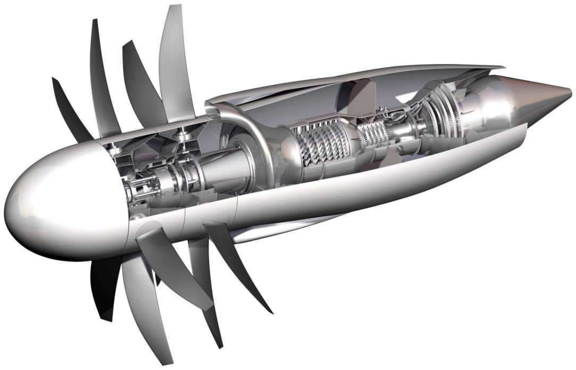

Figure 1.8: The puller configuration, shown above, has the rotor blades towards the front of the engine and is attached to the airframe downstream of the blades. Image reproduced with permission from Rolls-Royce. The rotor blades experience a cleaner inflow than in the pusher configuration, shown in Figure 1.1, which has the pylon upstream. Other upstream structures in the pusher configuration include the wing wake and exhaust flow (Pagano et al., 2009), making the rotor harder to optimise. Advantages of the pusher include potentially reduced cabin noise as the blades are further back on the aircraft.

Today, in 2011, rotor alone and rotor-rotor interaction noise can be fairly well quantified, but it is the interaction effects when the rotor is placed into atmospheric conditions, with the pylon and fuselage in close proximity, and with varying angle of attack, which are less well known. These effects are expected to mainly affect the tones generated by the front rotor, rather than the rear rotor. In this Ph.D. we address each of these features in the context of UDN, in particular by incorporating asymmetry into the model.

A note on noise certification

Noise regulations for airports in the UK are set at a number of levels. The International Civil Aviation Organisation (ICAO) has set increasingly strict certification conditions over time, as the frequency of flights increases. New aircraft today must comply with Chapter 4 regulations which mark a 10dB cumulative difference[14] from Chapter 3 which was in place for the 1980s propfan. Chapter 5 is expected to come in before long, and manufacturers are designing with this in mind.

As previously noted, tonal noise is more irritating than broadband and there are several different ‘weightings’ which attempt to take into account the increased annoyance level caused by pure tones. Each of these weightings only gives a representation, there is no one objective measure (Young et al., 2010) and since the 1980s standards have been developed primarily for turbofans. EPNL is currently the standard measure for certification, but McCurdy found that an alternative metric - A-weighted with tone/duration corrections - reduced the standard deviation between calculated results and people’s reaction to propfans.

In addition to the ICAO certification conditions, community noise contours around airports are also regulated, but a different metric is used for assessment of these contours (dBA). The difference between the dBA and EPNL metrics for typical turbofan spectra, and the difference for typical open rotor spectra are not the same, and this could be a source of discrepancy for future comparisons between engines, (Young et al., 2010).

It is not yet known exactly what regulations open rotors will be required to meet. For example, they could either be judged as a propeller or as an open fan, each of which is regulated differently. However, it seems that regulatory bodies would be keen not to exclude open rotors with the Chapter 5 target, due to their efficiency advantages.

1.2.3 Technological points of most relevance to our work

To summarise, open rotor technology has huge potential to address the need for the aviation industry to reduce its use of fossil fuels, and if oil prices continue to rise the business case for their use will continue to get stronger. Noise is seen as a potential barrier to full open rotor deployment; another new engine, the geared turbofan, is likely

---

[14] The ICAO regulations limit the total found when the measured noise at the three testing positions - takeoff, sideline and approach - is summed together. The Chapter 4 limit is 278.8 dB, Chapter 3 was 288.8 dB.

to be quieter but less fuel efficient. As part of the ongoing research effort in this area it is useful to develop quick analytical models for the many different aspects of open rotor noise. One aspect which has received less attention is that of Unsteady Distortion Noise, and in this thesis we focus on this particular mechanism. Little work has been done on the significance of UDN relative to other open rotor sources, but manufacturers are particularly interested in UDN generated at approach, when there is high distortion (i.e. a strong streamtube contraction into the rotors), and lower tonal levels from other sources.

Technological issues which we consider in the context of Unsteady Distortion Noise in this thesis are

- the presence of the 'bullet', and how this affects the mean flow onto the rotors.
- installation features which lie upstream of the rotors, including the pylon and the wing, and the use of appropriate upstream turbulent spectra to model these different sources.
- the introduction of asymmetries in the mean flow when the engine is installed (rather than in isolated testing conditions), including asymmetries due to the presence of the fuselage.
- angle of attack[15], which varies between about -/+3° for the pusher AOR configuration, but can be up to 12° for the puller configuration due to the close proximity of the wing.

Although we concentrate on the specific application of open rotors in this work, much is also relevant to turboprops, contra-rotating ducted fans and wind turbines.

1.3 Academic context: *review of the literature*

Within turbomachinery aeroacoustics, periodic interactions between the air flow and solid surfaces give rise to tonal noise. Analytic investigations of the most significant tonal sources for open rotors include Hanson (1985), Parry (1988) and Whitfield et al. (1990). In addition, the interaction of turbulence with solid surfaces is a source of broadband

---

[15] Angle of attack, also known as incidence, denotes the angle between the flight direction and the axis of the rotor.

noise, due to the random unsteady pressure field induced via the condition of zero normal velocity there. However, when turbulence is distorted, for example by a strong streamtube contraction, the eddies can become long enough to give rise to a correlation between the forces exerted on adjacent blades, and it is this which can then lead to a quasi-tonal noise component in addition to the broadband, see Figure 1.9. As noted by Hanson (1974), the peaks which arise due to correlated turbulence are 'narrow-band random noise', somewhere between pure harmonic and broadband. An infinitely long turbulent eddy would produce a tonal spike, but real eddies produce peaks with non-zero width, and it is the area under each peak which is of most interest. Increased blade-to-blade correlation (e.g. due to longer, thinner eddies) will lead to higher level, narrower peaks (Paterson and Amiet, 1982).

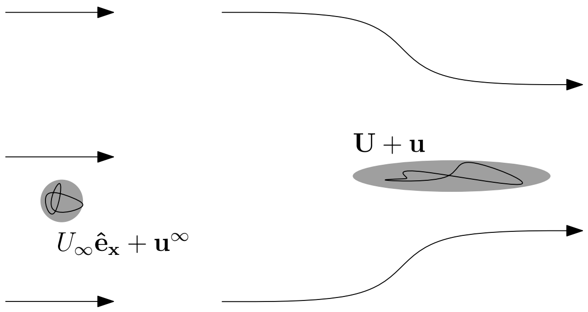

Figure 1.9: Illustration of the Unsteady Distortion Noise mechanism. A turbulent eddy can be thought of as a spherical-ish blob of moving fluid which has angular momentum (Davidson, 2004), and such structures naturally occur in the atmosphere. As turbulent eddies undergo a streamtube contraction, such as that induced by an open rotor, they are stretched. The long thin eddies then provide coherent forcing upon the rotor blades as they are 'chopped' many times by adjacent blades at the same location, leading to both tonal and broadband noise. The velocities denoted in this figure are upstream axial velocity, U_∞, upstream turbulent velocity, $\mathbf{u}^\infty$, mean flow velocity near the rotor, $\mathbf{U}$, and turbulent velocity near the rotor, $\mathbf{u}$.

There is much active research into aeroengine noise arising from turbulence, and in this half of the introductory chapter we give an overview. We note that distortion effects are often neglected in aeroacoustic research and testing. When undertaking this review, two approaches were used in order to get as complete a picture as possible. Firstly, papers from the recent AIAA/CEAS Aeroacoustics Conferences (2008-2011) and the 2010 CEAS-ASC workshop on open rotors were examined to see which areas of turbulence interaction noise are currently receiving the most attention. Secondly, a thorough literature search was done for publications concerning the interaction of blades with turbulence, which yielded in excess of 90 papers from the last 40 years. Of these, 18 were considered to be of the most direct relevance to this thesis, and these were analysed in detail.

1.3.1 Noise arising from turbulence

As already described, the tonal component of Unsteady Distortion Noise arises from blade loading pulses which exhibit coherence between blades. Hanson (1974) was the first to show the significance of the stretching of eddies which can take place during static testing, due to streamtube contraction. In experiments, he found streamwise turbulent length scales of over 100 rotor diameters, and correspondingly the forces on the rotor blades were found to be correlated for up to a second, see Figure 1.10. UDN was at that point recognised as a potentially significant noise source and could be used to explain results which had previously been attributed to fixed inflow distortion.

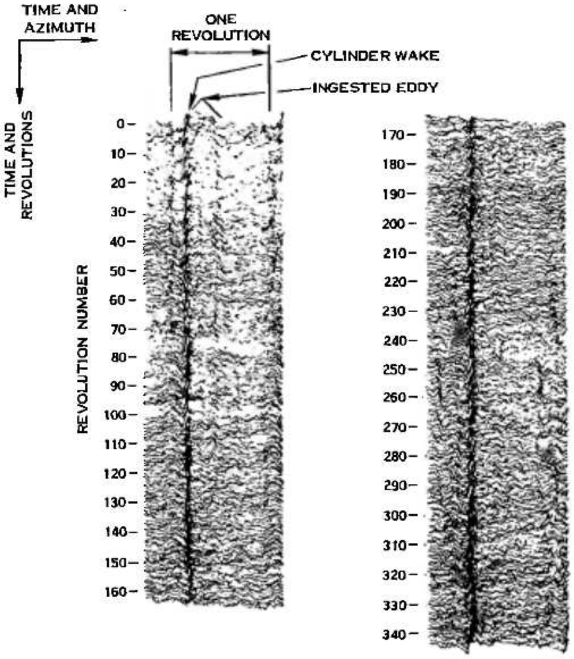

FIG. 12. Inlet distortion history using blade pressure signals.

Figure 1.10: Figure reproduced from Hanson (1974). The dark line indicates a very long eddy which interacts with the rotor blade at the same azimuthal position for hundreds of revolutions.

Although axial stretching is much reduced in flight (due to the reduced speed differential between the upstream velocity and the velocity at the rotor face) which leads to a reduction in tonal UDN levels, a broadband component is still present. In addition, the effects of transverse stretching due to asymmetries of the mean flow have not been fully quantified previously; most studies restrict themselves to the axisymmetric case. There are many potential sources of UDN, including externally generated turbulence, secondary inflow distortions and the boundary layers of ducts and blade wakes. However, we note that boundary layer and blade wake turbulence is less likely to exhibit coherence (Hanson, 1974), as it may not have time to undergo significant stretching.

These several sources of turbulence also give rise to other types of turbulence-solid body interaction noise which are distinct from UDN, but nonetheless can be examined to give insight into the variety of analytical, computational and experimental approaches commonly used. Firstly, the creation of turbulence as flow passes over structures on the airframe, for example high-lift flaps and slats, is itself a source of noise (Terracol and Kopiev, 2008). Such structures which lie several rotor diameters upstream of the rotor may produce turbulence which is significantly distorted as it travels towards the rotor, and therefore could, in addition, form a source of UDN. In Chapter 3 we indeed find that a significant proportion of the distortion induced by an idealised rotor takes place within an axial distance of 10 radii from the rotor face. Secondly, turbulent self-noise arises when turbulence produced by one part of a rotor interacts with another part of the same rotor. For example Turbulent Boundary Layer Trailing-Edge Interaction (TBL-TE) is a dominant noise source for wind turbines (Kamruzzaman et al., 2008), as well as being a subject of active research within aeroengine aeroacoustics (Pagano et al., 2009). Towards the trailing edge of a blade the boundary layer plays an important role, and Carolus and Stremel (2002) found that in this region the precise structure of ingested turbulence becomes less of a factor. Thirdly, when considering open rotor rather than turbofan engines, rotor-rotor interaction noise is generated when wakes and tip vortices from the front rotor hit the rear rotor (Redmann et al., 2010, Kingan and Self, 2009). As well as the mean flow component of the wakes, which produces tones when it interacts with the second row, the turbulent part gives rise to broadband noise (Blandeau et al., 2009). The corresponding phenomenon within ducted turbofans is the turbulent aspect within both fan-vane and rotor-stator interaction, although in both those cases one row is stationary and thus the velocity differential between the two rows is much smaller than for open rotors. Fourthly, an issue primarily within ducted turbofan aeroacoustics is interaction between the turbulent casing boundary layer and the rotor tips. Correspondingly for an open rotor is the issue of the interaction between the hub boundary layer and the roots of the rotor. Of these four mechanisms, rotor-rotor interaction noise from turbulent wakes involves a similar mechanism to UDN - unsteady forces impinging along the entire leading edge of a blade (rather than solely the root or tip) and giving rise to unsteady lift forces across it.

Once the turbulence source of interest has been specified the next key question in any analysis is deriving an appropriate model for this impinging turbulence, and central to this is the issue of isotropy and homogeneity vs. anisotropy and/or inhomogeneity. On the one hand, turbulence in turbomachinery is clearly not always perfectly isotropic and homogeneous, for example Hanson and Horan (1998) have used CFD to plot the turbulent kinetic energy behind a rotor, to illustrate the inhomogeneities present. Turbulence generated in the atmosphere is also not truly isotropic as it arises from a shear flow (Simonich et al., 1990), and certainly varies with height over topographical features. The assumption of homogeneity in each horizontal plane will also not hold in all conditions. However, it is very usual to use isotropic, homogeneous models for simplicity, and there are often reasonable justifications for doing so. For example, between the front and rear rotors it is believed there is not sufficient distance for significant distortion to take place, and it is therefore possible to use homogeneous, isotropic models for rotor interaction noise (Blandeau, 2011). Grid generated turbulence is often found to exhibit properties accurately described by an isotropic spectrum (Paterson and Amiet, 1982, Mish and Devenport, 2006a, Devenport et al., 2010) and this allows validation of isotropic analytical models through comparison with experiment. However, there are instances where grid turbulence has been seen to deviate from isotropic (Amiet, 1975).

Thus certain effects are often neglected, for example anisotropy can lead to ‘haystacking’ around tones (Stephens et al., 2008). Devenport et al. (2010) note that *‘wind tunnel grid-turbulence studies and isotropic turbulence calculations may significantly underestimate angle of attack effects seen in practical applications where anisotropic inflow turbulence is common’*, and this is of particular relevance to our work on incidence in Chapter 5. Anisotropy plays a key role in UDN generation, and much of the work in this thesis is concerned with deriving a model which accounts for the stretching of turbulence before it hits the rotors. Different methods for modelling inhomogeneity and anisotropy are discussed in more detail in Section 1.3.3.

When assessing turbulence, and the noise arising from turbulence, there are a range of difficulties inherent whichever method is chosen: experimental, analytical or computational. Experimental measurement is typically time-consuming and expensive, in addition to which quantities which you might wish to observe in order to compare to theoretical models may be impractical to measure, or require a very large number of measurements. It is challenging to formulate sufficiently accurate, and yet sufficiently simple, analytic models which perform well for a range of real-life situations. Computational Fluid Dynamics (CFD) calculations are associated with long run-times and it is still necessary to determine appropriate turbulence models to input into any numerical model. Next we discuss each of these approaches.

1.3.2 Use of experimental measurements

As the specific structure of ingested turbulence is a critical question in all of the turbulence noise problems listed above, ideally we would gain a more detailed knowledge of that structure from experiment. Hot-wire anemometry can be used to measure velocity correlations, for example. In addition, both computational and analytic work can overpredict tonal levels when compared to experiments, as not all real-life aspects of the flow-field can be included within any model and this tends to lead to the purely tonal components being over- or under-estimated. Mish and Devenport (2006a) noted a lack of experimental work available to validate the range of theories which have been developed around turbulence-blade interaction. This is partly due to a problem inherent in turbulent analysis, namely the lack of general models applicable to a wide range of situations (Davidson, 2004). Often each individual situation must be considered separately.

In addition to measurements of the turbulence structure itself, experimental measurements of the noise arising from turbulence are scarce, due to difficulties in separating this from the other rotor sources of varying strength, frequency and directivity (Paterson and Amiet, 1982, Simonich et al., 1990). Commercial sensitivity has also restricted experimental measurements of open rotor noise available in the open literature to some extent. The vast majority of testing is static, in wind tunnels, rather than in flight, and thus UDN is not often considered. Wind tunnel experiments do not include noise from ingested turbulence from external sources as a system of honeycomb grids is typically used to remove all turbulence and very low levels of turbulence can be successfully achieved, (Kamruzzaman et al., 2008). Attempts are also made to minimise incoming turbulent intensity in most flat plate studies (Carolus and Stremel, 2002).

Experimental measurements of leading edge noise arising from impinging turbulence tend to consider grid-generated turbulence only, where the aim is to create isotropic, homogeneous turbulence, (e.g. Staubs et al. (2008)). These grids are themselves noisy, and Devenport et al. (2010) recently used a special anechoic facility to overcome this and other methodological problems, such as the distortion of turbulence by angle of attack corrections.

We now highlight some key studies of turbulence-blade interaction noise spanning the last four decades which include experimental measurements, often in order to validate an accompanying theory. As already described, Hanson (1974) first observed the stretching of atmospheric turbulence eddies, which improved understanding of the mechanisms which lead from turbulence to noise. The aim was to compare theoretical lift to measured pressure for calibration, and then predict the sound. These experiments showed UDN to be a dominant noise source for subsonic blades in static testing. We note that a more complete prediction scheme for UDN is therefore of particular importance in extrapolating from static testing data to flight test results.

Elsewhere, much research has been concerned with a single airfoil immersed in turbulent flow, but the majority of investigators have considered isotropic turbulence. Amiet (1975) and Paterson and Amiet (1982) developed turbulence-airfoil interaction theories and then compared these to measurements of the Sound Pressure Level (SPL) due to an airfoil in a stream of grid-generated turbulence. They compared both high and medium turbulent intensity producing grids and found their inviscid, flat-plate theory gave reasonable agreement with measurements. No adjustable constants were used to fit their predictions to the results. Key quantities were shown to be the spanwise correlation length and the Power Spectral Density (PSD) of vertical velocity correlations. Carolus and Stremel (2002) also compared the turbulence produced by several different grids and honeycomb structures. The honeycomb was found to reduce the integral lengthscale and turbulent intensity somewhat. In contrast, the square grids led to high turbulent intensities and small values of the turbulence integral length scale. Devenport et al. (2010) also looked at an airfoil in grid-generated turbulence, but as mentioned above, using novel experimental techniques to improve results. They found little change in leading edge noise as angle of attack was varied in the case of isotropic turbulence, but predicted greater effects for the anisotropic case. Mish and Devenport (2006a) have also considered angle of attack effects experimentally and found differences between their results and variable angle of attack theory. They attributed this to the difference between a flat-plate model and the distortion induced by a real blade's leading edge.

Next we turn to three studies of ducted configurations, but where the stretching of turbulence is taken into account or anisotropic turbulence considered.

Hanson (2001), using Glegg's 3D cascade theory, further developed theory for both isotropic, homogeneous turbulence (specifically the Liepmann spectrum) and axisymmetric but axially stretched turbulence, convected into a cascade of stators. He compared his theoretical results with NASA experimental data of rotor noise - a Pratt & Whitney 22 inch fan model, an Allison 22 inch fan with swept and leaned stators, and a Boeing 18 inch fan. (We note that these sets of data are commonly used as benchmarks, for example see Cheong et al. (2006).) Of particular interest in Hanson's work was the effect of lean and sweep, as well as the possibility of accounting for inhomogeneities in the turbulence by appropriate averaging. Turbulent intensity and integral length scale were used as free parameters when fitting the data in that case, and agreement was good.

Considering the issue of anisotropy, Atassi and Logue (2009) recently looked at the interaction between anisotropic turbulence and a ducted fan, using a uniform distortion model. They compared their results with low-speed experiments (Stephens et al., 2008), however they found that the isotropic expressions fitted the data best, perhaps because their theory assumed turbulence across the whole span of the blades whereas the source of turbulence in the experiments was solely the duct wall boundary layer.

Finally, Koch (2009) undertook an experimental study of fan inflow distortion noise. The effect of turbulence shed from upstream radially orientated cylinders upon the noise spectra was considered with a honeycomb used to remove other incoming turbulence. The asymmetric Strouhal shedding led to extra peaks in the noise spectra, as well as raising the broadband level.

1.3.3 Analytic models

The open rotor design is younger than the turbofan. Especially during these early stages, fast analytic or semi-analytic methods which compare well to full CFD are advantageous, but necessarily will involve some degree of approximation. Here we review the development of theoretical turbulence-blade interaction modelling.

As noted by Paterson and Amiet (1982), the first analytical models of airfoil acoustics concentrated on relating a given set of blade forces to the resultant noise. From the mid-1970s, researchers widened their scope and began to consider in more detail how an impinging gust gives rise to forces on a blade in the first place, and thus to noise. A steady progression has then been seen whereby extra effects have been added, to determine more and more sophisticated airfoil response functions. To the incompressible, 2D model of an isolated airfoil in rectilinear motion (Sears, 1941) have been added compressibility, skewed gusts, non-convected gusts, quasi-3D strip theory and other cascade models (such as Smith (1973)), and rotation of sources. More realistic blade geometries have been considered including effects of camber, thickness, angle of attack, skewed 3D gusts, and non-compactness. The recent review in Mish and Devenport (2006a) gives detailed references for these various extensions. Pushing back the boundary in one of these directions may lead to sacrifices in other areas, or restrictions in the range of validity. For example Glegg's 3D cascade theory, as used by Hanson and Horan (1998), requires the approximation of infinite span.

In our present work we consider the surface pressure in response not just to a single gust but to a complete turbulent inflow field. Thus we aim to relate the distorted turbulence spectrum to the upwash spectrum.

Turbulence distortion

As previously mentioned in section 1.3.2, Amiet (1975) and Paterson and Amiet (1982) developed a foundational model for the far-field noise due to a single airfoil in terms of the turbulent energy spectrum and an airfoil's response function, and then compared this to experiment. Like other turbulence interaction theories previously developed (Sharland, 1964, Mani, 1971, Homicz and George, 1974) stretching of turbulence is not accounted for within their framework; the turbulence is considered isotropic.

Once the experiments of Hanson, and also Cumpsty and Lowrie (1974), had shown the importance of turbulent stretching, several models for this mechanism emerged. Hanson used a pulsing model to represent discrete, radially compact eddies, and found an expression for the average energy spectral density due to each eddy. He used a statistical distribution of discrete eddies rather than considering the complete turbulence spectrum. This involves assuming the turbulence takes the form of discrete eddies, whose characteristics are random variables, giving a 'pulse' theory formulation. Hanson assumed eddies acted as point forces in the radial direction. In this framework models must be input for the lift pulse due to an eddy and the joint probability density functions for turbulent eddy characteristics (lengths/widths etc.). Hanson (2001) has also developed a method whereby random offset times within turbulent velocities can be used to represent inhomogeneity.

In a pair of papers (Simonich et al., 1990, Amiet et al., 1990) a full method of UDN prediction was laid out which comprised several self-contained blocks, of which one is the distortion of the incoming turbulence. The analysis in this thesis follows a similar structure, as sketched within the Chapter 2 outline on page 33. They modelled a flat plate in rectilinear motion, and thus cascade effects were not treated. Crucially though, differential drift between particles on neighbouring streamlines was taken into account, thus allowing the consideration of non-uniform distortions. They were concerned with the case of a helicopter rotor in hover, vertical ascent and forward flight. An assumption of their model is that fluid planes upstream of the rotor remain fluid planes downstream. This becomes more valid as the scale of turbulence decreases, hence they treated only turbulence of lengthscale less than the scale of contraction. They plotted the PSD given different values of the distortion tensor. When comparing the distorted and isotropic cases they found widths of peaks in the noise spectra and depths of troughs varied most significantly, whereas the heights of peaks were comparable. In addition to the total amount of distortion, they also considered in some detail the effect of the direction of distortion. When distortion acts primarily along the axis of the rotor, the upwash velocity on the blades is reduced, leading to lower overall noise and reduced width peaks compared to the isotropic case within their model.

Majumdar (1996), in part formalising work by Cargill (1993), developed Simonich et al.'s analytic framework further. He used an approximate solution for the full distorted velocity field (rather than the assumption that fluid planes remain planes) and included cascade effects. The significant quantities within the expression for far-field radiated sound were found to be the distorted turbulence spectrum at the rotor face, and the Bessel functions which govern the radiation. Non-uniform distortions were considered (although still with some restrictions, such as axisymmetry) by applying Rapid Distortion Theory to an isotropic upstream turbulent field. This is the approach we extend, and will be laid out in detail in Chapter 2. Wright (2000) added effects of upstream swirl in the mean flow field to this model. In an alternative approach, Atassi and Logue (2009) have treated uniform turbulence distortions using an anisotropic spectral density tensor, with three constant distortion coefficients, and we discuss the direct use of anisotropic turbulence models further in Chapter 3, §3.3.2. Within their uniform distortion model, increased axial stretching was found to lead to a shift in acoustic energy towards the lower frequencies.

As mentioned in §1.3.2 in recent experiments Mish and Devenport (2006a) considered an airfoil immersed in isotropic turbulence for various angles of attack, and concluded that significant distortion takes place near to a blade's leading edge. They noted differences between the theoretical distortion found with a flat plate model (with large velocity gradients) used in the analytic model of Reba and Kerschen (1996), and real distortion by a blade with thickness. They went on to develop an analytic model for the observed distortion by modelling the leading edge as a sphere of the same radius. Similarly, Devenport et al. (2010) highlighted the important role of vorticity just upstream of the leading edge.

Turbulence properties

Whether modelled before or after distortion, the properties of the upstream turbulence will affect the UDN generated by a rotor. Increased turbulent intensity produces an increase in SPL at all frequencies (Carolus and Stremel, 2002, Hanson, 2001) whereas varying the turbulent integral lengthscale, L, has a more complex effect. SPL is found to increase as L increases only until a critical value is reached.

Turbulence, by its nature, will always contain a very wide range of lengthscales but L gives some measure of the average size of eddies. The role of L has been considered by Majumdar and Peake (1998), Hanson and Horan (1998) and Atassi and Logue (2008), and varying L appears within the latter's model to have greatest effect in the lower frequency range. The critical value of L, above which SPL does not increase, is believed to be related to the lengthscale of the streamtube radius. Eddies much larger than this will not appear as eddies to the rotor but rather as a varying background flow. However, Hanson, looking at noise and turbulence data from Boeing, believed it was not the mean eddies but those which were larger than average which dominated noise generation. In the high distortion case, it may be that it is the large eddies which give rise to tonal noise, whereas the smaller eddies have a similar effect as at low distortion (Majumdar and Peake, 1998) as they of course do not become very long even after stretching.

Regarding tonal noise, peaks are found to have higher magnitude and narrower width for increased L. At high frequency the results of Atassi and Logue showed little L dependence. Carolus similarly concluded that the influence of inflow turbulence characteristics diminishes in the high frequency range.

Finally we note the role of the intersection area between an eddy and a rotor blade, (Amiet et al., 1990). It is in part through changes to this quantity that we expect differences to arise in the asymmetric cases we consider, compared to the axisymmetric case.

High and low frequency limits

Certain effects become more important depending on whether a high or low frequency regime is being considered[16]. As one example, Carolus and Stremel (2002), looking at broadband noise due to incident turbulence, found the blade surface pressures of a rotating fan were dependent not only on the turbulent parameters but also on chordwise position, which side of the blade was being considered and on frequency range. From an analytical modelling point of view, as frequency is increased noise can be more and more accurately determined by representing the blade forces by point sources at the leading edge (Amiet, 1975, Evers and Peake, 2002). Also, long wavelength/low frequency disturbances will essentially see rotor blades as flat plates, whereas effects of blade thickness and geometry as well as boundary layer pressure fluctuations will be significant for short wavelength/high frequency eddies, see Mish and Devenport (2006a) and Atassi and Logue (2009) respectively. In the experiments of Mish and Devenport, a previously unseen effect was found; at low frequencies there was a reduction in spectral level as angle of attack was increased. However, certain effects, such as non-zero camber, diminish in significance when results are integrated over the full range of wavenumbers contained in an incoming turbulent field, as shown by Evers and Peake (2002).

Interaction between blades (cascade effects) will be critical for larger disturbances, whereas at high frequencies turbulence ingestion noise is caused by small eddies to which each blade appears isolated; the resultant noise in that case is expected to scale with blade number B. The critical frequency separating these two regimes was considered by Cheong et al. (2006) for the case of a 2D cascade of flat plates. Thus, for small eddies, both decreased chopping and reduced coherence between blade forces leads to broadband rather than tonal noise.

Wavenumber and frequency considerations come into our analysis in several ways. In Chapter 2 an expression for the stretched turbulence spectrum at the rotor face is derived, and requires the modulus of the wavevector $\gg 1/$(measure of distortion), and we show this is indeed a reasonable assumption. We also use a flat plate approximation in our blade response model.

---

[16] For a fixed sound speed, c_0, increasing frequency, ω, will lead to decreasing wavelength, $1/|\mathbf{k}|$, since $c_0 = \omega/|\mathbf{k}|$.

Three-dimensional effects

Efforts are continually being made to extend existing 2D theories to better include 3D effects, such as including radial variation (e.g. Majumdar and Peake (1996)) or modelling annular rather than rectilinear geometries (e.g. Atassi and Logue (2008)). Within a lengthy analysis 3D effects are often not included at every stage; Glegg's harmonic cascade theory uses a 2D mean flow and geometry, but a 3D unsteady input excitation and response and thus the spanwise wavevector component is included.

Dividing the blade into 2D strips is a common approach whereby we neglect radial gradients when calculating the blade response (Majumdar and Peake, 1998, Cheong et al., 2006). There are several variations of strip theory, and we follow the analysis of Smith (1973) in our work. However, the strip theory approximation breaks down in certain situations. For example, when duct modes are near to cut-off[17] one expects larger unsteady amplitudes, leading to spanwise motion. In addition, for large radial wavenumber (i.e. very small radial lengthscales) radial gradients can become large. In the analysis of Chapter 2 it will be necessary to impose limits on the integral over radial wavenumber to account for this.

Stators and ducted fans

We note, for completeness, that much work has also been done in the field of turbulence impinging upon stators. A key difference in that case is that the circumferential mode number is given by $nB - kV$ (Tyler and Sofrin, 1962) where B is the blade number, V is the number of stator vanes, and n and k are integers. Thus the modes are spaced out, and it is possible to choose B and V so that the first mode is cut-off[18]. In contrast, open rotors, with their counter-rotating blade rows, produce modes of order $m + lB$, which can take all integer values.

The interaction of turbulence with ducted rotors is of interest since as the bypass ratio of turbofans is increased, fan noise becomes more significant, (Dieste and Gabard, 2009). Atassi and Logue (2008) looked at the broadband noise of a fan within an annular duct caused by ingested isotropic turbulence, where distortion was not accounted for. They

---

[17] A cut-off mode is one where the axial wavenumber contains an imaginary component, and thus the mode decays away from the source.

[18] By fixing the circumferential mode number at a given tonal frequency, for example a multiple of the BPF, the axial wavenumber is forced to take imaginary values for disturbances of that frequency. Thus any particular tone can be cut-off.

investigated varying both the turbulence lengthscale and flight speed. The change in noise level as the turbulence lengthscale was varied depended on both frequency range and Mach no., with the largest differences being observed for low to medium frequencies at high Mach no.s. They also found that as the tip speed approached the flight speed the difference in height between peaks and troughs of the spectrum diminished.

Majumdar also treated the ducted rotor case, adapting his open rotor analysis by adding a condition of zero penetration at the duct radius. A simplifying assumption of parallel flow at the rotor face was used in that case. The overall spectrum was found not to be significant affected, but the directivity was altered.

1.3.4 Computational approaches

Today, effects of turbulence are often tackled using computational simulation. Extensive open rotor studies are currently running at Germany's DLR research centre, the French aerospace lab ONERA, and NASA in the US. Although powerful computing tools are now available, there are still limitations as to what can be achieved within a reasonable timeframe, and many studies restrict themselves to a few wavenumbers and frequencies only, as noted in Mish and Devenport (2006a). Disadvantages of CFD include the long run times needed for low frequencies, and the small grid and step sizes needed for high frequencies. Our focus is on developing a quick analytic framework but here we highlight some commonly used computational methods. Wang et al. (2006) provides a detailed review of current computational techniques used to predict flow-generated noise.

Full simulation of all the fluid dynamics and acoustics can be achieved with Direct Numerical Simulation (DNS), but this is restricted to fairly low Reynolds number and simple geometries. Large Eddy Simulation (LES) may also be used in this way, but in such simulations scales smaller than the mesh are modelled, rather than fully resolved.

Hybrid methods take a full non-linear approach near the source, but then use a simpler analytic model for the far-field noise, for example Lighthill or Linearized Euler (Deconinck et al., 2010). Thus, for example, LES can be used near the source and then coupled to an acoustic analogy model or Computational AeroAcoustics (CAA) code for the radiation.

Finally, the simplest computational codes model only the aerodynamics and acoustic sources and then compute the radiation using the acoustic analogy. Reynolds-Averaged Navier Stokes (RANS) is one such method, used to provide statistical properties only.

In all cases very careful consideration of boundary conditions is required to avoid spurious reflections. Resolving all scales and implementing non-reflecting boundary conditions can be particularly tricky for turbulent flow fields (Gloerfelt and Berland, 2009). Issues can also arise when trying to decide upon a realistic form for the turbulence input. Appropriate models for different forms of turbulence, such as within the boundary layer, can be input into CFD either using an analytical method (where the key input parameters are determined either from experiment or other simulations) or using a numerical method. Approximations may be made, such as using a flat plate boundary layer turbulence model rather than the full boundary layer over a real geometry (Carolus and Stremel, 2002). The anisotropy of turbulence is also difficult to treat as well as more computationally intensive. Many computational studies therefore also assume an isotropic/homogeneous turbulent flow - Kamruzzaman et al. (2008) recently looked at coming up with a simple way to account for anisotropy within RANS.

The optimum positioning of the engines of an open rotor on the airframe is still a somewhat open question (Envia, 2010) and ONERA have found within their CFD work that installation effects are of particular importance (Boisard et al., 2010). To study these effects in more detail, Omaïs and Ricouard (2010) at Airbus have implemented a RANS $k-\omega$ model for the pylon wake and found that the front BPF tones and azimuthal directivity were most affected. The role of the pylon wake is a motivating factor in our work considering flow asymmetries.

1.4 Summary

In summary, much work has been done on turbulence interaction noise to date but the distortion mechanism is not always modelled, with many studies restricted to the isotropic case. Since the illuminating experiments of Hanson in 1974, as far as we are aware, there have been no further experimental studies where the stretching of real atmospheric turbulence by a rotor has been quantitatively assessed. Certainly, this mechanism is not routinely considered during flight tests where there are many competing sources.

There has also been less attention given historically to non-axisymmetric flows. Our review in this chapter has highlighted many reasons why it is useful to consider the asymmetric case. Simonich et al. (1990) noted the importance of the direction of distortion, in addition to its strength. Using Rapid Distortion Theory they calculated distorted vorticity fields but did not produce full sound spectra. Secondary inflow distortions due to asymmetric installation features are also of much current interest.

This thesis builds in particular upon the work of Cargill (1993) and Majumdar (1996). Both these authors highlighted areas which could be revisited within their analytic framework which we now address. Cargill neglected radial variation of the distortion at the rotor face and differences in drift time, both of which can be significant (Paterson and Amiet, 1982, Hunt, 1973). Majumdar incorporated these effects in the axisymmetric case, but neglected the azimuthal angle dependence within the amplitude of the distorted velocity at the rotor face. We have now corrected this, allowing extension to the asymmetric case. Majumdar also noted the need to incorporate more realistic flow fields as well as non-uniform cross-section effects.

Our research aims are therefore as follows:

1. To re-evaluate Majumdar's analysis for the calculation of UDN, and to extend it to the asymmetric case.

2. To consider the important case of rotor incidence, which commonly occurs during flight. What effect will this particular form of asymmetric distortion have on UDN radiated to the far-field?

3. To incorporate realistic features of the mean flow into a next generation AOR, such as due to the hub (bullet) and fuselage, and installation features.

4. To undertake a thorough investigation of appropriate turbulence models and integral lengthscales to use in a prediction scheme for UDN, in order to allow manufacturers to successfully calibrate between rig testing and flight data.

In Chapter 2 we address point 1 above and find that, in order to extend to the asymmetric case, a reformulation of the analysis is required. Next, in Chapter 3 we improve the mean flow field model, but still within the axisymmetric framework. We consider the effects of the bullet and rear blade row as well as variable blade circulation along the span. We also address point 4 in the second half of Chapter 3. In Chapter 4 we extend the analysis to the asymmetric case and incorporate non-axisymmetric mean flow features for the first time, modelling the presence of the fuselage or a second rotor adjacent to the first. In Chapter 5 we consider the case of turbulence distortion into a rotor at incidence, and the effect this has on the far-field radiated sound.

Crucially, our work now allows for the use of any, not necessarily axisymmetric, mean flow within a fully detailed UDN prediction scheme.

Chapter 2

Axisymmetric Rotor Systems

2.1 Chapter outline

In this chapter we detail the key components of our analytic model for calculating the Unsteady Distortion Noise of an Advanced Open Rotor. This model extends previous work by Majumdar and Peake (1998), clarifying the role of extra terms which arise due to the dependence of the distortion amplitude upon azimuthal angle, ϕ; these terms were neglected in their work. The expressions for the distorted turbulence spectrum, blade pressures and radiated noise are all corrected. Our aims are always two-fold. Firstly, to gain insight into the problem by carefully examining quantities found analytically at intermediate stages on the way to the full noise calculation. Secondly, to produce computed results for the full noise spectrum, to allow comparison with other experimental and theoretical results. The schematic below gives the structure of our analysis. Different blocks are adjusted in each chapter, and where different models are used or expressions found in later chapters these are indicated in red.

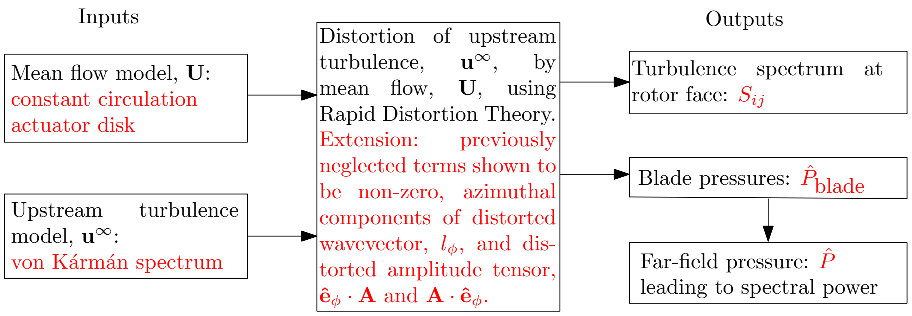

2.2 Calculating the turbulent perturbation, u

Our method of UDN calculation involves calculating several different components of the fluid velocity at different stages. Under suitable assumptions, described at each stage, the non-linear interactions between these components can be neglected. In addition, different physical assumptions are appropriate to each component, in particular concerning incompressibility. At all stages the flow is considered inviscid.

We begin by determining an expression for the distorted turbulent perturbation found at the rotor face, due to an isotropic turbulent field far upstream. Accurately modelling a turbulent velocity field while preserving an analytically tractable set of equations often poses a significant challenge. For this reason several, fairly limiting, assumptions are often made when considering a turbulent field. The most common of these assumptions is isotropy, which also implies homogeneity (Batchelor, 1953). In particular, atmospheric turbulence is often modelled as isotropic, and we will look in more depth at this approximation in Chapter 3. However, in certain situations, for example when the presence of solid boundaries provides a nearby source of vorticity, anisotropy of turbulence can play a significant role and accurate results may depend upon taking this into account. Unsteady Distortion Noise is a clear example of this, where the elongation of eddies in the axial direction leads to far higher tonal noise than would be experienced were the turbulence isotropic at the rotor face (Hanson, 1974).

Instead of attempting to model the turbulent field at the rotor face where experimental measurements are scarce, Majumdar and Peake (1998), building upon work by Cargill (1993), developed a method to assess the distortion of turbulent eddies as they travel downstream towards the rotor using Rapid Distortion Theory (RDT). RDT is concerned with calculating the change in a small velocity perturbation (in this case, the upstream turbulent field) as it is convected by a dominant, distortive, potential mean flow. In this way it is possible to quantify turbulent anisotropy at different points in the flow, while still using the more straightforward approximation of isotropy far upstream. Majumdar and Peake thus derived an expression for the spectrum of turbulence at the rotor face in terms of the spectrum of turbulence far upstream. A discussion of other approaches to modelling UDN was given in §1.3.3.

The work of this Ph.D. has incorporated new axisymmetric features into Majumdar's method (Chapter 3) as well as further extending the theory to asymmetric systems (Chapters 4 and 5). In re-examining the details in order to make these extensions, certain terms which were originally neglected, such as the contribution of the azimuthal wavenumber k_ϕ, have been shown to be non-zero, even in the axisymmetric case. Thus in this chapter we present the full analysis for calculating Unsteady Distortion Noise in an axisymmetric system.

2.2.1 Rapid Distortion Theory (RDT)

Firstly we describe Rapid Distortion Theory, which is the method we use to calculate the velocity field at the rotor face, given the upstream turbulence field.

Background

Batchelor and Proudman (1954), building on earlier work by Taylor, considered the effect of a uniform distortion on an isotropic turbulence field (in fact, uniform pure strains only as the effect of rotation is straightforward). The turbulent eddies are assumed to be distorted by the mean flow before they can exchange energy with each other, hence the term ‘rapid distortion’. The restriction of this analysis to uniform distortions only means explicit expressions for the downstream perturbation velocities can be determined without integrating over the entire history of the flow. The approximation of uniformity will be valid only over restricted portions of any real background mean flow. For our purposes the distortion of a turbulent eddy with a lengthscale comparable to that of the rotor is of particular relevance, as these are believed to contribute most to tonal levels. Distortion of these eddies will certainly not be uniform at different axial locations and will also vary between the interior and the edge of the eddy.

Hunt (1973) went on to extend RDT to situations of non-uniform distortion induced by the presence of a solid body, and to satisfy the condition of no-penetration on that body. Hunt starts with the full Navier-Stokes equations and proceeds to justify neglecting viscosity, the body’s boundary layer and the possible wake behind the body through scaling arguments. The assumptions used are also examined *a posteriori* and found to be valid as long as the turbulent wavenumber being considered isn’t too large or the scale of the turbulence too small, as the boundary layer must then be taken into account. Hunt’s analysis also highlights the two different effects at play; that of distortion by the mean flow and the separate effect of the presence of solid boundaries upon which the condition of zero normal velocity must be satisfied. These two effects can be made explicit by splitting the perturbation velocity into two separate terms, as shown in the re-working of RDT undertaken by Goldstein (1978). Goldstein showed that Hunt's analysis could be simplified by reducing the number of equations to be solved. He also extended the analysis to compressible flows, and included the possibility of entropy fluctuations. Over the next three pages we review the major results contained in Goldstein, who gave a very clear formulation for the application of RDT. For our purposes we assume zero entropy fluctuations throughout.

Theory

The development of a small **unsteady vorticity disturbance**, introduced far upstream of a **steady potential mean flow**, as it is convected downstream by that mean flow is calculated. The mean flow is assumed to tend to a uniform value far upstream, as would be the case for the potential flow induced around an object placed in a uniform, inviscid flow.

Mean flow: We split the flow variables into mean and perturbation quantities: velocity $\mathbf{v} = \mathbf{U}\left(\mathbf{x}\right) + \mathbf{u}\left(\mathbf{x}, t\right)$, pressure $p = p_0\left(\mathbf{x}\right) + p'\left(\mathbf{x}, t\right)$ and density $\rho = \rho_0\left(\mathbf{x}\right) + \rho'\left(\mathbf{x}, t\right)$. (We note that the mean flow must be steady in order to apply RDT.) The steady mean flow quantities then satisfy the steady flow equations

$$\rho_0 \mathbf{U} \cdot \nabla \mathbf{U} = -\nabla p_0, \tag{2.1}$$

$$\mathbf{U} \cdot \nabla \rho_0 + \rho_0 \nabla \cdot \mathbf{U} = 0, \tag{2.2}$$

with boundary conditions

$$\mathbf{U} \rightarrow U_\infty \hat{\mathbf{e}}_x \quad \text{as} \quad x \rightarrow -\infty, \tag{2.3}$$

$$\hat{\mathbf{n}} \cdot \mathbf{U} = 0 \quad \text{on the solid surface of the object,} \tag{2.4}$$

corresponding to uniform flow at upstream infinity and zero penetration on the object (in our case the blades of the rotor). Note that throughout this thesis we work in a reference frame in which the engine is stationary, and so U_∞ corresponds to the forward flight speed of the aircraft.

We assume that the turbulence is of a low-level compared to the mean flow, by which we mean of a low enough intensity for linearisation to be justified ($\left|\mathbf{u}\right| / \left|\mathbf{U}\right| \ll 1$) and of a large enough scale to make the approximation that the eddies are distorted before exchanging energy with each other. Thus we require

$$\frac{L_U \delta u}{L \delta U} \ll 1, \tag{2.5}$$

where L_U is a typical lengthscale of the mean flow, L is the turbulent integral lengthscale, and δu and δU are typical perturbation and mean velocity changes respectively.

For our application the mean flow $\mathbf{U}$ is the flow induced by the engine. It is assumed to be steady and incompressible. The flight speeds of interest in this work are subsonic, take-off Mach numbers typically being in the range 0.2-0.25. As the mean flow tends to a uniform flow far upstream it must be irrotational there, and as vorticity is conserved in inviscid, axisymmetric flows, it follows that $\mathbf{U}$ is irrotational everywhere.

Upstream boundary conditions: Considering the full (mean plus perturbation) flow equations, linearising and subtracting out the mean flow equations (2.1) and (2.2) we find

$$\rho_0 \left(\frac{D_0 \mathbf{u}}{Dt} + \mathbf{u} \cdot \nabla \mathbf{U} \right) + \rho' \mathbf{U} \cdot \nabla \mathbf{U} = -\nabla p', \tag{2.6}$$

$$\frac{D_0 \rho'}{Dt} + \rho' \nabla \cdot \mathbf{U} + \nabla \cdot (\rho_0 \mathbf{u}) = 0, \tag{2.7}$$

where $D_0/Dt = \partial/\partial t + \mathbf{U} \cdot \nabla$. Far upstream, where $\rho_0 \to \rho_\infty =$ constant, these equations become

$$\rho_\infty \frac{D_\infty \mathbf{u}}{Dt} = -\nabla p', \tag{2.8}$$

$$\frac{D_\infty \rho'}{Dt} + \rho_\infty (\nabla \cdot \mathbf{u}) = 0, \tag{2.9}$$

where $D_\infty/Dt = \partial/\partial t + U_\infty \partial/\partial x$. We can deduce various properties of the perturbation velocity if we restrict attention to harmonic disturbances of the form

$$\mathbf{u} = (\overline{u}, \overline{v}, \overline{w}) \exp\left\{ i \left(\alpha x + \beta y + \gamma z + \omega t \right) \right\}. \tag{2.10}$$

Then $D_\infty/Dt = i(\omega + U_\infty \alpha)$ and, considering equation (2.8), we find two possibilities:

1. $\omega + U_\infty \alpha = 0$ and hence $p' = 0$ and, from equation (2.9), $\nabla \cdot \mathbf{u} = 0$, i.e. the disturbance is incompressible; or
2. $\omega + U_\infty \alpha \neq 0$, in which case $p' \neq 0$ and equation (2.8) gives us $\overline{u}/\alpha = \overline{v}/\beta = \overline{w}/\gamma$,

i.e. the disturbance is irrotational.

We consider disturbances whose pressure fluctuations tend to zero far upstream as we do not wish to impose incoming acoustic disturbances (as in Goldstein). The turbulent disturbance, $\mathbf{u}^{\infty}$, is 'non-acoustic' and vortical far upstream, i.e. it is a type 1 disturbance. This is purely convected with the flow far upstream and so its x and t dependence are coupled. We therefore find the following upstream boundary conditions for the full velocity and pressure fields

$$\mathbf{v}\left(x,y,z,t\right) \rightarrow U_{\infty}\hat{\mathbf{e}}_x + \mathbf{u}^{\infty}\left(x - U_{\infty}t, y, z\right), \tag{2.11}$$

$$\text{and} \quad p\left(x,y,z,t\right) \rightarrow p_{\infty}, \tag{2.12}$$

$$\text{as} \quad x \rightarrow -\infty.$$

Full flow equations: We now turn our attention to the main region of the flow, near the rotor. Using equation (2.1) we can rewrite (2.6) as

$$\frac{D_0\mathbf{u}}{Dt} + \mathbf{u}\cdot\nabla\mathbf{U} = -\frac{1}{\rho_0}\nabla p' + \frac{\rho'}{\rho_0^2}\nabla p_0. \tag{2.13}$$

For an ideal gas at constant entropy, we have the relation $p/\rho^{\gamma} = C$ where $\gamma = c_p/c_v$ is the ratio of specific heats and C is a constant. Using

$$p' \simeq \gamma C \rho_0^{\gamma-1}\rho' = c_0^2\rho', \tag{2.14}$$

where c_0 is the speed of sound, we rewrite the last two terms of (2.13) as

$$\frac{D_0\mathbf{u}}{Dt} + \mathbf{u}\cdot\nabla\mathbf{U} = -\nabla\left(\frac{p'}{\rho_0}\right). \tag{2.15}$$

Form of solution: We can distinguish between two different effects at play by writing the induced perturbation velocity as the sum of two components: $\mathbf{u} = \nabla\psi + \mathbf{u}^{\text{vort}}$. The first term, $\nabla\psi$, gives the non-acoustic[1] pressure perturbation and ensures the right hand side of (2.15) is satisfied, but it is irrotational and so must tend to zero far upstream. Therefore the second term, $\mathbf{u}^{\text{vort}}$, (which satisfies the homogeneous form of (2.15)) is needed to meet the upstream boundary condition.

---

[1] By examining the phase of ψ_0, given later in equation (2.27), it can be seen that $\nabla\psi$ is indeed non-acoustic.

The novel part of Goldstein's approach, as compared to Hunt's analysis, is the expression found for $\mathbf{u}^{\mathrm{vort}}$. As will be shown below, we can always define a quantity $\mathbf{X} = X\hat{\mathbf{e}}_{\mathbf{x}} + Y\hat{\mathbf{e}}_y + Z\hat{\mathbf{e}}_z$ with the following properties

$$\frac{D_0}{Dt}\left(\mathbf{X} - U_\infty t\hat{\mathbf{e}}_x\right) = 0, \tag{2.16}$$

$$\text{and} \quad \mathbf{X} \to \mathbf{x} \quad \text{as} \quad x \to -\infty. \tag{2.17}$$

In the key step we then find that the combination of

$$u_i^{\mathrm{vort}} = \mathbf{u}^\infty\left(\mathbf{X} - U_\infty t\hat{\mathbf{e}}_x\right) \cdot \frac{\partial \mathbf{X}}{\partial x_i}, \tag{2.18}$$

$$\text{and} \quad -\rho_0 \frac{D_0\psi}{Dt} = p', \tag{2.19}$$

satisfies (2.15) and the upstream boundary conditions. (We have used the fact that $\mathbf{U}$ is irrotational and so $\partial U_i/\partial x_j = \partial U_j/\partial x_i$.) Finally the mass conservation equation (2.7) must be satisfied and so the following inhomogeneous wave equation for ψ is found

$$\frac{D_0}{Dt}\left(\frac{1}{c_0^2}\frac{D_0\psi}{Dt}\right) - \frac{1}{\rho_0}\nabla\cdot\left(\rho_0\nabla\psi\right) = \frac{1}{\rho_0}\nabla\cdot\rho_0\mathbf{u}^{\mathrm{vort}}. \tag{2.20}$$

Applying RDT to any given situation therefore comes down to two mathematical problems, finding $\mathbf{X}$ and hence $\mathbf{u}^{\mathrm{vort}}$, and then solving (2.20) for ψ. At this stage, we can further split ψ into two components, ψ_0 satisfying the inhomogeneous RHS of the wave equation above and ψ' being the upwash velocity needed to satisfy the no penetration boundary condition on the blades (satisfying the homogeneous version of (2.20)). By definition, it is ψ' which induces an unsteady pressure jump across the blades of the rotor, and we will calculate this later using the LINSUB theory in §2.3.1.

The problem of calculating ψ_0 can be simplified by considering the incompressible limit (as Majumdar did) for which (2.20) reduces to

$$-\nabla^2\psi_0 = \nabla\cdot\mathbf{u}^{\mathrm{vort}} = \frac{\partial}{\partial x_i}\left\{u_j^\infty\left(\mathbf{X} - U_\infty t\hat{\mathbf{e}}_x\right)\frac{\partial X_j}{\partial x_i}\right\}. \tag{2.21}$$

Thus, within this formulation, certain components of the turbulent perturbation, $\mathbf{u}^{\mathrm{vort}} + \nabla\psi_0$, are assumed to be incompressible. At this stage of the analysis we are primarily concerned with approximating the velocity found immediately upstream of the rotor, and the assumption of incompressibility allows us to calculate this velocity analytically. Later, when calculating the far-field pressure, the compressible component of velocity, ψ', is re-introduced.

Much of the work in this thesis is concerned with formulating a non-axisymmetric UDN theory, and we note that the formulation of Rapid Distortion Theory we have given in this section does not depend on whether the flow is axi- or a-symmetric. However, as we will see in §2.2.4, the existence of a streamfunction greatly simplifies the problem of calculating $\mathbf{X}$.

2.2.2 The quantity X

We previously claimed that, for a flow $\mathbf{U}$ which tends to a uniform velocity far upstream $U_\infty \hat{\mathbf{e}}_x$, it is always possible to define a quantity $\mathbf{X}(x, y, z) = X\hat{\mathbf{e}}_x + Y\hat{\mathbf{e}}_y + Z\hat{\mathbf{e}}_z$ which satisfies conditions (2.16) and (2.17). Condition (2.16) is a statement that the three quantities $X - U_\infty t$, Y and Z remain constant when moving with the flow. We can label each streamline uniquely according to its y and z coordinate far upstream and then, for every point along that streamline, define Y and Z to be these upstream values. The third quantity, X, is defined via the drift function (Lighthill, 1956) which gives the time taken by individual particles to move along streamlines from some reference position[2]. The drift function $\Delta(\mathbf{x})$ is defined as

$$\Delta(\mathbf{x}) \equiv \frac{x}{U_\infty} + \int_{-\infty}^{x} \left[\frac{1}{(U_\infty + U_x)} - \frac{1}{U_\infty} \right] dx', \tag{2.22}$$

where $(U_\infty + U_x)$ is the total axial velocity, including the uniform upstream component, and the path of integration is taken along a streamline. The difference in Δ at two points $\mathbf{x_1}$ and $\mathbf{x_2}$ on the same streamline gives the time taken by a fluid particle to travel from $\mathbf{x_1}$ to $\mathbf{x_2}$. Thus the quantity $(\Delta - t)$ remains constant when moving with the flow. We use $X = U_\infty \Delta$ as the axial component of $\mathbf{X}$ in Rapid Distortion Theory and note that $\Delta \to x/U_\infty$ as $x \to -\infty$.

For the most general three-dimensional mean flow we have

$$\begin{aligned} \mathbf{X}(\mathbf{x}) &= X(x, y, z)\hat{\mathbf{e}}_x + Y(x, y, z)\hat{\mathbf{e}}_y + Z(x, y, z)\hat{\mathbf{e}}_z \\ &= X\hat{\mathbf{e}}_x + R\cos(\Phi - \phi)\,\hat{\mathbf{e}}_r + R\sin(\Phi - \phi)\,\hat{\mathbf{e}}_\phi \end{aligned} \tag{2.23}$$

---

[2] The integral expression for drift will converge for an irrotational three-dimensional flow field induced around an object, but would not necessarily converge for a two-dimensional flow field, e.g. along a streamline which leads to a stagnation point.

where $R^2 = Y^2 + Z^2$ and $\tan\Phi = Z/Y$ (R is therefore the far upstream r value for the streamline running through $\mathbf{x}$, and Φ is its far upstream azimuthal angle). Note that $R \neq \mathbf{X}\cdot\hat{\mathbf{e}}_r$ in general. For a mean flow with no $\hat{\mathbf{e}}_\phi$ component ($\mathbf{U}\cdot\hat{\mathbf{e}}_\phi = 0$), each streamline will maintain a constant azimuthal position, that is $\Phi = \phi$ everywhere, and it is this case we consider in this chapter.

The **distortion tensor**, $\partial X_i/\partial x_j$, gives a measure of the distortion which has taken place in the flow. Values larger than 1 are found when the flow has been compressed while travelling downstream, and values less than 1 are found when streamlines have spread apart. As $x \to -\infty$ we have $\partial X_i/\partial x_j \to \delta_{ij}$.

Finally we note that

$$\left|\frac{\partial \mathbf{X}}{\partial \mathbf{x}}\right| = \frac{\rho_0}{\rho_\infty}, \tag{2.24}$$

(Goldstein, 1978). For an incompressible mean flow, we therefore have $\det\left(\partial X_i/\partial x_j\right) = 1$ which gives a useful check on the numerics when calculating the distortion tensor.

2.2.3 Majumdar's solution to the RDT equation, A_{ij}

We can decompose any upstream turbulent field, $\mathbf{u}^\infty$, into harmonics of separate wavevector $\mathbf{k}$. This is a common approach (Atassi and Logue, 2008, 2009) and will later allow us to input specific forms for the upstream spectra. As the upstream turbulence is being convected at the flight speed we consider individual gusts of the form

$$u_i^\infty(\mathbf{x}) = a_i \exp\left\{i\mathbf{k}\cdot(\mathbf{x} - U_\infty t\hat{\mathbf{e}}_x)\right\}, \tag{2.25}$$

(where the a_i are constant factors). Substituting into equation (2.18), this gives

$$u_i^{\mathrm{vort}}(\mathbf{x}) = u_j^\infty\left(\mathbf{X} - U_\infty t\hat{\mathbf{e}}_x\right)\frac{\partial X_j}{\partial x_i} = a_j\frac{\partial X_j}{\partial x_i}\exp\left\{i\mathbf{k}\cdot(\mathbf{X} - U_\infty t\hat{\mathbf{e}}_x)\right\}. \tag{2.26}$$

(summation convention assumed). By essentially neglecting terms which come from differentiating the amplitude of $\mathbf{u}^{\mathrm{vort}}$ and ψ_0, Majumdar found the following approximate solution to equation (2.21)

$$\psi_0\left(\mathbf{x},t\right) \approx \frac{il_m}{|\mathbf{l}|^2}\frac{\partial X_j}{\partial x_m}a_j \exp\left\{i\mathbf{k}\cdot\left(\mathbf{X}-U_\infty t\hat{\mathbf{e}}_x\right)\right\}, \tag{2.27}$$

where

$$l_i = k_m\frac{\partial X_m}{\partial x_i}. \tag{2.28}$$

This result is valid in the range $|\mathbf{k}| \gg 1/\left|\mathbf{X}\right|$, since we neglect terms of order $\partial^2 X_j/\partial x_i\partial x_i$ in favour of terms of order $k_l(\partial X_j/\partial x_i)(\partial X_l/\partial x_j)$. The justification for this assumption is given in §2.4.2, after integral expressions for quantities of interest (such as the turbulent spectrum at the rotor face) are found, based on the fact that the dominant contribution to these integrals comes from the region $|\mathbf{k}| \gg 1/\left|\mathbf{X}\right|$.

Thus we find the full distorted velocity field, $\mathbf{u}^{\text{vort}} + \nabla\psi_0$, is given by

$$u_i\left(\mathbf{x},t\right) = \left(\delta_{im} - \frac{l_i l_m}{|\mathbf{l}|^2}\right)\frac{\partial X_j}{\partial x_m}a_j \exp\left\{i\mathbf{k}\cdot\left(\mathbf{X}-U_\infty t\hat{\mathbf{e}}_x\right)\right\}, \tag{2.29}$$

to leading order in $\mathbf{k}$. We thus define the **distortion amplitude**

$$A_{ij} = \left(\delta_{im} - \frac{l_i l_m}{|\mathbf{l}|^2}\right)\frac{\partial X_j}{\partial x_m}. \tag{2.30}$$

Note that $A_{ji} \neq A_{ij}$ in general, one involves derivatives of X_i, the other derivatives of X_j. Also, $|\mathbf{l}|$ is always non-zero (and thus we avoid a vanishing denominator) since if $|\mathbf{l}|$ were zero this would imply either $\mathbf{k} = 0$ or one whole row or column of $\partial X_i/\partial x_j$ is zero, which cannot be the case from equation (2.24). For the case of zero distortion we have $\partial X_j/\partial x_m = \delta_{jm}$.

Majumdar assumed A_{ij} was independent of azimuthal angle ϕ when the mean flow was axisymmetric. As we will see, when the flow is axisymmetric, it is more precise to state that A_{ij} only depends upon ϕ through the particular wavevector $\mathbf{k}$ of interest. More specifically, it is the components of $\mathbf{k}$ in the $y-z$ plane which bring in ϕ dependence and thus, if A_{ij} is integrated over k_y and k_z, it does indeed become independent of ϕ.

Exact solution

We note that an analytic exact solution to equation (2.21) can be written down, as the integral solution to a Laplacian equation

$$\psi_0\left(\mathbf{r_0}\right) = \frac{1}{4\pi}\int_V \frac{\nabla\cdot\mathbf{u}^{\text{vort}}}{\left|\mathbf{r_0}-\mathbf{r}\right|}dV. \tag{2.31}$$

However, as this involves an infinite volume integral, it is likely to take a long time to numerically compute a convergent solution using this expression. This will not be considered further.

2.2.4 A_{ij} for zero azimuthal mean flow (when $\mathbf{U}\cdot\hat{\mathbf{e}}_\phi = 0$)

If the $\hat{\mathbf{e}}_\phi$ component of the mean flow is zero during distortion, as is the case for the mean flow considered in this chapter, the form of $\mathbf{X}$ in (2.23) simplifies to

$$\mathbf{X}\left(\mathbf{x}\right) = X\left(x,r\right)\hat{\mathbf{e}}_x + R\left(x,r\right)\hat{\mathbf{e}}_r. \tag{2.32}$$

Further, R can be easily found if the streamfunction $\Psi\left(x,r\right)$ is known. Since $\Psi = U_\infty r^2/2$ and $r = R$ far upstream, we see $R = \sqrt{2\Psi/U_\infty}$ everywhere. In the expression for distorted velocity (equation (2.29)), the quantity $\mathbf{X}$ is involved via $\mathbf{k}\cdot\mathbf{X}$ (in the phase) and $\mathbf{l} = \nabla\left(\mathbf{k}\cdot\mathbf{X}\right)$ and $\partial X_i/\partial x_j$ (in the amplitude). At this point care is needed; although X and R have no ϕ dependence, k_r does and so $\mathbf{l}\cdot\hat{\mathbf{e}}_\phi$ is non-zero:

$$\mathbf{k}\cdot\mathbf{X} = k_xX + k_rR = k_xX + \left(k_y\cos\phi + k_z\sin\phi\right)R, \tag{2.33}$$

$$\begin{aligned}\mathbf{l} &= \nabla\left(\mathbf{k}\cdot\mathbf{X}\right)\\ &= \left[k_x\frac{\partial X}{\partial x} + k_r\frac{\partial R}{\partial x}\right]\hat{\mathbf{e}}_{\mathbf{x}} + \left[k_x\frac{\partial X}{\partial r} + k_r\frac{\partial R}{\partial r}\right]\hat{\mathbf{e}}_{\mathbf{r}} + \frac{k_\phi R}{r}\hat{\mathbf{e}}_\phi,\end{aligned} \tag{2.34}$$

where $k_r = \mathbf{k}\cdot\hat{\mathbf{e}}_{\mathbf{r}}$ and $k_\phi = \mathbf{k}\cdot\hat{\mathbf{e}}_\phi$, and the vectors $\hat{\mathbf{e}}_{\mathbf{x}}$, $\hat{\mathbf{e}}_{\mathbf{r}}$ and $\hat{\mathbf{e}}_\phi$ are based on $\mathbf{x}$. The final term of equation (2.34) was not included within Majumdar's analysis. Since k_ϕ is given by

$$k_\phi = -k_y\sin\phi + k_z\cos\phi, \tag{2.35}$$

we see that the final term of equation (2.34) is zero when the vectors $(\mathbf{k} - k_x\hat{\mathbf{e}}_{\mathbf{x}})$ and $(\mathbf{x} - x\hat{\mathbf{e}}_{\mathbf{x}})$ lie in the same radial direction (as illustrated later in Figure 2.1). In general however, this will not be the case. The contribution of the k_ϕ term to $\mathbf{l}$ is also minimised when k_y and k_z are small compared to k_x, i.e. when $\mathbf{k}$ lies primarily in the axial direction. However, as we see later in §2.4.2, we will ultimately choose to sum over modes which correspond to small k_x, due to the sharp drop off of the upstream turbulence spectrum as k_x increases. Thus k_ϕ is a potentially significant term in the regions of interest.

We note briefly that the most general axisymmetric flow could, in addition, have a constant swirl component, leading to

$$\mathbf{X} = X\hat{\mathbf{e}}_x + R\cos\Phi_0\hat{\mathbf{e}}_r + R\sin\Phi_0\hat{\mathbf{e}}_\phi, \tag{2.36}$$

where Φ_0 is constant. This would lead to extra terms within $\mathbf{l}$. This example was treated by Wright (2000), who found swirl in the same direction as the propellers reduces spectral peaks and counter-rotating swirl increases them, and we take $\Phi_0 = 0$ here.

In Chapters 4 and 5, where the $\hat{\mathbf{e}}_\phi$ component of the mean flow is non-zero, all three components of $\mathbf{X}$ depend upon ϕ as well as upon x and r (or equivalently, upon x, y and z). The general, non-axisymmetric expression for $\mathbf{l}$ is given in equations (4.11) - (4.13) in Chapter 4.

Returning to the form for $\mathbf{X}$ given in (2.32), components of the tensor $\mathbf{A}$ in the polar coordinate directions[3] of $\mathbf{x}$ are then given by

$$\begin{aligned}
\hat{\mathbf{e}}_\mathbf{x}\cdot\mathbf{A}\cdot\hat{\mathbf{e}}_\mathbf{x} &= \left(1-\frac{l_xl_x}{|\mathbf{l}|^2}\right)\frac{\partial X}{\partial x} - \frac{l_xl_r}{|\mathbf{l}|^2}\frac{\partial X}{\partial r},\\
\hat{\mathbf{e}}_\mathbf{x}\cdot\mathbf{A}\cdot\hat{\mathbf{e}}_\mathbf{r} &= \left(1-\frac{l_xl_x}{|\mathbf{l}|^2}\right)\frac{\partial R}{\partial x} - \frac{l_xl_r}{|\mathbf{l}|^2}\frac{\partial R}{\partial r},\\
\hat{\mathbf{e}}_\mathbf{x}\cdot\mathbf{A}\cdot\hat{\mathbf{e}}_\phi &= -\frac{l_xl_\phi}{|\mathbf{l}|^2}\frac{R}{r},\\
\hat{\mathbf{e}}_\mathbf{r}\cdot\mathbf{A}\cdot\hat{\mathbf{e}}_\mathbf{x} &= -\frac{l_rl_x}{|\mathbf{l}|^2}\frac{\partial X}{\partial x} + \left(1-\frac{l_rl_r}{|\mathbf{l}|^2}\right)\frac{\partial X}{\partial r},\\
\hat{\mathbf{e}}_\mathbf{r}\cdot\mathbf{A}\cdot\hat{\mathbf{e}}_\mathbf{r} &= -\frac{l_rl_x}{|\mathbf{l}|^2}\frac{\partial R}{\partial x} + \left(1-\frac{l_rl_r}{|\mathbf{l}|^2}\right)\frac{\partial R}{\partial r},\\
\hat{\mathbf{e}}_\mathbf{r}\cdot\mathbf{A}\cdot\hat{\mathbf{e}}_\phi &= -\frac{l_rl_\phi}{|\mathbf{l}|^2}\frac{R}{r},\\
\hat{\mathbf{e}}_\phi\cdot\mathbf{A}\cdot\hat{\mathbf{e}}_\mathbf{x} &= -\frac{l_\phi l_x}{|\mathbf{l}|^2}\frac{\partial X}{\partial x} - \frac{l_\phi l_r}{|\mathbf{l}|^2}\frac{\partial X}{\partial r},
\end{aligned}$$

---

[3] Note that, strictly speaking, a tensor's components cannot be expressed with polar suffices, e.g. A_{xr}. If we dotted A_{ij} with two different vectors, their polar bases would differ in general, and we would need to decide on a common basis to express the two vectors and $\mathbf{A}$ in before proceeding. By A_{xr} we therefore mean $\hat{\mathbf{e}}_\mathbf{x}\cdot\mathbf{A}\cdot\hat{\mathbf{e}}_\mathbf{r}$.

$$
\begin{aligned}
\hat{\mathbf{e}}_\phi \cdot \mathbf{A} \cdot \hat{\mathbf{e}}_\mathbf{r} &= -\frac{l_\phi l_x}{|\mathbf{l}|^2}\frac{\partial R}{\partial x} - \frac{l_\phi l_r}{|\mathbf{l}|^2}\frac{\partial R}{\partial r}, \\
\hat{\mathbf{e}}_\phi \cdot \mathbf{A} \cdot \hat{\mathbf{e}}_\phi &= \left(1 - \frac{l_\phi l_\phi}{|\mathbf{l}|^2}\right)\frac{R}{r}. \qquad (2.37)
\end{aligned}
$$

Particular care is needed when calculating the components involving contraction with $\hat{\mathbf{e}}_\phi$. We see that, even in the case where $l_\phi = 0$ as assumed by Majumdar, $\hat{\mathbf{e}}_\phi \cdot \mathbf{A} \cdot \hat{\mathbf{e}}_\phi$ is non-zero. From equation (2.34) we have

$$
\begin{aligned}
l_x &= k_x \frac{\partial X}{\partial x} + k_r \frac{\partial R}{\partial x} = k_x \frac{\partial X}{\partial x} + (k_y \cos\phi + k_z \sin\phi)\frac{\partial R}{\partial x}, \\
l_r &= k_x \frac{\partial X}{\partial r} + k_r \frac{\partial R}{\partial r} = k_x \frac{\partial X}{\partial r} + (k_y \cos\phi + k_z \sin\phi)\frac{\partial R}{\partial r}, \\
l_\phi &= \frac{k_\phi R}{r} = (-k_y \sin\phi + k_z \cos\phi)\frac{R}{r}, \qquad (2.38) \\
|\mathbf{l}|^2 &= l_x^2 + l_r^2 + l_\phi^2. \qquad (2.39)
\end{aligned}
$$

Note that $|\mathbf{l}|^2$ will vary with ϕ for a particular $\mathbf{k} = (k_x, k_y, k_z)$, which makes the integration of A_{ij} over ϕ non-trivial analytically. We wish to do this later, when calculating the Fourier components of A_{ij}.

Polar representation of k

For numerical calculation of later expressions it is more convenient to re-express $\mathbf{k}$ in polar form, as then any integrals over the $k_y - k_z$ plane can be reduced from two infinite integrals to a finite integral and a one-sided infinite integral. As illustrated in Figure 2.1, we define

$$r_k = \sqrt{k_y^2 + k_z^2}, \qquad (2.40)$$

$$\phi_k = \tan^{-1}\left(\frac{k_z}{k_y}\right). \qquad (2.41)$$

We can then re-express k_r, k_ϕ for use in the above expressions for A_{ij} as

$$k_r = \mathbf{k} \cdot \hat{\mathbf{e}}_\mathbf{r} = r_k \cos(\phi_k - \phi), \qquad (2.42)$$

$$k_\phi = \mathbf{k} \cdot \hat{\mathbf{e}}_\phi = r_k \sin(\phi_k - \phi). \qquad (2.43)$$

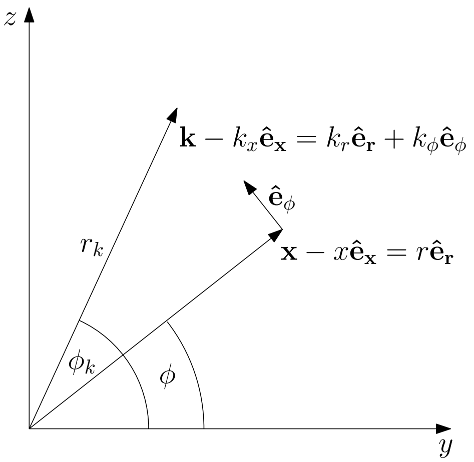

Figure 2.1: Re-expressing $\mathbf{k}$ in polar form: $k_y\hat{\mathbf{e}}_\mathbf{y} + k_z\hat{\mathbf{e}}_\mathbf{z} \rightarrow k_r\hat{\mathbf{e}}_\mathbf{r} + k_\phi\hat{\mathbf{e}}_\phi$, where polar coordinates are taken with respect to $\mathbf{x}$. Integrating over $dk_y dk_z \rightarrow r_k dr_k d\phi_k$.

This leads to

$$\mathbf{k} \cdot \mathbf{X} = k_x X + r_k \cos\left(\phi_k - \phi\right) R, \tag{2.44}$$

and

$$\begin{aligned}\mathbf{l} = &\left(k_x \frac{\partial X}{\partial x} + r_k \cos\left(\phi_k - \phi\right) \frac{\partial R}{\partial x}\right) \hat{\mathbf{e}}_\mathbf{x} + \left(k_x \frac{\partial X}{\partial r} + r_k \cos\left(\phi_k - \phi\right) \frac{\partial R}{\partial r}\right) \hat{\mathbf{e}}_\mathbf{r} \\ &+ r_k \sin\left(\phi_k - \phi\right) \frac{R}{r} \hat{\mathbf{e}}_\phi.\end{aligned} \tag{2.45}$$

Note on alternative Fourier decomposition

Our approach differs from that of some authors, for example Blandeau (2011), who decompose the turbulent velocity into components with constant k_r, k_ϕ components, as opposed to constant k_y, k_z components. Thus, in Blandeau's framework, k_r is defined to be the component of $\mathbf{k}$ in the $\hat{\mathbf{e}}_\mathbf{r}$ direction on a particular blade, and the following strip theory approximation for the phase

$$e^{i\left(k_r r + k_\phi \phi r + k_x x\right)} \tag{2.46}$$

is valid on nearby blades, for which ϕ is small. For our purposes, and in particular in Chapter 4 where we specifically wish to account for extra ϕ dependence within the velocity field, we need to obtain general expressions valid for all ϕ between 0 and 2π, hence our current approach.

In order to apply our newly found expression for A_{ij} to the case of Unsteady Distortion Noise of an Advanced Open Rotor, we need appropriate models for the mean flow and the upstream turbulence. We consider these models in the next two subsections.

2.2.5 Mean flow model - introducing the actuator disk

Here we introduce a simple streamtube contraction model, to simulate the flow into a rotor. An 'actuator disk' is a mathematical tool widely used to capture the prominent features of a streamtube contraction. Recently Yin and Stuermer (2010) compared an actuator disk model to a uRANS (unsteady RANS) calculation for propeller thrust loading and found that the actuator disk captured well the qualitative features of the more detailed calculation. As our present task of calculating the turbulence distortion relies only on the flow upstream of the rotor, the detailed flow around the blades is of less significance. The blade passage region is re-examined more closely later when calculating the pressure jumps using strip theory. In this chapter we outline a simple constant circulation actuator disk model. In Chapter 3 we will give the derivation of the model in more detail and then adapt it to incorporate more realistic features such as variable blade circulation.

An actuator disk is defined to be a surface over which certain flow properties vary discontinuously due to the force exerted by the rotor, such as the axial and tangential velocities (Horlock (1978), Cooper and Peake (1999)). An actuator disk may be thought of as an infinitely bladed propeller, in the limit of which we retain steady velocities only. For a model of the detailed velocity components and, crucially for our purposes, the streamlines of the flow, we turn to the classical vortex theory of a propeller, as given in Hough and Ordway (1965), where each blade is modelled as a vortex line, providing us with relatively simple analytic expressions. The details of this method are given in Chapter 3, §3.2.1. The steady component of this solution reproduces the results of actuator disk theory, and is therefore a reasonable physical model.

For the case of a constant circulation actuator disk of radius r_d positioned at $x = 0$, we take the circulation along the blade span to be given by $\Gamma(r) = \Gamma$ for $r < r_d$ and zero otherwise. The induced axial and radial actuator disk velocities upstream of the disk are then as follows

$$U_x = \frac{U_d x}{2\pi r^{\frac{3}{2}}} \int_0^{r_d} \frac{1}{\sqrt{r'}} Q'_{-\frac{1}{2}}(\omega') dr' \quad \text{for} \quad x < 0, \tag{2.47}$$

$$U_r = -\frac{U_d}{2\pi}\sqrt{\frac{r_d}{r}} Q_{\frac{1}{2}}(\omega_d). \tag{2.48}$$

(Hough and Ordway, 1965). Here we have defined

$$U_d = \frac{T}{\pi r_d^2 \rho_0 U_\infty}, \tag{2.49}$$

where T is total propeller thrust. The only input parameters into this actuator disk mean flow model are therefore upstream velocity, total thrust generated and radius. The axial and radial velocities involve Legendre functions $Q_{\frac{1}{2}}$, $Q'_{-\frac{1}{2}}$, see Appendix A for the full expressions for these. The arguments of the Legendre functions used above are defined as follows

$$\omega' = 1 + \frac{x^2 + (r - r')^2}{2rr'}, \tag{2.50}$$

$$\omega_d = 1 + \frac{x^2 + (r - r_d)^2}{2rr_d}. \tag{2.51}$$

We denote the total axial velocity at the disk face by U_f. At $x = 0$, Hough and Ordway's model gives $U_x = U_d/2$, and thus we have $U_f = U_\infty + U_d/2$. In Figure 2.2 we show the axisymmetric streamlines induced by a constant circulation actuator disk.

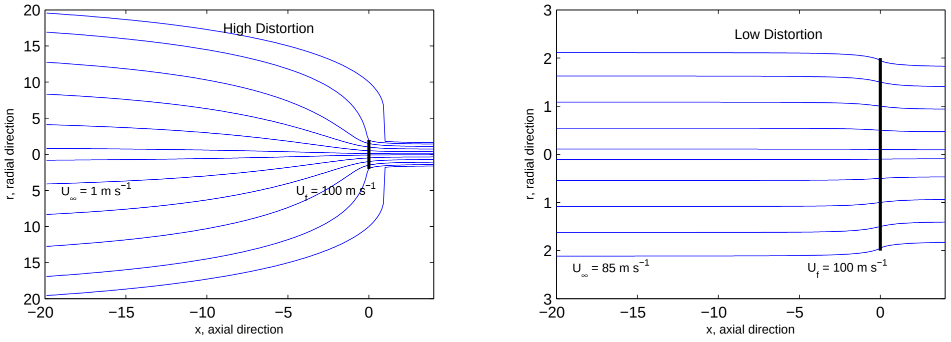

Figure 2.2: Streamlines induced by a constant circulation actuator disk located between $y = -2$ and $y = 2$ at $x = 0$. Both a high distortion ($U_f/U_\infty = 100$) and low distortion ($U_f/U_\infty = 1.18$) example are shown.

2.2.6 Turbulence model - introducing the von Kármán spectrum

Upstream turbulence spectrum

Davidson (2004) provides a good reference for the derivation of the quantities introduced in this section. The majority of turbulence models are specified via the Fourier transform of the spatial velocity correlation tensor, known as the spectrum tensor. That is

$$S_{ij}^{\infty}\left(\mathbf{k}\right) = \frac{1}{\left(2\pi\right)^{3}} \int_{\Re^{3}} R_{ij}^{\infty}\left(\boldsymbol{\eta}\right) \exp\left(-i\mathbf{k}\cdot\boldsymbol{\eta}\right) d^{3}\boldsymbol{\eta}, \tag{2.52}$$

where

$$R_{ij}^{\infty}\left(\boldsymbol{\eta}\right) = \langle u_i^{\infty}\left(\mathbf{x}', t\right), u_j^{\infty}\left(\mathbf{x}'+\boldsymbol{\eta}, t\right)\rangle. \tag{2.53}$$

Angle brackets here denote an **ensemble average**, an average over many realisations, as if an experiment to measure u_i^{∞} and u_j^{∞} had been run many times. As we assume $\mathbf{u}^{\infty}$ is both statistically stationary and homogeneous, R_{ij}^{∞} will be independent of both t and $\mathbf{x}'$. Thus, in this case, the ensemble average is equivalent to a long-time average or volume average (Batchelor, 1953).

When working with turbulent quantities, correlation tensors, such as R_{ij}^{∞}, are often used. These are statistical quantities which give a measure of the average product of velocities at two different points in the flow, which are separated either by a given distance in space ($\boldsymbol{\eta}$) or time (τ) or both. A value of a correlation tensor which is far from zero indicates strong correlation, a value close to zero indicates weak correlation and we expect a value of zero for velocities which have no influence on each other. In terms of spatial separation, we expect high correlations up to the size of an eddy, and low correlations beyond that. Of course, turbulence contains eddies of many sizes, so there will not be a sudden cut-off.

We can make use of Taylor's 'frozen turbulence' hypothesis to remove explicit time dependence from equation (2.53). The quantity $\mathbf{u}^{\infty}$ (non-averaged) represents a turbulent velocity which will vary in time. Its t dependence has two aspects. Firstly, $\mathbf{u}^{\infty}$ is convected by a uniform mean flow at upstream infinity and we can write $\mathbf{x}' = \mathbf{x} - \hat{\mathbf{e}}_{\mathbf{x}} U_{\infty} t$, to explicitly show this (thus $\boldsymbol{\eta}$ could indicate a spatial or temporal separation, or a combination). Secondly, $\mathbf{u}^{\infty}$ has a t dependence which is not tied to the $\mathbf{x}$ dependence, that is if $U_{\infty} = 0$, the turbulent velocity at a particular point in space would still vary with t. Taylor's hypothesis gives conditions under which a convected eddy can be assumed to remain a coherent structure for an infinitely long time. If these conditions are met then correlations across the eddy remain constant when convecting with the mean flow speed. Essentially this implies that if turbulent intensity is small, $\sqrt{\langle \mathbf{u}^2 \rangle}/U_\infty \ll 1$, then when a correlation is taken the second of these time dependencies can be neglected. Thus we can write

$$R_{ij}^{\infty}(\boldsymbol{\eta}) = \langle u_i^{\infty}(\mathbf{x}'), u_j^{\infty}(\mathbf{x}' + \boldsymbol{\eta}) \rangle. \tag{2.54}$$

For isotropic incompressible turbulence, the most general form for the spectrum tensor is

$$S_{ij}^{\infty}(\mathbf{k}) = \frac{E(k)}{4\pi k^4}\left(k^2\delta_{ij} - k_i k_j\right), \tag{2.55}$$

$$\text{where} \quad E(k) = k^3 \frac{d}{dk}\left(\frac{1}{k}\frac{d}{dk}\Theta_{xx}^{\infty}(k)\right). \tag{2.56}$$

Here Θ_{xx}^{∞} is the one-dimensional energy spectrum[4] of $\hat{\mathbf{e}}_{\mathbf{x}} \cdot \mathbf{u}^{\infty}(x, 0, 0)$,

$$\Theta_{xx}^{\infty}(k) = \frac{1}{\pi}\int_0^{\infty} R_{xx}^{\infty}(r\hat{\mathbf{e}}_{\mathbf{x}})\cos(kr)dr. \tag{2.57}$$

Θ_{xx}^{∞} is easier to measure experimentally than the energy spectrum, $E(k)$, (Davidson, 2004) and can be related back to the axial component of S_{ij}^{∞}

$$\Theta_{xx}^{\infty}(k_x) = \int_{\Re^2} S_{xx}^{\infty}(\mathbf{k})\, dk_y dk_z. \tag{2.58}$$

We have used this analytic expression for the one-dimensional spectrum to validate our numerics for the spectra at the rotor face.

von Kármán model

In his 1999 paper, Wilson summarised the assumptions commonly used by acousticians about the form of atmospheric turbulence and compared these to the findings of atmospheric scientists. In particular, he indicated that the von Kármán spectrum fitted the measured atmospheric spectrum well, see Figure 2.3.

The primary turbulence model we use therefore is the von Kármán spectrum, given

---

[4] The one-dimensional energy spectrum is denoted by F_{11} in Davidson's notation.

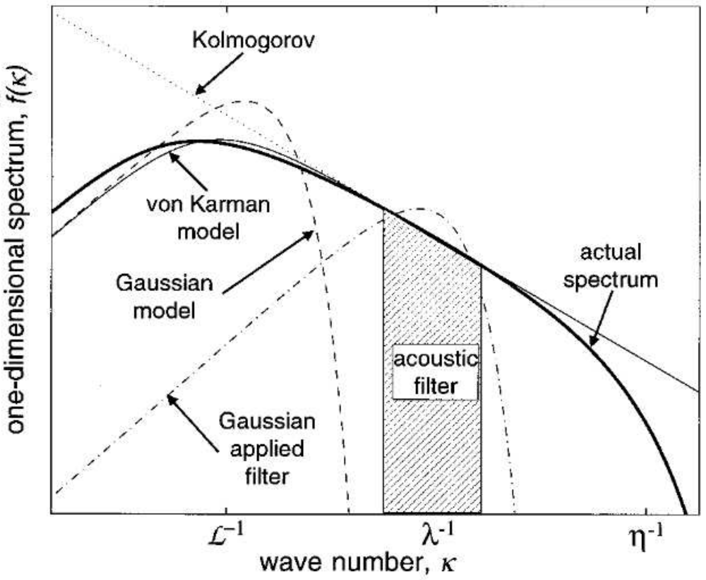

Figure 2.3: Figure from Wilson et al. (1999) showing the atmospheric turbulence one-dimensional spectrum, together with a range of different models. The Gaussian model is mathematically the simplest, whereas the von Kármán model approximates the energy containing range better, and gives the $k^{-\frac{5}{3}}$ decay observed for small scale atmospheric turbulence in the inertial subrange. Note that the drop off at high k is steeper in the actual spectrum than in the von Kármán model, hence our use later of the Liepmann spectrum, which falls off as k^{-2}. The 'acoustic filter' region indicates those lengthscales which play the most significant role in the scattering of sound as it travels through turbulence.

by

$$E\left(k\right)=\frac{55g_1\overline{u_{\infty,1}^2}L^5k^4}{9\left(g_2+k^2L^2\right)^{\frac{17}{6}}}, \tag{2.59}$$

where $g_1\approx 0.1955$ and $g_2\approx 0.558$, $\overline{u_{\infty,1}^2}$ is the mean square speed of the axial component of turbulent velocity and L is the integral lengthscale. As $k_y, k_z\to\infty$, we have $S_{ij}^{\infty}\sim k^{-11/3}$, ensuring our integrals converge. This is one of the most commonly used spectra (e.g. Lloyd (2009), Blandeau (2011)) and allows ready comparison to other models.

The integral lengthscale, L, is often taken by acousticians to be around 1 metre, however this is far lower than many observed measurements, which often find L to vary proportionally to height off the ground. In Chapter 3 we revisit the question of appropriate values for L, as well as considering turbulence models other than the von Kármán model.

2.2.7 Distorted turbulence spectrum

We are now in a position to calculate the distorted turbulence spectrum at the rotor face for any particular mean flow and turbulence model. As we are ultimately interested in the frequency domain for the acoustics, the spectrum we calculate is the Fourier transform of the correlation between velocities at the same point in space, separated in time by τ. That is

$$S_{ij}\left(\mathbf{x},\omega\right)=\int_{-\infty}^{\infty}R_{ij}\left(\mathbf{x},\tau\right)\exp\left(i\omega\tau\right)d\tau, \tag{2.60}$$

where the velocity correlation tensor for velocities separated in time but not space, R_{ij}, is given by

$$R_{ij}\left(\mathbf{x},\tau\right)=\langle u_i\left(\mathbf{x},t\right),u_j\left(\mathbf{x},t+\tau\right)\rangle. \tag{2.61}$$

We wish to compute $S_{ij}\left(\mathbf{x},\omega\right)$ in terms of $S_{ij}^{\infty}\left(\mathbf{k}\right)$. Note that S_{ij} is a temporal Fourier transform whereas S_{ij}^{∞} is a spatial Fourier transform. The appropriate comparison of S_{ij} to the undistorted spectrum is found by substituting $\partial X_i/\partial x_j=\delta_{ij}$ into the expression for S_{ij}.

Velocity correlation, R_{ij}

The full distorted velocity, integrated over all wavenumbers, from equations (2.25), (2.29) and (2.30), is given by

$$\begin{aligned}u_i\left(\mathbf{x},t\right)=\frac{1}{\left(2\pi\right)^3}\int_{\Re^3}&A_{ij}\left(\mathbf{x},\mathbf{k}\right)\exp\left\{i\left[k_x\left(X\left(\mathbf{x}\right)-U_{\infty}t\right)+k_yY\left(\mathbf{x}\right)+k_zZ\left(\mathbf{x}\right)\right]\right\}\\&\left[\int_{\Re^3}u_j^{\infty}\left(\mathbf{y},t\right)\exp\left(-i\mathbf{k}\cdot\mathbf{y}\right)d^3\mathbf{y}\right]d^3\mathbf{k},\end{aligned} \tag{2.62}$$

(real part understood). This expression for u_i does not depend upon ϕ for an axisymmetric flow field, due to integration over k_y, k_z. However, we note that this is for one particular realisation of the upstream turbulent velocity field u_i^{∞} and, as we will never be in a position to input this exactly, the only meaningful expressions are ones in which we have averaged over many possible realisations.

We wish to input the form of the upstream turbulence via its velocity correlation in wavevector space, S_{ij}^{∞}, as we have analytic models for this. Thus in the next section we will treat each $\mathbf{k}$ component separately. Due to this decomposition, ϕ dependence will be reintroduced in the expressions for blade pressure jump etc., as the difference in

$\mathbf{k} \cdot \mathbf{x}$ between blades must be accounted for. Note that t dependence appears via the $\exp\left(-ik_x U_\infty t\right)$ term (t dependence in $\mathbf{u}^\infty$ will be removed when the autocorrelation is taken, see discussion of Taylor's hypothesis above). Thus the frequency of the distorted velocity for a particular wavenumber component $\mathbf{k}$ is $\omega = k_x U_\infty$.

Substituting into (2.61) we have

$$\begin{aligned}
R_{ij}\left(\mathbf{x},\tau\right) =& \Big\langle \frac{1}{\left(2\pi\right)^3} \int_{\Re^3} A_{ik}\left(\mathbf{x},\mathbf{k}\right) \exp\left\{i\left[k_x\left(X\left(\mathbf{x}\right) - U_\infty t\right) + k_y Y\left(\mathbf{x}\right) + k_z Z\left(\mathbf{x}\right)\right]\right\} \\
&\quad \left[\int_{\Re^3} u_k^\infty\left(\mathbf{y}\right) \exp\left(-i\mathbf{k}\cdot\mathbf{y}\right) d^3\mathbf{y}\right] d^3\mathbf{k}, \\
&\frac{1}{\left(2\pi\right)^3} \int_{\Re^3} A_{jl}\left(\mathbf{x},\mathbf{k}'\right) \exp\left\{i\left[k'_x\left(X\left(\mathbf{x}\right) - U_\infty t - U_\infty \tau\right) + k'_y Y\left(\mathbf{x}\right) + k'_z Z\left(\mathbf{x}\right)\right]\right\} \\
&\quad \left[\int_{\Re^3} u_l^\infty\left(\mathbf{y}'\right) \exp\left(-i\mathbf{k}'\cdot\mathbf{y}'\right) d^3\mathbf{y}'\right] d^3\mathbf{k}' \Big\rangle \\
=& \frac{1}{\left(2\pi\right)^6} \int_{\Re^3}\int_{\Re^3}\int_{\Re^3} A_{ik}\left(\mathbf{x},\mathbf{k}\right) A_{jl}\left(\mathbf{x},\mathbf{k}'\right) \exp\left(-ik'_x U_\infty \tau\right) \\
&\exp\left\{-i\left[\left(k_x - k'_x\right)\left(X\left(\mathbf{x}\right) - U_\infty t\right) + \left(k_y - k'_y\right) Y\left(\mathbf{x}\right) + \left(k_z - k'_z\right) Z\left(\mathbf{x}\right)\right]\right\} \\
&\left[\int_{\Re^3} \left\langle u_k^\infty\left(\mathbf{y}\right), u_l^\infty\left(\mathbf{y}'\right)\right\rangle \exp\left(i\mathbf{k}\cdot\mathbf{y}\right) \exp\left(-i\mathbf{k}'\cdot\mathbf{y}'\right) d^3\mathbf{y}\right] d^3\mathbf{k}' d^3\mathbf{y}' d^3\mathbf{k}. \qquad (2.63)
\end{aligned}$$

The ensemble average acts upon the $\mathbf{u}^\infty$ terms only. We make the substitution $\mathbf{y}' = \mathbf{y} + \boldsymbol{\eta}$ and note that, due to homogeneity, $\left\langle u_k^\infty\left(\mathbf{y}\right), u_l^\infty\left(\mathbf{y}+\boldsymbol{\eta}\right)\right\rangle$ is independent of $\mathbf{y}$. Performing the $d^3\mathbf{y}$ integral of the last line above brings out a factor of $(2\pi)^3\delta(\mathbf{k}-\mathbf{k}')$, and setting $\mathbf{k}' = \mathbf{k}$ when performing the $d^3\mathbf{k}'$ integral allows us to cancel most of the exponential terms.

We now have

$$\begin{aligned}
R_{ij}\left(\mathbf{x},\tau\right) &= \frac{1}{\left(2\pi\right)^3} \int_{\Re^3} A_{ik}\left(\mathbf{x},\mathbf{k}\right) A_{jl}\left(\mathbf{x},\mathbf{k}\right) \exp\left(-ik_x U_\infty \tau\right) \\
&\quad \left[\int_{\Re^3} \left\langle u_k^\infty\left(\mathbf{y}\right), u_l^\infty\left(\mathbf{y}+\boldsymbol{\eta}\right)\right\rangle \exp\left(-i\mathbf{k}\cdot\boldsymbol{\eta}\right) d^3\boldsymbol{\eta}\right] d^3\mathbf{k} \\
&= \int_{\Re^3} A_{ik}\left(\mathbf{x},\mathbf{k}\right) A_{jl}\left(\mathbf{x},\mathbf{k}\right) \exp\left(-ik_x U_\infty \tau\right) S_{kl}^\infty\left(\mathbf{k}\right) d^3\mathbf{k}. \qquad (2.64)
\end{aligned}$$

Finally we Fourier transform in τ

$$S_{ij}\left(\mathbf{x},\omega\right) = \frac{2\pi}{U_\infty} \int_{\Re^2} A_{ik}\left(\mathbf{x},\mathbf{k}\right) A_{jl}\left(\mathbf{x},\mathbf{k}\right) S_{kl}^\infty\left(\mathbf{k}\right) dk_y dk_z, \qquad (2.65)$$

and now $k_x = \omega/U_\infty$. In contrast to Majumdar's result, this expression includes all azimuthal order terms and has no ϕ dependence in the axisymmetric mean flow case.

2.2.8 Distorted turbulence plots

We have written a MATLAB program to calculate the distorted turbulence spectrum, as given in equation (2.65). Figure 2.4 shows how the turbulent energy at the rotor face increases with distortion level, at all lengthscales.

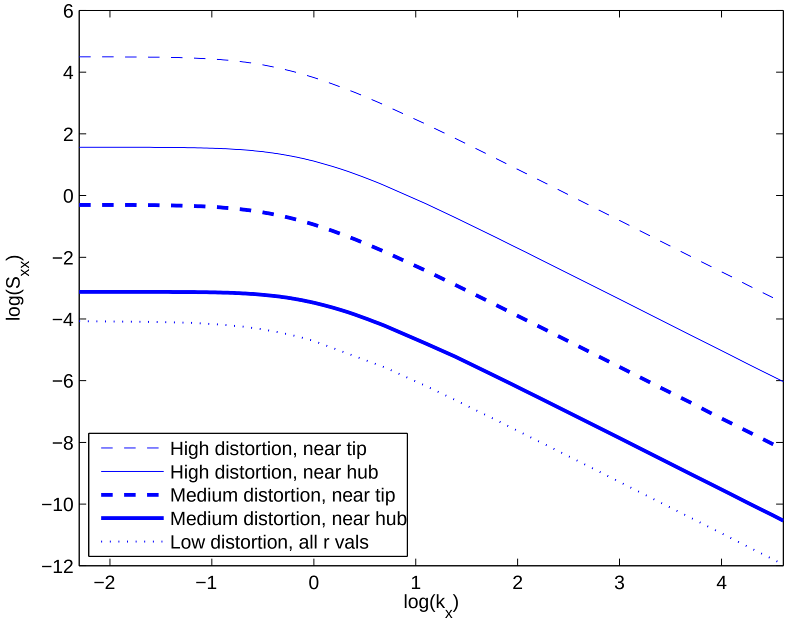

Figure 2.4: Distorted turbulence spectrum (axial component) at different positions along the rotor blade, for varying distortion levels. $L = 1$ in all cases. High distortion corresponds to $U_f/U_\infty = 100$, medium to $U_f/U_\infty = 10$ and low to $U_f/U_\infty = 1.18$. The radial position chosen near the hub is $r/r_d = 0.4$ and near the tip is $r/r_d = 0.9$.

We find that for low levels of distortion the resulting turbulence spectrum does not vary with r position, that is the streamlines which intersect with each radial position along the blade have experienced approximately the same distortion. In contrast, for high levels of streamtube contraction there are significant differences experienced between points near the rotor hub versus the rotor tip. We see that the effect of increasing the distortion level is to shift the spectrum upward at all frequencies. As can be seen from the definition of S_{xx} (in equation (2.65)) and A_{xk} (in equation (2.30)), all nine components of the $\partial X_i/\partial x_j$

tensor appear within S_{xx}. The spectrum shift is thus due to a combination of both the change in magnitude of individual components, and the change in the ratios between components. When the distortion level is increased, but the radial blade position is kept constant, it appears that the primary mechanism for the spectrum shift is the increase in the magnitude of the $\partial X/\partial x$ term. This term corresponds to axial stretching of the turbulent eddies, and a higher value of $\partial X/\partial x$ means increased axial stretching, and thus a shift to larger lengthscales i.e. lower k_x values. In Chapter 3 we calculate $\partial X_i/\partial x_j$ as functions of r at the rotor face, and examine how changes in these quantities translate directly to changes in the distorted turbulence spectrum.

Positioning the actuator disk

Note that, within our model, the position chosen for the actuator disk relative to the leading edge of the blades will affect the velocities within the model at the leading edge of the blade. Throughout this work, we place the actuator disk at $x = 0$. The blade's leading edge should lie just ahead of the jump in flow properties, and we usually place the leading edge at $x = -0.005r_d$ in our calculations. In turbofan tests a bellmouth inlet is sometimes used to better simulate the streamtube contraction, in which case positioning the actuator disk somewhat upstream of the leading edge of the blades may be a more appropriate modelling assumption. However bellmouth inlets are not used for open rotor tests.

2.3 Blade pressure jump

Unsteady distortion noise is generated when a turbulent velocity field impinges upon a rotors' blades and, due to the condition of zero normal velocity on the blades' surfaces, induces a pressure jump across those blades. In this section we use Smith's cascade theory to determine the lift response of the blades to the particular incoming distorted velocity u_i given in equation (2.62). This is not the only possible approach, alternatives include neglecting the cascade effect and using an Amiet model (Blandeau et al., 2009, Blandeau and Joseph, 2010) or Sears function (Wright, 2000, Brouwer, 2010) to consider the response of individual blades, or the use of alternative linear cascade models (Atassi and Logue, 2009). Recent work by Roger and Carazo (2010) has begun to take into account a more realistic representation of the open rotor blade shape within a blade response function, including effects of sweep, continuous variation of chord length in the spanwise direction (for correct tone prediction), and the rectangular blade tips typical of open rotors. In their work, incorporating sweep was found to have the most significant effect, and this is possible within our model by adjusting the axial position of the leading edge, $x_0(r)$.

2.3.1 LINSUB

Outline of Smith's theory

Smith (1973) analysed the response of a cascade of idealised flat plate blades to an input velocity perturbation. The aim of the paper was to treat the discrete frequency noise generated, transmitted and reflected by a blade row. Five particular forms of upwash velocity are treated by Smith: bending vibration; torsional vibration; a convected sinusoidal wake; an upstream or downstream going acoustic wave. In each case there are then five different physical quantities which can be calculated directly as output: total lift; total moment; the vortex sheet shed from the blades (when the lift force varies in time new vortices are shed); and, if conditions are not cut-off, the upstream and downstream travelling waves.

Certain modelling assumptions apply. Firstly, radial gradients are neglected, and thus we treat each radial station separately - i.e. 'unwrapping' the blades and considering a two-dimensional set-up. (Within analytic models it is usual for the blade normal to be assumed to lie in the $\hat{\mathbf{e}}_{\mathbf{x}}$ and $\hat{\mathbf{e}}_{\phi}$ directions only, and hence radial gradients will not come into the $\nabla \cdot \mathbf{f}$ forcing term in the wave equation, (2.107).) This approximation allows the interaction between adjacent blades to be taken into account, rather than treating each blade individually. Radial variation is still taken into account via the leading edge velocity. Secondly, at each radial station the blades are modelled as a continuous distribution of line vortices (lying along the third dimension) along the chord, see Figure 2.5. In addition, only subsonic flows are considered and the blades are assumed to operate at zero incidence to the mean flow at their leading edge.

This model further extends the vortex theory of a propeller employed in the actuator disk flow model; we now represent the rotor blades by two-dimensional flat plates rather than one-dimensional lines. A vortex at $\hat{z}_0$ gives rise to upstream and downstream going pressure perturbations (leading to contributions to the upwash velocity at all $\hat{z} \neq \hat{z}_0$), and a downstream going vorticity wave (leading to contributions to the upwash velocity at $\hat{z} > \hat{z}_0$). There is a singularity in the lift at the leading edge where, in this inviscid model, the fluid is forced to turn at a sharp angle.

Our input velocity takes the form of a convected sinusoidal wake and we are interested

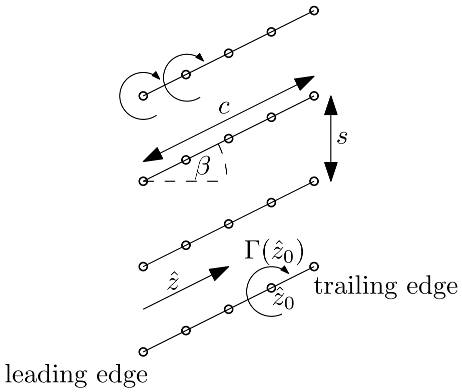

Figure 2.5: The vortices provide a representation of the circulation generated by the motion of the aerofoils (a viscous effect), while using the inviscid equations of motion in the surrounding fluid.

in the lift output from the model. We do not directly use the acoustic waves as calculated by Smith, because this two-dimensional cascade theory model is only valid very near the rotor. If we simply considered the output sound waves as they propagate, this would not give a good prediction for the far-field noise. Instead the lift distribution is input as the forcing term in the cylindrical far-field wave equation in §2.4.

Smith's strip theory analysis gives a computationally efficient method for calculating the strengths of the vortices, $\Gamma(\hat{z})$, and equivalently the force distribution induced along the blade due to the condition of zero normal velocity on the blades' surfaces. Whitehead (1987) then created the LINearized SUBsubsonic (LINSUB) code to implement Smith's theory where a discrete number of points, n_c, are considered along the blade in order to calculate Γ.

LINSUB theory shows particularly good agreement with experiment under conditions of low Mach no., zero mean blade loading, and a high hub-to-tip ratio, and is extremely widely used in analytic aeroacoustics (e.g. Cheong et al. (2006), Evers and Peake (2002)). There are three potential limitations of strip theory in the present context of our work. Firstly, the key assumption of neglecting radial gradients becomes more acceptable as the hub-to-tip ratio increases, but for open rotors the hub-to-tip ratio tends to lie in the fairly low range of 0.3-0.4. Incorporating radial effects into LINSUB can lead to significant changes at low frequencies (Lloyd, 2009), and we give a method for including the contribution of the radial wavenumber to ∇^2 in §2.3.3. Secondly, varying the camber of open rotor blades is an important tool used when designing blades where variable tip speed is used to achieve optimum performance at different operating conditions. In contrast, LINSUB employs a flat blade approximation. However, Evers and Peake (2002) showed that, whereas for an individual frequency component the camber can have a significant effect, when averaging over many frequencies, the effects of camber cancel out to a large degree. Finally, LINSUB seems to underpredict the output wave amplitudes in the case of non-zero blade loading, but we do not use these acoustic waves. In all the cases considered in this thesis we assume that locally the blades operate at zero incidence.

As the number of blades on an open rotor is typically small, cascade effects will be less significant than for high blade number fans. As mentioned at the start of this section, an alternative approach would be to use an isolated blade model for the blade response. This could be a useful area for future model development, as it would allow other effects (for example, a more detailed blade geometry) to be taken into account.

Application of LINSUB

In using this theory, we assume that as soon as a velocity perturbation wave reaches the rotor, it is simply convected by the mean flow there (which is in the chordwise direction) i.e. it becomes 'frozen in the flow' at that point and there are no further distortion effects. We decompose the normal velocity at the leading edge into azimuthal and temporal harmonics of the form $e^{-i\omega_\Gamma t+im\phi}$, and treat each harmonic separately; different azimuthal harmonics will have different inter-blade phase angles. Note that Smith used the opposite sign convention ($e^{i\omega_\Gamma t}$) in his analysis. We input the mean flow speed in the chordwise direction, W, and the assumption of pure convection within the LINSUB model then sets the upwash velocities at each chordal station.

In the notation of Smith, at a particular radial station, the lift across the blade aerofoil is given by

$$-\rho_0 W w_W \int_0^1 \Gamma_{WW}\left(\hat{z}\right) d\hat{z}, \tag{2.66}$$

where the circulation Γ_{WW} and chordwise coordinate $\hat{z}$ have been non-dimensionalised with respect to the amplitude of the velocity perturbation times chord length, $w_W c$, and chord length, c, respectively. The upwash velocity along the chord, $w(\hat{z})$, is given by

$$\frac{w(\hat{z})}{w_W} = \int_0^1 K(\hat{z}-\hat{z}_0)\Gamma_{WW}(\hat{z}_0)d\hat{z}_0, \tag{2.67}$$

where K contains all the information regarding the contribution of the vortex at $\hat{z}_0$ to the normal velocity at $\hat{z}$ (see equation (31) in Smith (1973) for the full expression for K).

This integral equation is converted to a matrix equation in order to solve numerically for Γ_{WW}. The kernel, K, and the upwash velocity, w, are calculated at a discrete number, n_c, of collocation points. The upwash velocity at those points is then given in a vector U. We determine Γ_{WW} by solving the matrix equation

$$U = K\Gamma, \tag{2.68}$$

(equation (50) in Smith (1973)). The l^{th} entry of the matrix Γ then gives

$$\frac{\pi}{2n_c}\sin\left(\frac{\pi l}{n_c}\right)\Gamma_{WW}(\hat{z}_l), \tag{2.69}$$

$$\text{where} \quad \hat{z}_l = \frac{1}{2}\left(1 - \cos\frac{\pi(2l+1)}{2n_c}\right). \tag{2.70}$$

A MATLAB program[5] was used to solve equation (2.68). Inputs are

stagger angle $\beta(r) = \tan^{-1}\left(\Omega r/U_f\right)$,
Mach no. in chordwise direction $M_W = W/c_0 = \left(\Omega^2 r^2 + U_f^2\right)^{\frac{1}{2}}/c_0$,
inter-blade phase angle $\chi = -2\pi m/B$,
reduced frequency $\lambda = -\omega_\Gamma c/W$,
space-chord ratio s/c,
number of collocation points n_c.

The inter-blade phase angle was arrived at as follows. The difference in incident velocity between blades as ϕ varies is given by $e^{-i\chi}$ (by definition). For a velocity with $e^{im\phi}$ dependence, if $\phi \to \phi + \frac{2\pi}{B}$, the velocity is multiplied by a factor $e^{\frac{2m\pi i}{B}}$, and thus we set $\chi = -\frac{2\pi m}{B}$. The optimum n_c is dependent upon the other parameters. For our purposes $n_c \geq 6$ is sufficient, and we use $n_c = 10$ in our numerical calculations, since this does not significantly slow down the calculations.

Once Γ_{WW} has been calculated, the pressure jump at $\hat{z}$ is given by

$$\Delta p = \rho_0 W w_W \Gamma_{WW}\left(\hat{z}, r; \omega_\Gamma, \chi\right) e^{-i\omega_\Gamma t} e^{im\phi}. \tag{2.71}$$

---

[5] Based on one developed by Dr Vincent Jurdic at the Institute of Sound and Vibration Research, University of Southampton.

2.3.2 Calculating the blade pressures

Since our information about the form of the upstream turbulence comes via its spectrum tensor in wavevector space we treat each upstream $\hat{u}_j^\infty(\mathbf{k})$ gust separately. We can then take the correlation of the blade pressure jump due to gusts of this form to obtain an expression for the total blade pressure spectrum in terms of S_{ij}^∞. Decomposing u_i (as given in equation (2.62)) with respect to $\mathbf{k}$ gives

$$\begin{aligned} u_i(\mathbf{x},t) =& \frac{1}{(2\pi)^3}\int_{\Re^3} A_{ij}(\mathbf{x},\mathbf{k})\,\hat{u}_j^\infty(\mathbf{k})\exp\left\{i\left[k_x\left(X(\mathbf{x})-U_\infty t\right)+k_yY(\mathbf{x})+k_zZ(\mathbf{x})\right]\right\}d^3\mathbf{k} \\ =& \frac{1}{(2\pi)^3}\int_{\Re^3} u_i^{\text{gust}}(\mathbf{x},t;\mathbf{k})\,d^3\mathbf{k}. \end{aligned} \tag{2.72}$$

The quantity we require in order to use LINSUB is the normal velocity $(\mathbf{N}\cdot\mathbf{u})$ at the leading edge of a blade, in a reference frame which rotates with the blades, decomposed into $e^{im\phi}$ harmonics. Majumdar also took the approach of treating each $\hat{u}_j^\infty(\mathbf{k})$ gust separately, but neglected the ϕ dependence in the amplitude A_{ij} which arises when considering a specific $\mathbf{k}$ value, treating only the ϕ dependence in the phase term of the velocity, $\exp\{i[k_yY+k_zZ]\}$.

The unit normal to the blade is given by

$$\mathbf{N}(r,\phi)=\sin\beta(r)\hat{\mathbf{e}}_{\mathbf{x}}+\cos\beta(r)\hat{\mathbf{e}}_\phi. \tag{2.73}$$

As Majumdar did, we use the relation

$$\exp\left\{i\left(k_y\cos\phi+k_z\sin\phi\right)R\right\}=\sum_{n=-\infty}^{\infty}J_n\left(\sqrt{k_y^2+k_z^2}R\right)\exp\left\{in\left[\phi-\tan^{-1}\left(\frac{k_z}{k_y}\right)\right]\right\}, \tag{2.74}$$

where the J_n denote Bessel functions, thus finding

$$\begin{aligned} &[\mathbf{N}\cdot\mathbf{A}]_j\exp\left\{i\left[k_xX+\left(k_y\cos\phi+k_z\sin\phi\right)R\right]\right\}= \\ &\qquad\exp\left(ik_xX\right)\left[\sin\beta A_{xj}+\cos\beta A_{\phi j}\right]\sum_{n=-\infty}^{\infty}J_n\left(r_kR\right)\exp\left\{in\left(\phi-\phi_k\right)\right\}, \end{aligned} \tag{2.75}$$

where $r_k=\sqrt{k_y^2+k_z^2}$, $\phi_k=\tan^{-1}\left(k_z/k_y\right)$ as in Figure 2.1.

In order to bring out the ϕ dependence of A_{ij} in exponential form we define a new tensor C_{ij}^{p} as follows

$$A_{ij}\left(x,r,\phi;\mathbf{k}\right)=\sum_{p=-\infty}^{\infty}C_{ij}^{p}\left(x,r;\mathbf{k}\right)e^{ip\phi},\tag{2.76}$$

$$\text{where}\quad C_{ij}^{p}\left(x,r;\mathbf{k}\right)=\frac{1}{2\pi}\int_{0}^{2\pi}A_{ij}\left(x,r,\phi;\mathbf{k}\right)e^{-ip\phi}d\phi.\tag{2.77}$$

Note that in the asymmetric case the integrand of C_{ij}^{p} will need to include the phase terms $e^{i(k_xX+k_yY+k_zZ)}$ as X, Y and Z then have ϕ dependence which cannot be written out in explicit form so readily as in equation (2.74).

Since ϕ_k only appears within A_{ij} in the form $(\phi_k-\phi)$ (via $k_r=r_k\cos\left(\phi_k-\phi\right)$ and $k_\phi=r_k\cos\left(\phi_k-\phi\right)$), we note that

$$A_{ij}\left(x,r,\phi;k_x,r_k,\phi_k\right)=A_{ij}\left(x,r,\phi-\phi_k;k_x,r_k,0\right),\tag{2.78}$$

and thus

$$\begin{aligned}C_{ij}^{p}\left(x,r;k_x,r_k,\phi_k\right)&=\frac{1}{2\pi}\int_{-\phi_k}^{2\pi-\phi_k}A_{ij}\left(x,r,\tilde{\phi};k_x,r_k,0\right)e^{-ip\left(\tilde{\phi}+\phi_k\right)}d\tilde{\phi}\\&=e^{-ip\phi_k}C_{ij}^{p}\left(x,r;k_x,r_k,0\right),\end{aligned}\tag{2.79}$$

making the substitution $\tilde{\phi}=\phi-\phi_k$, and using the fact that all terms in the integrand are 2π periodic.

Going back to the expression (2.72), it will be easiest to use the cartesian components of $\hat{u}_j^{\infty}(\mathbf{k})$, as we wish to use the cartesian definition of S_{ij}^{∞}. A polar representation is trickier, as quantities such as $\mathbf{\hat{e}_r}$ become ambiguous - depending on whether they relate to $\mathbf{x}$ (when calculating A_{ij}) or $\mathbf{k}$ (when inputting S_{ij}^{∞}). However we would also like to express A_{ij} as a function of $x,r,\phi,X,R,\partial X/\partial x,\partial X/\partial r,\partial R/\partial x,\partial R/\partial r,R/r$ (rather than the cartesian equivalents), as these are simpler to calculate. We therefore calculate the ‘polar’ coefficients C_{xx}^{p}, C_{xr}^{p}, $C_{x\phi}^{p}$, $C_{\phi x}^{p}$, $C_{\phi r}^{p}$, $C_{\phi\phi}^{p}$, and then translate these to ‘mixed suffix’ quantities A_{xx}, A_{xy}, A_{xz}, $A_{\phi x}$, $A_{\phi y}$, $A_{\phi z}$ for use in (2.75). This process is shown in the following example

$$\begin{aligned}\mathbf{\hat{e}_x}\cdot\mathbf{A}\cdot\mathbf{\hat{e}_y}&=\left[\mathbf{\hat{e}_x}\cdot\mathbf{A}\cdot\mathbf{\hat{e}_r}\right]\cos\phi-\left[\mathbf{\hat{e}_x}\cdot\mathbf{A}\cdot\mathbf{\hat{e}}_\phi\right]\sin\phi\\&=\frac{1}{2}\sum_{p=-\infty}^{\infty}\left\{e^{i\phi}\left(C_{xr}^{p}+iC_{x\phi}^{p}\right)+e^{-i\phi}\left(C_{xr}^{p}-iC_{x\phi}^{p}\right)\right\}e^{ip\phi}.\end{aligned}\tag{2.80}$$

Similarly, we substitute the appropriate C_{ij}^{p} terms into the following

$$\begin{aligned}
&\hat{\mathbf{e}}_{\mathbf{x}} \cdot \mathbf{A} \cdot \hat{\mathbf{e}}_{\mathbf{z}} = [\hat{\mathbf{e}}_{\mathbf{x}} \cdot \mathbf{A} \cdot \hat{\mathbf{e}}_{\mathbf{r}}] \sin\phi + [\hat{\mathbf{e}}_{\mathbf{x}} \cdot \mathbf{A} \cdot \hat{\mathbf{e}}_{\phi}] \cos\phi, \\
&\hat{\mathbf{e}}_{\phi} \cdot \mathbf{A} \cdot \hat{\mathbf{e}}_{\mathbf{x}}, \\
&\hat{\mathbf{e}}_{\phi} \cdot \mathbf{A} \cdot \hat{\mathbf{e}}_{\mathbf{y}} = [\hat{\mathbf{e}}_{\phi} \cdot \mathbf{A} \cdot \hat{\mathbf{e}}_{\mathbf{r}}] \cos\phi - [\hat{\mathbf{e}}_{\mathbf{x}} \cdot \mathbf{A} \cdot \hat{\mathbf{e}}_{\phi}] \sin\phi, \\
&\hat{\mathbf{e}}_{\phi} \cdot \mathbf{A} \cdot \hat{\mathbf{e}}_{\mathbf{z}} = [\hat{\mathbf{e}}_{\phi} \cdot \mathbf{A} \cdot \hat{\mathbf{e}}_{\mathbf{r}}] \sin\phi + [\hat{\mathbf{e}}_{\mathbf{x}} \cdot \mathbf{A} \cdot \hat{\mathbf{e}}_{\phi}] \cos\phi.
\end{aligned} \tag{2.81}$$

Defining D_j^p

We next define new quantities D_j^p, for use in the expression given in equation (2.75), as follows

$$\begin{aligned}
\sin\beta A_{xx} + \cos\beta A_{\phi x} &= \sum_{p=-\infty}^{\infty} \left[\sin\beta C_{xx}^{p} + \cos\beta C_{\phi x}^{p}\right] e^{ip\phi} \\
&\equiv \sum_{p=-\infty}^{\infty} D_x^p\left(x, r; k_x, r_k, \phi_k\right) e^{ip\phi} \\
&= \sum_{p=-\infty}^{\infty} D_x^p\left(x, r; k_x, r_k, 0\right) e^{ip(\phi-\phi_k)}, \\
\sin\beta A_{xy} + \cos\beta A_{\phi y} &= \sum_{p=-\infty}^{\infty} \Bigg[\sin\beta \frac{1}{2}\left\{\left(C_{xr}^{p-1} + iC_{x\phi}^{p-1}\right) + \left(C_{xr}^{p+1} - iC_{x\phi}^{p+1}\right)\right\} \\
&\quad + \cos\beta \frac{1}{2}\left\{\left(C_{\phi r}^{p-1} + iC_{\phi\phi}^{p-1}\right) + \left(C_{\phi r}^{p+1} - iC_{\phi\phi}^{p+1}\right)\right\}\Bigg] e^{ip\phi} \\
&\equiv \sum_{p=-\infty}^{\infty} D_y^p\left(x, r; k_x, r_k, \phi_k\right) e^{ip\phi}, \\
\sin\beta A_{xz} + \cos\beta A_{\phi z} &= \sum_{p=-\infty}^{\infty} \Bigg[\sin\beta \frac{1}{2}\left\{\left(-iC_{xr}^{p-1} + C_{x\phi}^{p-1}\right) + \left(iC_{xr}^{p+1} + C_{x\phi}^{p+1}\right)\right\} \\
&\quad + \cos\beta \frac{1}{2}\left\{\left(-iC_{\phi r}^{p-1} + C_{\phi\phi}^{p-1}\right) + \left(iC_{\phi r}^{p+1} + C_{\phi\phi}^{p+1}\right)\right\}\Bigg] e^{ip\phi} \\
&\equiv \sum_{p=-\infty}^{\infty} D_z^p\left(x, r; k_x, r_k, \phi_k\right) e^{ip\phi}.
\end{aligned} \tag{2.82}$$

From our previous relation for C_{ij}^{p} given in equation (2.79), we have used

$$D_j^p\left(x, r; k_x, r_k, \phi_k\right) = e^{-ip\phi_k} D_j^p\left(x, r; k_x, r_k, 0\right) + E. \tag{2.83}$$

The extra terms within E include additional $e^{\pm i\phi_k}$ factors. However, when the full integral over $d^3\mathbf{k}$ is taken these terms integrate to zero, and thus we do not include E in subsequent expressions.

Investigation of dominant p modes

Looking back at the definition of A_{ij} (equation (2.37)) we see that the denominator and numerator of each term (except the unity terms) contain pairs of l_i components. As ϕ only appears within $\mathbf{l}$ through $\cos(\phi_k - \phi)$ and $\sin(\phi_k - \phi)$ (see equation (2.45)) we see that the numerators and denominators contain only terms with $e^{i\hat{p}\phi}$ dependence where $\hat{p}$ varies between -2 and 2. We find in fact that the coefficients D_j^p die off fairly rapidly, and for most values of $\mathbf{k}$ seven or fewer values of p are significant, as seen in Figure 2.6.

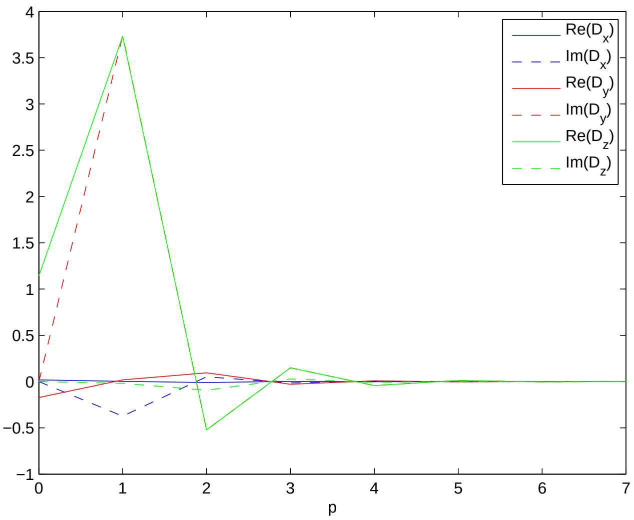

Figure 2.6: Here we see the rapid decay of all D_j^p values as p increases. Since $D_j^{-p} = \left(D_j^p\right)^*$ we do not need to calculate D_j^p for negative values of p to assess their decay. (Due to other terms which appear in the sum over p in the final expression for radiated sound the $+p$ and $-p$ terms do not directly cancel each other.)

Further investigation has shown that as $r_k \to \infty$ or $k_x \to \infty$ or $k_x \to 0$, fewer and fewer terms are significant, (i.e. we only require $p = -2, -1, ..., 2$ for convergence), whereas for small r_k and k_x mid-range a few more terms are needed. Including $p = -3, -2, ...3$ is sufficient for our results.

Moving to rotating frame

Substituting equations (2.82) into equation (2.72) via equation (2.74) we find

$$\begin{aligned}\mathbf{N}\cdot\mathbf{u} &= \frac{1}{2\pi^3}\int_{\Re^3}\hat{u}_j^{\infty}(\mathbf{k})\,e^{-ik_xU_\infty t}\left[\mathbf{N}\cdot\mathbf{A}\right]_j\exp\left\{i\left[k_xX+\left(k_y\cos\phi+k_z\sin\phi\right)R\right]\right\}d^3\mathbf{k}\\ &= \frac{1}{2\pi^3}\int_{\Re^3}\hat{u}_j^{\infty}(\mathbf{k})\,e^{-ik_xU_\infty t}\exp\left(ik_xX\right)\\ &\quad\sum_{m=-\infty}^{\infty}\sum_{p=-\infty}^{\infty}J_{m-p}\left(r_kR\right)D_j^p\left(x,r;k_x,r_k,0\right)e^{im(\phi-\phi_k)}d^3\mathbf{k}. \end{aligned} \tag{2.84}$$

We move into the rotating frame by substituting $\phi=\phi'+\Omega t$, where ϕ' is the angular coordinate which remains constant when rotating with the rotor, creating $u_i^{\text{rot.}}$. The amplitude of the normal velocity at the leading edge of a blade, in the rotating frame, to be substituted into equation (2.71), is given by

$$\begin{aligned}\sum_{m=-\infty}^{\infty}w_We^{-i\omega_\Gamma t+im\phi'} &= N_iu_i^{\text{rot.}}\big|_{\text{leading edge}}\\ &= N_i\left(x_0(r),r,\phi'\right)u_i^{\text{rot.}}\left(x_0(r),r,\phi',t;\mathbf{k}\right)\\ &= e^{ik_xX}\sum_{m=-\infty}^{\infty}\left\{\sum_{p=-\infty}^{\infty}J_{m-p}\left(r_kR\right)D_j^p\left(x_0(r),r;k_x,r_k,0\right)\right\}\\ &\quad\hat{u}_j^{\infty}(\mathbf{k})\exp\left[i\left(m\Omega-k_xU_\infty\right)t\right]\exp\left[im\left(\phi'-\phi_k\right)\right], \end{aligned} \tag{2.85}$$

where $x_0(r)$ is the axial position of the leading edge of the blade. The effect of moving to the rotating frame has determined the correct frequency for use in the response function, $\omega_\Gamma=k_xU_\infty-m\Omega$; we can now replace ϕ' by $\phi-\Omega t$ again. Substituting into equation (2.71), the pressure jump across a blade which passes through the position x, r, ϕ at time t, due to an upstream gust of the form $\hat{\mathbf{u}}^{\infty}(\mathbf{k})e^{i(\mathbf{k}\cdot\mathbf{x}-k_xU_\infty t)}$, is

$$\begin{aligned}\Delta p\left(x,r,\phi,t\right)=&\rho_0W\sum_{m=-\infty}^{\infty}\Gamma_{WW}^{m}\left(\hat{z}=\frac{x-x_0\left(r\right)}{\cos\beta(r)},r;\omega_\Gamma=k_xU_\infty-m\Omega,\chi=-\frac{2m\pi}{B}\right)\\ &\sum_{p=-\infty}^{\infty}J_{m-p}\left(r_kR\right)D_j^p\left(x_0(r),r;k_x,r_k,0\right)\hat{u}_j^{\infty}(\mathbf{k})\,e^{ik_xX}e^{-ik_xU_\infty t}e^{im(\phi-\phi_k)}. \end{aligned} \tag{2.86}$$

The arguments of Γ_{WW} have moved the leading edge of the blade to the correct position, and defined the frequency ω_Γ and inter-blade phase angle χ. The full pressure jump is found by integrating equation (2.86) over $\mathbf{k}$ $\left(\frac{1}{(2\pi)^3}\int ...d^3k\right)$. The pressure jump across blade b which cuts through the position x, r at time t, denoted by $\Delta p^b\left(x,r,\phi,t\right)$, is found by substituting the azimuthal position of the leading edge of the b^{th} blade, $\phi^b = \phi_0(r) + 2\pi b/B + \Omega t$ into the above expression.

Definition of $\hat{P}_{\mathbf{blade}}$

We are now in a position to calculate the spectrum of blade pressures, defined as

$$\begin{aligned}\hat{P}_{\mathrm{blade}}\left(x,r,\omega\right) &= \int_{-\infty}^{\infty} P_{\mathrm{blade}}\left(x,r,\tau\right)e^{i\omega\tau}d\tau \\ &= \int_{-\infty}^{\infty}\left\langle\overline{\left(\Delta p^b\left(x,r,t\right)\right)^*, \Delta p^b\left(x,r,t+\tau\right)}\right\rangle e^{i\omega\tau}d\tau. \qquad (2.87)\end{aligned}$$

This expression denotes taking a large number of different realisations of the upstream turbulence, i.e. a large number of different $u_k^\infty\left(\mathbf{x}'\right)$, averaging over these and then averaging over time as well. We denote the ensemble average by $\langle,\rangle$ and the temporal average by the overbar. In this way we obtain a statistical average over many rotations of the blade pressure differences across a particular point on a blade - a potentially useful quantity for calibration against experimental observation. By averaging over time we should remove the dependence upon blade number b.

Substituting in the expression from equation (2.86) we find

$$\begin{aligned}P_{\mathrm{blade}}\left(x,r,\tau\right) = \Bigg\langle &\rho_0 W\int_{\Re^3}\sum_{m=-\infty}^{\infty}\left[\Gamma_{WW}^m\left(x,r,k_x\right)\right]^*\exp\left(ik_xU_\infty t\right)\exp\left(-ik_xX\right) \\ &\left\{\sum_{p=-\infty}^{\infty}J_{m-p}\left(r_kR\right)e^{-im\phi_k}D_j^p\left(x_0(r),r;k_x,r_k,0\right)\right\}^* \\ &\exp\left[-im\phi^b(r,t)\right]\left[\frac{1}{\left(2\pi\right)^3}\int_{\Re^3}u_j^\infty\left(\mathbf{y}\right)\exp\left(i\mathbf{k}\cdot\mathbf{y}\right)d^3\mathbf{y}\right]d^3\mathbf{k}, \\ &\rho_0 W\int_{\Re^3}\sum_{m'=-\infty}^{\infty}\Gamma_{WW}^{m'}\left(x,r,k_x'\right)\exp\left(-ik_x'U_\infty(t+\tau)\right)\exp\left(ik_x'X\right) \\ &\left\{\sum_{p'=-\infty}^{\infty}J_{m'-p'}\left(r_k'R\right)e^{-im'\phi_k'}D_k^{p'}\left(x_0(r),r;k_x',r_k',0\right)\right\} \\ &\exp\left[im'\phi^b(r,t+\tau)\right]\left[\frac{1}{\left(2\pi\right)^3}\int_{\Re^3}u_k^\infty\left(\mathbf{y}'\right)\exp\left(-i\mathbf{k}'\cdot\mathbf{y}'\right)d^3\mathbf{y}'\right]d^3\mathbf{k}'\Bigg\rangle\end{aligned}$$

$$
\begin{aligned}
={}&\rho_0^2 W^2 \int_{\Re^3} \int_{\Re^3} \sum_{m=-\infty}^{\infty} \left[\Gamma_{WW}^{m}\left(x,r,k_x\right)\right]^* e^{-im\left(\phi_0(r)+\frac{2\pi b}{B}\right)} \\
&\left\{\sum_{p=-\infty}^{\infty} J_{m-p}\left(r_k R\right) e^{-im\phi_k} D_j^p\left(x_0(r),r;k_x,r_k,0\right)\right\}^* \\
&\sum_{m'=-\infty}^{\infty} \Gamma_{WW}^{m'}\left(x,r,k_x'\right) e^{im'\left(\phi_0(r)+\frac{2\pi b}{B}\right)} \\
&\left\{\sum_{p'=-\infty}^{\infty} J_{m'-p'}\left(r_k' R\right) e^{-im'\phi_k'} D_k^{p'}\left(x_0(r),r;k_x',r_k',0\right)\right\} \\
&\frac{1}{(2\pi)^6}\left[\int_{\Re^3}\int_{\Re^3} \left\langle u_j^{\infty}\left(\mathbf{y}'\right), u_k^{\infty}\left(\mathbf{y}\right)\right\rangle_{\infty} e^{i\mathbf{k}\cdot\mathbf{y}} e^{-i\mathbf{k}'\cdot\mathbf{y}'} d^3\mathbf{y}\, d^3\mathbf{y}'\right] \\
&\left\langle\, e^{i(m'-m)\Omega t} e^{i(k_x-k_x')U_\infty t}\,\right\rangle_t e^{i(k_x'-k_x)X} e^{-i(k_x'U_\infty-m'\Omega)\tau} d^3\mathbf{k}'\, d^3\mathbf{k}.
\end{aligned} \tag{2.88}
$$

As before (when calculating the velocity correlation R_{ij}, equation (2.63)) the double integral over $\mathbf{y}$ and $\mathbf{y}'$ reduces to $(2\pi)^6\delta(\mathbf{k}-\mathbf{k}')S_{kl}^{\infty}\left(\mathbf{k}\right)$ via a change of variables, $\mathbf{y}' = \mathbf{y}+\boldsymbol{\eta}$, and setting $\mathbf{k}' = \mathbf{k}$ when performing the $\mathbf{k}'$ integral removes several terms. The long time average then acts on $e^{i(m'-m)\Omega t}$ only, which reduces to $\delta_{mm'}$ using

$$
\delta_{mm'} = \lim_{T\to\infty} \frac{1}{2T} \int_{-T}^{T} e^{i(m-m')t'} dt'. \tag{2.89}
$$

Note that blade number dependence in the expression given in equation (2.88) has indeed vanished.

We take the Fourier transform in τ to obtain $\hat{P}_{\text{blade}}$; a factor $\frac{2\pi}{U_\infty}\delta\left(k_x - \omega/U_\infty - m\Omega/U_\infty\right)$ is brought in and we can perform the k_x integral. Thus only one value of k_x contributes for a particular value of ω and m. We can integrate over polar $\mathbf{k}$ instead of the cartesian representation by writing $k_y = r_k\cos\phi_k, k_z = r_k\sin\phi_k$

$$
\begin{aligned}
\hat{P}_{\text{blade}}\left(x,r,\omega\right) = {}& \frac{2\pi\rho_0^2 W^2}{U_\infty} \sum_{m=-\infty}^{\infty} \left|\Gamma_{WW}^{m}\left(x,r,\omega\right)\right|^2 \int_0^{\infty} \left\{\sum_{p=-\infty}^{\infty} J_{m-p}\left(r_k R\right) D_j^p\left(x_0(r),r;k_x^m,r_k,0\right)\right\}^* \\
&\left\{\sum_{p'=-\infty}^{\infty} J_{m-p'}\left(r_k R\right) D_k^{p'}\left(x_0(r),r;k_x^m,r_k,0\right)\right\} \left[\int_0^{2\pi} S_{jk}^{\infty}\left(k_x^m,k_y,k_z\right) d\phi_k\right] r_k dr_k.
\end{aligned} \tag{2.90}
$$

where in the above expression $k_x^m = (\omega + m\Omega)/U_\infty$, that is the time dependence has been set to $e^{-i\omega\tau}$, and we sum over cartesian suffices $j = x, y, z$.

The ϕ_k integral above can be carried out analytically

$$\int_0^{2\pi} S_{jk}^{\infty}(k_x, k_y, k_z)\, d\phi_k = 0 \quad \text{if} \quad j \neq k, \tag{2.91}$$

as these terms involve only the integral of $\sin\phi_k$, $\cos\phi_k$ or $\sin\phi_k \cos\phi_k$ over a 2π period, and

$$\int_0^{2\pi} S_{xx}^{\infty}(k_x, k_y, k_z)\, d\phi_k = 2\pi r_k^2 G, \tag{2.92}$$

$$\int_0^{2\pi} S_{yy}^{\infty}(k_x, k_y, k_z)\, d\phi_k = \int_0^{2\pi} S_{zz}^{\infty}(k_x, k_y, k_z)\, d\phi_k = \left(2\pi k^2 - \pi r_k^2\right) G, \tag{2.93}$$

where $G = 55 g_1 \overline{u_{\infty,1}^2} / 36\pi L^{\frac{2}{3}} \left(g_2/L^2 + k_x^2 + r_k^2\right)^{17/6}$ for the von Kármán spectrum. We thus have an integral expression for the blade pressures which involves an infinite summation over m, and an infinite integral over r_k. Evaluation of $\hat{P}_{\text{blade}}$ numerically requires further analysis to determine which indices and regions of the integral give the dominant contributions; we discuss the latter in the next subsection. The sum over p is less problematic as the coefficients die off rapidly as outlined above.

2.3.3 Limiting the r_k integral

As highlighted previously, LINSUB neglects radial gradients. If we consider 3D input gusts which take the form $e^{ik_x x + im\phi + ik_t r}$, LINSUB will treat the $e^{ik_t r}$ factor as part of the amplitude at a particular r station[6]. Eventually, for large k_t, the approximation of neglecting the contribution of the wavenumber in the radial direction to derivatives will break down. The output we use from LINSUB, the blade pressure jumps, do not need to satisfy a dispersion relation. However, the sound waves which we will ultimately obtain from solving the wave equation will satisfy a dispersion relation obtained via the $(\nabla^2 - \omega^2/c_0^2)$ operator. Thus here we limit our attention to k_t values which eventually contribute to the radiated sound, and in this way obtain a convergent integral expression.

---

[6] Note that LINSUB assumes that once a disturbance reaches the leading edge it is simply convected. This means the wavenumbers within the LINSUB analysis are not the same as for the incident velocity. The axial wavenumber within LINSUB, denoted by Smith as α, is not equal to k_x as we define it in the expression for $\mathbf{N} \cdot \mathbf{u}$; m is input via the inter-blade phase angle but then several different tangential wavenumbers, β, are found, some of which will correspond to imaginary α.

Determining the effective radial wavenumber

The expression for the velocity field input into LINSUB, as it stands in equation (2.84), does not have r dependence written explicitly in the form $e^{ik_t r}$, where we can simply pick out the appropriate k_t upon which to impose limits. We therefore need to determine an expression for the 'effective' radial wavenumber given a general r dependence within the velocity input. The situation is not completely straightforward as we wish to translate between a full cylindrical gust and the rectilinear system of LINSUB in a consistent manner and this requires some approximations.

Posson et al. (2010) and Glegg and Jochault (1998) have looked at similar problems of translating between these two coordinate systems. Posson noted that, in addition to the wave equation being satisfied in each of the two frames, there are two conditions which we might like to satisfy when moving from the annular to the rectilinear frame. Firstly, keeping the tangential wavevector the same in the two frames and secondly keeping the structure of the radial function the same, e.g. by decomposing Bessel functions into cosines, and then into exponentials, and taking k_t from these waves. However, she showed it was not possible to satisfy both of these conditions at once, in general.

We identify r in the annular frame with z in the rectilinear one. Given a disturbance of the form $f(r)e^{ik_p x+i\frac{m}{r}r\phi-i\omega t}$ we wish to equate this to a wave in the rectilinear set-up of the form $e^{ik_x x+ik_y y+ik_t z-i\omega t}$ (where x remains the axial direction and y is the transverse direction), and thus pick out k_t. For a disturbance which satisfies the wave equation, and has the same time dependence, this comes down to equating the output of ∇^2 in the two frames. If we also wish to keep the wavenumber vector in a plane of constant radius the same in the unwrapped configuration then

$$k_p^2+\left(\frac{m}{r}\right)^2=k_x^2+k_y^2, \tag{2.94}$$

$$\tan\hat{\theta}=\frac{m}{k_p r}=\frac{k_y}{k_x}, \tag{2.95}$$

(Posson et al., 2010). Thus we identify k_p with k_x and m/r with k_y. Equating the result of applying the ∇^2 operator we find

$$k_x^2+k_y^2+k_t^2=-\frac{\frac{1}{r}\frac{\partial}{\partial r}\left(r\frac{\partial f}{\partial r}\right)}{f(r)}+\frac{m^2}{r^2}+k_p^2, \tag{2.96}$$

$$\Rightarrow \quad k_t^2=-\frac{\frac{1}{r}\frac{\partial}{\partial r}\left(r\frac{\partial f}{\partial r}\right)}{f(r)}. \tag{2.97}$$

This gives a general formula for picking out the effective radial wavenumber from an expression with r dependence. The r dependence within our velocity expression is given by $J_n(r_k R)$. Thus we find

$$k_t^2 = r_k^2 \left(\frac{\partial R}{\partial r}\right)^2 \left(1 - \frac{n^2}{r_k^2 R^2}\right) - \left(\frac{r_k}{r}\frac{\partial R}{\partial r} + \frac{r_k}{r}\frac{\partial^2 R}{\partial r^2} - \frac{r_k}{R}\left(\frac{\partial R}{\partial r}\right)^2\right) \frac{J_n'(r_k R)}{J_n(r_k R)}, \tag{2.98}$$

and we can rewrite $J_n'(r_k R) = \frac{1}{2}\left(J_{n-1}(r_k R) - J_{n+1}(r_k R)\right)$. The second set of terms here comes to zero if R is a linear function of r. In Figure 2.7 we see that R is indeed close to a linear function of r for the actuator disk model we employ, except near the blade tip. In his work on UDN, Cargill (1993) took $R = \alpha r$, and thus used a simplified form for the effective radial wavenumber with $\partial R/\partial r = \alpha$. Note that, as Cargill did, we have neglected the r dependence within $e^{ik_x X(x,r)}$ in determining k_t.

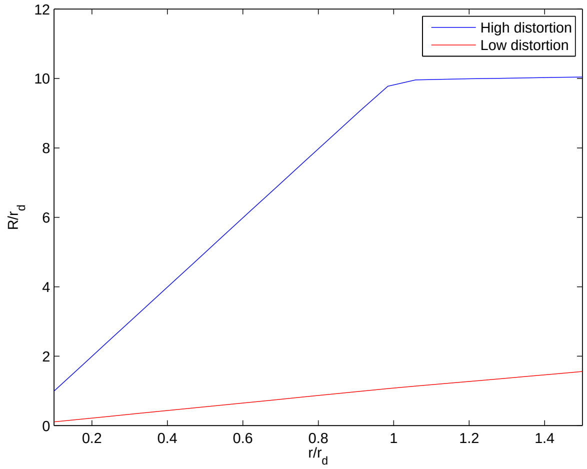

Figure 2.7: The upstream r value of a streamline which originates at the rotor face, denoted by R, is shown to be linear in the case of low distortion, and near to linear along the majority of the blade span in the high distortion case. Very near the blade tip in the high distortion case linearity does break down, but in our numerical calculation of radiated sound we will consider discrete radial positions, the outermost of which can be chosen to lie within the linear range.

Limiting condition

We invert expression (2.98) in order to impose finite limits upon the r_k integral in (2.90). We therefore find

$$r_k^2 = \frac{k_t^2}{\left(\frac{\partial R}{\partial r}\right)^2} + \frac{(m-p)^2}{R^2}. \tag{2.99}$$

A first approximation limit upon k_t^2, taking into account its contribution to ∇^2, is given by $k_t^2 \leq \omega^2/c_0^2$. This is essentially the limit that would be imposed if we were considering a stationary source on an infinite span airfoil. An area for future work, outlined in Appendix D, is to implement more precise limits for r_k^2 based on a rigorous stationary phase argument. For now, in our numerical calculation of expression (2.90), we impose

$$\sqrt{\frac{(m-p)^2}{R^2}} \leq r_k \leq \sqrt{\left(\frac{\partial R}{\partial r}\right)^{-2} \frac{\omega^2}{c_0^2} + \frac{(m-p)^2}{R^2}}. \tag{2.100}$$

Since $(m-p)$ is the order of the Bessel function which governs radiation, and $r_k R$ is its argument, the lower limit here is a statement that it is when the argument is greater than the order that we get radiation, as noted by Parry (1988). Within the upper limit the quantity $\partial R/\partial r$ appears, which gives the magnitude of the streamtube contraction. Far upstream we have $\partial R/\partial r = 1$, and it increases as we travel towards the rotor. This contraction is analogous to that experienced in a contracting duct. For a duct of radius a the Helmholtz number, $\omega a/c_0$, gives the non-dimensional frequency and controls the number of propagating modes. In our case, we therefore interpret the quantity

$$\left(\frac{\partial R}{\partial r}\right)^{-1} \frac{\omega}{c_0}, \tag{2.101}$$

as proportional to an effective Helmholtz number.

2.3.4 Blade pressure plots

In Figures 2.8 and 2.9 we plot the blade pressure spectra as calculated from equation (2.90) for a range of distortion levels and integral lengthscales. Peaks are found at all integer multiples of Ω.

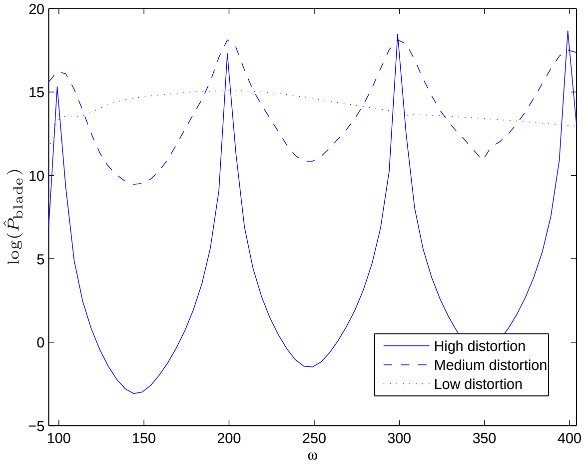

Figure 2.8: The blade pressure spectrum at the leading edge of the blades, near the hub ($r/r_d = 0.4$). High distortion corresponds to $U_f/U_\infty = 100$; medium to $U_f/U_\infty = 10$; low to $U_f/U_\infty = 1.18$. As distortion is increased, the blade pressure peaks increasingly sharply at integer multiples of the rotor angular velocity.

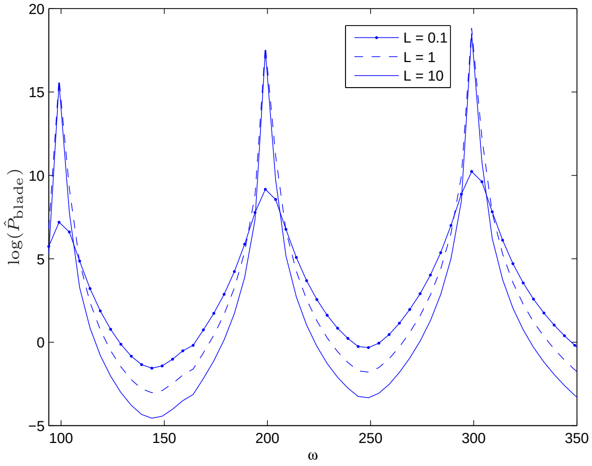

Figure 2.9: High distortion case ($U_f/U_\infty = 100$), comparing L values. As L is increased above the streamtube radius ($L \sim 1$) the peaks remain but the overall level is lowered.

2.3.5 Unsteady force generated by a single rotor

Single wavevector component

The total force per unit volume, $\mathbf{f}$, generated by the rotor is found by summing the pressure jumps across each blade, as given in equation (2.86). The argument which follows is similar to Majumdar's analysis (where we have expanded details of the use of the delta function), the difference being our treatment of the ϕ dependence within A_{ij} terms. Blade number is denoted by b and runs from $1, ..., B$ and we first consider a single upstream wavevector component $\mathbf{k}$, with amplitude $\hat{u}_j^\infty(\mathbf{k})$, for which the force upon the fluid is given by

$$\begin{aligned} f_i^k\left(x, r, \phi, t; \mathbf{k}\right) = &\sum_{b=1}^{B} \rho_0 W N_i(r) \exp\left(-ik_x U_\infty t\right) \sum_{m=-\infty}^{\infty} \Gamma_{WW}^m\left(x, r; k_x, \chi^m\right) \\ &e^{ik_x X} \sum_{p=-\infty}^{\infty} J_{m-p}\left(r_k R\right) \exp\left(-im\phi_k\right) D_j^p\left(x_0(r), r; k_x, r_k, 0\right) \\ &\hat{u}_j^\infty(\mathbf{k}) \exp\left(im\left[\phi_0(r) + \frac{2b\pi}{B} + \Omega t\right]\right) \\ &\sum_{s=-\infty}^{\infty} \delta\left[r\left(\phi - \Omega t - \phi_0(r) - \frac{2b\pi}{B}\right) - \left(x - x_0(r)\right)\tan\beta(r) - 2\pi s\right]. \end{aligned} \tag{2.102}$$

Here N_i gives the direction of the force, normal to the blade. The sum over p has come from $e^{ip\phi}$ dependence within A_{ij}. The delta function[7] defines the blade surface, noting that $\Gamma_{WW}^m = 0$ for x values outside the chord.

We wish to separate out the ϕ and t dependence within $\mathbf{f}$ explicitly which will allow us to solve the wave equation in the next section. Firstly we re-express the delta function as

$$\begin{aligned} &\sum_{s=-\infty}^{\infty} \delta\left[r\left(\phi - \Omega t - \phi_0(r) - \frac{2b\pi}{B}\right) - \left(x - x_0(r)\right)\tan\beta(r) - 2s\pi\right] \\ &\qquad = \frac{1}{2\pi r} \sum_{s=-\infty}^{\infty} \exp\left(is\left[\left(\phi - \Omega t - \phi_0(r) - \frac{2b\pi}{B}\right) - \frac{\left(x - x_0(r)\right)\tan\beta(r)}{r}\right]\right), \end{aligned} \tag{2.103}$$

---

[7] The dimension of the delta function's argument is of length, and thus the delta function's output has dimensions 1/length, giving the correct dimensions for the full expression of a force per unit volume.

where we have used the relation $\delta(rx) = \delta(x)/r$ (for $r \neq 0$), and the Poisson summation formula $2\pi \sum_{-\infty}^{\infty} \delta(x - 2\pi s) = \sum_{-\infty}^{\infty} \exp(-isx)$. For particular values of m and l we can now collect together all those terms in equation (2.102) involving blade number b, which are

$$\sum_{b=1}^{B} \exp\left(\frac{2bm\pi i}{B}\right) \frac{1}{2\pi r} \sum_{s=-\infty}^{\infty} \exp\left(is\left[\left(\phi - \Omega t - \phi_0(r) - \frac{2b\pi}{B}\right) - \frac{(x - x_0(r))\tan\beta(r)}{r}\right]\right)$$
$$= \frac{B}{2\pi r} \sum_{l=-\infty}^{\infty} \exp\left(-i(m + lB)\left[(\phi - \Omega t - \phi_0(r)) - \frac{(x - x_0(r))\tan\beta(r)}{r}\right]\right). \qquad (2.104)$$

Here we have used

$$\begin{aligned} \sum_{b=1}^{B} \exp\left(\frac{2\pi i b(m+s)}{B}\right) &= 0 \quad \text{if} \quad \frac{m+s}{B} \quad \text{non-integer}, \\ &= B \quad \text{if} \quad \frac{m+s}{B} \quad \text{integer}, \end{aligned} \qquad (2.105)$$

and thus we have set $s = -lB - m$ and summed over l instead of s. For a particular l and m value, collecting together all the t dependent terms in (2.102), we find $\exp(-i[k_x U_\infty + lB\Omega]t)$ dependence. The ϕ dependence is given by $\exp(i[m + lB]\phi)$.

2.3.6 Total force

Thus, if we now consider the full incident velocity over all wavenumbers in place of a single harmonic, $\hat{u}_j^\infty(\mathbf{k})$, we find the force term is given by

$$\begin{aligned} f_i(x, r, \phi, t) =& \rho_0 W N_i(r) \frac{B}{2\pi r} \sum_{m=-\infty}^{\infty} \frac{1}{(2\pi)^3} \int_{\Re^3} \Gamma_{WW}^m(x, r; k_x, \chi^m) \exp(-ik_x U_\infty t) \\ & e^{ik_x X} \sum_{p=-\infty}^{\infty} J_{m-p}(r_k R) \exp\{-im\phi_k\} D_j^p(x_0(r), r; k_x, r_k, 0) \\ & \left[\int_{\Re^3} u_j^\infty(\mathbf{x}') \exp(-i\mathbf{k}\cdot\mathbf{x}')\, d^3\mathbf{x}'\right] d^3\mathbf{k} \\ & \sum_{l=-\infty}^{\infty} \exp\left(i(m + lB)\left[\frac{(x - x_0(r))\tan\beta(r)}{r}\right]\right) \exp(-ilB\phi_0(r)) \\ & \exp(-ilB\Omega t) \exp(i[m + lB]\phi). \end{aligned} \qquad (2.106)$$

2.4 Far-field solution of the wave equation

The final part of our calculation is to substitute the forcing term (2.106) into the wave equation, in order to calculate the far-field pressure spectrum, and hence the Unsteady Distortion Noise heard by someone beneath the flight-path of an Advanced Open Rotor driven aircraft.

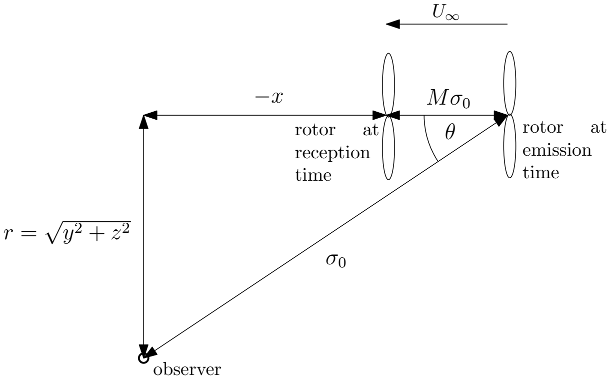

Figure 2.10: Far-field coordinate system.

We work in two sets of coordinates (as shown in Figure 2.10): reception coordinates, (x, y, z) or (x, r, ϕ), where the observer's position is given at the time the sound is heard; and emission ('wind-tunnel') coordinates, (σ_0, θ, ϕ), where the observer's position is given at the time the sound was emitted. In addition, the source coordinates (x_s, r_s, ϕ_s) give the position of a blade source with respect to the rotor's origin. We work in the reference frame in which the rotor is stationary in the axial direction, and assume a uniform flight speed U_∞, in which case the wave equation is given by

$$\nabla^2 p - \frac{1}{c_0^2}\left(\frac{\partial}{\partial t} + U_\infty \frac{\partial}{\partial x}\right)^2 p = \nabla \cdot \mathbf{f}\left(\mathbf{x}, t\right). \tag{2.107}$$

In the previous section we saw that the ϕ dependence within each term of the triple infinite series which makes up $\mathbf{f}$ takes the form $\exp\left(iq\phi\right)$, where $q = m + lB$. Similarly, we saw that each t harmonic is of the form $\exp\left(-i\omega t\right)$ where $\omega = k_x U_\infty + lB\Omega$, and all terms are subsequently integrated over k_x. It is the extra $k_x U_\infty$ term within the frequency ω which contains information about the turbulent aspect of the problem, these are not purely periodic source terms. We can solve for each value of l, m, p and k_x separately and then integrate over k_x and sum over all indices.

Thus we seek the solution, $p^{l,m,p}(\mathbf{x},t,k_x)$, to the problem

$$\nabla^2 p^{l,m,p} - \frac{1}{c_0^2}\left(\frac{\partial}{\partial t} + U_\infty \frac{\partial}{\partial x}\right)^2 p^{l,m,p} = \nabla \cdot \left\{\mathbf{N}(r) F^{l,m,p}(x,r,k_x)\exp(iq\phi)\right\}\exp(-i\omega t), \tag{2.108}$$

where

$$\begin{aligned} F^{l,m,p}(x,r,k_x) =& \rho_0 W \frac{B}{2\pi r}\Gamma^m_{WW}(x,r;k_x,\chi^m)\, e^{ik_x X} \\ & \frac{1}{(2\pi)^3}\int_{\Re^2} J_{m-p}(r_k R)\exp\{-im\phi_k\}\, D^p_j(x_0(r),r,k_x,r_k,0) \\ & \left[\int_{\Re^3} u^\infty_j(\mathbf{x}')\exp(-i\mathbf{k}\cdot\mathbf{x}')\, d^3\mathbf{x}'\right] dk_y dk_z \\ & \exp\left(-i(m+lB)\left[\frac{(x-x_0(r))\tan\beta(r)}{r}\right]\right)\exp(-ilB\phi_0(r))]. \end{aligned} \tag{2.109}$$

Note that, as u^∞_j is a statistical quantity, we will only be able to calculate explicitly the auto-correlation or some other average of p.

Since there is no diffraction in our problem, p must have the same azimuthal and time dependence as F. Writing

$$p^{l,m,p}(\mathbf{x},t,k_x) = \hat{p}^{l,m,p}(x,r,k_x)\exp(iq\phi)\exp(-i\omega t), \tag{2.110}$$

we find $\hat{p}^{l,m,p}$ obeys the equation

$$\begin{aligned} \frac{1}{r}\frac{\partial}{\partial r}\left(r\frac{\partial \hat{p}^{l,m,p}}{\partial r}\right) - \frac{q^2}{r^2}\hat{p}^{l,m,p} + \frac{\partial^2 \hat{p}^{l,m,p}}{\partial x^2} - \frac{1}{c_0^2}\left(-i\omega + U_\infty\frac{\partial}{\partial x}\right)^2 \hat{p}^{l,m,p} = \\ \sin\beta(r)\frac{\partial F^{l,m,p}}{\partial x} + \frac{iq}{r}\cos\beta(r) F^{l,m,p}. \end{aligned} \tag{2.111}$$

Here we have substituted $\mathbf{N} = (\sin\beta(r), 0, \cos\beta(r))$ for the blade normal and thus we neglect any radial component of $\mathbf{N}$, i.e. we do not consider lean of the blade. We can find the solution to (2.111) in integral form by seeking the appropriate Green's function, $H^{l,m}$, in x and r. The solution will then be given by (noting that (σ_0, θ) can be directly related to (x, r))

$$\hat{p}^{l,m,p}(\sigma_0, \theta, k_x) = \int_{r_s}\int_{x_s} H^{l,m}(\sigma_0, \theta; x_s, r_s) \left[\sin\beta(r_s)\frac{\partial F^{l,m,p}(x_s, r_s, k_x)}{\partial x_s} + \frac{iq}{r_s}\cos\beta(r_s) F^{l,m,p}(x_s, r_s, k_x)\right] r_s dr_s dx_s. \tag{2.112}$$

We now derive the Green's function using the same framework as Hanson (1995), which will allow us to extend to the non-zero incidence case in a straightforward manner in Chapter 5. In Hanson[8], the force term is re-expressed as

$$\nabla \cdot \mathbf{f} = -\sum_{\omega} Q_\omega(x, y, z)\, e^{-i\omega t}, \tag{2.113}$$

where ω is given by $mB\Omega$. Thus he treats periodic sources with frequencies which are multiples of BPF only. The exact solution is then given by

$$p(x, y, z, t) = \sum_{\omega} P_\omega(x, y, z)\, e^{-i\omega t}, \tag{2.114}$$

where

$$P_\omega(x, y, z) = \int_{\Re^3} \frac{Q_\omega(x_s, y_s, z_s)\, e^{i\frac{\omega}{c_0}\sigma}}{4\pi S} dx_s dy_s dz_s, \tag{2.115}$$

$$S = \sqrt{(x - x_s)^2 + (1 - M^2)\left[(y - y_s)^2 + (z - z_s)^2\right]}, \tag{2.116}$$

$$\sigma = \frac{\left[-M(x - x_s) + S\right]}{(1 - M^2)}. \tag{2.117}$$

Here $M = U_\infty / c_0$.

Our sources Q_ω take the form

$$\begin{aligned} Q_\omega(x_s, r_s, \phi_s) &= -\nabla \cdot \left\{\mathbf{N}(r_s) F^{l,m,p}(x_s, r_s; k_x)\exp(iq\phi_s)\right\} \\ &= -\widetilde{F}(x_s, r_s)\, e^{iq\phi_s}. \end{aligned} \tag{2.118}$$

In the far-field we can make some simplifying approximations to (2.116) and (2.117) and then find the appropriate Green's function by substituting (2.118), which has simple ϕ

---

[8] Note that the positive x direction in Hanson (1995) is the reverse of ours.

dependence, into (2.115). The first simplifying approximation is to substitute the leading order term of S into the denominator of (2.115). This leading order approximation is given by

$$S \approx S_0 = \sqrt{x^2 + \left(1 - M^2\right)\left(y^2 + z^2\right)} = \sigma_0 \left(1 - M \cos\theta\right), \tag{2.119}$$

using $-x = \sigma_0 \left(\cos\theta - M\right)$ and $y^2 + z^2 = \sigma_0^2 \left(1 - \cos^2\theta\right)$ (see Figure 2.10). The second simplifying approximation is to calculate terms up to the first order of S and substitute this into the phase. We find

$$\begin{aligned} S &= \sqrt{x^2 + \left(1 - M^2\right)\left(y^2 + z^2\right) - 2xx_s + \left(1 - M^2\right)\left(-2yy_s - 2zz_s\right) + O(\mathbf{x_s}^2)} \\ &= S_0 \sqrt{1 - \frac{2xx_s}{S_0^2} + \frac{\left(1 - M^2\right)\left(-2yy_s - 2zz_s\right)}{S_0^2} + O(\mathbf{x_s}^2)}, \end{aligned} \tag{2.120}$$

$$\begin{aligned} \Rightarrow \quad S \approx S_0 + S_1 &= S_0 - \frac{xx_s}{S_0} - \left(1 - M^2\right) \frac{\left(yy_s + zz_s\right)}{S_0} \\ &= S_0 - \frac{xx_s}{S_0} - \left(1 - M^2\right) \frac{\left(r \cos\phi r_s \cos\phi_s + r \sin\phi r_s \sin\phi_s\right)}{S_0}. \end{aligned} \tag{2.121}$$

The phase approximation is therefore

$$\begin{aligned} \sigma &\approx \frac{-M\left(x - x_s\right) + S_0 + S_1}{1 - M^2} \\ &= \frac{-M\left(x - x_s\right) + S_0 - \frac{xx_s}{S_0}}{1 - M^2} - \frac{rr_s\left(\cos\phi\cos\phi_s + \sin\phi\sin\phi_s\right)}{S_0} \\ &= \sigma_0 + \frac{\cos\theta}{1 - M\cos\theta} x_s - \frac{\sin\theta}{1 - M\cos\theta} r_s \cos\left(\phi - \phi_s\right), \end{aligned} \tag{2.122}$$

using $S_0 = \sigma_0 \left(1 - M\cos\theta\right)$, $x = -\sigma_0 \left(\cos\theta - M\right)$ and $r = \sigma_0 \sin\theta$. Substituting (2.118), (2.119) and (2.122) into (2.115), we find

$$\begin{aligned} P_\omega\left(x, y, z\right) &= \int_{\Re^3} \frac{-\widetilde{F}\left(x_s, r_s\right) e^{iq\phi_s}}{4\pi\sigma_0\left(1 - M\cos\theta\right)} e^{i\frac{\omega}{c_0}\left[\sigma_0 + \frac{\cos\theta}{1 - M\cos\theta}x_s - \frac{\sin\theta}{1 - M\cos\theta}r_s\cos(\phi - \phi_s)\right]} r_s dx_s dr_s d\phi_s \\ &= \frac{e^{i\frac{\omega}{c_0}\sigma_0}}{4\pi\sigma_0\left(1 - M\cos\theta\right)} \int_{\Re^2} -\widetilde{F}\left(x_s, r_s\right) e^{i\frac{\omega\cos\theta}{c_0(1 - M\cos\theta)}x_s} \\ &\qquad \left[\int_{-\pi}^{\pi} e^{-i\frac{\omega\sin\theta}{c_0(1 - M\cos\theta)}r_s\cos(\phi - \phi_s)} e^{iq\phi_s} d\phi_s\right] r_s dx_s dr_s. \end{aligned} \tag{2.123}$$

The ϕ_s integral can be found analytically, yielding a Bessel function, as follows. Defining $\gamma_0 = \omega \sin\theta / c_0 \left(1 - M\cos\theta\right)$, and $\tau = -\pi/2 + (\phi - \phi_s)$ we have

$$\begin{aligned}\int_{-\pi}^{\pi} e^{-i\frac{\omega\sin\theta}{c_0(1-M\cos\theta)}r_s\cos(\phi-\phi_s)} e^{iq\phi_s} d\phi_s &= -\int_{-\pi}^{\pi} e^{-i\gamma_0 r_s\sin(-\tau)} e^{iq\left(-\tau+\phi-\frac{\pi}{2}\right)} d\tau \\ &= -2\pi e^{iq\phi} e^{-iq\frac{\pi}{2}} J_q\left(\gamma_0 r_s\right),\end{aligned} \qquad (2.124)$$

using the definition of the Bessel function

$$J_q\left(\gamma_0 r_s\right) = \frac{1}{2\pi}\int_{-\pi}^{\pi} e^{-i(q\tau-\gamma_0 r_s\sin\tau)}. \qquad (2.125)$$

We thus obtain the following Green's function

$$H^{l,m}\left(\sigma_0,\theta;x_s,r_s\right) = \frac{e^{i\frac{\omega}{c_0}\sigma_0}}{4\pi\sigma_0\left(1-M\cos\theta\right)}\left(-2\pi\right) J_{m+lB}\left(\gamma_0 r_s\right) e^{i\frac{\omega\cos\theta}{c_0(1-M\cos\theta)}x_s} e^{-\frac{i(m+lB)\pi}{2}}. \qquad (2.126)$$

A final trick (now that we know the x_s dependence of $H^{l,m}$) is to integrate the $\partial F^{l,m,p}/\partial x_s$ term within (2.112) by parts, yielding

$$\begin{aligned}\hat{p}^{l,m,p}\left(\sigma_0,\theta,k_x\right) = \int_{r_s}\int_{x_s} & H^{l,m}\left(\sigma_0,\theta;x_s,r_s\right) F^{l,m,p}\left(x_s,r_s,k_x\right) \\ & \left[\frac{-i\omega\cos\theta\sin\beta(r_s)}{c_0\left(1-M\cos\theta\right)} + \frac{i\left(m+lB\right)\cos\beta(r_s)}{r_s}\right] r_s dr_s dx_s.\end{aligned} \qquad (2.127)$$

The full acoustic pressure in the far-field will then be given by

$$p\left(\sigma_0,\theta,\phi,t\right) = \sum_{l=-\infty}^{\infty}\sum_{m=-\infty}^{\infty}\sum_{p=-\infty}^{\infty}\int_{-\infty}^{\infty}\hat{p}^{l,m,p}\left(\sigma_0,\theta,k_x\right)\exp\left(-i\omega t\right) dk_x \exp\left(iq\phi\right). \qquad (2.128)$$

In this triple summation, the p index arose from splitting the distortion amplitude A_{ij} into circumferential harmonics (see equation (2.76)) and the m index corresponds to the total azimuthal order of the incident turbulence field upon the blades. Thus m includes the contribution to azimuthal order from the phase of the distorted turbulence field, as expanded in equation (2.74). Therefore if A_{ij} was perfectly axisymmetric we would still have a summation over m. The l index arose from the $2\pi/b$ periodicity of the blades, as shown in §2.3.5.

2.4.1 Auto-correlation of pressure

We take the auto-correlation of p to form $P(\mathbf{x}, \tau)$, and then take the Fourier transform to find the Power Spectral Density (PSD), $\hat{P}(\mathbf{x}, \omega)$, as follows

$$\begin{aligned} \hat{P}(\mathbf{x}, \omega) &= \int_{-\infty}^{\infty} \langle (p(\sigma_0, \theta, \phi, t))^* \, p(\sigma_0, \theta, \phi, t+\tau) \rangle \, e^{i\omega\tau} d\tau \\ &= \int_{-\infty}^{\infty} P(\sigma_0, \theta, \phi, \tau) \, e^{i\omega\tau} d\tau. \end{aligned} \tag{2.129}$$

We see that $\hat{P}$ has dimensions of $[\text{pressure}^2 \cdot \text{time}] = \left[\rho^2 \frac{L^4}{T^3}\right]$. Majumdar (1996) then integrated $\hat{P}$ over a shell of radius σ_0, removing ϕ and σ_0 dependence, to find

$$P(\omega) = \int_{\phi=0}^{2\pi} \int_{\theta=0}^{\pi} \hat{P}(\mathbf{x}, \omega) \, \sigma_0^2 \sin\theta d\theta d\phi, \tag{2.130}$$

which has dimensions of $\left[\rho^2 \frac{L^6}{T^3}\right]$; power has dimensions of $\left[\rho \frac{L^5}{T^3}\right]$. Using the plane wave result, acoustic intensity $= p'^2 / \rho_0 c_0$, we can therefore obtain a measure of power per frequency as follows

$$P_f(\omega) = \frac{P(\omega)}{\rho_0 c_0}, \tag{2.131}$$

where P_f has dimensions $\left[\rho \frac{L^5}{T^2}\right]$. To obtain a Power Level (PWL) quantity we could integrate P_f over ω. However, in this thesis, we instead plot a 'spectral power' quantity

$$\mathrm{SP}(\omega) = 10 \log_{10} \left(\frac{P(\omega)}{10^{-12}} \right) \mathrm{dB}. \tag{2.132}$$

This quantity gives the correct trends of location and relative heights of tones which are the key results of this work, since the absolute levels are ultimately controlled by the magnitude of the turbulence intensity. In Appendix B we discuss further the use of different sound metrics.

The first action of the statistical average of equation (2.129) is upon the Fourier transforms of $\mathbf{u}^\infty$ (contained within $F^{l,m,p}$), which become $(2\pi)^6 \delta(\mathbf{k} - \mathbf{k}') S_{kl}^\infty(\mathbf{k})$. The time average then acts upon $\exp(ilB\Omega t)$ and $\exp(-il'B\Omega t)$, leading to a $\delta_{ll'}$ term, and reducing the remaining infinite series from four (l, l', m and m') to three. The Fourier transform integral over τ brings out a $\delta(k_x U_\infty + lB\Omega - \omega)$ factor. The expression[9] for $\hat{P}$ is therefore given by

$$\begin{aligned}
\hat{P}\left(\sigma_0,\theta,\phi,\omega\right) =&\rho_0^2 \frac{B^2}{4\pi^2 U_\infty} \frac{1}{4\sigma_0^2\left(1-M\cos\theta\right)^2} \\
&\sum_{l,m,m'} \int_{r_s,x_s} \left[J_{m+lB}\left(\gamma_0 r_s\right)\right]^* \left[W(r_s)\Gamma_{WW}^{m}\left(x_s,r_s;\omega\right)\right]^* e^{-ik_x X} \\
&\left[\frac{i\omega\cos\theta\sin\beta(r_s)}{c_0\left(1-M\cos\theta\right)} - \frac{i(m+lB)\cos\beta(r_s)}{r_s}\right] \\
&\exp\left\{\frac{-i\omega\cos\theta x_s}{c_0\left(1-M\cos\theta\right)} + i(m+lB)\frac{\left[x_s - x_0(r_s)\right]\tan\beta(r_s)}{r_s} + ilB\phi_0(r_s)\right\} \\
&\int_{r_s',x_s'} J_{m'+lB}\left(\gamma_0 r_s'\right) W(r_s')\Gamma_{WW}^{m'}\left(x_s',r_s';\omega\right) e^{ik_x X'} \\
&\left[-\frac{i\omega\cos\theta\sin\beta(r_s')}{c_0\left(1-M\cos\theta\right)} + \frac{i(m'+lB)\cos\beta(r_s')}{r_s'}\right] \\
&\exp\left\{\frac{i\omega\cos\theta x_s'}{c_0\left(1-M\cos\theta\right)} - i(m'+lB)\frac{\left[x_s' - x_0(r_s')\right]\tan\beta(r_s')}{r_s'} - ilB\phi_0(r_s')\right\} \\
&\sum_{p,p'} \int_{\Re} J_{m-p}^*\left(r_k R\right) D_k^{p*}\left(x_0(r_s),r_s;k_x,r_k,0\right) J_{m'-p'}\left(r_k R'\right) D_l^{p'}\left(x_0(r_s'),r_s';k_x,r_k,0\right) \\
&\left[\int_0^{2\pi} e^{i(m-m')\phi_k} S_{kl}^\infty\left(\mathbf{k}\right) d\phi_k\right] r_k dr_k dr_s' dx_s' dr_s dx_s e^{i(m'-m)\left(\phi-\frac{\pi}{2}\right)}. \qquad (2.133)
\end{aligned}$$

Here $R' = R(x_0(r_s'),r_s')$, and $X' = X(x_0(r_s'),r_s')$. Note that, unlike for the spectrum of blade pressures, the $e^{-ik_x X}$ and $e^{ik_x X'}$ terms do not cancel each other[10]. Averaging over ϕ, when calculating P, leads to $m = m'$. The input parameters to this expression are: c_0, ρ_0 (physical parameters); U_∞, S_{ij}^∞ (far upstream conditions); $A_{ij}\left(\mathbf{x}\right), U_f$ (dependent on mean flow model); $B, \Omega, r_d, \phi_0(r), x_0(r), c(r)$ (rotor parameters). In addition, the following quantities depend upon those parameters: $k_x = (\omega - lB\Omega)/U_\infty$, $M = U_\infty/c_0$, $\beta(r) = \tan^{-1}(\Omega r/U_f)$, $W = \sqrt{U_f^2 + (\Omega r)^2}$ and $\omega_\Gamma = \omega - (m + lB)$.

---

[9] Checking dimensions of the above expression, it should have dimensions of pressure^2.time $\equiv \left[\rho^2 \frac{L^4}{T^3}\right]$. We find $\left[\hat{P}\right] = \left[\rho_0^2 \frac{1}{U_\infty \sigma_0^2} W^2 \frac{1}{r_s^2} S^\infty dk_y dk_z dr_s dx_s dr_s' dx_s'\right] \equiv \rho^2 \frac{L^4}{T^3}$, using $\left[S^\infty\right] \equiv \frac{L^5}{T^2}$.

[10] Majumdar and Peake (1998) did not include these terms in their expression for radiated sound.

2.4.2 Modal analysis

Here we detail the approximations employed when implementing (2.133) numerically for a given frequency ω.

Summation over the l and m indices

We wish to restrict the infinite sums over the l, m indices to the dominant terms only in order to reduce the computational intensity of calculations. To achieve this, we consider first the l values which result in $k_x = \omega - lB\Omega/U_\infty$ being as close to zero as possible, due to the sharp decay of S_{kl}^∞ as $\mathbf{k}$ increases. Majumdar included $l = 0, 1, 2$ only for all ω from 0 to 2 BPF. However, for some values of ω within this range it is more appropriate to take values of l centred on 0 or 2. The difference between using a total of 3 or 5 l values is found to be negligible and so we take n_l (the total number of l values included in the sum) to be 3 in all our calculations. Next, we include an odd number of m values centred on $-lB$, due to the decay of the J_{m+lB} term as the order increases. This sum is more sensitive to the total number of m values, n_m, as the decay of the Bessel functions is not as rapid as that of S_{kl}^∞. A noticeable difference is found in SP between the $n_m = 3$ (the number included by Majumdar) and $n_m = 5$ cases for the low distortion conditions - an increase in m values leads to an increase in broadband level. In the high distortion case, the height of the tonal peaks is unaffected by n_m, although the broadband level does change slightly. We set $n_m = 5$ in our calculations.

Sum over p, p', and r_k integral limits

When calculating the SP (and thus the ϕ-averaged version of (2.133)) numerically a discrete set of r_s, r_s' values are chosen (typically around 6 values). The integrand is then evaluated for all pairs of r_s, r_s' and summed using the trapezium rule, first over r_s' then over r_s. The integral

$$\int_{\Re} J_{m-p}^* \left(r_k R\right) D_j^{p*} \left(x_0(r_s), r_s; k_x, r_k, 0\right) J_{m-p} \left(r_k R'\right) D_k^p \left(x_0(r_s'), r_s'; k_x, r_k, 0\right)$$
$$\left[\int_0^{2\pi} S_{kl}^\infty \left(\mathbf{k}\right) d\phi_k\right] r_k dr_k, \tag{2.134}$$

for a particular pair of r_s, r_s' does not converge with an infinite upper limit for r_k. We use a limited range for this integral, as discussed earlier in §2.3.3, of

$$\sqrt{\frac{(m-p)^2}{R^2}} \leq r_k \leq \sqrt{\left(\frac{\partial R}{\partial r}\right)^{-2} \frac{\omega^2}{c_0^2} + \frac{(m-p)^2}{R^2}}. \tag{2.135}$$

Since R and $\partial R/\partial r$ differ for r_s and r_s' we have a choice as to whether to take the inner or outer of each limit. We use the outer limits, thus using the larger value of R and the smaller value of $\partial R/\partial r$, although in fact there is little difference if the inner limits are used. We also find that setting $p = p'$ gives sufficiently accurate results which are very close to the $p \neq p'$ case, as well as significantly speeding up the numerics.

Justifying $|\mathbf{k}| \gg 1/|\mathbf{X}|$

Finally, we remember that the expression for A_{ij} required $|\mathbf{k}| \gg 1/|\mathbf{X}|$. We can now check this assumption. Note that, for the r_k limits outlined above

$$|\mathbf{k}| = \sqrt{k_x^2 + r_k^2} \geq r_k \geq \frac{|m-p|}{R}, \tag{2.136}$$

and for $m \neq p$ then

$$\frac{|m-p|}{R} \geq \frac{1}{R} \geq \frac{1}{\sqrt{X^2+R^2}} = \frac{1}{|\mathbf{X}|}. \tag{2.137}$$

Since $m \sim lB$ and $|p| \leq 3$ we see that $|m-p|$ will be of the same order as B except in the case of $l = 0$. Thus for $l \neq 0$, since B is typically greater than 10, $|\mathbf{k}| \gg 1/|\mathbf{X}|$ holds. For $l = 0$ we have $k_x = \omega/U_\infty$, and thus require $\omega \gg U_\infty/\sqrt{X^2+R^2}$ to satisfy $|\mathbf{k}| \gg 1/|\mathbf{X}|$. We are primarily interested in frequencies at and above the BPF, for which ω is an order of magnitude larger than typical values of U_∞/r_h (where r_h is the hub radius) and since $\sqrt{X^2+R^2} > R > r_h$ for a streamtube contraction, the condition on ω will be satisfied for the parameter ranges of interest.

2.4.3 SP plots

In Figures 2.11 and 2.12 we have plotted SP, as given in equation (2.132), for a range of distortion levels and integral lengthscales. The main points to note are that the broadband level in the low distortion case (which corresponds approximately to take-off at Mach no.

0.25) is 30-40 dB lower than the tonal peaks which occur in the high distortion case (which corresponds approximately to static testing), and that the integral lengthscales which produce the highest tonal peaks are of the order of the rotor radius.

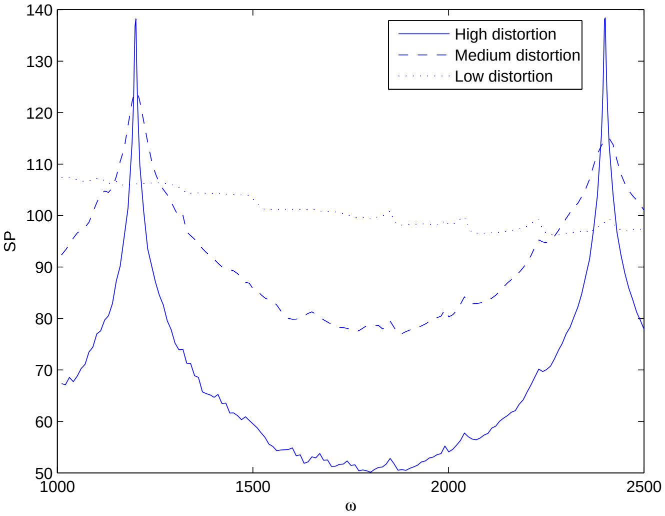

Figure 2.11: Radiated sound results, varying levels of distortion. $L = 1$ in all cases. We see the strikingly tonal nature for high distortion levels. Peaks are at BPF and 2 BPF.

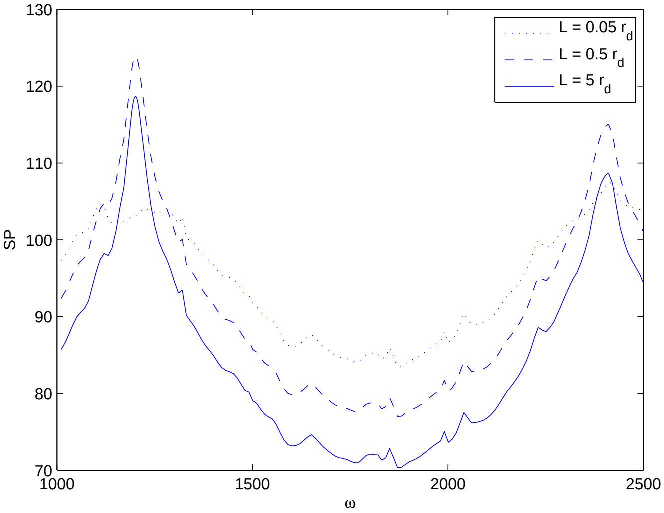

Figure 2.12: Varying the turbulent integral lengthscale, L, whilst keeping the distortion level constant, $U_f/U_\infty = 10$. As L increases we see sharper tonal peaks, but once L has passed a critical value the whole spectrum shifts down almost uniformly.

In Figure 2.13 we have reproduced the two sets of parameter values which were calculated in Majumdar and Peake (1998), as shown in Figure 2.14. We see excellent qualitative agreement between the prediction schemes, however the effect of full inclusion of the non-zero k_ϕ and $A_{\phi\phi}$ terms and consideration of ϕ dependence within the distorted amplitude as well as the phase is seen to lower the broadband level in flight with respect to the static testing tonal peaks.

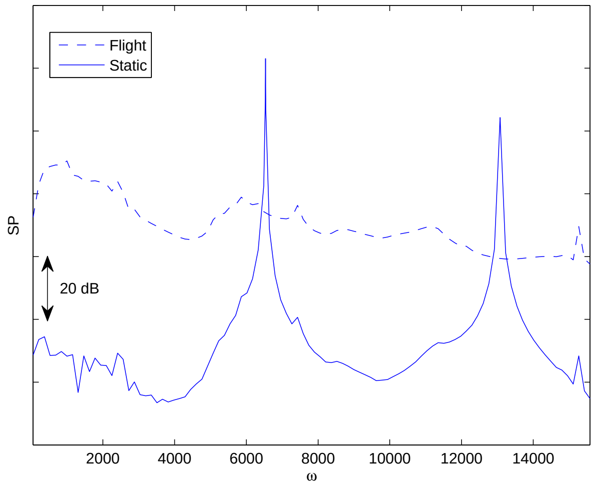

Figure 2.13: Results from our prediction scheme, run for the same parameter values as in Figure 2.14. We note that this meant n_m was taken to be 3, and thus a lower number of azimuthal orders were included than in Figures 2.11 and 2.12.

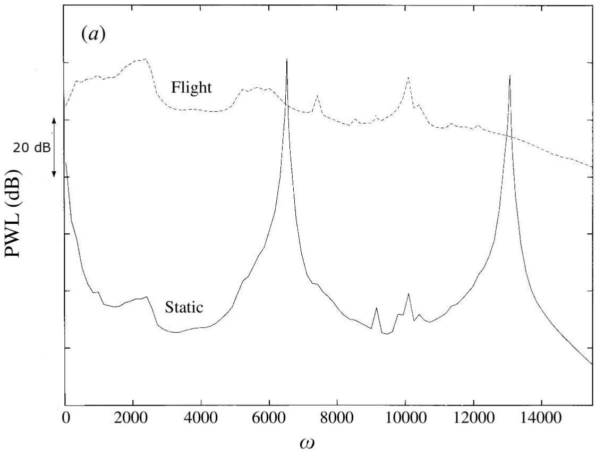

Figure 2.14: Figure reproduced from Majumdar and Peake (1998), comparing the radiated sound in the flight and static testing cases.

Chapter 3

Alternative inputs: *mean flow and turbulence models*

3.1 Chapter outline

In this chapter we firstly revisit the mean flow model employed in Chapter 2, introducing extra features to more realistically simulate the flow into an AOR, see schematic below. Note that it is possible to input any axisymmetric flow (which is irrotational and tends to a uniform velocity far upstream) into the analysis of Chapter 2, if we can track along the streamlines sufficiently far back to find convergent values for X and R. For example a computationally generated flow could be used. However, analytic models allow for more rapid calculation of the distortion quantities. Secondly, we explore the use of different input turbulence models and integral lengthscales to more accurately capture the key features of atmospheric turbulence. As part of this work, two approximations for the distorted turbulence 3D energy spectrum, $\mathcal{E}_1(k)$ and $\mathcal{E}_2(k)$, are proposed.

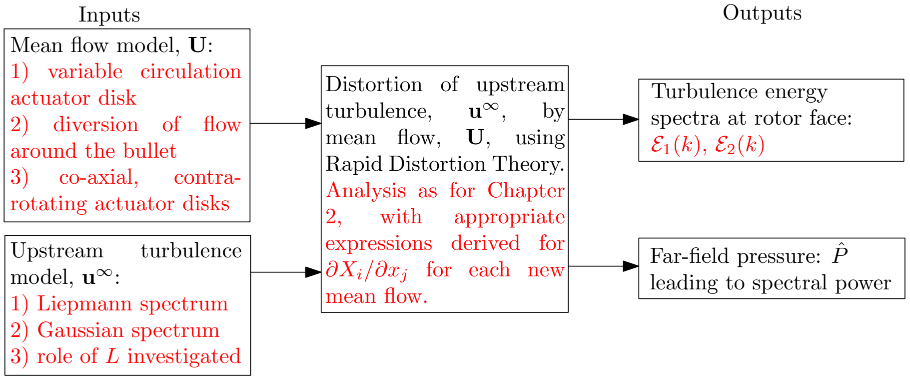

3.2 Mean flow model

We consider three new axisymmetric mean flows in this chapter, see Figure 3.1.

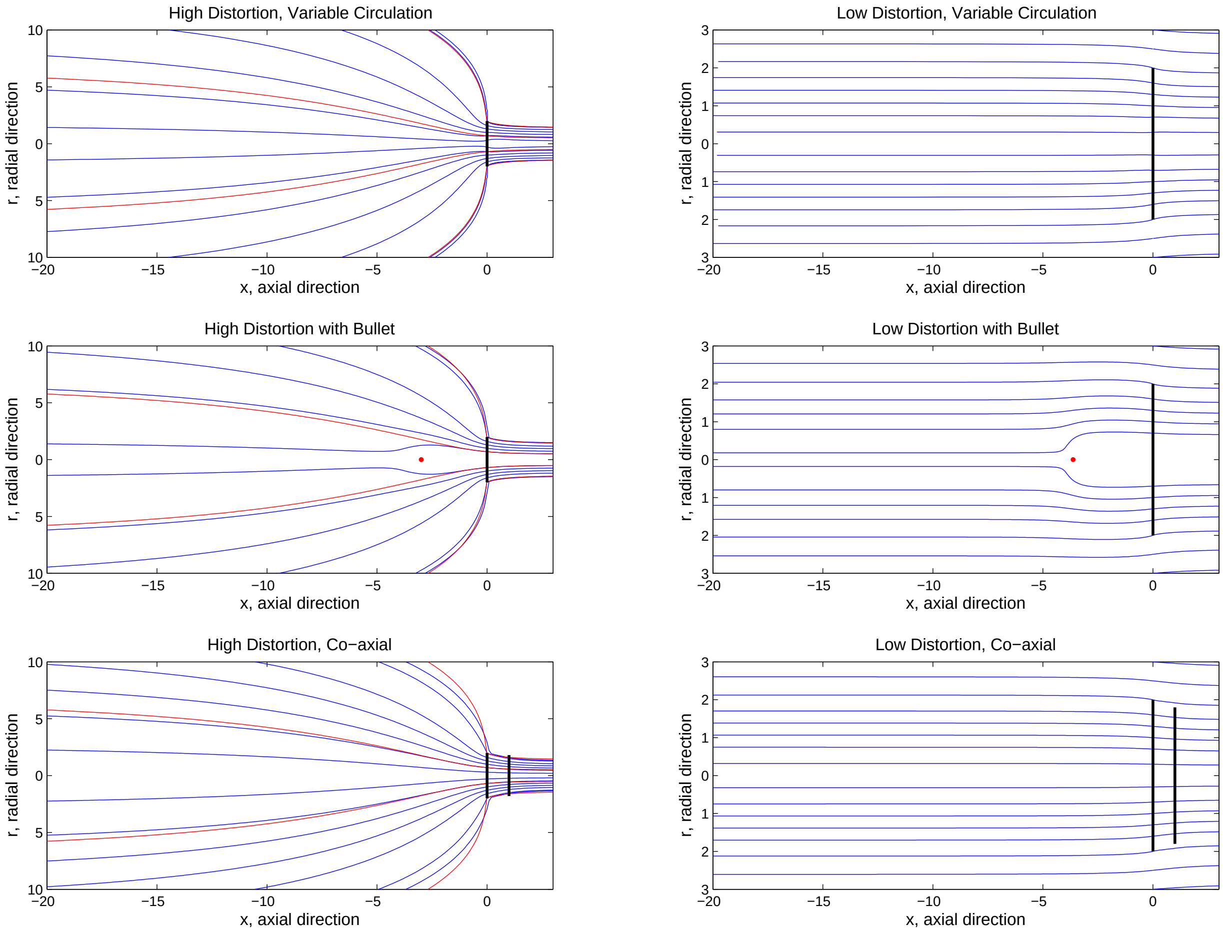

Figure 3.1: Illustration of the three new mean flows we consider in this chapter. Top: a variable circulation actuator disk model. Middle: a model which simulates diversion of the flow streamlines around the engine hub (the bullet), using a point source (whose position is shown in red). Bottom: two co-axial actuator disks, modelling the presence of the rear blade row. Shown in red for comparison on the high distortion plots are streamlines which run through the root and tip of the blade in a constant circulation actuator disk model. Note that the flow for $x > 0$ includes a non-zero azimuthal component, not shown here.

The actuator disk remains the basis for these improved mean flow models. However, we note briefly here a couple of alternative flow models found during the literature review undertaken in Chapter 1. Simonich et al. (1990) used a set of discrete vortex rings to represent the wake of the rotor, rather than our continuous vortex line shedding model. One disadvantage of the vortex ring model is that it cannot predict velocities very close to the blade tip. Mish and Devenport (2006b), when modelling the distortion of an isotropic turbulence field incident upon an airfoil, applied Rapid Distortion Theory with the mean flow given by the flow around a cylinder, to simulate the leading edge of the blade. In Paterson and Amiet (1982), first the noise spectrum due to each point along the blade is calculated and then blade-to-blade correlations are introduced. This means a non-axial, azimuthally varying flow can be used, allowing consideration of a non-zero shaft angle; this is discussed in more detail in Chapter 5. Finally, we note that whilst the effects of swirl upstream of the rotor are neglected in our work, this extension was made by Wright (2000), as discussed in §2.2.4.

3.2.1 Vortex theory of a propeller

In Chapter 2 we simply stated, in equations (2.47) and (2.48), the mean flow velocities found within Hough and Ordway's vortex theory model for the constant circulation actuator disk. We now outline the derivation in more detail, before introducing the variable circulation actuator disk model.

In Hough and Ordway's vortex model for rotor-induced flow each blade is modelled as a vortex line. Thus information about the blade shape is used only as far as it influences circulation, denoted at each radial location by $\Gamma(r)$. Trailing helical vortex sheets are shed behind the blades as the propeller translates forward, with circulation given by $-\Gamma'(r)$, as shown in Figure 3.2. In the limit of infinite blade number this model reproduces the actuator disk jump in flow properties, but also provides us with expressions for the velocity field everywhere.

The Biot-Savart Law gives the velocity induced by a line vortex of unit length and strength lying in direction $\hat{\mathbf{e}}$ from (x_v, r_v, ϕ_v) as follows

$$\mathbf{u}(x,r,\theta) = \frac{\hat{\mathbf{e}} \times \mathbf{r}}{4\pi |\mathbf{r}|^3}, \tag{3.1}$$

where $\hat{\mathbf{e}}$ is a unit vector, and $\mathbf{r}$ is the vector $(x - x_v, r - r_v, \phi - \phi_v)$. This can be integrated along each vortex line, and summed to give the full induced velocity fields. We find that the vortices along the blades contribute solely to the tangential velocity, U_ϕ. In fact it

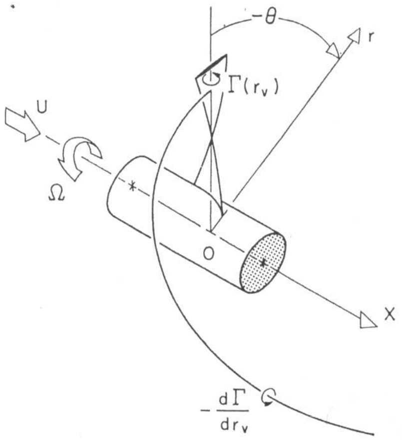

Figure 3.2: Illustration reproduced from Hough and Ordway (1965) showing the vortex line system we are considering for a single blade, together with one of the trailing helical vortex lines which are shed from each point along the blade. Here U is the axial velocity at upstream infinity, denoted by U_∞ in this thesis. Thus the shed vortices lie along the vector $U_\infty \hat{\mathbf{e}}_\mathbf{x} + \Omega r \hat{\mathbf{e}}_\phi$.

is found that upstream of the propeller (i.e. in the region $x < 0$) and also in the region $r > r_d$ this contribution is exactly balanced by the contribution to U_ϕ from the trailing vortex sheets. Thus there is zero swirl upstream of the propeller and in $r > r_d$, but this jumps to a non-zero value immediately downstream.

In Chapter 2 we used a simple constant circulation actuator disk model, i.e. with circulation along each blade given by $\Gamma(r) = \Gamma$. The assumption of constant blade loading along the length of each blade is essentially a statement that each part of the blade contributes equally to the thrust generated. Although certain properties of open rotor blades, such as their chord length, vary little over the majority of the blade, this approximation will certainly break down near the tip. It is therefore of interest to examine the difference that a more realistic, variable circulation model makes to our predictions, and this is the first new model we consider.

3.2.2 Variable circulation actuator disk

The constant circulation actuator disk model gives a constant velocity profile at the rotor face, whereas in reality it will vary along the span. For a real rotor the axial velocity increases with r as we move out from the hub to reach a maximum within the region of greatest loading, and then decreases towards the tip. This qualitative behaviour can be seen in Figure 3.3, where we have plotted output from a typical numerical strip theory calculation, as used by industry.

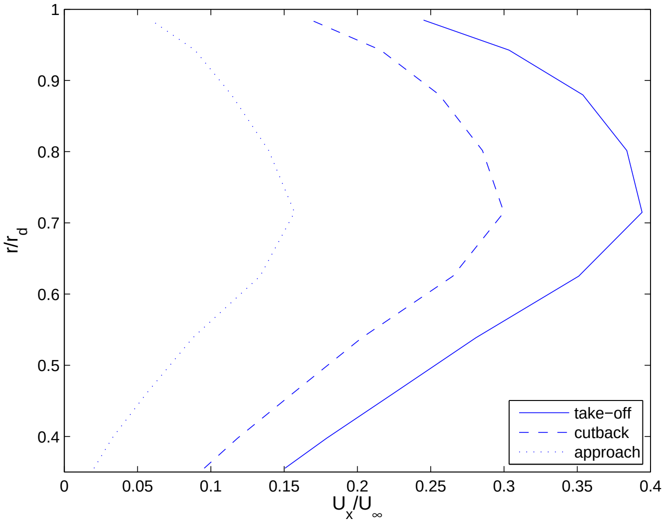

Figure 3.3: Representative profiles of the axial velocity at the rotor face as output from a typical industry numerical strip theory calculation. This data was provided by Dr. M. Kingan, Dr P. J. G. Schwaller and Dr A. B. Parry.

We can therefore model the velocity profile more realistically using Hough and Ordway's variable blade circulation model, where the circulation is given by

$$\Gamma(r) = \frac{105}{16}\frac{\pi U_\infty U_d}{B\Omega}\frac{r}{r_d}\sqrt{1-\frac{r}{r_d}}, \tag{3.2}$$

$$\Gamma'(r) = \frac{105}{16}\frac{\pi U_\infty U_d}{B\Omega}\frac{\left(1-\frac{3r}{2r_d}\right)}{r_d\sqrt{1-\frac{r}{r_d}}}. \tag{3.3}$$

This profile was developed by Hough and Ordway as it compares well to the Goldstein optimum distribution of blade loading, which minimises the energy lost in the slip stream for a given propeller thrust (Goldstein, 1929). For this form of $\Gamma(r)$, the induced axial and radial steady velocities upstream of the rotor (equivalent to equations (2.47) and (2.48)) are

$$U_x^{\text{var.}}(x,r) = \frac{105}{32}\frac{U_d x}{2\pi r^{\frac{3}{2}}}\int_0^{r_d}\frac{\sqrt{r'}}{r_d}\sqrt{1-\frac{r'}{r_d}}Q'_{-\frac{1}{2}}(\omega')dr'; \text{ for } x<0, \tag{3.4}$$

$$U_r^{\text{var.}}(x,r) = \frac{105}{32}\frac{U_d}{2\pi r^{\frac{1}{2}}}\int_0^{r_d}\frac{\left(1-\frac{3r'}{2r_d}\right)}{r_d\sqrt{1-\frac{r'}{r_d}}}\sqrt{r'}Q_{\frac{1}{2}}(\omega')dr'. \tag{3.5}$$

As before, Q_n are Legendre functions, see Appendix A for definitions. The variable and constant circulation axial velocity profiles differ significantly from each other at the disk face. However, moving upstream they quickly produce very similar profiles, see Figure 3.4. From this figure we also note that the majority of the axial distortion occurs within five disk radii, and this leads us to conclude that coherent flow structures shed from airframe features which lie several radii upstream of an open rotor could undergo significant distortion before they hit the rotor blades.

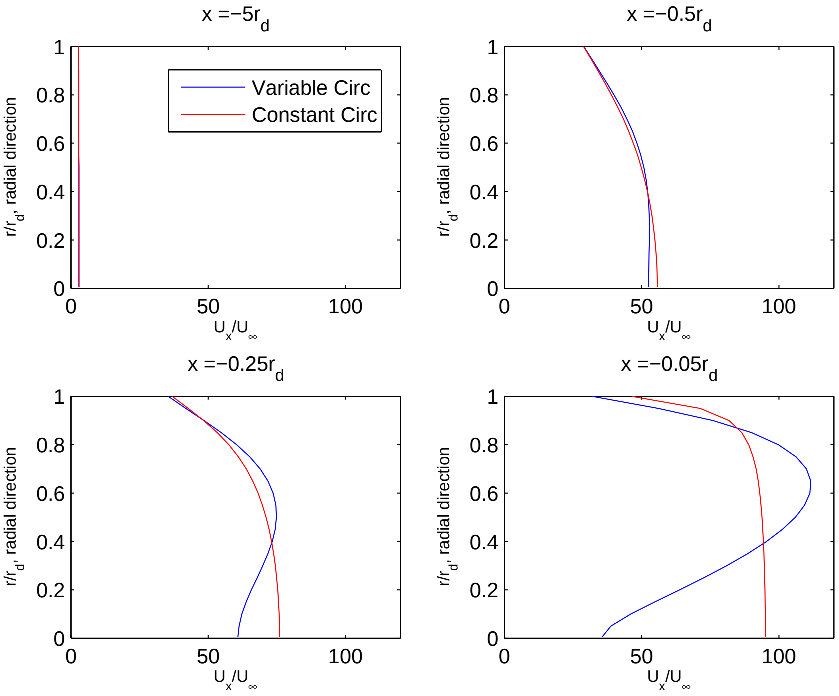

Figure 3.4: Here we show the axial velocities at $x=-5r_d$, $x=-0.5r_d$, $x=-0.25r_d$, $x=-0.05r_d$. The total thrust generated is held constant between the constant and variable circulation actuator disk models and thus the captured streamtube is the same in both cases. Within a distance of half of the radius of the disk the variable and constant circulation profiles are virtually the same.

In Figure 3.5a we compare the streamlines of the constant and variable circulation cases. The streamlines behave quite differently close to the disk. Instead of r decreasing monotonically along each streamline as we travel toward the disk, in the variable circulation case the radius increases as the streamline gets very close to the disk, as seen in the zoomed in Figure 3.5b. This leads to negative values of $\partial X/\partial x$ and $\partial R/\partial x$ at the disk face for lower values of r, as seen in Figure 3.6.

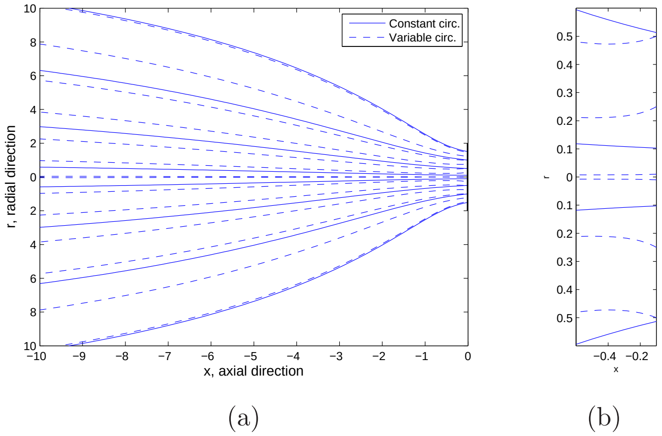

(a) (b)

Figure 3.5: a) The variable circulation model leads to slightly decreased R values at the disk face over most of the blade span. b) Zoomed-in figure near to the disk.

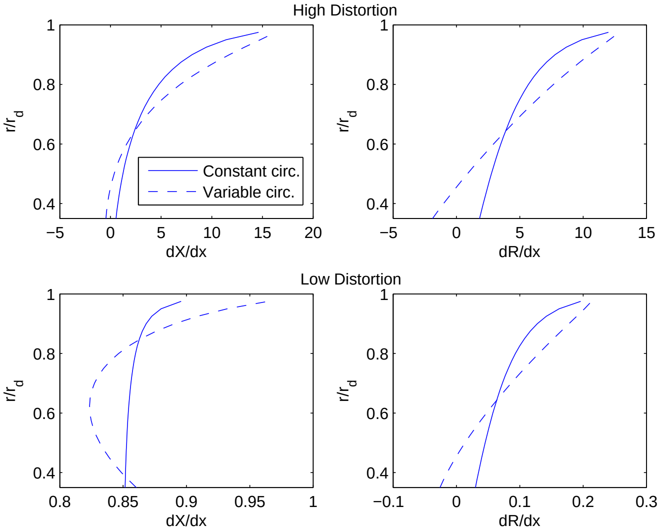

Figure 3.6: Plot of $\partial X/\partial x$ and $\partial R/\partial x$ at the disk face, comparing the constant and variable circulation cases.

These altered values of the derivatives of $\mathbf{X}$ then affect the distorted turbulence spectrum at the rotor face, plotted in Figure 3.7 (we recall that S_{xx} was defined in equation (2.60)). In Figure 3.6 we see that for the high distortion case the values of the derivatives, $\partial X/\partial x$ and $\partial R/\partial x$, are higher in the variable circulation case towards the blade tip, and reduced near the hub when compared to the constant circulation case. There is a corresponding increase in distorted turbulence level towards the tip of the blades and a reduction near the hub seen in Figure 3.7. For low levels of distortion we see very little change to the turbulence spectrum between the two flows, as might be expected. Even though the values of $\partial X_i/\partial x_j$ differ in that case too, they are much smaller in absolute size and are dominated by the δ_{ij} term of A_{ij} (given in equation (2.30)). The largest difference in turbulence level between the constant and variable cases is found near the hub, for medium levels of distortion.

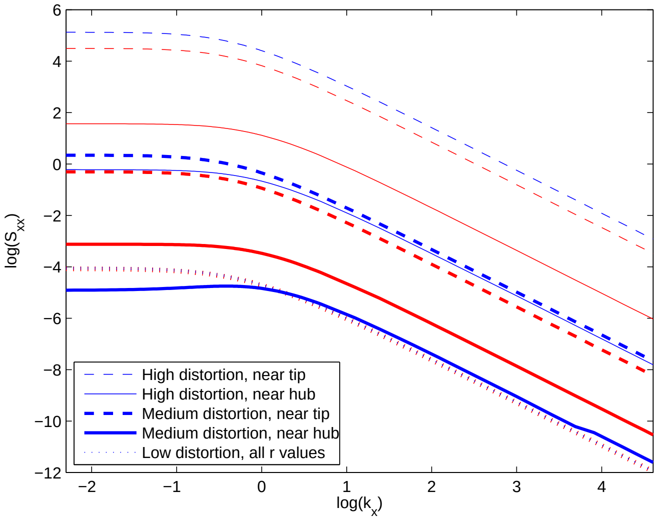

Figure 3.7: Distorted turbulence spectrum (axial component) for the variable circulation model, at different positions along the rotor blade and for varying distortion levels. The constant circulation case with the same input parameters is shown in red (as was shown in Figure 2.4 in blue). $L = 1$ in all cases.

Validation against numerical data

In Figure 3.8 we compare the axial velocity as output from a typical strip theory calculation with that given by the variable circulation actuator disk model. It is found that a significantly closer fit to the strip theory data can be obtained by scaling the velocity field as follows

$$U_x(x,r) = U_x^{\text{var.}}\left(x, \frac{(r-r_h)}{(r_d-r_h)}r_d\right), \tag{3.6}$$

where r_h is the radius of the hub and the 'var' superscript indicates Hough and Ordway's original variable circulation model, equations (3.4) and (3.5). That is, we take account of the radial limits of the blade, $r_h \leq r \leq r_d$, and scale the profile to lie between these limits.

In §3.4, we examine the effect of these different mean flows on the radiated sound, including an investigation of the use of a scaled velocity profile as given above.

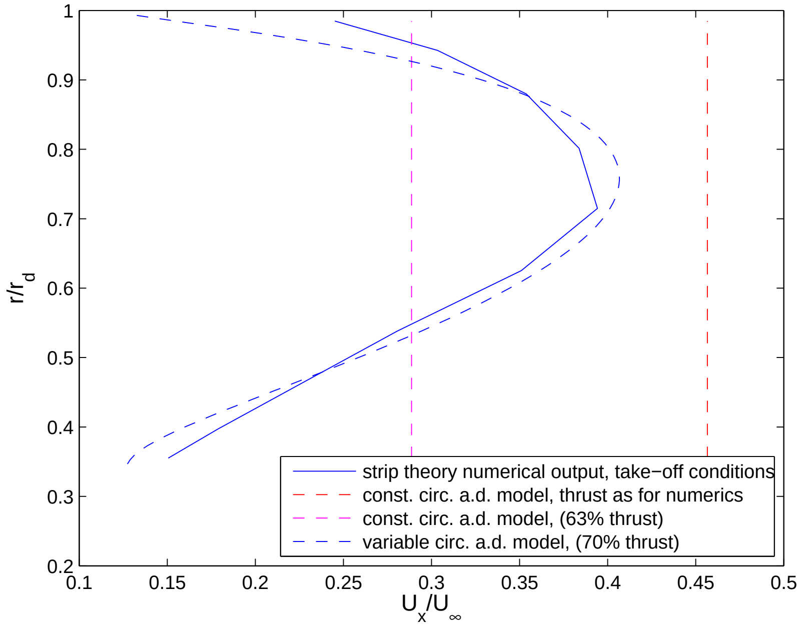

Figure 3.8: Here we have used the adjusted variable circulation model (given in equation (3.6)) to fit to the output from the numerical strip theory calculation. Note also the use of a lower thrust than that output from the numerics gives an improved fit.

3.2.3 Modelling the bullet

The engine core extends upstream of an AOR in rig testing, as shown in Figure 3.9, and affects the mean flow onto the rotors. Previous work by Zachariadis and Hall (2009) has indicated that the bullet can make a significant difference to the thrust generated by the rotors, altering the axial velocity onto the blades as well as the flow angle. To simulate the mean flow distortion around the bullet we have developed a new and simple analytical model whereby a point source is added to the flow upstream of an actuator disk. This is similar to a Rankine half-body model, except the point source is superposed upon an actuator disk flow rather than a uniform flow.

Figure 3.9: The large 'bullet' protruding upstream of the rotors in Rig 140 testing in the 1980s. Reproduced with permission from Rolls-Royce.

The streamfunction for a general source of strength m, placed at $x = x_0$, along the axis $r = 0$, is given in cylindrical polar coordinates (x, r, ϕ) by

$$\Psi^{\mathrm{s}} = -\frac{m\,(x - x_0)}{\sqrt{r^2 + (x - x_0)^2}}. \tag{3.7}$$

Superposing this upon an actuator disk flow $\left(U_\infty + U_x^{\mathrm{a.d.}}(x,r)\right)\hat{\mathbf{e}}_{\mathbf{x}} + U_r^{\mathrm{a.d.}}(x,r)\hat{\mathbf{e}}_{\mathbf{r}}$ will lead to a stagnation point upstream of x_0, on the $r = 0$ axis, and we denote its position by $x = x_1$. The two source parameters, m and x_0, can be chosen to specify x_1 and the downstream radius r_h of the centremost streamline, see Figure 3.10.

The axial velocity due to the point source is

$$U_x^{\mathrm{s}} = \frac{1}{r}\frac{\partial \Psi^{\mathrm{s}}}{\partial r} = \frac{m\,(x - x_0)}{\left(r^2 + (x - x_0)^2\right)^{\frac{3}{2}}}. \tag{3.8}$$

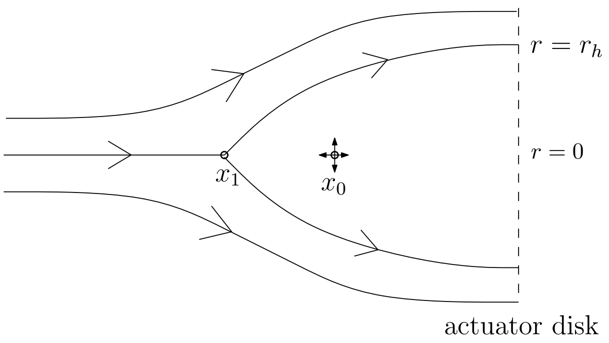

Figure 3.10: Actuator disk streamlines diverted around a point source at x_0. The streamline which runs along $r = 0$ as $x \to -\infty$ intersects the disk at $r = r_h$. By adjusting the strength and position of the point source, x_1 and r_h can be specified.

As the axial velocity, $U_\infty + U_x^{\mathrm{s}} + U_x^{\mathrm{a.d.}}$, vanishes at the stagnation point x_1 we find

$$x_0 = x_1 + \sqrt{\frac{m}{U_\infty + U_x^{\mathrm{a.d.}}\left(x_1, 0\right)}}. \tag{3.9}$$

The positive square root has been chosen since $(x_1 - x_0) < 0$. Here $\left(U_\infty + U_x^{\mathrm{a.d.}}\left(x_1, 0\right)\right)$ is the axial velocity which would be obtained with an actuator disk only. This is the first condition needed to specify x_0 and m. The second condition is found by equating the value of the streamfunction at two points on the centremost streamline (which starts on $r = 0$ as $x \to -\infty$). The actuator disk streamfunction, $\Psi^{\mathrm{a.d.}}$, tends to zero as $x \to -\infty$ (see Appendix A for the full definition of $\Psi^{\mathrm{a.d.}}$). Thus, if the total streamfunction for this flow is given by Ψ, we have

$$\Psi\left(x, 0\right)\big|_{x \to -\infty} = \frac{1}{2} U_\infty r^2\Big|_{r=0} + \Psi^{\mathrm{s}}\left(x, 0\right)\big|_{x \to -\infty} + \Psi^{\mathrm{a.d.}}\left(x, 0\right)\big|_{x \to -\infty} = m. \tag{3.10}$$

At the rotor face, the value of the streamfunction is

$$\Psi\left(0, r_h\right) = \frac{m x_0}{\sqrt{r_h^2 + x_0^2}} + \frac{1}{2}\left(U_\infty + \frac{U_d}{2}\right) r_h^2. \tag{3.11}$$

Setting these two values equal, we find the desired source strength is given by

$$m = \frac{r_h^2\left(U_\infty + \frac{U_d}{2}\right)}{2\left(1 - \frac{x_0}{\sqrt{r_h^2 + x_0^2}}\right)}. \tag{3.12}$$

We can solve for x_0 and m by specifying the length of the bullet as x_1, and the hub width as r_h, then substituting (3.12) into (3.9) and seeking x_0 numerically. For example, if the length of the bullet is chosen as $-x_1 = 2r_d$ and the hub radius is $r_h = 0.35r_d$, then for a low distortion case, (an actuator disk which induces a velocity at the rotor face of $U_f = 1.18U_\infty$) we find $x_0 = -1.8r_d$ and $m = 2.9r_d^2U_\infty$. If instead we consider a medium distortion case, $U_f = 10U_\infty$, the source position moves toward the disk, $x_0 = -1.5r_d$, and the source strength decreases proportionally to the change in U_∞, $m = 0.29r_d^2U_\infty$.

In Figure 3.11 we have plotted the axial component of the distorted turbulence spectrum, comparing the cases with and without the bullet. We see that the addition of the point source simulating the bullet tends to raise the energy level slightly, but not in all cases (for example the medium distortion case near the hub). There will be a level of distortion between the high and medium cases shown where the contraction induced by the actuator disk balances the expansion induced by the bullet, and the two spectra will coincide. However, the value of U_∞ (which determines the level of distortion) at which this occurs will vary for different points along the blade. There will be no level of distortion for which the spectra exactly coincide at all radial positions. This low level of change indicates that although the values of $\mathbf{X}$ change within this new model, the derivatives $\partial X_i/\partial x_j$ do not vary significantly from the no-bullet case.

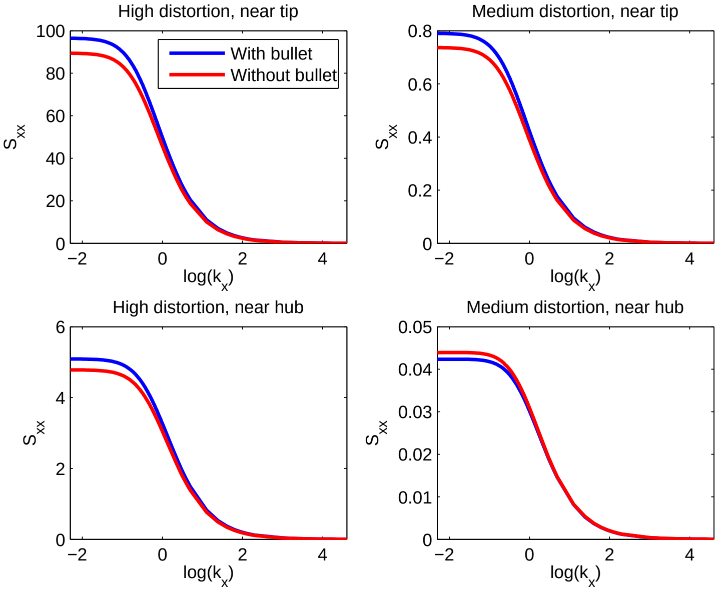

Figure 3.11: Distorted turbulence spectrum at the rotor face with and without the bullet, $L = 1$ in all cases. The differences observed are not large enough to show up on a log-log plot.

3.2.4 Co-axial propellers

Finally, a simple adjustment to the model can be made by including the effect of the rear blade row upon the distortion. This was in fact a first step towards more realistically capturing the flow through an AOR undertaken at the start of this Ph.D. We can model the mean flow induced by a co-axial, contra-rotating, propeller system by superposing two actuator disks, separated by a mid-chord to mid-chord gap of length g. We note that both the radius, r_d, and the 'strength', U_d, may vary between the two rotors, as they do not in general contribute equally to the thrust generated. Essentially this involves replacing x by $(x-g)$ in the velocities induced by the second rotor, as given in equations (2.47) and (2.48), remembering that the arguments of the Legendre functions also involve x

$$\mathbf{U}^{\text{co-ax.}}(x,r) = \mathbf{U}^{\text{a.d.}}(x,r;U_{d1},r_{d1}) + \mathbf{U}^{\text{a.d.}}(x-g,r;U_{d2},r_{d2})\,. \tag{3.13}$$

Figure 3.12 shows the streamlines induced by such a system. We see that a smaller upstream streamtube radius intersects with the front blade row, compared to the single disk case, also shown.

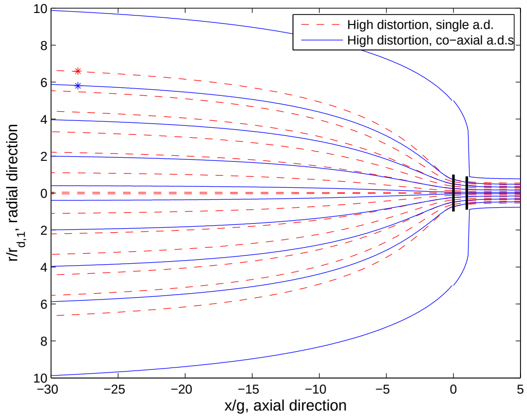

Figure 3.12: Comparing the streamlines of the single actuator disk to the co-axial disk case. The total thrust generated is kept constant between the two cases, but in the twin disk case the thrust is split front:rear in the ratio 60:40. Indicated by asterisks are two streamlines which intersect the front disk at the same position.

We compare $\partial X_i/\partial x_j$ between the single actuator disk and co-axial disk systems in Figure 3.13. The opposite effect from the variable circulation case is found, with values of the derivatives being increased near the tip when compared to the single actuator disk. The tip is also where most change is seen in S_{xx}, as plotted in Figure 3.14. This is due to the effect of the second blade row on the captured streamtube.

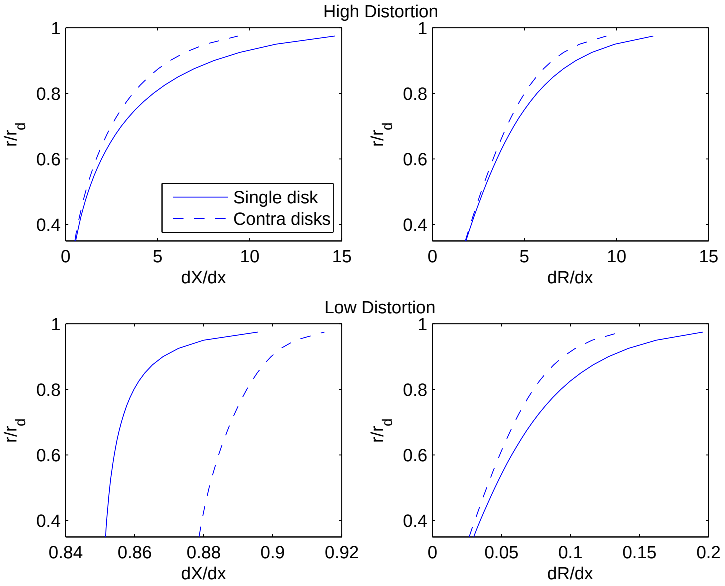

Figure 3.13: Plot of $\partial X/\partial x$ and $\partial R/\partial x$, comparing the single and co-axial disk cases. R also changes in order to preserve $\det(\partial X_i/\partial x_j) = 1$. All parameters are as in Figure 3.6.

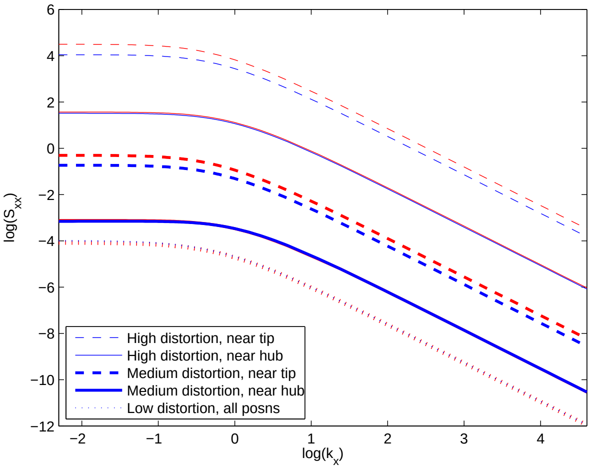

Figure 3.14: Distorted turbulence for the co-axial case (shown in blue). The level is the same as the single actuator disk case (shown in red) near the hub, but lowered near the tips.

These results raise the question of the level of UDN produced by the rear row, especially towards the tip of the rear blades. Modelling the flow there would require taking account of the tip vortices shed by the front row, and we do not pursue this analysis here.

3.2.5 Calculating $\partial X_i/\partial x_j$ for new flows

In order to calculate the distortion amplitude A_{ij} in each of the new mean flow cases, we require the derivatives of $\mathbf{X}$. By substituting $R = \sqrt{2\Psi/U_\infty}$, we find the following relations for any axisymmetric flow

$$\begin{aligned}
\frac{\partial R}{\partial x} &= -\frac{rU_r}{RU_\infty}, \\
\frac{\partial R}{\partial r} &= \frac{r\left(U_\infty + U_x\right)}{RU_\infty}, \\
\frac{\partial X}{\partial x} &= \left.\frac{\partial X}{\partial x}\right|_R + \left.\frac{\partial X}{\partial R}\right|_x \left.\frac{\partial R}{\partial x}\right|_r \\
&= \frac{U_\infty}{\left(U_\infty + U_x\right)} + \left.\frac{\partial X}{\partial R}\right|_x \left(-\frac{rU_r}{RU_\infty}\right), \\
\frac{\partial X}{\partial r} &= \left.\frac{\partial X}{\partial R}\right|_x \left.\frac{\partial R}{\partial x}\right|_x \\
&= \left.\frac{\partial X}{\partial R}\right|_x \left(\frac{r\left[U_\infty + U_x\right]}{RU_\infty}\right).
\end{aligned} \tag{3.14}$$

Thus, when altering the mean flow model most of the changes can be made by simply inserting the appropriate expression for U_x and U_r. The only term which requires rederivation is

$$\left.\frac{\partial X}{\partial R}\right|_x = U_\infty \left.\frac{\partial \hat{\Delta}}{\partial R}\right|_x, \tag{3.15}$$

where $\hat{\Delta}$ is the drift function re-expressed as a function of R and x, rather than r and x. Now, referring to the definition of drift given in equation (2.22), we have

$$\begin{aligned}
\left.\frac{\partial \hat{\Delta}(x, R(x,r))}{\partial R}\right|_x &= -\int_{-\infty}^{x} \frac{\left.\frac{\partial U_x}{\partial r_s}\right|_{x_s} \left.\frac{\partial r_s}{\partial R}\right|_{x_s}}{\left(U_\infty + U_x\right)^2} dx_s, \\
&= -U_\infty R \int_{-\infty}^{x} \frac{\left.\frac{\partial U_x}{\partial r_s}\right|_{x_s}}{r_s\left(U_\infty + U_x\right)^3} dx_s,
\end{aligned} \tag{3.16}$$

(Majumdar (1996)). Here (x_s, r_s) are coordinates along the streamline which runs through (x, r). For the case of a single constant circulation actuator disk we had

$$\frac{\partial U_x^{\text{a.d.}}}{\partial r_s} = r_s^{-\frac{3}{2}} \frac{\partial f^{\text{a.d.}}}{\partial r_s} - \frac{3}{2} r_s^{-\frac{5}{2}} f^{\text{a.d.}}, \tag{3.17}$$

where

$$
\begin{aligned}
f^{\text{a.d.}} &= \frac{U_d x}{2\pi} \int_0^{r_d} \frac{1}{\sqrt{r_v}} Q'_{-\frac{1}{2}}\left(\omega_1\right) dr_v, && (3.18)\\
\frac{\partial f^{\text{a.d.}}}{\partial r_s} &= \frac{U_d x}{2\pi} \int_0^{r_d} \frac{1}{\sqrt{r_v}} Q''_{-\frac{1}{2}}\left(\omega_1\right) \frac{\left(r_s^2 - r_v^2 - x'^2\right)}{2 r_v r_s^2} dr_v. && (3.19)
\end{aligned}
$$

This expression for $\partial U_x/\partial r_s$ is thus inserted into (3.16). For the case of variable circulation, f is adjusted as follows

$$
\begin{aligned}
f^{\text{var.}} &= \frac{105}{32}\frac{U_d x}{2\pi} \int_0^{r_d} \frac{\sqrt{r_v}}{r_d}\sqrt{1 - \frac{r_v}{r_d}} Q'_{-\frac{1}{2}}\left(\omega_1\right) dr_v, && (3.20)\\
\frac{\partial f^{\text{var.}}}{\partial r_s} &= \frac{105 U_d x}{64\pi} \int_0^{r_d} \frac{\sqrt{r_v}}{r_d}\sqrt{1 - \frac{r_v}{r_d}} Q''_{-\frac{1}{2}}\left(\omega_1\right) \frac{\left(r_s^2 - r_v^2 - x'^2\right)}{2 r_v r_s^2} dr_v. && (3.21)
\end{aligned}
$$

For the case of flow around the bullet

$$
\begin{aligned}
U_x^{\text{bul.}} &= U_x^{\text{a.d.}} + U_x^{\text{s}}, && (3.22)\\
U_x^{\text{s}} &= \frac{m\left(x' - x_0\right)}{\left(r_s^2 + \left(x' - x_0\right)^2\right)^{\frac{3}{2}}}, && (3.23)\\
\frac{\partial U_x^{\text{s}}}{\partial r_s} &= -\frac{3m\left(x' - x_0\right) r_s}{\left(r_s^2 + \left(x' - x_0\right)^2\right)^{\frac{5}{2}}}. && (3.24)
\end{aligned}
$$

The extra term, given in equation (3.24), can be directly substituted into the numerator of (3.16). For the case of twin, co-axial rotors, f is straightforward to adjust

$$
\begin{aligned}
f^{\text{co-ax.}} &= \frac{U_{d1} x}{2\pi} \int_0^{r_{d1}} \frac{1}{\sqrt{r_v}} Q'_{-\frac{1}{2}}\left(\omega_1\right) dr_v + \frac{U_{d2}\left(x - g\right)}{2\pi} \int_0^{r_{d2}} \frac{1}{\sqrt{r_v}} Q'_{-\frac{1}{2}}\left(\omega_2\right) dr_v, && (3.25)\\
\frac{\partial f^{\text{co-ax.}}}{\partial r_s} &= \frac{U_{d1} x}{2\pi} \int_0^{r_{d1}} \frac{1}{\sqrt{r_v}} Q''_{-\frac{1}{2}}\left(\omega_1\right) \frac{\left(r_s^2 - r_v^2 - x'^2\right)}{2 r_v r_s^2} dr_v\\
&\quad + \frac{U_{d2}\left(x - g\right)}{2\pi} \int_0^{r_{d2}} \frac{1}{\sqrt{r_v}} Q''_{-\frac{1}{2}}\left(\omega_2\right) \frac{\left(r_s^2 - r_v^2 - \left(x' - g\right)^2\right)}{2 r_v r_s^2} dr_v, && (3.26)
\end{aligned}
$$

where $\omega_2 = 1 + [(x' - g)^2 + (r_s - rv)^2]/2 r_s r_v$. When calculating $\partial\hat{\Delta}/\partial R$ or Δ numerically, it is most efficient to cut off the integral at some large lower limit, and then add on the 'tail' of the integral as calculated analytically using the leading order behaviour for U_x and $\partial U_x/\partial r_s$ as $x \to -\infty$.

In the second section of the chapter we consider in more detail the input turbulence model, which in Chapter 2 was taken to be the von Kármán spectrum. In the third and final section of the chapter we will look at the effect that the various different mean flow and turbulence input models have on the radiated sound spectrum.

3.3 Atmospheric turbulence models

A fundamental challenge of modelling turbulence is that no closed set of equations exists for determining statistical properties, such as $\langle u^2 \rangle$, the ensemble average of velocity. Much work in turbulence theory is therefore concerned with obtaining closed, solvable sets of equations for statistical quantities by introducing further laws, for example based on experimental observation. The need for modelling assumptions to close the set of turbulence equations, and also because there are often significant differences between turbulence generated in seemingly similar situations, means a wide range of turbulence models exists. It also means that numerical simulations are heavily relied upon in this field. Here we undertake a review of different analytical descriptions of turbulence generated in the atmosphere. Any model will of course be an approximation to this complex phenomenon. Simonich et al. (1990) previously reviewed several studies in order to choose an appropriate turbulence spectrum for their UDN model, and in particular they highlighted the work of Snyder (1981) which includes effects of heat transfer.

3.3.1 The three-dimensional energy spectrum

As described in Chapter 1, the two primary methods of turbulence representation are either through modelling the statistical distribution of key eddy characteristics or via a spectrum representation. In Ganz's UDN model (1980), the former method was employed. The von Kármán spectrum was represented by a statistical distribution of elements and then RDT was used to simulate the distortion of these elements. A key conclusion of Ganz's work was that tonal noise may be dominated by a relatively limited range of transverse eddy lengthscales, of the order of 25% of the blade spacing at the rotor tip.

An 'instantaneous' spectrum is a further type of approximation, as used in Paterson and Amiet (1982) and Simonich et al. (1990). Here, results for a flat-plate airfoil in rectilinear motion are averaged over time, weighted by the appropriate Doppler factor. This approximation will be valid if the rotor directivity does not change significantly during each blade-eddy interaction, i.e. for eddies which are sufficiently small.

We use the full spectrum representation of turbulence, as defined in Chapter 2 equations (2.54) - (2.57) and (2.60) - (2.61). Turbulence spectra give an approximation of the turbulent kinetic energy contained within a range of eddy frequencies. Given a turbulent signal, for example experimental measurements of velocity correlations, we might wish to reconstruct a picture of the distribution of eddy sizes to get an idea of what the turbulence 'looks like'. The three-dimensional energy spectrum, $E(k)$, gives one (imperfect) measure for this distribution of eddy sizes[1]. In equation (2.55), we introduced the general expression for an isotropic turbulence spectrum, in terms of $E(k)$. If all eddies present are of the same size, L, then $E(k)$ will peak at $k \sim \pi/L$, however it is important to remember that eddies of a fixed size contribute to $E(k)$ for all k. In addition, the Fourier Transform involved in obtaining S^∞_{ij} means information about the phase of the velocities is lost, and this is why $E(k)$ is imperfect: an infinite number of different distributions of eddy size can give rise to the same spectrum. However, changes in $E(k)$ do give an indication of changes in turbulent behaviour.

Our upstream spectrum, which is assumed to be isotropic, obeys the following relations

$$E(k) = 2\pi k^2 S^\infty_{ii}(\mathbf{k}) \tag{3.27}$$

$$= k^3 \frac{d}{dk}\left[\frac{1}{k}\frac{d\Theta^\infty_{xx}}{dk}\right], \tag{3.28}$$

(summation convention assumed). The quantity $E(k)dk$ gives the contribution of wavenumber k to $\frac{1}{2}\langle u^2\rangle$, and is therefore seen as representing energy.

We can construct two corresponding expressions, $\mathcal{E}_1(k)$ and $\mathcal{E}_2(k)$, for our distorted spectrum S_{ij}, as follows

$$\mathcal{E}_1(\mathbf{x},\omega) = 2\pi S_{ii}(\mathbf{x},\omega), \tag{3.29}$$

$$\mathcal{E}_2(\mathbf{x},\omega) = k_x^3 \frac{d}{dk_x}\left[\frac{1}{k_x}\frac{d\Theta_{xx}}{dk_x}\right], \tag{3.30}$$

$$\text{where} \quad \Theta_{xx} = \int_{\Re^2} A_{xk}(\mathbf{x};\mathbf{k}) A_{xl}(\mathbf{x};\mathbf{k}) S^\infty_{kl}(\mathbf{k}) dk_y dk_z. \tag{3.31}$$

These quantities will not represent energy spectra, as S_{ij} is a temporal (rather than spatial) Fourier Transform and is no longer isotropic. However, they allow comparison of the change in total spectral level, rather than a single component, such as S_{xx}.

---

[1] An alternative measure is given by the structure function, (Davidson, 2004).

In Figures 3.15 - 3.17 we have plotted S_{xx}, $\mathcal{E}_1(k)$ and $\mathcal{E}_2(k)$ for the full range of mean flows defined in this chapter, both near the hub and the blade tip. In Figure 3.15 the biggest differences in S_{xx} between the different flows are seen for the co-axial case near the tip, and for the variable circulation case near the hub. By summing all diagonal components and plotting S_{ii} (Figure 3.16) the hub and tip results are brought closer together, although the variable circulation case near the hub is still seen to differ significantly from all other cases. These results indicate that, within the variable circulation model, the turbulent energy is shifted somewhat away from the hub, towards the mid-blade. In the co-axial case, a lower level of turbulent energy is seen near the tips of the front row of blades, as some of the upstream turbulence has been diverted to the rear row.

The plot of $\mathcal{E}_2$ (Figure 3.17) compares closely to S_{xx}, as it is based on the axial component Θ_{xx}. However, the spectra now display a clear peak at the dominant lengthscale, which is

$$L_d \sim \frac{\pi}{k_x} = \frac{\pi U_\infty}{\omega_d} \approx 1.7. \tag{3.32}$$

having increased from the upstream integral lengthscale of 1.

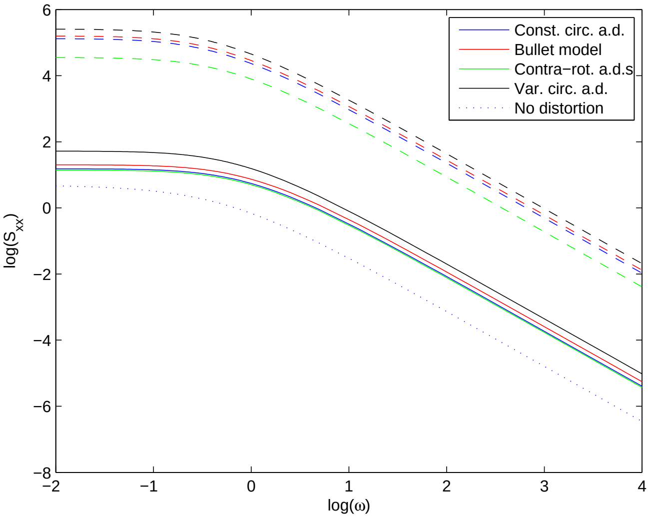

Figure 3.15: This figure shows the S_{xx} component of the distorted turbulence spectrum, the quantity which was investigated by Majumdar and Peake (1998), for all the flows considered in this chapter. The dashed lines indicate calculations at points near the blade tip ($r/r_d = 0.96$), the solid lines are near the hub ($r/r_d = 0.34$ for the const. and contra cases and 0.35 for the bullet and var. cases). $U_f/U_\infty = 100$ in all cases, i.e. high distortion.

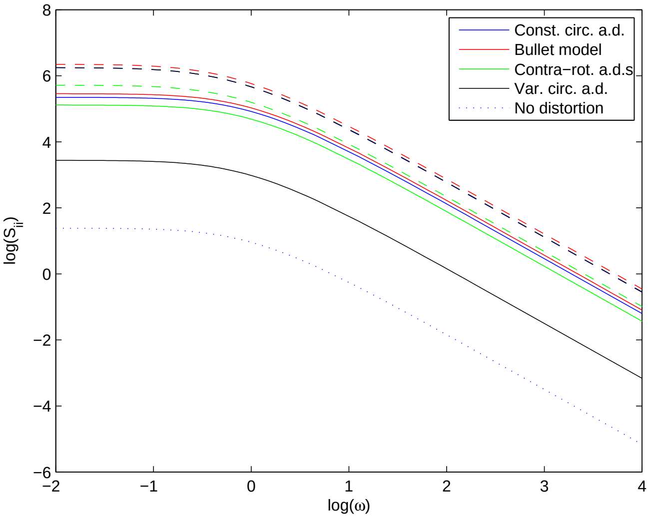

Figure 3.16: Sum of all diagonal elements $S_{ii} = \mathcal{E}_1/2\pi$. The dashed lines indicate points near the blade tip, the solid lines are near the hub.

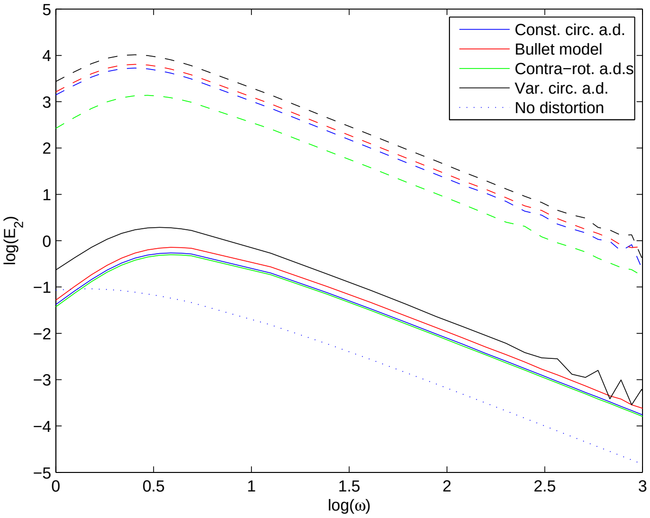

Figure 3.17: Plot of $\mathcal{E}_2$. The dashed lines indicate points near the blade tip, the solid lines are near the hub. We see that the spectra peak at $\log(\omega_d) \approx 0.6$.

3.3.2 Turbulence shed by installation features

Hanson's comparison in 1974 of experimental results of the blade pressure spectrum due to UDN with that due to a cylinder placed in the inlet flow led him to conclude that atmospheric turbulence may in fact be similar to that caused by a narrow cylinder. Sharland (1964) had previously undertaken an experimental study of noise caused by a circular rod bent into a ring placed upstream of a model fan rotor, and found this increased broadband levels. The lack of ducting around an open rotor leads to interaction with flow structures shed from installation features, such as the large pylon which joins the engine to the airframe. In this section we explore the possibilities for modelling such interactions.

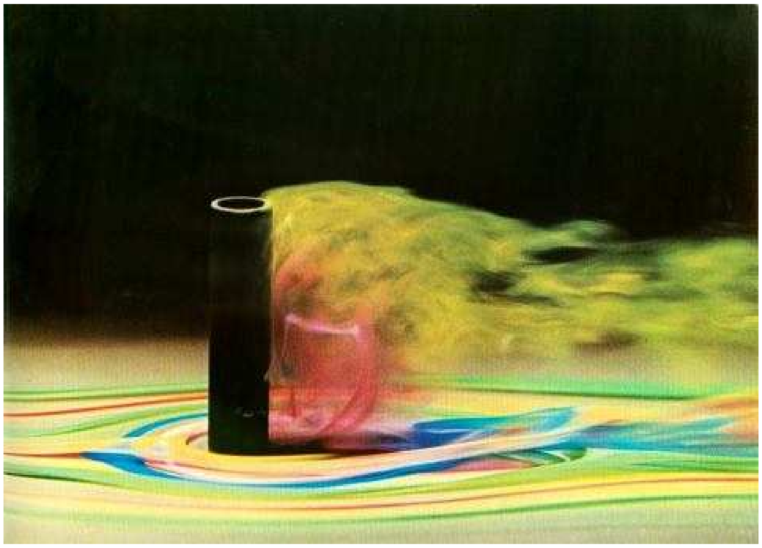

Figure 3.18: Turbulence behind a chimney. Image reproduced from Davidson (2004). Image copyright Henri Werlé of ONERA.

By considering different upstream turbulence models we are able to assess the impact of different forms of S_{ij}^{∞}, to see how critical this choice may be. We look at two new models here: the Liepmann and Gaussian spectra.

Liepmann spectrum

The Liepmann spectrum is given by

$$\Theta_{xx}^{LM}(k_x) = \frac{\overline{u_{\infty,1}^2} L}{2\pi\left(1 + k_x^2 L^2\right)}, \tag{3.33}$$

$$\Rightarrow \quad E^{LM}(k) = \frac{8L^5 \overline{u_{\infty,1}^2}}{\pi} \frac{k^4}{\left(1 + L^2 k^2\right)^3}, \tag{3.34}$$

$$\Rightarrow \quad S_{ij}^{LM}(\mathbf{k}) = \frac{2L^5 \overline{u_{\infty,1}^2}}{\pi^2} \frac{\left[k^2 \delta_{ij} - k_i k_j\right]}{\left(1 + L^2 k^2\right)^3}, \tag{3.35}$$

and is widely used (Cheong et al., 2006, Lloyd, 2009). For $kL \ll 1$, we have $E^{LM} \sim k^4$, as for the von Kármán spectrum. This power law fits that observed for grid-generated turbulence (Davidson, 2004). For $kL \gg 1$ we see that E^{LM} decays like k^{-2}, and this differs from the von Kármán spectrum for which $E(k) \sim k^{-\frac{5}{3}}$ as $k \to \infty$.

Gaussian spectrum

The Gaussian spectrum is given by

$$\Theta_{xx}^{G}(k_x) = \frac{\overline{u_{\infty,1}^2}}{2\sqrt{\pi}} l_G \exp\left(-\frac{k_x^2 l_G^2}{4}\right), \tag{3.36}$$

$$\text{where} \quad l_G = \frac{2\Gamma\left(\frac{5}{6}\right)}{\Gamma\left(\frac{1}{3}\right)} L. \tag{3.37}$$

Thus

$$E^G(k) = \frac{k^4 l_G^5 \overline{u_{\infty,1}^2}}{8\sqrt{\pi}} \exp\left(-\frac{k^2 l_G^2}{4}\right), \tag{3.38}$$

$$\Rightarrow \quad S_{ij}^{G}(\mathbf{k}) = \frac{l_G^5 \overline{u_{\infty,1}^2}}{32\pi^{\frac{3}{2}}} \frac{\left(k^2 \delta_{ij} - k_i k_j\right)}{\exp\left(\frac{k^2 l_G^2}{4}\right)}. \tag{3.39}$$

Using the Gaussian spectrum to represent atmospheric turbulence has been shown to underpredict ingestion noise due to isotropic turbulence at low and very high frequencies, and overpredict for high frequencies (Atassi and Logue, 2008). However, as we are also interested in representing the turbulence shed by features like the pylon we include it for comparison.

Figure 3.19 compares the von Kármán, Liepmann and Gaussian energy spectra. A particular point of difference is the rate of fall off. The very rapid fall off of the Gaussian spectrum is unrealistic for atmospheric turbulence, and this model is most useful in a restricted region of smaller kL values, as might be found for wakes due to coherent shedding from bluff bodies.

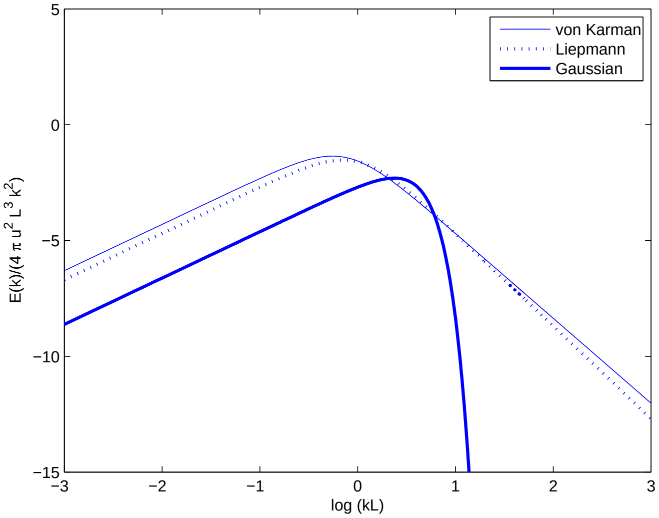

Figure 3.19: Here we compare possible candidates for the upstream spectrum model: von Kármán, Liepmann and Gaussian. The main difference between the three is their behaviour as kL increases. Note the separation between the energy containing and inertial subranges (located at the peak of $E(k)$) is found at $k = L^{-1}$ for the von Kármán and Liepmann spectra, and is slightly shifted to $k > L^{-1}$ for the Gaussian spectrum.

Effect of turbulence model on distorted spectrum

In Figures 3.20 and 3.21 we have plotted S_{xx} when the upstream turbulence field is given by the Liepmann and Gaussian models respectively, compared to the von Kármán case. We see in the Liepmann case a slight change in decay rate. The very rapid drop off in the Gaussian case means that under that model very little energy is transferred to eddies with higher values of k_x (that is, eddies with a smaller lengthscale than the integral lengthscale).

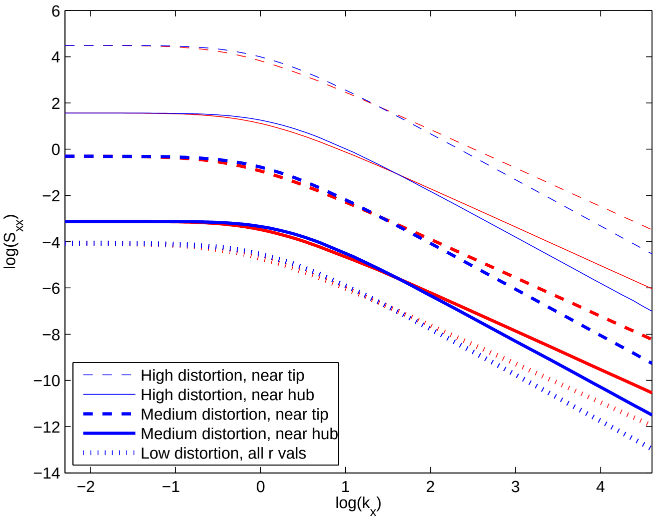

Figure 3.20: Axial component of the distorted turbulence spectrum, with the mean flow induced by a single actuator disk. The Liepmann spectrum case is shown in blue, with von Kármán in red for comparison. $L = 1$ in all cases.

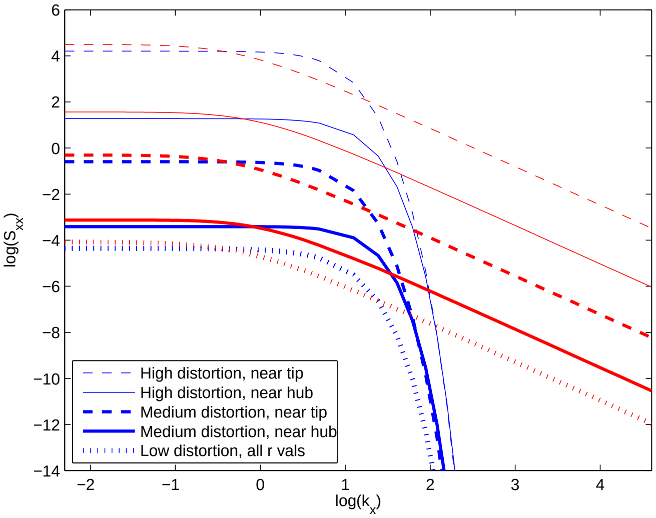

Figure 3.21: Axial component of the distorted turbulence spectrum, mean flow induced by a single actuator disk. The Gaussian spectrum case is shown in blue, with von Kármán in red for comparison. $L = 1$ in all cases.

Anisotropic models

For completeness we note here certain UDN models which directly model the turbulence at the rotor face, instead of the process of distortion.

Kerschen and Gliebe (1981) developed an axisymmetric, but anisotropic, model for turbulence at the rotor face. The axial and transverse lengthscales, denoted by L_a and L_t, are independent within this model (as well as the axial and transverse mean square speeds $\overline{u^2_{\infty,a}}$ and $\overline{u^2_{\infty,t}}$). An interesting area for future work would be to investigate mapping our distorted spectrum onto their expression, by choosing appropriate values for L_a, L_t, $\overline{u^2_{\infty,a}}$ and $\overline{u^2_{\infty,t}}$.

In the case of uniform distortion it is possible to write down an analytic expression for the distorted, anisotropic turbulence, using the Batchelor and Proudman (1954) model. The distorted wavevector, given in our model by equation (2.34), is then given by

$$l_i = \frac{k_i}{e_i}, \tag{3.40}$$

(no summation convention). The constant factors e_i give the distortion in each direction and so must multiply to give 1 to satisfy incompressibility. This model has been recently used by Atassi and Logue (2009) and Devenport et al. (2010).

3.3.3 Integral lengthscale, L

Along with the form of $E(k)$, which defines S^{∞}_{ij}, our model requires an input value for the integral lengthscale parameter, L. The integral lengthscale can be defined via R_{ij} (referring back to equation (2.61)) as follows

$$L = \int_0^{\infty} \frac{R_{xx}(r\hat{\mathbf{e}}_{\mathbf{x}})}{\overline{u^2_{\infty,1}}} dr, \tag{3.41}$$

(Davidson, 2004). As before, $\overline{u^2_{\infty,1}}$ is the mean square speed of the axial component of turbulent velocity. The dependence of the eventual spectrum on this second parameter, $\overline{u^2_{\infty,1}}$, is purely multiplicative i.e. doubling $\overline{u^2_{\infty,1}}$ will lead to a $10\log_{10} 2$ dB rise in PWL.

Turbulence always contains a wide range of scales; the value of L shifts the dominant eddy size but there will still be a range of eddy sizes present. We input L for the upstream turbulence, and the particular form of distortion will then determine the dominant lengthscale of the distorted turbulence. In the case of distortion due to a streamtube contraction, this distortion lengthscale will be related to the rotor radius (Hanson and Horan, 1998). In view of this, UDN studies often restrict themselves to turbulent lengthscales less than the scale of the streamtube contraction, claiming that larger eddies appear only as slowly varying mean flow changes (Simonich et al., 1990). The experimental study of Mish and Devenport (2006b) did indeed confirm that for integral scales which are large relative to the chord, the distortion of inflow is not as critical. However, we note that experimental studies do not always measure turbulence lengthscales, and a study by Wilson and Thomson (1994) found that large-scale turbulence can cause acoustic fluctuations which are often neglected.

Hanson and Horan (1998), when considering turbulent flow onto a stator, observed that the 1/3 Octave Band Power was highly sensitive to L, exhibiting distinct behaviour in the low or high frequency regimes. They used the Liepmann spectrum as the basis for their inhomogeneous model (equation (3.35)) and thus for high frequencies, with large k, the 1 in the denominator is dominated by L^2k^2, and the spectrum behaves as $1/L$. The noise was thus found to decrease like $1/L$ at high frequencies. Conversely, for low frequencies when both terms in the denominator play a role, the noise was found to increase with L.

Measurements of L

Choosing an appropriate value for L is not straightforward, as it will vary with atmospheric conditions from place to place and from day to day. In addition, it is important to take account of the effects of scaling when extrapolating from rig testing to flight data. Wilson and Thomson (1994) reviewed the large range of experimental measurements which had been made up to that date, and in Table 3.1 we have summarised their results. We see that L is found to vary with height off the ground, z, but different regimes are observed depending on whether buoyancy (due to temperature differences) or inertia (due to wind) is the dominant turbulence generation mechanism. The ratio of buoyancy to inertia forces can be quantified by the 'normalized height'

$$\zeta = z/L_{\mathrm{mo}}, \tag{3.42}$$

where L_{mo} is the Monin-Obukhov length (see Wilson and Thomson (1994) equation (3) for full definition). When $|\zeta| \ll 1$, shear instabilities (i.e. inertia forces) dominate, and when $|\zeta| \gg 1$, buoyancy dominates.

Note that in several instances in Table 3.1 the scales found are significantly larger than 1 metre, the order of L commonly used by acousticians. Wilson observed that the short timescale of typical acoustic measurements, of a few minutes, contrasted with atmospheric measurements which are often taken over several days, and this may lead to large scale structures being missed in acoustic tests. In addition, the lengthscales in the two transverse directions, L_u and L_v, are often found to differ, an indication of the distortion and elongation of eddies which can take place in atmospheric conditions even before a rotor is introduced.

Study	Correlation lengthscales (for velocities separated in the wind direction) dimensional quantities given in metres	Height off ground measurement taken (in metres)
Kader et al, 1989	$L_u \approx 10.3z$, $L_v \approx 7.5z$	(not given)
Johnson et al, 1987	$L_u \approx 0.3z + \exp(-0.3z)$	$1\text{m} < z < 33\text{m}$
Zubkovskii and Fedorov, 1986	$L_u \approx 18\text{m} - 26\zeta$	(not given)
Lenschow and Stankov, 1986	$L_u = L_v \approx 0.45z$	$z > 20\text{m}$ (from aircraft)
Daigle et al, 1983	$0.5\text{m} < L_u < 1.2\text{m}$	$0.15\text{m} < z < 1.2\text{m}$
Mizuno, 1982	$20\text{m} < L_u, L_v < 40\text{m}$	$z = 10\text{m}$
Kaimal et al, 1972	$L_u \approx 22z$, mainly shear $L_u \approx 1.3z$, mainly buoyancy	(not given)
Panofsky, 1962	$L_u = 34\text{m}$, $L_v = 55\text{m}$	$z = 2\text{m}$

Table 3.1: L_u denotes the lengthscale measure based on velocities in the axial (wind) direction, L_v is based on velocities in transverse horizontal direction. All measurements are taken from observation towers except Lenschow and Stankov.

Simonich et al. (1990) also obtained expressions for the turbulent integral lengthscale and mean square velocity at a variety of heights (50, 120 and 150m), see Table 3.2. They found $L \approx 0.4z$, and $\overline{u^2_{\infty,1}}$ decreases slightly with height. Simonich's values give us an indication of the range of appropriate values for $\overline{u^2_{\infty,1}}$ to use when making predictions.

Height, z	L_u	$\sqrt{\overline{u_{\infty,1}^2}}$	$\overline{u_{\infty,1}^2}$
50m	20m	0.296 m/s	0.0876 $\mathrm{m}^2/\mathrm{s}^2$
122m	48.8m	0.261 m/s	0.0681 $\mathrm{m}^2/\mathrm{s}^2$
152m	61m	0.248 m/s	0.0615 $\mathrm{m}^2/\mathrm{s}^2$

Table 3.2: Atmospheric turbulence parameters given by Simonich et al. (1990) at a range of heights.

It is possible that if the sub-range of lengthscales which have most significant effect on the sound are modelled closely then results will be accurate even if the model spectrum diverges significantly elsewhere from that observed. Thus for UDN modelling, use of an integral lengthscale of the order of the rotor radius can be justified as we expect these eddies to contribute most to the noise (Ganz, 1980).

In conclusion, Wilson's summary of L values indicates it would be informative to consider some higher values of L. We note that in Figure 2.12 tonal peaks were observed for large values of L, although the highest noise case was confirmed to be when $L \sim r_d$.

3.4 Radiated noise results

In this final section of the chapter we plot the radiated sound, as predicted by our model, for a wide range of inputs. Firstly we consider the different mean flows defined in this chapter, namely the variable circulation model, the 'bullet' simulation model, and the co-axial twin rotor model. Each of these is compared back to the single actuator disk model employed in Chapter 2. Secondly we consider different upstream turbulence models, namely the Liepmann and Gaussian spectra, and compare these to the results obtained with the von Kármán model. Thirdly we consider a wider range of L values than previously, including those used by Simonich et al. (1990).

3.4.1 Adjusting the mean flow

Variable circulation

In Figures 3.22 and 3.23 we investigate the use of different profile scalings, as first outlined in equation (3.6). The first adjustment is made to the values of $\partial X_i/\partial x_j$ used within A_{ij}

and to the quantity R which appears in the phase term of the velocity, as follows

$$\left.\frac{\partial X_i}{\partial x_j}\right|_{(\hat{x},\hat{r})} = \left.\frac{\partial X_i^{\text{var.}}}{\partial x_j}\right|_{x=\hat{x},r=\frac{(\hat{r}-r_h)}{(r_d-r_h)}r_d}, \tag{3.43}$$

$$R(x,r) = R^{\text{var.}}\left(x, \frac{(r-r_h)}{(r_d-r_h)}r_d\right). \tag{3.44}$$

Here $X^{\text{var.}}$ and $R^{\text{var.}}$ are the values which would be obtained using the original variable circulation model, and thus we have scaled the X and R values from the region $(0, r_d)$ at the disk face to lie between r_h and r_d instead. A secondary adjustment can be made to R as follows

$$R(x,r) = r_h + R^{\text{var.}}\left(x, \frac{(r-r_h)}{(r_d-r_h)}r_d\right). \tag{3.45}$$

Here the addition of r_h ensures that R is always greater than r, as occurs in a streamtube contraction. In order to compare like with like, in Figure 3.23 we plot the PWL found in the constant circulation actuator disk case using exactly the same adjustments.

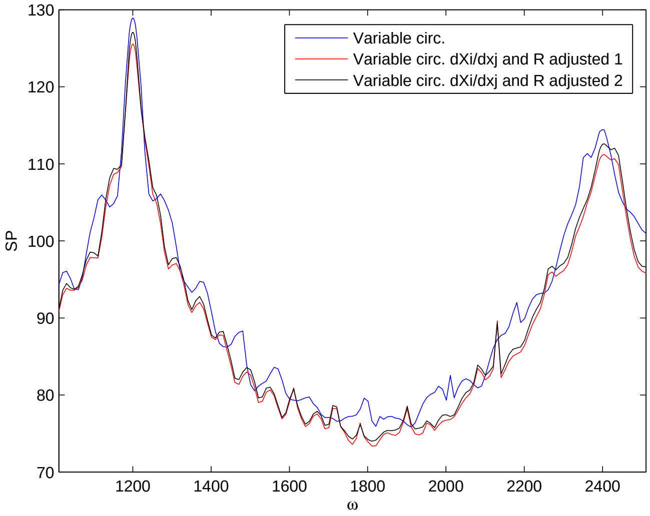

Figure 3.22: Medium distortion level, $L = 1$, comparing the original variable circulation mean flow model with two different types of profile scaling. 'Adjusted 1' corresponds to $\partial X_i/\partial x_j$ and R being evaluated at a new radial position as given in equations (3.43) and (3.44), and 'adjusted 2' corresponds to the same values for $\partial X_i/\partial x_j$, but R being given by the expression in equation (3.45).

In Figure 3.22 we see that the change in $\partial X_i/\partial x_j$ values leads to a lowering of PWL

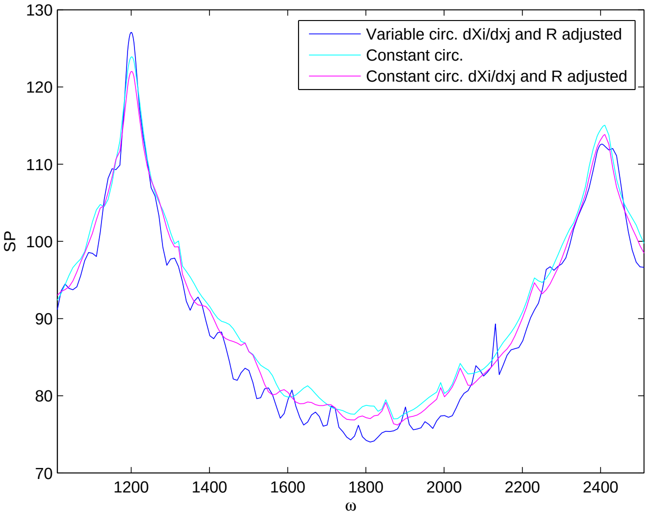

Figure 3.23: Medium distortion level, $L = 1$, comparing the variable and constant circulation mean flow models, where profile scaling has been implemented identically.

at all frequencies. Interestingly, when the value of R is further adjusted the broadband level is unaffected, but the tonal peaks are. We conclude that the broadband level is most affected by the detailed nature of the distortion, as parametrised by $\partial X_i/\partial x_j$, whereas the peaks are primarily affected by the overall magnitude of the streamtube contraction, as given by R. In Figure 3.23 we see that the difference between the constant and variable circulation cases is in fact increased when both models use the 'scaled' profiles, with a difference of more than 5 dB seen in the peak tonal level.

Figure 3.24 compares the (scaled) variable and (non-scaled) constant circulation cases at several levels of distortion. We see a shift in broadband level in each case when the variable model is used, but the direction of the shift depends on the level of distortion. For high distortion, the broadband level is lowered in the variable case whereas for low distortion, it is raised. As the variable flow model is more realistic, UDN models which use a constant circulation actuator disk to represent the streamtube contraction may under- or over-estimate broadband levels due to this.

In Figure 3.25 we again compare the variable and constant circulation cases, but now varying the integral lengthscale parameter. The qualitative change in all three cases is the same as L is increased, with the variable circulation model resulting in a lowered broadband PWL at all frequencies, but a raised tonal peak around 1 BPF, and a lowered peak around 2 BPF.

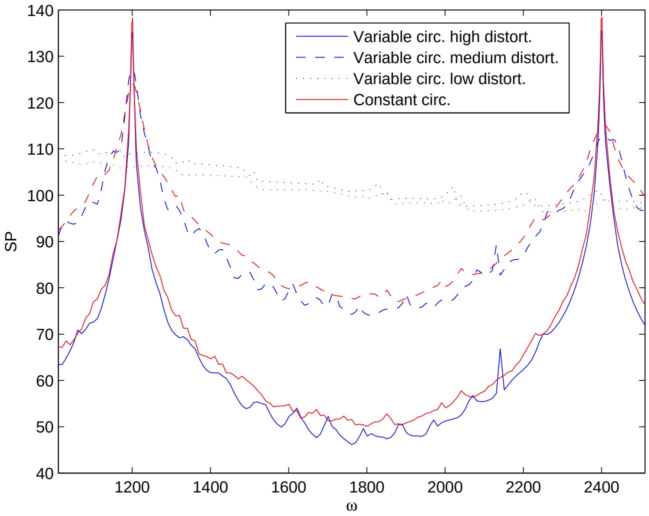

Figure 3.24: Variable vs. constant circulation models, varying the distortion level. The actuator disk strength, U_d, is kept constant between the two models.

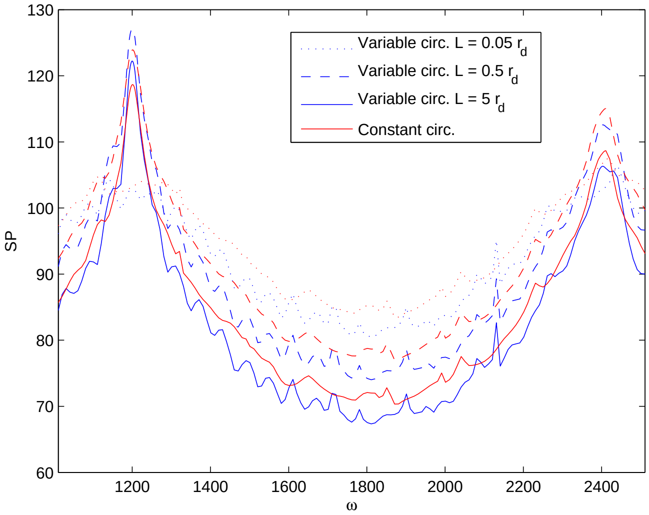

Figure 3.25: Variable vs. constant circulation, varying the integral lengthscale L. The actuator disk strength, U_d, is kept constant between the two models.

Bullet and co-axial cases

Figure 3.26 shows the effect on the radiated sound of adding a point source to the upstream flow, simulating the bullet. The broadband level is consistently reduced for all distortion levels by 1-3 dB, however the peak tonal level remains unchanged. We note that it is not completely straightforward to predict the final sound spectrum from the distorted turbulence spectrum at the rotor face, as plotted for example in Figure 3.11. This is because the changes in S_{xx} tend to differ at different radial positions along the blade, each of which contributes a component to the far-field pressure.

In Figure 3.27 we have plotted the radiated sound comparing the co-axial and single disk cases at different distortion levels. The difference seen is minimal, as is the case when different L values are compared.

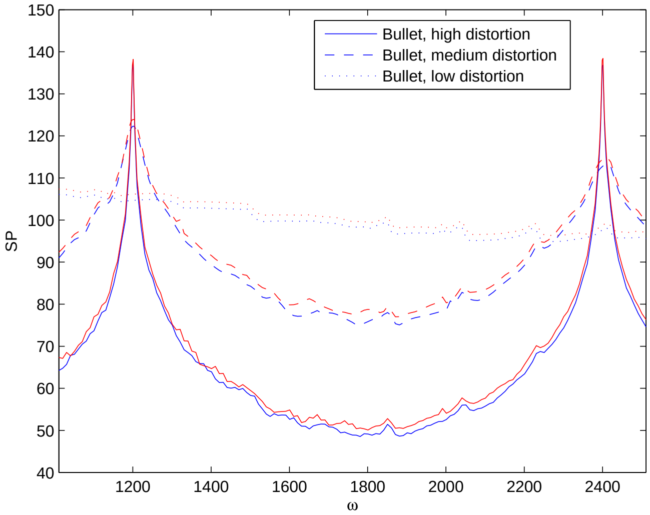

Figure 3.26: Bullet (blue) vs. no bullet (red) case, for a variety of distortion levels.

3.4.2 Adjusting the turbulence spectrum

In order to implement a different upstream turbulence model in the code for calculating the radiated sound expression (as given in equation 2.133) we must adjust the integral of S^{∞}_{jk} over ϕ_k, which was given in equations (2.91) - (2.93) for the von Kármán spectrum.

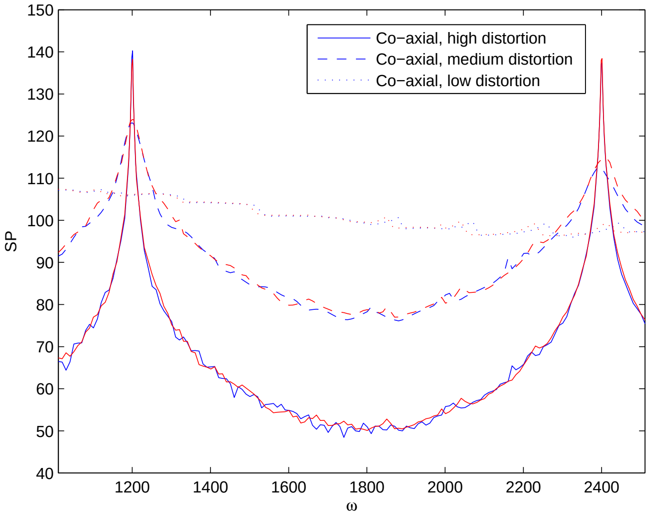

Figure 3.27: Comparing the co-axial (blue) and single disk (red) cases, for a variety of distortion levels.

We find

$$\int_0^{2\pi} S_{xx}^{\infty}\left(k_x^m, k_y, k_z\right) d\phi_k = 2\pi r_k^2 G, \tag{3.46}$$

$$\int_0^{2\pi} S_{yy}^{\infty}\left(k_x^m, k_y, k_z\right) d\phi_k = \int_0^{2\pi} S_{zz}^{\infty}\left(k_x^m, k_y, k_z\right) d\phi_k = \left(2\pi k^2 - \pi r_k^2\right) G, \tag{3.47}$$

$$\text{where, for the Liepmann spectrum,} \quad G = \frac{2L^5 \overline{u_{\infty,1}^2}}{\pi^2 \left(1 + L^2 k^2\right)^3}, \tag{3.48}$$

$$\text{and, for the Gaussian spectrum,} \quad G = \frac{l_G^5 \overline{u_{\infty,1}^2}}{32\pi^{\frac{3}{2}}} \exp\left(-\frac{k^2 l_G^2}{4}\right). \tag{3.49}$$

In both cases we still have

$$\int_0^{2\pi} S_{jk}^{\infty}\left(k_x^m, k_y, k_z\right) d\phi_k = 0 \quad \text{if} \quad j \neq k, \tag{3.50}$$

as these terms involve only the integral of $\sin\phi_k$, $\cos\phi_k$ or $\sin\phi_k \cos\phi_k$ over a 2π period.

We compare the Liepmann to von Kármán models in Figure 3.28. Batchelor and Proudman (1954) found that, in the uniform distortion case, the turbulence distortion becomes independent of the precise form of the homogeneous upstream turbulence as the distortion level is increased. However, in this non-uniform case, we see that in fact the broadband PWL is lowered by 5-10 dB at all levels of distortion when the Liepmann spectrum is used in place of the von Kármán, although the tonal peak heights remaining unchanged.

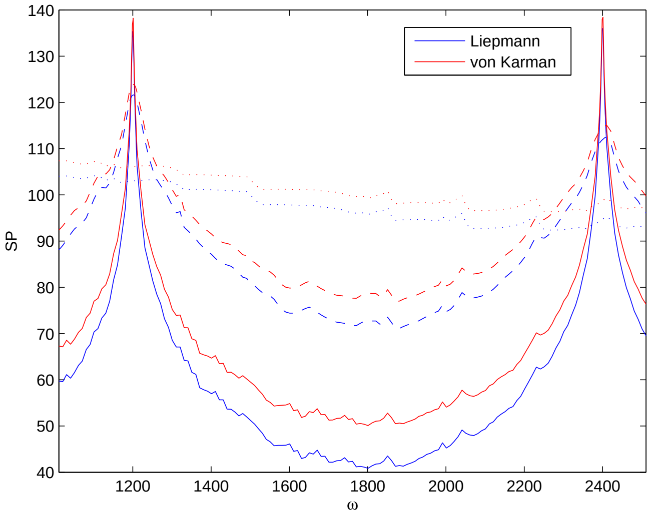

Figure 3.28: Comparing the von Kármán and Liepmann models for the upstream turbulence, for varying distortion level. Highly peaked = high distortion; somewhat peaked = medium distortion; broadband = low distortion.

In Figure 3.29 we compare the Gaussian and von Kármán models. As predicted, the Gaussian model produces a less realistic spectrum, which is very highly peaked around multiples of BPF for $L = 0.5r_d$. For larger values of L the dB level found is extremely low (off the scale plotted here), due to the rapid decay of the Gaussian spectrum as L increases that was seen in Figure 3.19.

Varying the integral lengthscale

Lastly, we have input a wider range of L values to include the higher values which are observed in the real atmosphere. In Figure 3.30 we can confirm that the highest tonal levels are seen when $L = r_d$, however even when $L \gg r_d$ the tonal peaks remain, whereas for $L \ll r_d$ we find a broadband spectrum with no tones. In Figure 3.31 we see a decrease of 4-5 dB in UDN level as the open rotor travels from 50m to 122m height, primarily due to the change in atmospheric turbulence intensity. The difference between 122m and 152m height is less pronounced. The high distortion cases are given for comparison, as would be seen if realistic atmospheric conditions were successfully simulated in static testing.

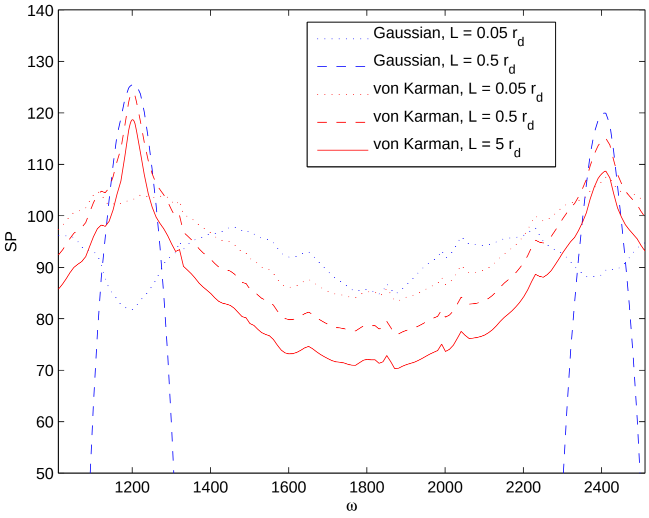

Figure 3.29: Here we compare the von Kármán and Gaussian models for the upstream turbulence for a variety of integral lengthscales, all at the same level of distortion

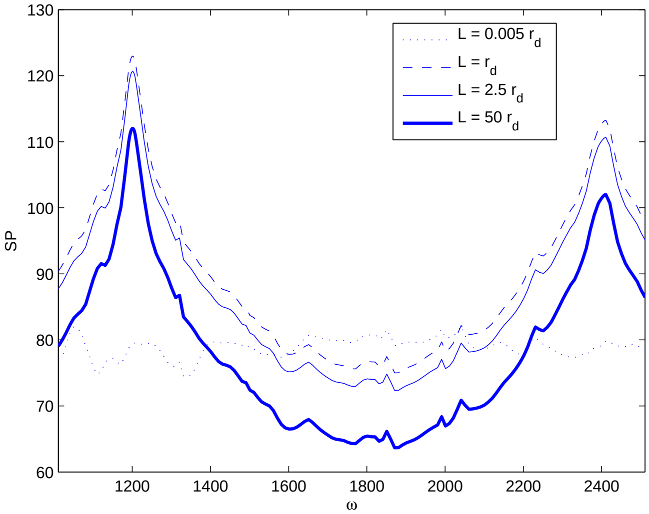

Figure 3.30: Comparing several L values for the medium distortion case ($U_f/U_\infty = 10$). A single actuator disk model is used for the mean flow.

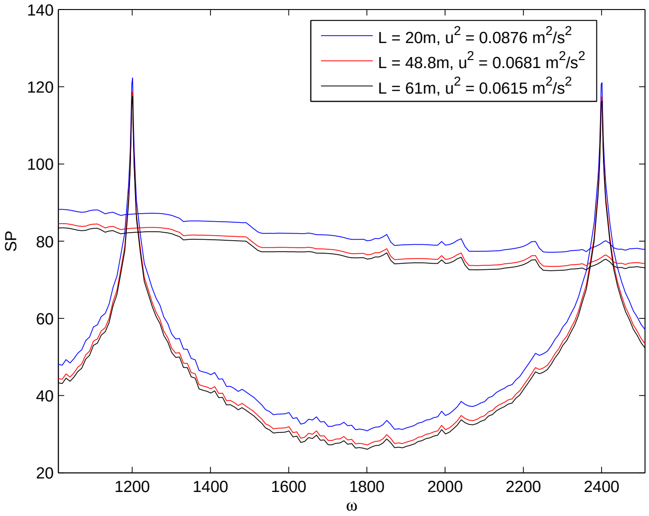

Figure 3.31: Implementing the values of L and $\overline{u^2_{\infty,1}}$ as used by Simonich to simulate atmospheric conditions at 50m ($L = 20$m), 122m ($L = 48.8$m) and 152m ($L = 61$m).

Chapter 4

Generalisation to asymmetric rotor systems

4.1 Chapter outline

In this chapter, we rework the analysis of Chapter 2 for non-axisymmetric mean flows. This involves changes to the Fourier Transform of the distortion amplitude, denoted in Chapter 2 by C_{ij}^{p}. We test the model by inputting a simple mean flow which is asymmetric at the rotor face, given by two actuator disks side by side. The turbulence spectrum at the rotor face now varies with azimuthal angle, ϕ, as values of $\partial X_i/\partial x_j$ depend upon ϕ. This then leads to changes in the ϕ dependence of the force term in the wave equation. Both the sound from one rotor with an asymmetric inflow, and that which arises from the two rotor system are calculated.

The extensions made in this chapter allow any irrotational mean flow, which tends to a uniform velocity far upstream, to be incorporated within our UDN model.

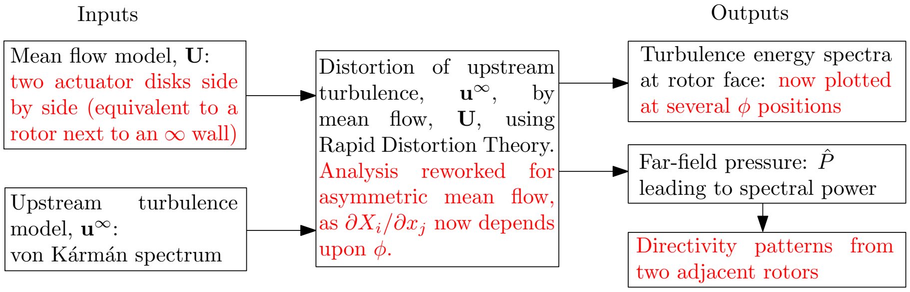

4.2 Effects of asymmetry

The mean flow of air into a fully installed open rotor on an aircraft will vary with ϕ due to the presence of the fuselage and airframe features, such as the pylon each engine is mounted on. Such 'installation effects' are a current priority in AOR noise testing programmes (Peake and Parry, in press, 2012) and are receiving much attention from engine manufacturers, for example within the current Airbus/Rolls-Royce programme of wind tunnel testing discussed below, and the CFD programmes at ONERA and Airbus mentioned in §1.3.4. With the positioning of the engines still an open question both the pusher and puller configurations are being investigated; each of these presents its own challenges. In the pusher configuration, the rotor is mounted behind the pylon and therefore interacts with the (asymmetric) pylon wake. The puller configuration entails higher blade angle of attack (due to the flow induced by the nearby wing) and we discuss non-zero incidence in detail in Chapter 5.

In Chapter 3 we discussed the modelling of turbulent structures shed by installation features, and found that for large-scale turbulent structures (i.e. higher L values), the broadband UDN level was significantly affected by the precise form of the upstream turbulence. However, as in many of the studies reviewed in Chapter 1, we dealt solely with the axisymmetric situation. Such analyses neglect a key aspect of real installation effects, namely asymmetry. Cargill (1993) noted the need to consider whether an axisymmetric inflow is good enough to model real intakes, but also highlighted the increased complexity of the analysis in the asymmetric case.

4.2.1 Previous work on asymmetry

Recent joint Airbus/Rolls-Royce wind tunnel testing of Rig 145 has included both rotor alone testing, and testing with mock-ups of the pylon in place, as shown in Figure 4.1 (see also the discussion of pylon blowing in §1.2.2, Figure 1.7). This testing has confirmed the asymmetry of pylon-rotor interaction, with azimuthal directivity being affected (Ricouard et al., 2010). Pylon-rotor interaction noise was found to be less sensitive to operating conditions than rotor alone tones, and dominated the isolated rotor noise. The exact design of the pylon did not affect results significantly. The presence of the pylon was also found to affect the front rotor tones more than the rear rotor or interaction tones, and in this chapter we consider the noise from the front rotor only.

Further experimental observations of asymmetry include work by Carolus and Stremel

Figure 4.1: Rig 145 testing between 2008-2010 included measurements with the pylon in place. Image reproduced with permission from Rolls-Royce. The pylon of an open rotor must be substantial in order to withstand blade-off failure testing.

(2002), who conducted experiments measuring the pressure fluctuations on rotating fan blades due to ingested grid generated turbulence. Interestingly, they noted unexpected peaks at the Rotational Shaft Frequency (RSF) which they believed to be due to a slight asymmetry of the mean flow, which they could not remove. More recently, Koch (2009) measured the SPL generated by a rotor placed downstream of an asymmetrical array of cylindrical rods, as a model for fan inflow distortion noise. Extra peaks were observed between BPF tones, which were somewhat 'haystacked'. The BPF tonal level was also increased in some cases, see Figure 4.2.

As described in §1.3.3, the extension of analytic models to include three-dimensional effects is of interest generally, to more realistically capture true flow characteristics. Simonich et al. (1990) and Amiet et al. (1990) looked at the effect of the direction of distortion (not just its strength) on UDN levels, and noted that the eddy-blade intersection area would be affected by asymmetries in the mean flow. In their model, turbulence stretching along the rotor axis was found to decrease noise, compared to stretching which occurred at an angle to the axis. The work of both Simonich et al. and Paterson and Amiet (1982) primarily dealt with helicopter rotors, hence their interest in asymmetric inflows. Paterson and Amiet noted that non-axial mean flows tend to smooth harmonic peaks and shift them away from BPFs. They highlighted three different asymmetric effects. Firstly, radial wandering of an ingested eddy with respect to the blade leads to the amplitude of tones varying in time, as the relative velocity between eddy and blade will vary with r. Secondly, random azimuthal wandering may lead to varying frequency

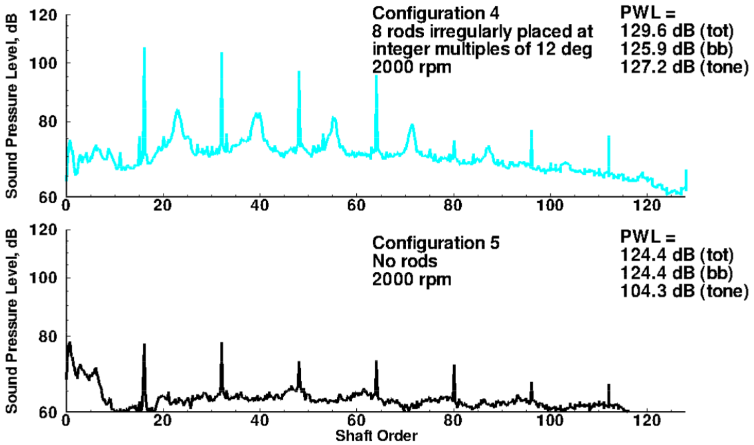

Figure 4.2: Image reproduced from Koch (2009). Plotted here is the spectrum radiated from a fan placed in an inflow which has been distorted by an upstream array of cylindrical rods. The top figure is for the case of an asymmetric array, the bottom is the baseline plot with no rods present.

of tones, away from BPF. Thirdly, steady asymmetry of the mean flow will lead to non-random azimuthal and radial wandering, potentially shifting the frequency of tones, but this effect will be steady in time.

4.3 Asymmetric turbulence distortion

In this chapter we aim to investigate the general effects of asymmetry upon UDN. We do not try to recreate all aspects of a realistic AOR inflow-field, for example we do not try to approximate the flow field around the pylon. However, any mean flow (including a numerically defined flow) could now be substituted into our framework. This is a substantial extension of Majumdar's work where only flows which had a streamfunction were considered, thus limiting attention to two-dimensional or axisymmetric flows.

4.3.1 A simple asymmetric mean flow

We consider in this chapter a simple asymmetric system where the mean flow is readily calculated. The set-up is shown in Figure 4.3, and consists of two actuator disks which lie in the $y-z$ plane, separated by a distance d in the direction perpendicular to their axes.

The mean flow we use is therefore given by the sum of two actuator disk flows, centred

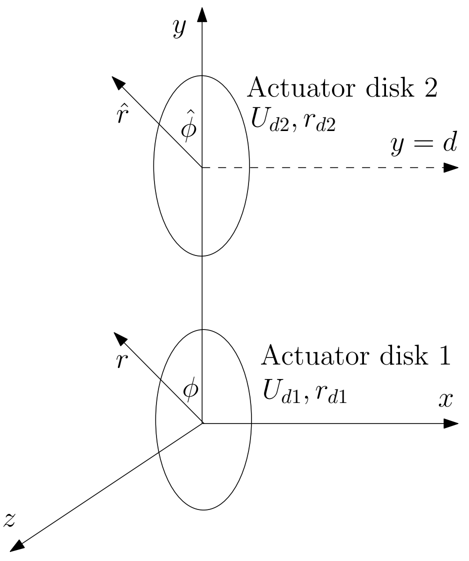

Figure 4.3: Illustration of our coordinate system. These two actuator disks side by side give rise to an asymmetric flow.

at $(0, 0, 0)$ and $(0, d, 0)$. Note that the sign of $U_d = B\Omega\Gamma/2\pi U_\infty = T/\pi r_d^2 \rho_0 U_\infty$, the 'strength' of each actuator disk, does not indicate the direction of rotation but rather the direction of thrust generation[1].

The above set-up can be used to model two adjacent rotors of different strengths and/or sizes, and below we give the expression for the mean flow induced by two actuator disks with general $U_{d1}, U_{d2}, r_{d1}, r_{d2}$. Examples of aircraft with four engines, two beneath each wing in close proximity to each other, include the Airbus A340 and A400, and the military Avro Shackleton, see Figure 4.4. Pusher configurations of AOR, with fuselage-mounted rather than wing-mounted rotors also have two adjacent rotors.

If the properties of both actuator disks are the same ($U_{d1} = U_{d2}$ and $r_{d1} = r_{d2}$) then by symmetry we have zero velocity in the $\hat{\mathbf{e}}_\mathbf{y}$ direction across the surface $y = d/2$. This set-up is thus equivalent to a system in which a single rotor at the origin is placed next to an infinite wall running through the plane $y = d/2$, on which a condition of zero normal velocity is satisfied. This flow can therefore be used to approximate the presence of the fuselage alongside a single open rotor. Note that we will not be considering the effect of sound scattering off the fuselage. This has been treated recently by Kingan and McAlpine (2010), who approximated the fuselage by an infinite cylinder, leading to an adjusted Green's function.

---

[1] The direction of rotation has no bearing on the velocities given in an actuator disk model, which is steady in time and can be thought of as the limit of an infinitely bladed propeller.


(a) (b) (c)

Figure 4.4: a) The Airbus A400m. b) The counter-rotating propellers of the Avro Shackleton. Photo by NJR ZA, licenced under Creative Commons Licence. c) Example of the rear mounted AOR concept being developed by Airbus.

For the axisymmetric, single actuator disk system we considered in Chapter 2, cylindrical polar coordinates were most appropriate, with mean flow velocities given in equations (2.47) and (2.48). When considering an asymmetric set-up it is more convenient to switch to cartesian coordinates. For the first disk, centred at $(0,0,0)$, we re-write r dependence within the velocity expressions in terms of y and z (using $r^2 = y^2 + z^2$), and there is no ϕ dependence. For the second rotor, we replace r with $\hat{r}$, where $\hat{r}^2 = (y-d)^2 + z^2$. We also decompose the radial velocities, U_r, induced by the two disks into velocity components in the y and z directions. The azimuthal velocity, U_ϕ, is zero upstream of the disks. Thus

$$\mathbf{U} \cdot \mathbf{\hat{e}_y} \equiv U_y = U_{r1} \cos\phi + U_{r2} \cos\hat{\phi} = \frac{U_{r1} y}{\left(y^2+z^2\right)^{\frac{1}{2}}} + \frac{U_{r2}\left(y-d\right)}{\left[\left(y-d\right)^2+z^2\right]^{\frac{1}{2}}}, \tag{4.1}$$

$$\mathbf{U} \cdot \mathbf{\hat{e}_z} \equiv U_z = U_{r1} \sin\phi + U_{r2} \sin\hat{\phi} = \frac{U_{r1} z}{\left(y^2+z^2\right)^{\frac{1}{2}}} + \frac{U_{r2} z}{\left[\left(y-d\right)^2+z^2\right]^{\frac{1}{2}}}, \tag{4.2}$$

where $\tan\phi = z/y$ and $\tan\hat{\phi} = z/(y-d)$. We therefore find the velocities in the region $x < 0$ are given by

$$\begin{aligned} U_x =& \frac{U_{d1} x}{2\pi\left(y^2+z^2\right)^{\frac{3}{4}}} \int_0^{r_{d1}} \frac{1}{\sqrt{r'}} Q'_{-\frac{1}{2}}\left[\omega\left(y,r'\right)\right] dr' \\ &+ \frac{U_{d2} x}{2\pi\left[\left(y-d\right)^2+z^2\right]^{\frac{3}{4}}} \int_0^{r_{d2}} \frac{1}{\sqrt{r'}} Q'_{-\frac{1}{2}}\left[\omega\left(y-d,r'\right)\right] dr', \end{aligned} \tag{4.3}$$

$$U_y = -\frac{U_{d1}\sqrt{r_{d1}}\, y Q_{\frac{1}{2}}\left[\omega\left(y, r_{d1}\right)\right]}{2\pi\left(y^2+z^2\right)^{\frac{3}{4}}} - \frac{U_{d2}\sqrt{r_{d2}}\left(y-d\right) Q_{\frac{1}{2}}\left[\omega\left(y-d, r_{d2}\right)\right]}{2\pi\left(\left[y-d\right]^2+z^2\right)^{\frac{3}{4}}}, \tag{4.4}$$

$$U_z = -\frac{U_{d1}\sqrt{r_{d1}}\, z Q_{\frac{1}{2}}\left[\omega\left(y, r_{d1}\right)\right]}{2\pi\left(y^2+z^2\right)^{\frac{3}{4}}} - \frac{U_{d2}\sqrt{r_{d2}}\, z Q_{\frac{1}{2}}\left[\omega\left(y-d, r_{d2}\right)\right]}{2\pi\left(\left[y-d\right]^2+z^2\right)^{\frac{3}{4}}}. \tag{4.5}$$

The argument, ω, of the Legendre functions Q_n and their derivatives is defined as

$$\omega\left(y', r'\right) = 1 + \frac{x^2 + \left[\left(y'^2+z^2\right)^{\frac{1}{2}} - r'\right]^2}{2\left(y'^2+z^2\right)^{\frac{1}{2}} r'}. \tag{4.6}$$

Note that ω is even in its y' argument. Thus by inspection of equation (4.4) we see that for $y = d/2$ we have $U_y = 0$, i.e. the no penetration condition on the line of symmetry is satisfied.

By following a particular streamline far upstream, we can use these velocities to find the unique y and z position at which it originated. See Figure 4.5 for an example of the streamlines generated by this velocity field. Figure 4.6 compares the asymmetric streamlines to the axisymmetric case. We can compute quantities of interest for different values of d, the distance between the disks, and thus quantify the asymmetric effect.

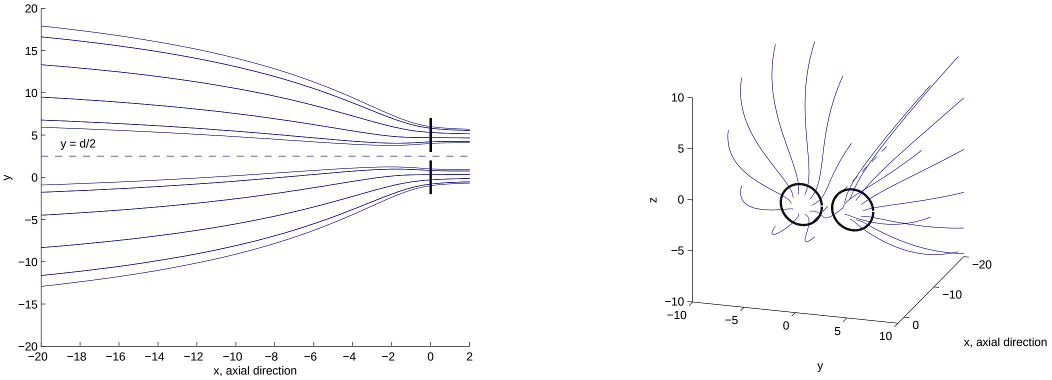

Figure 4.5: Streamlines for the asymmetric, two-disk system (with $U_{d1} = U_{d2} = 198U_\infty$ and $r_{d1} = r_{d2}$), side-on and head-on views. The disk positions are indicated in black. The surface of zero normal velocity is indicated by a dashed line.

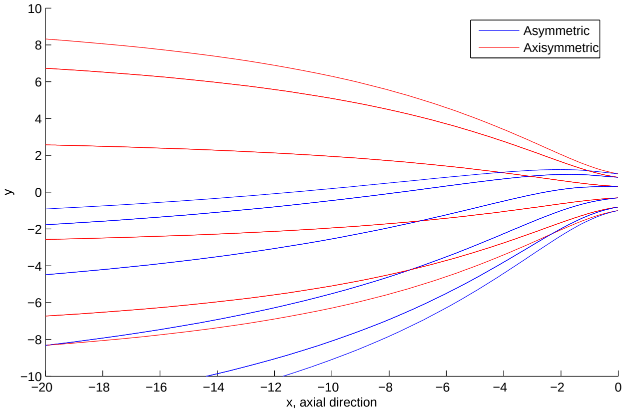

Figure 4.6: Comparing the asymmetric streamlines to the axisymmetric case. The values of U_d and r_d are kept constant between the two. The infinite wall is located at $y = 2.5$, above the asymmetric streamlines shown.

4.3.2 Turbulence at the rotor face

In Chapter 2 we found the distorted turbulence spectrum was given by the simple expression

$$S_{ij}\left(\mathbf{x},\omega\right) = \frac{2\pi}{U_\infty}\int_{\Re^2} A_{ik}\left(\mathbf{x},\mathbf{k}\right)A_{jl}\left(\mathbf{x},\mathbf{k}\right)S^{\infty}_{kl}\left(\mathbf{k}\right)dk_y dk_z, \tag{4.7}$$

where, in the above expression, $k_x = \omega/U_\infty$, i.e. only one k_x component contributes for each particular frequency ω. When calculating this numerically, it is more successful to make the substitutions

$$k_y = r_k\cos\phi_k, \quad k_z = r_k\sin\phi_k, \tag{4.8}$$

reducing the two infinite integrals to one infinite and one finite integral as follows

$$S_{ij}\left(\mathbf{x},\omega\right) = \frac{2\pi}{U_\infty}\int_0^\infty\int_0^{2\pi} A_{ik}\left(\mathbf{x},\mathbf{k}\right)A_{jl}\left(\mathbf{x},\mathbf{k}\right)S^{\infty}_{kl}\left(\mathbf{k}\right)r_k d\phi_k dr_k. \tag{4.9}$$

The main point to note is that for an asymmetric mean flow the ϕ dependence within A_{ij} is not removed when the k integrals are performed, as it was for the axisymmetric situation where ϕ dependence only came in through k_r and k_ϕ (as seen in equations (2.42) and (2.43)). Thus, when we consider the various S_{ij} spectra for an asymmetric mean flow, their levels will be different at different azimuthal positions around the rotor.

In Figures 4.7 and 4.8 we have plotted the axial component of the distorted turbulence spectrum, S_{xx}, at a range of azimuthal positions around the disk at the origin. We see, in Figures 4.7 and 4.8, that the spectrum increases as we move round from $\phi = 0$, nearest the second rotor where less streamtube contraction occurs, to $\phi = \pi$, where the greatest level of contraction occurs, see Figure 4.6. In Figures 4.9 and 4.10 we show the spectra for a range of distortion levels and radial positions, holding the azimuthal position constant. The spectrum level near the blade tip is found to be higher than that near the hub in all cases. However, the dependence of spectrum level on distortion level is not so straightforward, as the low distortion case lies between the high and medium distortion cases, in contrast to the axisymmetric case. Finally, in Figure 4.11, we have varied the separation between rotors, d. As expected, as d increases, and the mean flow approaches the axisymmetric mean flow, the spectra at different ϕ positions get closer together.

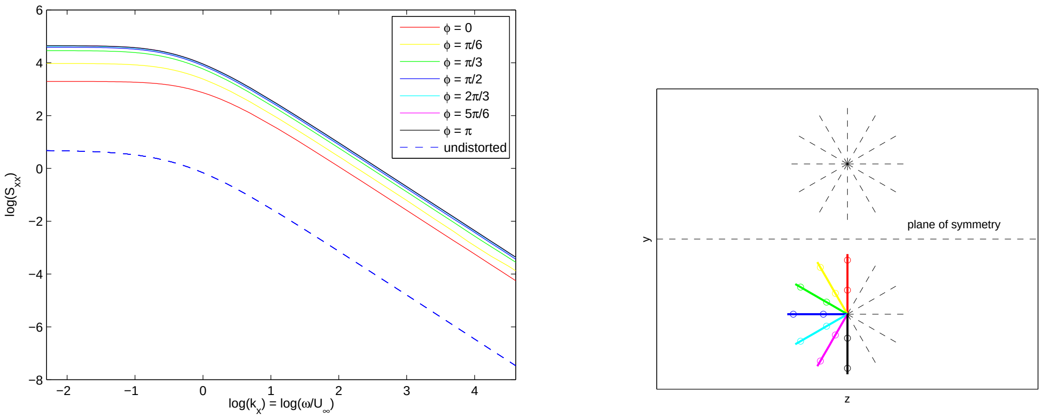

(a) (b)

Figure 4.7: a) Here we have calculated S_{xx} in the high distortion case ($U_f/U_\infty = 100$) near the rotor tip ($r/r_d = 0.9$), at a range of azimuthal positions. We see the energy level is higher than the undistorted spectrum in all cases. As we move from $\phi = 0$ (nearest the other rotor) to $\phi = \pi$ in equal increments of ϕ, the levels get closer together. b) This subfigure shows the positions at which S_{xx} has been calculated.

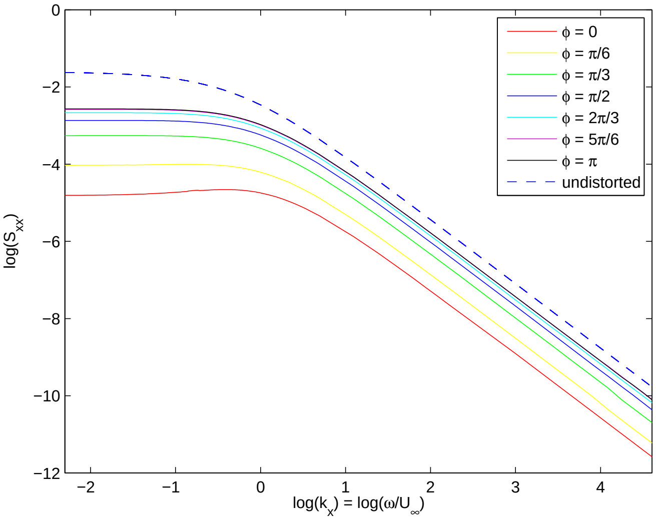

Figure 4.8: Here we show a medium distortion case ($U_f/U_\infty = 10$) near the rotor hub ($r/r_d = 0.4$). At this position the energy level is below that of the undistorted spectrum in all cases. We also see a peak in the $\phi = 0$ spectrum not present in the other spectra.

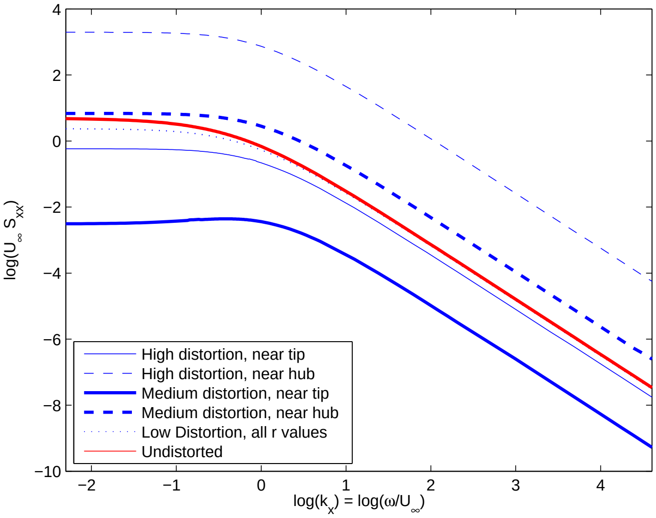

Figure 4.9: Here we show the spectrum at $\phi = 0$ for a range of distortion levels and radial positions. We have collapsed the data by multiplying S_{xx} by U_∞. By normalising in this way the undistorted case (which corresponds to $\partial X_i/\partial x_j = \delta_{ij}$) is the same for each of the three cases (high, medium and low distortion levels). The level near the tip is higher than that near the hub in all cases, but dependence on distortion level is more complex, with the low distortion case in between the high and medium distortion cases.

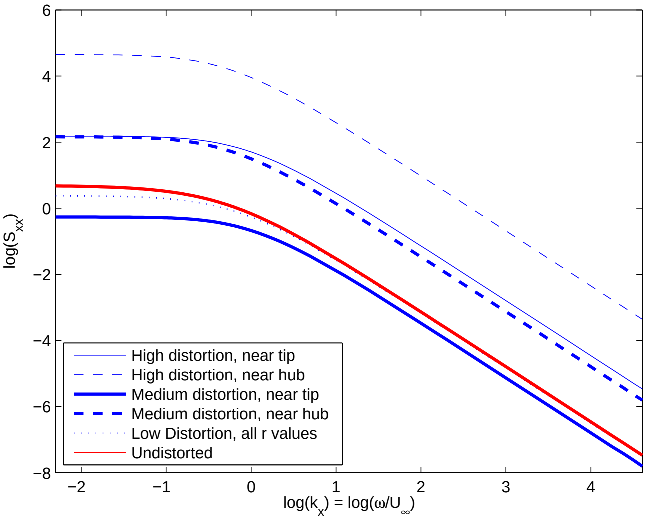

Figure 4.10: Plot as in Figure 4.9 above, but at $\phi = \pi$. There is less variation in spectrum level between the hub and tip than at $\phi = 0$.

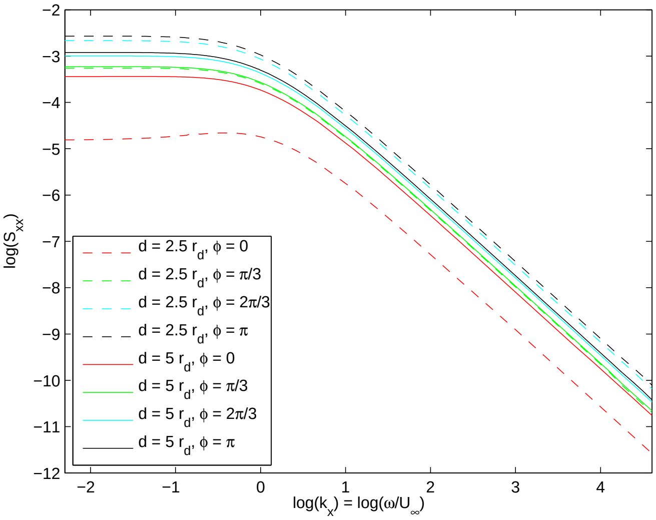

Figure 4.11: Here we have adjusted d, the level of asymmetry in the mean flow. As expected, the more highly asymmetric flow (with the smaller value of d) leads to larger differences between the spectrum at different azimuthal positions. As d increases the $\phi = 0$ and $\phi = \pi$ spectra move towards each other.

4.4 Blade pressures

In order to calculate $N_i A_{ij}$ (to substitute into the expression for the normal velocity at the leading edge, for use in LINSUB) we require expressions for A_{xx}, A_{xy}, A_{xz} and the 'mixed suffices' quantities $A_{\phi x}$, $A_{\phi y}$, $A_{\phi z}$. For this we would like to calculate the most general form for the components of A_{ij} in the polar directions, in terms of the polar expressions l_r, l_ϕ, $\partial/\partial r$, $\partial/\partial\phi$, R, Φ,and ϕ. In the next subsection we derive these quantities, before going on to calculate the normal velocity at the leading edge. We can then obtain expressions for the blade pressure jumps, spectrum of blade pressures, and the forcing term to substitute into the wave equation, all within the asymmetric framework.

4.4.1 The general form of A_{ij}

In Chapter 2, an approximation to the distorted amplitude was given

$$A_{ij} = \left(\delta_{im} - \frac{l_i l_m}{|\mathbf{l}|^2}\right)\frac{\partial X_j}{\partial x_m}, \tag{4.10}$$

(summation convention assumed). This quantity is straightforwardly interpreted in the cartesian reference frame, but care must be taken when considering the components with respect to polar coordinates. The most general form for $\mathbf{l}$ is

$$\begin{aligned} \mathbf{l} &= k_i \nabla X_i \\ &= \left\{\hat{\mathbf{e}}_\mathbf{x}\frac{\partial}{\partial x} + \hat{\mathbf{e}}_\mathbf{y}\frac{\partial}{\partial y} + \hat{\mathbf{e}}_\mathbf{z}\frac{\partial}{\partial z}\right\}\left[k_x X + k_y Y + k_z Z\right], \end{aligned} \tag{4.11}$$

where $\mathbf{k}$ is a constant wavevector. Thus l_r and l_ϕ are given in terms of the polar quantities X, R, Φ as follows

$$\begin{aligned} l_r = \mathbf{l}\cdot\hat{\mathbf{e}}_\mathbf{r} = k_x\frac{\partial X}{\partial r} &+ k_\phi\left(-\sin\phi\frac{\partial(R\cos\Phi)}{\partial r} + \cos\phi\frac{\partial(R\sin\Phi)}{\partial r}\right) \\ &+ k_r\left(\cos\phi\frac{\partial(R\cos\Phi)}{\partial r} + \sin\phi\frac{\partial(R\sin\Phi)}{\partial r}\right), \end{aligned} \tag{4.12}$$

$$\begin{aligned} l_\phi = \mathbf{l}\cdot\hat{\mathbf{e}}_\phi = k_x\frac{1}{r}\frac{\partial X}{\partial\phi} &+ k_\phi\frac{1}{r}\left(-\sin\phi\frac{\partial(R\cos\Phi)}{\partial\phi} + \cos\phi\frac{\partial(R\sin\Phi)}{\partial\phi}\right) \\ &+ k_r\frac{1}{r}\left(\cos\phi\frac{\partial(R\cos\Phi)}{\partial\phi} + \sin\phi\frac{\partial(R\sin\Phi)}{\partial\phi}\right). \end{aligned} \tag{4.13}$$

To calculate the mixed suffices components of A_{ij} we first write out the 'polar' components in terms of the cartesian components

$$\begin{aligned}
\hat{\mathbf{e}}_{\mathbf{x}} \cdot \mathbf{A} \cdot \hat{\mathbf{e}}_{\mathbf{x}} &= A_{xx}, \\
\hat{\mathbf{e}}_{\mathbf{x}} \cdot \mathbf{A} \cdot \hat{\mathbf{e}}_{\mathbf{r}} &= \cos\phi A_{xy} + \sin\phi A_{xz}, \\
\hat{\mathbf{e}}_{\mathbf{x}} \cdot \mathbf{A} \cdot \hat{\mathbf{e}}_{\phi} &= -\sin\phi A_{xy} + \cos\phi A_{xz}, \\
\hat{\mathbf{e}}_{\mathbf{r}} \cdot \mathbf{A} \cdot \hat{\mathbf{e}}_{\mathbf{x}} &= \cos\phi A_{yx} + \sin\phi A_{zx}, \\
\hat{\mathbf{e}}_{\mathbf{r}} \cdot \mathbf{A} \cdot \hat{\mathbf{e}}_{\mathbf{r}} &= \cos^2\phi A_{yy} + \cos\phi\sin\phi\left(A_{yz} + A_{zy}\right) + \sin^2\phi A_{zz}, \\
\hat{\mathbf{e}}_{\mathbf{r}} \cdot \mathbf{A} \cdot \hat{\mathbf{e}}_{\phi} &= -\cos\phi\sin\phi A_{yy} + \cos^2\phi A_{yz} - \sin^2\phi A_{zy} + \sin\phi\cos\phi A_{zz}, \\
\hat{\mathbf{e}}_{\phi} \cdot \mathbf{A} \cdot \hat{\mathbf{e}}_{\mathbf{x}} &= -\sin\phi A_{yx} + \cos\phi A_{zx}, \\
\hat{\mathbf{e}}_{\phi} \cdot \mathbf{A} \cdot \hat{\mathbf{e}}_{\mathbf{r}} &= -\sin\phi\cos\phi A_{yy} - \sin^2\phi A_{yz} + \cos^2\phi A_{zy} + \sin\phi\cos\phi A_{zz}, \\
\hat{\mathbf{e}}_{\phi} \cdot \mathbf{A} \cdot \hat{\mathbf{e}}_{\phi} &= \sin^2\phi A_{yy} - \sin\phi\cos\phi\left(A_{yz} + A_{zy}\right) + \cos^2\phi A_{zz}.
\end{aligned} \tag{4.14}$$

We then rewrite each cartesian component of A_{ij} using the following relations

$$l_y = \cos\phi l_r - \sin\phi l_\phi, \tag{4.15}$$

$$l_z = \sin\phi l_r + \cos\phi l_\phi, \tag{4.16}$$

$$\frac{\partial}{\partial y} = -\frac{\sin\phi}{r}\frac{\partial}{\partial\phi} + \cos\phi\frac{\partial}{\partial r}, \tag{4.17}$$

$$\frac{\partial}{\partial z} = \frac{\cos\phi}{r}\frac{\partial}{\partial\phi} + \sin\phi\frac{\partial}{\partial r}, \tag{4.18}$$

$$Y = R\cos\Phi, \tag{4.19}$$

$$Z = R\sin\Phi. \tag{4.20}$$

For example

$$\begin{aligned}
A_{xy} &= \left(1 - \frac{l_x l_x}{|\mathbf{l}|^2}\right)\frac{\partial Y}{\partial x} - \frac{l_x l_y}{|\mathbf{l}|^2}\frac{\partial Y}{\partial y} - \frac{l_x l_z}{|\mathbf{l}|^2}\frac{\partial Y}{\partial z} \\
&= \left(1 - \frac{l_x l_x}{|\mathbf{l}|^2}\right)\frac{\partial\left(R\cos\Phi\right)}{\partial x} - \frac{l_x l_r}{|\mathbf{l}|^2}\frac{\partial\left(R\cos\Phi\right)}{\partial r} - \frac{l_x l_\phi}{|\mathbf{l}|^2}\frac{1}{r}\frac{\partial\left(R\cos\Phi\right)}{\partial\phi}.
\end{aligned} \tag{4.21}$$

Finally, substituting the expressions for the cartesian A_{ij} components, in terms of the polar quantities l_r, l_ϕ, R, Φ, into the expressions of (4.14), we find

$$\begin{aligned}
A_{ix} &= \left(\delta_{ix} - \frac{l_i l_x}{|\mathbf{l}|^2}\right)\frac{\partial X}{\partial x} + \left(\delta_{ir} - \frac{l_i l_r}{|\mathbf{l}|^2}\right)\frac{\partial X}{\partial r} + \left(\delta_{i\phi} - \frac{l_i l_\phi}{|\mathbf{l}|^2}\right)\frac{1}{r}\frac{\partial X}{\partial \phi}, \\
A_{ir} &= \left(\delta_{ix} - \frac{l_i l_x}{|\mathbf{l}|^2}\right)\frac{\partial X_r}{\partial x} + \left(\delta_{ir} - \frac{l_i l_r}{|\mathbf{l}|^2}\right)\frac{\partial X_r}{\partial r} \\
&\quad + \left(\delta_{i\phi} - \frac{l_i l_\phi}{|\mathbf{l}|^2}\right)\left[\frac{\cos\phi}{r}\frac{\partial\left(R\cos\Phi\right)}{\partial\phi} + \frac{\sin\phi}{r}\frac{\partial\left(R\sin\Phi\right)}{\partial\phi}\right], \\
A_{i\phi} &= \left(\delta_{ix} - \frac{l_i l_x}{|\mathbf{l}|^2}\right)\frac{\partial X_\phi}{\partial x} + \left(\delta_{ir} - \frac{l_i l_r}{|\mathbf{l}|^2}\right)\frac{\partial X_\phi}{\partial r} \\
&\quad + \left(\delta_{i\phi} - \frac{l_i l_\phi}{|\mathbf{l}|^2}\right)\left[-\frac{\sin\phi}{r}\frac{\partial\left(R\cos\Phi\right)}{\partial\phi} + \frac{\cos\phi}{r}\frac{\partial\left(R\sin\Phi\right)}{\partial\phi}\right],
\end{aligned} \tag{4.22}$$

where $X_r = R\cos(\Phi - \phi)$, and $X_\phi = R\sin(\Phi - \phi)$. In these expressions the suffix i runs over x, r and ϕ, and $\delta_{xx} = \delta_{rr} = \delta_{\phi\phi} = 1$, with all other values of δ_{ij} being zero. We note that, for example, $A_{\phi r} \neq \left(\delta_{\phi m} - l_\phi l_m/|\mathbf{l}|^2\right)\left(\partial X_r/\partial x_m\right)$, as might have been expected. Essentially, the derivatives within A_{ij} do not act upon ϕ within the expressions for X_r and X_ϕ.

In the axisymmetric case, we have $\Phi = \phi$, $X_r = R$, $X_\phi = 0$ and $\partial X/\partial\phi = \partial R/\partial\phi = 0$, and thus we regain equations (2.37).

4.4.2 Input into LINSUB

To implement LINSUB we require the normal velocity at the leading edge of a blade. That is, we require

$$\frac{1}{2\pi^3}\int_{\Re^3} \hat{u}_j^\infty\left(\mathbf{k}\right)e^{-ik_xU_\infty t}\left[\mathbf{N}\cdot\mathbf{A}\right]_j \exp\left\{i\left[k_xX + k_yY + k_zZ\right]\right\}d^3\mathbf{k}, \tag{4.23}$$

re-written in a reference frame which rotates with the blades and decomposed into $e^{im\phi'}$ harmonics, where $\phi' = \phi - \Omega t$. Thus we wish to rewrite the above in the form

$$\sum_{m=-\infty}^{\infty} w_W\left(x, r\right)e^{i\omega_\Gamma t + im\phi'}, \tag{4.24}$$

which will allow us to pick out the appropriate frequency ω_Γ.

Using the fact that $Y = R\cos\Phi$, $Z = R\sin\Phi$, and the relation

$$\exp\left\{i\left(k_y\cos\Phi + k_z\sin\Phi\right)R\right\} = \sum_{n=-\infty}^{\infty} J_n\left(\sqrt{k_y^2+k_z^2}R\right)\exp\left\{in\left[\Phi - \tan^{-1}\left(\frac{k_z}{k_y}\right)\right]\right\}, \tag{4.25}$$

we have

$$\begin{aligned}\left[\mathbf{N}\cdot\mathbf{A}\right]_j \exp\left\{i\left[k_xX + k_yY + k_zZ\right]\right\} &= \exp\left(ik_xX\left(x,r,\phi\right)\right)\left[\sin\beta A_{xj} + \cos\beta A_{\phi j}\right] \\ &\quad \sum_{n=-\infty}^{\infty} J_n\left(r_kR\left(x,r,\phi\right)\right)\exp\left\{in\left(\Phi\left(x,r,\phi\right) - \phi_k\right)\right\},\end{aligned} \tag{4.26}$$

where $r_k = \sqrt{k_y^2+k_z^2}$ and $\phi_k = \tan^{-1}\left(k_z/k_y\right)$, as in Figure 2.1. Note that $X, R,$ and Φ depend upon ϕ in this asymmetric case.

Defining new quantities $\widetilde{C}_{ij}^{m,n}$ and $\widetilde{D}_{j}^{m,n}$

Next we need to bring out the ϕ dependence of equation (4.26) explicitly in exponential form. Previously we did this by expanding A_{ij} as a Fourier Series, but now that we have extra ϕ dependence within the e^{ik_xX}, $J_n(r_kR)$ and $e^{in\Phi}$ terms we must define a new quantity $\widetilde{C}_{ij}^{m,n}$ (note the extra superscript in comparison to the corresponding quantities in Chapter 2) as follows

$$A_{ij}\left(x,r;\mathbf{k}\right)e^{ik_xX}J_n(r_kR)e^{in\Phi} = \sum_{m=-\infty}^{\infty}\widetilde{C}_{ij}^{m,n}\left(x,r;\mathbf{k}\right)e^{im\phi}, \tag{4.27}$$

$$\text{where}\quad \widetilde{C}_{ij}^{m,n}\left(x,r;\mathbf{k}\right) = \frac{1}{2\pi}\int_0^{2\pi} A_{ij}\left(x,r;\mathbf{k}\right)e^{ik_xX}J_n(r_kR)e^{in\Phi}e^{-im\phi}d\phi.$$

The relation

$$\widetilde{C}_{ij}^{m,n}\left(x,r;k_x,r_k,\phi_k\right) = e^{-im\phi_k}\widetilde{C}_{ij}^{m,n}\left(x,r;k_x,r_k,0\right), \tag{4.28}$$

still holds, since ϕ_k does not appear in the extra terms within the $\widetilde{C}_{ij}^{m,n}$ integrand.

As in §2.3.2, we next define $\widetilde{D}_{ij}^{m,n}$ as follows

$$\begin{aligned}
\widetilde{D}_x^{m,n} &\equiv \left[\sin\beta \widetilde{C}_{xx}^{m,n} + \cos\beta \widetilde{C}_{\phi x}^{m,n}\right], \\
\widetilde{D}_y^{m,n} &\equiv \left[\sin\beta \frac{1}{2}\left\{\left(\widetilde{C}_{xr}^{m-1,n} + i\widetilde{C}_{x\phi}^{m-1,n}\right) + \left(\widetilde{C}_{xr}^{m+1,n} - i\widetilde{C}_{x\phi}^{m+1,n}\right)\right\}\right. \\
&\qquad \left. + \cos\beta \frac{1}{2}\left\{\left(\widetilde{C}_{\phi r}^{m-1,n} + i\widetilde{C}_{\phi\phi}^{m-1,n}\right) + \left(\widetilde{C}_{\phi r}^{m+1,n} - i\widetilde{C}_{\phi\phi}^{m+1,n}\right)\right\}\right], \\
\widetilde{D}_z^{m,n} &\equiv \left[\sin\beta \frac{1}{2}\left\{\left(-i\widetilde{C}_{xr}^{m-1,n} + \widetilde{C}_{x\phi}^{m-1,n}\right) + \left(i\widetilde{C}_{xr}^{m+1,n} + \widetilde{C}_{x\phi}^{m+1,n}\right)\right\}\right. \\
&\qquad \left. + \cos\beta \frac{1}{2}\left\{\left(-i\widetilde{C}_{\phi r}^{m-1,n} + \widetilde{C}_{\phi\phi}^{m-1,n}\right) + \left(i\widetilde{C}_{\phi r}^{m+1,n} + \widetilde{C}_{\phi\phi}^{m+1,n}\right)\right\}\right].
\end{aligned} \tag{4.29}$$

Here we have used the relation

$$\widetilde{D}_j^{m,n}(x, r; k_x, r_k, \phi_k) = e^{-im\phi_k} \widetilde{D}_j^{m,n}(x, r; k_x, r_k, 0). \tag{4.30}$$

Normal velocity at the blade leading edge

We can now obtain our leading edge velocity. For each wavevector $\mathbf{k}$ we have

$$\begin{aligned}
\sum_{m=-\infty}^{\infty} w_W e^{i\omega_\Gamma t + im\phi'} = \sum_{m=-\infty}^{\infty} &\left\{\sum_{n=-\infty}^{\infty} \widetilde{D}_j^{m,n}(x_0(r), r; k_x, r_k, 0) \exp\left[-i(m+n)\phi_k\right]\right\} \\
&\hat{u}_j^{\infty}(\mathbf{k}) \exp\left[i\left(m\Omega - k_x U_\infty\right)t\right] \exp\left[im\phi'\right].
\end{aligned} \tag{4.31}$$

We note the changes to this expression from the axisymmetric case, as given in equation (2.85). Firstly, for fixed frequency and azimuthal order (given by $(m\Omega - k_x U_\infty)$ and m respectively), the ϕ_k dependence now contains an extra factor n, which previously exactly balanced the $\exp(in\Phi)$ term. Secondly, we pick out (via $\widetilde{D}_j^{m,n}$) the $e^{im\phi}$ component of $A_{ij} J_n e^{in\Phi} e^{ik_x X}$, rather than the $e^{ip\phi}$ component of A_{ij} alone.

4.4.3 Output from LINSUB

As in Chapter 2, we use Smith's LINSUB method to calculate the blade pressure jumps induced by a sinusoidal disturbance impinging upon a cascade of blades. As we wish to substitute the forcing term obtained into the RHS of the wave equation (2.107), we calculate both the pressure jump across a single blade and the force found after summing over all blades.

Pressure jump

Substituting (4.31) into equation (2.71), the pressure jump across a blade which passes through the position x, r, ϕ at time t, due to an upstream gust of the form $\hat{\mathbf{u}}^{\infty}(\mathbf{k})e^{i(\mathbf{k}\cdot\mathbf{x}-k_xU_\infty t)}$, is now given by

$$\begin{aligned}\Delta p\left(x,r,\phi,t\right) =& \rho_0 W \sum_{m=-\infty}^{\infty} \Gamma_{WW}^{m}\left(\hat{z} = \frac{x - x_0\left(r\right)}{\cos\beta(r)}, r; \omega_\Gamma = k_x U_\infty - m\Omega, \chi = -\frac{2m\pi}{B}\right) \\ & \left\{\sum_{n=-\infty}^{\infty} \widetilde{D}_j^{m,n}\left(x_0(r), r; k_x, r_k, 0\right) e^{-i(m+n)\phi_k}\right\} \hat{u}_j^{\infty}\left(\mathbf{k}\right) e^{-ik_xU_\infty t} e^{im\phi}. \qquad (4.32)\end{aligned}$$

Again, we note the differences from the axisymmetric expression of equation (2.86): the Bessel function has been absorbed into the quantity $\widetilde{D}_j^{m,n}$, and the order of the ϕ_k exponent has been adjusted by n.

Spectrum of blade pressures

For completeness we give the expression for the blade pressure spectrum for this asymmetric system. The equivalent to equation (2.90) is

$$\begin{aligned}\hat{P}_{\text{blade}}(x,r,\omega) =& \frac{2\pi\rho_0^2 W^2}{U_\infty} \sum_{m=-\infty}^{\infty} \left|\Gamma_{WW}^{m}\left(x,r,\omega\right)\right|^2 \\ & \int_0^\infty \left\{\sum_{n=\infty}^{\infty} \widetilde{D}_j^{m,n}\left(x_0(r), r; k_x, r_k, 0\right)\right\}^{*} \left\{\sum_{n'=\infty}^{\infty} \widetilde{D}_k^{m,n'}\left(x_0(r), r; k_x, r_k, 0\right)\right\} \\ & \left[\int_0^{2\pi} S_{jk}^{\infty}\left(k_x^m, k_y, k_z\right) e^{i(n-n')\phi_k} d\phi_k\right] r_k dr_k, \qquad (4.33)\end{aligned}$$

where $k_x^m = (\omega + m\Omega)/U_\infty$. The main difference here is the appearance of a new exponential term within the integral over ϕ_k.

Forcing term

To obtain the force exerted by the rotor on the fluid, $\mathbf{f}$, we must sum the blade pressure jumps from equation (4.32) over all blades, exactly as in §2.3.5. This involves defining the blades' surfaces through use of a delta function, and then re-expressing that delta function as a sum of exponentials. The sum over blade number b, from 1 to B, then means certain combinations of terms sum to zero, and we can sum instead over the new index l, with ϕ dependence given by $m + lB$. We find

$$\begin{aligned} f_i\left(x, r, \phi, t\right) = & \rho_0 W N_i(r) \frac{B}{2\pi r} \sum_{m=-\infty}^{\infty} \frac{1}{\left(2\pi\right)^3} \int_{\Re^3} \Gamma_{WW}^{m}\left(x, r; k_x, \chi^m\right) \exp\left(-ik_x U_\infty t\right) \\ & \sum_{n=-\infty}^{\infty} \widetilde{D}_j^{m,n}\left(x_0(r), r; k_x, r_k, 0\right) \exp\left\{-i(m+n)\phi_k\right\} \\ & \left[\int_{\Re^3} u_j^{\infty}\left(\mathbf{x}'\right) \exp\left(-i\mathbf{k}\cdot\mathbf{x}'\right) d^3\mathbf{x}'\right] d^3\mathbf{k} \\ & \sum_{l=-\infty}^{\infty} \exp\left(i\left(m + lB\right)\left[\frac{\left(x - x_0(r)\right)\tan\beta(r)}{r}\right]\right) \exp\left(-ilB\phi_0(r)\right) \\ & \exp\left(-ilB\Omega t\right) \exp\left(i\left[m + lB\right]\phi\right). \end{aligned} \tag{4.34}$$

4.5 Far-field noise

4.5.1 Spectrum of radiated sound

In order to calculate the SP level (defined in (2.132)) we take the correlation of the sound pressure, using the same procedure and the same Green's function as in Chapter 2. The equivalent to equation (2.133) is found to be

$$
\begin{aligned}
\hat{P}\left(\sigma,\theta,\phi,\omega\right) =& \rho_0^2 \frac{B^2}{4\pi^2 U_\infty} \frac{1}{4\sigma_0^2 \left(1-M\cos\theta\right)^2} \\
& \sum_{l,m,m'} \int_{r_s,x_s} \left[J_{m+lB}\left(\gamma_0 r_s\right)\right]^* \left[W(r_s)\Gamma^{m}_{WW}\left(x_s,r_s;\omega\right)\right]^* \\
& \left[\frac{i\omega\cos\theta\sin\beta(r_s)}{c_0\left(1-M\cos\theta\right)} - \frac{i(m+lB)\cos\beta(r_s)}{r_s}\right] \\
& \exp\left\{\frac{-i\omega\cos\theta x_s}{c_0\left(1-M\cos\theta\right)} + i(m+lB)\frac{\left[x_s - x_0(r_s)\right]\tan\beta(r_s)}{r_s} + ilB\phi_0(r_s)\right\} \\
& \int_{r_s',x_s'} J_{m'+lB}\left(\gamma_0 r_s'\right) W(r_s')\Gamma^{m'}_{WW}\left(x_s',r_s';\omega\right) \\
& \left[-\frac{i\omega\cos\theta\sin\beta(r_s')}{c_0\left(1-M\cos\theta\right)} + \frac{i(m'+lB)\cos\beta(r_s')}{r_s'}\right] \\
& \exp\left\{\frac{i\omega\cos\theta x_s'}{c_0\left(1-M\cos\theta\right)} - i(m'+lB)\frac{\left[x_s' - x_0(r_s')\right]\tan\beta(r_s')}{r_s'} - ilB\phi_0(r_s')\right\} \\
& \sum_{p,p'} \int_{\Re} \left[\widetilde{D}_j^{m,p}\left(x_0(r_s),r_s;k_x,r_k,0\right)\right]^* D_k^{m',p'}\left(x_0(r_s'),r_s';k_x,r_k,0\right) \\
& \left[\int_0^{2\pi} e^{i(m+p-m'-p')\phi_k} S^{\infty}_{kl}\left(\mathbf{k}\right) d\phi_k\right] r_k dr_k dr_s' dx_s' dr_s dx_s e^{i(m'-m)\left(\phi-\frac{\pi}{2}\right)}. \qquad (4.35)
\end{aligned}
$$

4.5.2 SP plots

In Figures 4.12 and 4.13 we have plotted the radiated sound from the rotor at the origin, with an asymmetrical inflow as described in this chapter. Also shown are the axisymmetric SP spectra for comparison. We see that in the asymmetric case, the broadband level is generally lowered, although the heights of the tonal peaks remain at the same level. The exception is the broadband level around 1BPF in the low distortion (flight) case, which is raised for the asymmetric inflow. This effect on the broadband level is consistent with our earlier observation that the precise form of distortion primarily affects the broadband level rather than tones.

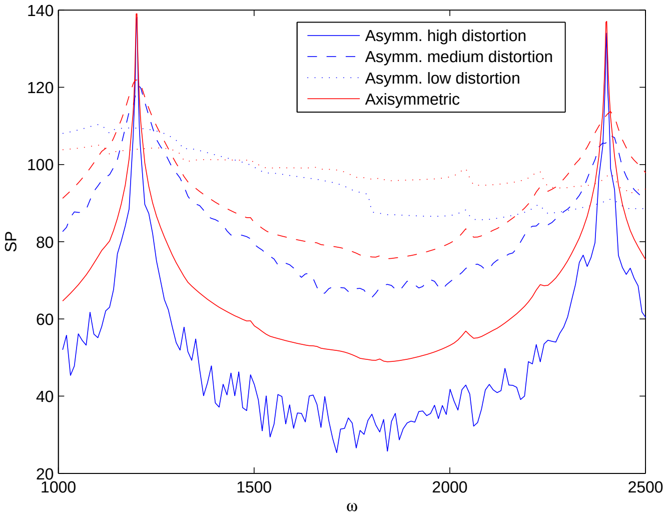

Figure 4.12: In blue are plotted the SP as radiated from a single rotor which experiences an asymmetric inflow of varying distortion levels. Shown in red are the equivalent axisymmetric levels. We note that the number of azimuthal harmonics summed over, n_m, was taken to be 3.

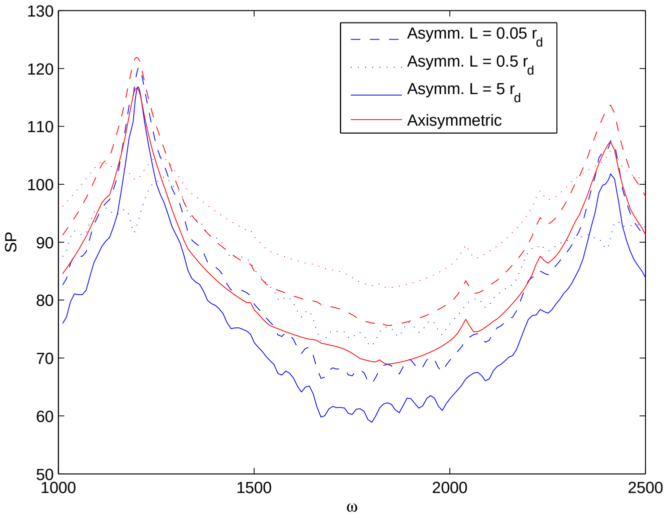

Figure 4.13: As in the figure above we have plotted, in blue, the SP as radiated from a single rotor which experiences an asymmetric inflow, this time as L is varied. Shown in red are the equivalent axisymmetric levels.

In Figure 4.14 we have compared two different values of d, thus varying the level of asymmetry. In the case of increased d, both the high and low distortion cases are similar, whereas for a medium level of distortion we see a lowering of the tonal peak at 1 BPF and an increase in broadband level.

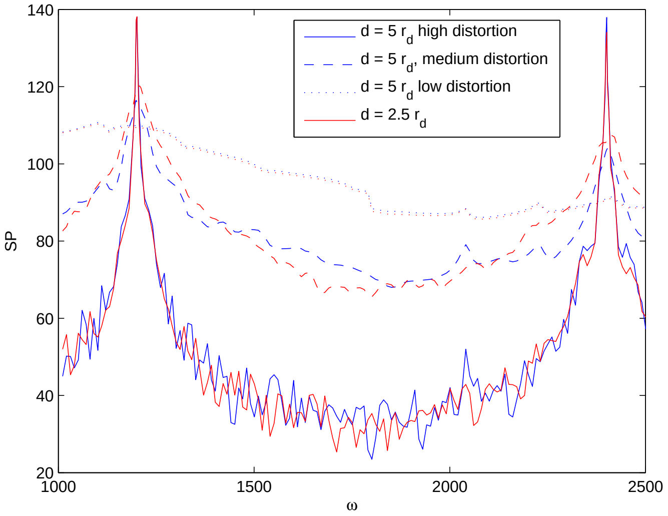

Figure 4.14: In blue is shown the radiated sound from a single rotor with an asymmetric inflow due to two actuator disks separated by a distance $d = 5r_d$. The case $d = 2.5r_d$, which is more highly asymmetric and was also plotted in blue in Figure 4.12, is shown in red for comparison. We see that the level is most affected by asymmetry in the medium distortion case.

4.5.3 Sound from two adjacent rotors

Thus far in this chapter we have calculated the sound as radiated from one rotor only, that at the origin, where the inflow to that rotor was asymmetric. We can also obtain an expression for the far-field pressure generated by the two rotors side by side by superposing two single rotor solutions. To leading order in the far-field, within the expression for pressure, we only need adjust the observer position in the frequency phase term, $e^{\frac{i\omega\sigma}{c_0}}$, in the Green's function, which we recall is given by

$$H^{l,m}\left(\sigma_0,\theta;x_s,r_s\right) \sim \frac{e^{i\frac{\omega}{c_0}\sigma_0}}{4\pi\sigma_0\left(1-M\cos\theta\right)}\left(-2\pi\right)J_{m+lB}\left(\gamma_0 r_s\right)e^{i\frac{\omega\cos\theta}{c_0\left(1-M\cos\theta\right)}x_s}e^{-\frac{i(m+lB)\pi}{2}}. \tag{4.36}$$

Terms in the amplitude which depend upon observer position decay much more rapidly in the far field, and the same far-field coordinates can be used for both rotors.

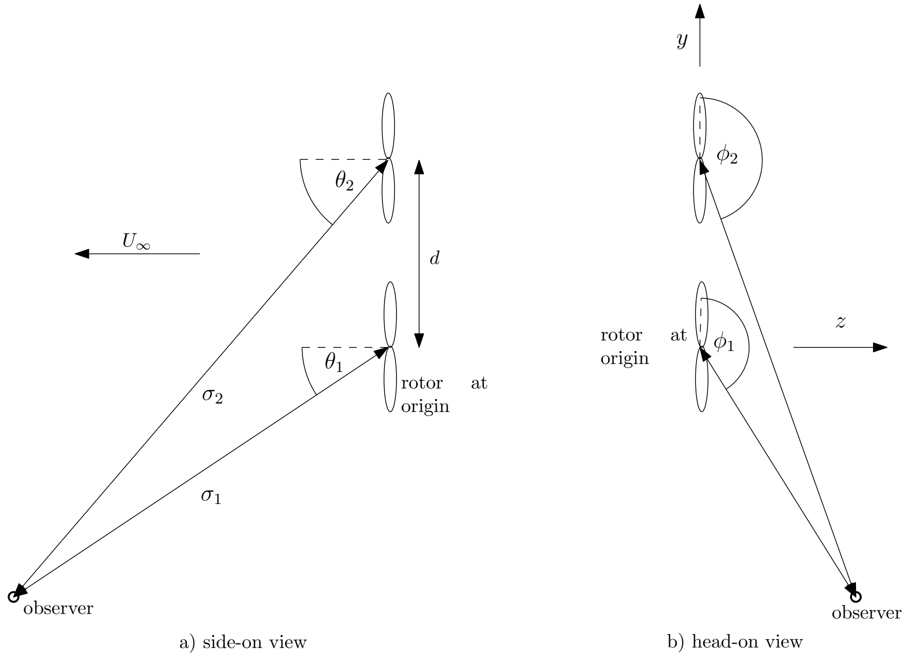

Figure 4.15: The far-field observer coordinate system, for two adjacent rotors.

The observer's position with respect to the rotor centred at the origin is given in spherical polars by $(\sigma_1, \theta_1, \phi_1)$, as shown in Figure 4.15, and we require an expression for the distance of the observer from the second rotor, σ_2, in terms of $(\sigma_1, \theta_1, \phi_1)$. The cartesian distances from the observer to the second rotor are given by

$$x_2 = \sigma_1 \cos\theta_1, \tag{4.37}$$

$$y_2 = \sigma_1 \sin\theta_1 \cos\phi_1 + d, \tag{4.38}$$

$$z_2 = \sigma_1 \sin\theta_1 \sin\phi_1. \tag{4.39}$$

Combining to give σ_2^2 we find

$$\begin{aligned}\sigma_2^2 &= x_2^2 + y_2^2 + z_2^2 \\ &= \sigma_1^2 + 2d\sigma_1 \sin\theta_1 \cos\phi_1 + d^2. \end{aligned} \tag{4.40}$$

Thus, to first order in d/σ_1, the distance of the observer from the second rotor is

$$\sigma_2 \approx \sigma_1 + d \sin\theta_1 \cos\phi_1, \tag{4.41}$$

and we substitute this into the $e^{\frac{i\omega\sigma_2}{c_0}}$ factor of the sound pressure due to the second rotor. As $\sigma_1 \to \infty$, we have $\theta_2 \to \theta_1$ and $\phi_2 \to \phi_1$, and thus no changes need be made to the θ and ϕ terms.

The properties of each of the two rotors (radius, strength, angular velocity) may of course vary - U_∞ will necessarily be the same. We consider here the case of identical rotors, and for completeness give the full general solution in Appendix C.

Identical rotors - co-rotation

If both rotors have the same properties, including $\Omega_1 = \Omega_2$, then only the observer's distance from the rotor will need to be adjusted. Thus the pressure field due to two rotors is

$$\begin{aligned} p_{2\mathrm{r}}(\sigma_1, \theta_1, \phi_1) &= p(\sigma_1, \theta_1, \phi_1; \Omega_1, r_{d1}, U_{d1}) + p(\sigma_1 - d\sin\theta_1\cos\phi_1, \theta_1, \phi_1; \Omega_1, r_{d1}, U_{d1}) \\ &= p_1(\sigma_1, \theta_1, \phi_1) + \exp\left[\frac{i\omega d\sin\theta_1\cos\phi_1}{c_0}\right] p_2(\sigma_1, \theta_1, \phi_1). \end{aligned} \tag{4.42}$$

Here we have denoted the pressure fields due to each rotor by p_1 and p_2. This is because, within the expression for p, the quantity $u_j^\infty(\mathbf{x}')$ occurs in the force term, as was seen in equation (4.34). This upstream field, u_j^∞, will be different for p_1 and p_2, as each rotor experiences a different inflow of turbulence. We can recognise this by using the notation $u_{1,j}^\infty(\mathbf{x}')$ and $u_{2,j}^\infty(\mathbf{x}')$ within p_1 and p_2 respectively. However, when the cross-correlation is taken between $u_{1,j}^\infty(\mathbf{x}')$ and $u_{2,j}^\infty(\mathbf{x}')$ (or the cross-correlation of either field with itself) we regain the same turbulence spectrum, S_{ij}^∞, as both fields originate in the same region far upstream.

When calculating $\hat{P}$ in the single rotor case, complex conjugation meant the exponential terms $e^{\frac{i\omega\sigma}{c_0}}$ cancelled out, but now we obtain two cross terms where it does not cancel and thus

$$\begin{aligned} \hat{P}_{2\mathrm{r}}(\mathbf{x}, \omega) &= \int_{-\infty}^{\infty} \langle p_{2\mathrm{r}}^*, p_{2\mathrm{r}} \rangle \, e^{i\omega\tau} d\tau \\ &= \left(2 + 2\cos\left(\frac{\omega d\sin\theta_1\cos\phi_1}{c_0}\right)\right) \hat{P}(\mathbf{x}, \omega). \end{aligned} \tag{4.43}$$

To plot the Sound Pressure Level (SPL) directivity we calculate the expression given in equation (4.35) with $m \neq m'$ for one particular frequency, such as 1 BPF. (See Appendix

B for the definition of SPL.) In Figure 4.16 we have plotted the (single rotor) directivity at a range of distortion levels for two different values of separation distance d. We see that the highest noise level is straight ahead of the rotor, due to the presence of zeroth order Bessel functions in our radiated sound expression.

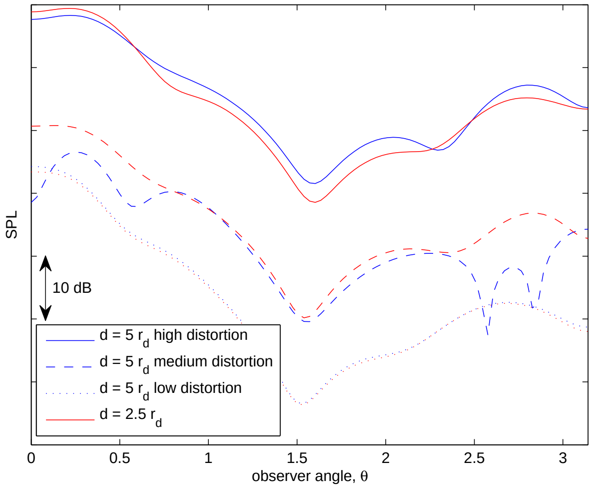

Figure 4.16: Directivity patterns for a single rotor for the frequency $\omega = 1$ BPF, at a variety of distortion levels. In blue are shown the patterns when $d = 5r_d$, in red are the patterns for a more asymmetric mean flow when $d = 2.5r_d$. Absolute levels have not been given in this case, as they will depend upon the observer's distance from the rotor, σ_0.

Figure 4.17 then compares the UDN radiated from both rotors together, as given in (4.42), against the UDN radiated from a single rotor. Directly beneath the rotors, at $\phi = \pi/2$, the sound simply adds (the argument of the cosine function becomes zero in equation (4.43)), but out to the sides at $\phi = 0$ (or π) we find a significantly altered directivity pattern due to interference when $\cos\phi_1 = \pm 1$. The sound level directly ahead and behind the rotors is raised and the sound level for a section underneath the flight path is reduced.

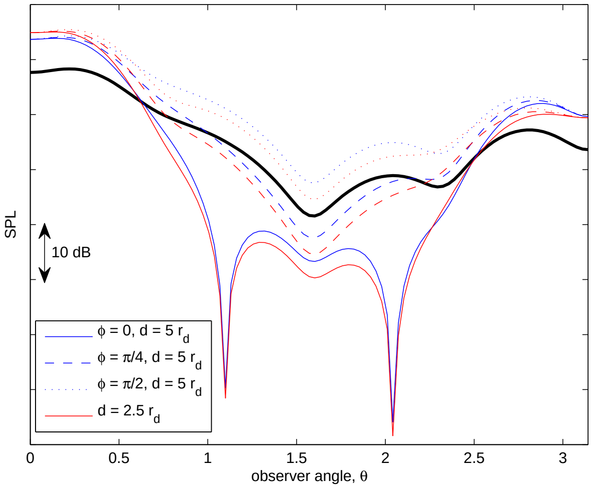

Figure 4.17: Directivity patterns for the twin rotor system, for the frequency $\omega = 1$ BPF, at three different azimuthal positions. Again both the $d = 5r_d$ and $d = 2.5r_d$ cases are plotted. Shown in black is the single rotor case.

Chapter 5

Rotor at incidence: *an important asymmetric case*

5.1 Chapter outline

At the start of this Ph.D. one of the questions we asked was: what might the effect of asymmetry due to incidence be on both the distortion of turbulence and the subsequent radiation of UDN to the far-field? As a first step towards investigating this, in Chapter 4 we considered a more straightforward system in which the distortion is asymmetric (due to an asymmetric mean flow) but the radiation is calculated for a rotor travelling in the direction of its axis, as in Chapters 2 and 3. In this chapter, we consider the full case of UDN for a rotor at incidence.

Our model must be altered in a number of ways, in particular the mean flow streamlines, and the appropriate Green's function.

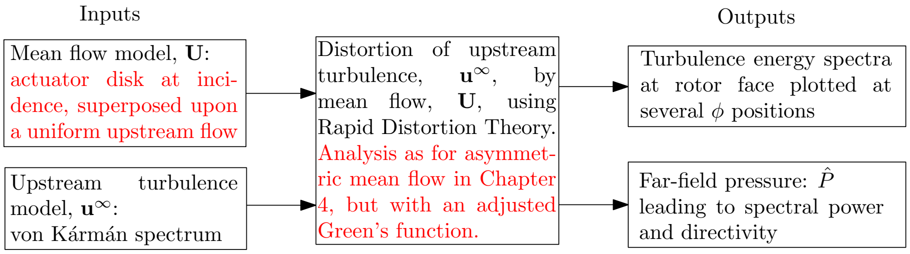

5.2 Effects of incidence

In reality, most aeroplane engines operate at 'incidence', that is with their shaft at some non-zero angle to the flight direction, for some periods during flight; incidence typically being highest during take-off. For AOR engines, incidence is significantly increased in the puller configuration (as compared to the pusher) due to the proximity of the wing which induces an altered mean flow upstream of the rotors. In addition, AOR driven aircraft can climb and descend more steeply than turbofan driven aircraft (high blade stresses being a limiting factor for the latter) which also increases incidence. The effect of incidence is often neglected in theoretical work as the assumption of axisymmetry simplifies the analysis. It is standard procedure to assume sound radiates into a uniform flow parallel to the rotor's axis, and this is the approach we employed in previous chapters.

Incidence could potentially affect UDN levels in several ways. Firstly, the mean flow is altered, and thus the distortion of turbulence will differ from the axisymmetric case. Secondly, the location where each turbulent eddy hits the blades will vary. Thirdly, the blade response will change. Fourthly, the sound now radiates into an angular inflow. In the model presented here we do not consider the effect of incidence upon blade response. We continue to assume zero mean blade loading, as this is one of the modelling assumptions within the LINSUB theory. Authors who have considered angle of attack effects on blade response include Myers and Kerschen (1995) and Peake and Kerschen (1997). Incorporating a different blade response function into our framework could be an area for future model development.

Incidence mainly affects the sound radiated from the front rotor, and we continue to assess the UDN produced by the front rotor only, as in previous chapters.

5.2.1 Previous work on non-zero incidence

Little work has been done previously on the effect of incidence upon the process of turbulence distortion, with most authors concentrating on the effect of angle of attack upon a blade's response to isotropic turbulence.

In a recent example, Devenport et al. (2010) undertook a series of experiments upon a single blade in isotropic turbulence, and found that angle of attack effects upon the resulting sound spectrum were small. This was due to significant cancellation between components with varying k_2, the wavenumber in the direction of lift. This finding is consistent with that of Paterson and Amiet (1976), who showed that for incompressible flows (i.e. for low frequencies) it is the component of an incident gust in the direction of the blade normal which induces the unsteady response, and this will be proportional to angle of attack, which is typically small. For anisotropic turbulence however, blade response is expected to vary more significantly with angle of attack, due to a reduced level of cancellation, although this may not necessarily result in a significantly altered noise spectrum.

Mish and Devenport (2006a) had previously examined angle of attack effects, again for a blade immersed in grid-generated (and therefore close to isotropic) turbulence, but with particular consideration of the eddy stretching which takes place at the leading edge of the blade. Their measurements of surface pressure showed a lack of dependence on angle of attack, and they concluded that the additional eddy stretching due to incidence in the leading edge region does not significantly affect the intensity of pressure fluctuations. They suggested that incidence effects would only be significant for turbulence of a small scale compared to the airfoil chord. Within our model we can now include the altered eddy stretching due to incidence not just in the leading edge region, but throughout the full upstream flow.

Paterson and Amiet (1976, 1982) noted that non-zero incidence can shift the dominant frequency of turbulence ingestion noise away from multiples of BPF, due to the change in azimuthal position at which each eddy passes through the rotor. The effect of non-convected turbulence, such as random wanderings due to a non-uniform inflow, was found to be a reduction in tonal peaks and an increase in their widths.

The effect of incidence upon radiation to the far-field was considered in detail by Hanson (1995), and we follow his framework for our coordinate system in order to use his form of Green's function. Hanson noted that authors considering the problem of a rotor whose shaft is at some non-zero angle of attack previously had assumed that the resultant unsteady loading would be the dominant effect, rather than radiation into a non-axial flow field. In fact, as his paper confirmed, flow angularity can be more significant than unsteady loading in certain cases.

5.3 Distortion of turbulence by rotor at incidence

5.3.1 Adapting the mean flow model

We wish to model the streamtube contraction induced by a rotor placed at a non-zero angle, α, to the flight direction. The set-up is shown in Figure 5.1.

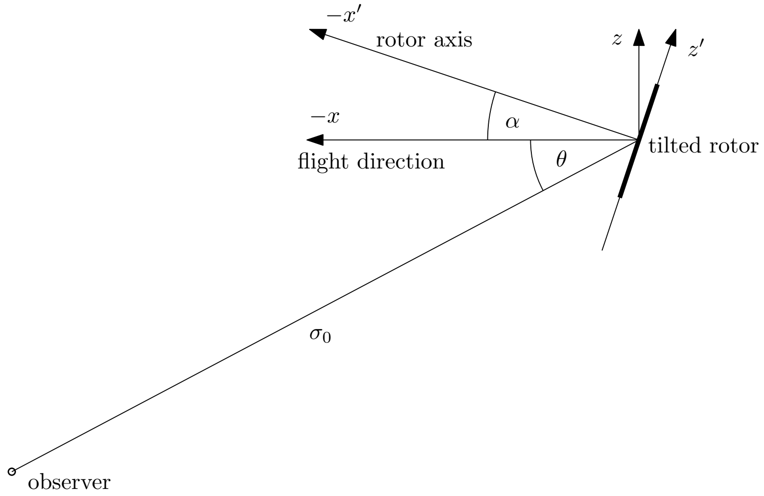

(a) Side on view. The angle between the flight direction and the vector between the rotor origin and the observer is denoted by θ. We denote the angle between the rotor axis and vector between rotor origin and the observer by θ'. Note that $\theta' \neq \theta + \alpha$, in general.

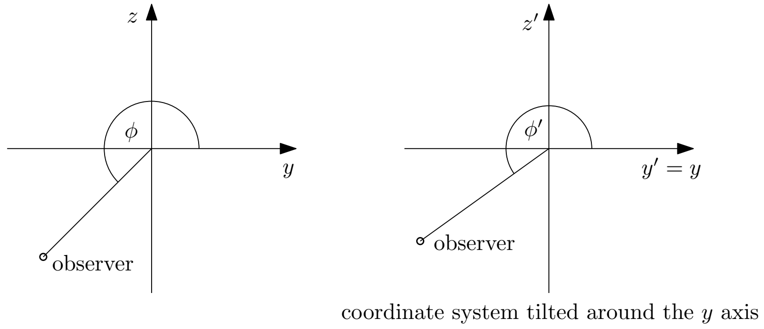

(b) Head-on view.

Figure 5.1: Coordinate system of interest, after Hanson (1995), except the directions of both the positive x and x' axes have been reversed. Note that in this chapter, ϕ' denotes the azimuthal coordinate in the tilted system, not in the rotating frame, as it did in Chapter 2.

The tilted coordinates (denoted by primes) are related to the flight-direction coordinates via

$$\begin{aligned}
x' &= x\cos\alpha - z\sin\alpha, \\
y' &= y, \\
z' &= x\sin\alpha + z\cos\alpha, \\
r'^2 &= y'^2 + z'^2, \\
\tan\phi' &= \frac{z'}{y'}.
\end{aligned} \tag{5.1}$$

We construct the new flow by superposing an actuator disk flow in the $\mathbf{x}'$ coordinate system, on top of the flight component $U_\infty \hat{\mathbf{e}}_\mathbf{x}$, which tends to $U_\infty \cos\alpha \hat{\mathbf{e}}_{\mathbf{x}'}$ as $x' \to -\infty$. We neglect the interaction between the cross-wind component of the flight speed, $U_\infty \sin\alpha \hat{\mathbf{e}}_{\mathbf{z}'}$, and the actuator disk flow. This approximation will be valid when α is sufficiently small, or when the strength of the actuator disk is sufficiently high. As given in Chapter 1, for the pusher configuration of AOR, $|\alpha|$ is typically less than 3° (negative values of α can occur during approach) whereas in the puller configuration the maximum value of $|\alpha|$ is of the order of 15°. Therefore the cross-wind component will be dominated by the axial component in the parameter regimes of interest to us.

The mean flow field is therefore given by

$$\mathbf{U}\cdot\hat{\mathbf{e}}_\mathbf{x} = U_\infty + U_x^{\text{inc.}}(x,y,z) = U_\infty + U_x(x',y',z')\cos\alpha + U_r(x',y',z')\sin\phi'\sin\alpha, \tag{5.2}$$

$$\mathbf{U}\cdot\hat{\mathbf{e}}_\mathbf{y} = U_y^{\text{inc.}}(x,y,z) = U_r(x',y',z')\cos\phi', \tag{5.3}$$

$$\mathbf{U}\cdot\hat{\mathbf{e}}_\mathbf{z} = U_z^{\text{inc.}}(x,y,z) = -U_x(x',y',z')\sin\alpha + U_r(x',y',z')\sin\phi'\cos\alpha, \tag{5.4}$$

where (U_x, U_r) is an axisymmetric actuator disk flow as given in equations (2.47) and (2.48), with strength

$$U_d' = \frac{T}{\pi r_d^2 \rho_0 (U_\infty \cos\alpha)}. \tag{5.5}$$

Figure 5.2 shows some representative plots of the streamlines for this tilted actuator disk set-up.

5.3.2 Distorted turbulence spectrum

In Figures 5.3 - 5.7 the axial component of the distorted turbulence spectrum has been plotted for a range of positions at the tilted rotor face, and at a number of distortion

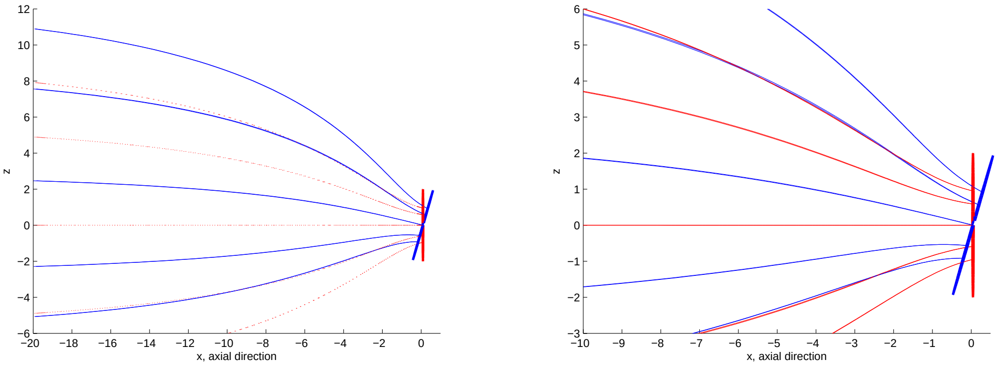

(a) (b)

Figure 5.2: a) In blue are shown the streamlines induced by the tilted actuator disk system. Also shown for comparison are the axisymmetric streamlines (in red). The position of the disk in each case is shown by a bold line. Total thrust, T, is kept constant between the two cases. b) A zoomed-in view nearer the disk.

levels. In the first four figures we have taken $\alpha = \pi/12$ rad $= 15^\circ$. We see in Figures 5.3 and 5.4 that, as before, the spectrum level is greater at the blade tip than the hub in all circumstances.

From Figure 5.2 (the plot of the streamlines at incidence) we see that the tilting of the actuator disk increases the streamtube contraction in the region $\phi' = \pi/2$ (where the disk is tilted away from the negative x axis) and decreases it in the region $\phi' = 3\pi/2$ (where the disk is tilted toward the negative x axis). Correspondingly, the spectrum level is highest at $\phi' = \pi/2$ in all cases, as seen in Figures 5.5 and 5.6 which show the variation of S_{xx} with ϕ' for two different sets of parameters.

Finally, in Figure 5.7 we vary the angle of incidence, α. Interestingly, as α increases the variation of the turbulence spectrum with ϕ' decreases. It is for small, but non-zero, values of α that we have the greatest azimuthal variation. This is explained by considering that as α is increased, and the radial position of interest r' is kept constant, then the variation in radial position, r, as we move around the disk decreases.

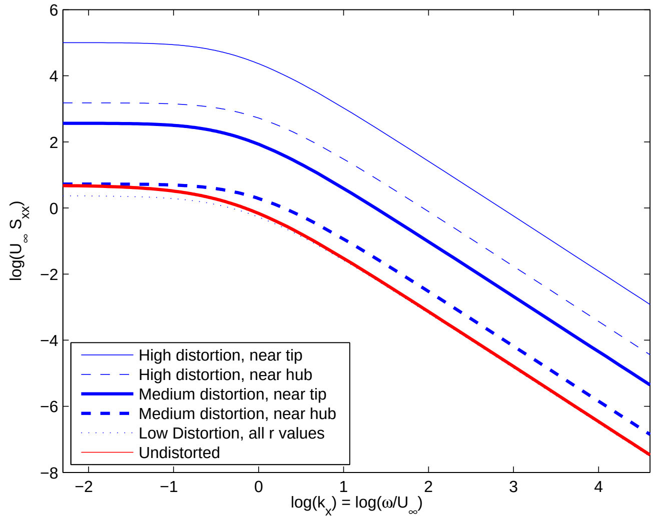

Figure 5.3: Here we show the spectrum at $\phi' = \pi/2$ for a range of distortion levels and radial positions. The level near the tip is higher than that near the hub in all cases, and as distortion is decreased the level also decreases. We have collapsed the data by multiplying S_{xx} by U_∞.

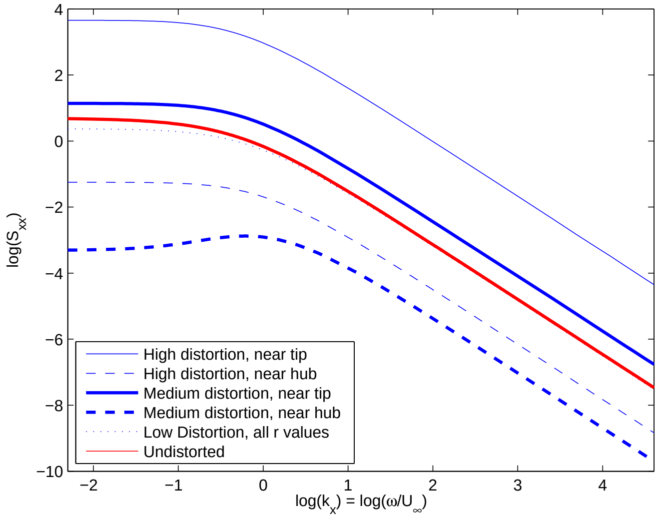

Figure 5.4: Plot as in Figure 5.3, but at $\phi' = 3\pi/2$. The spectrum levels at the hub and tip are now further apart than in the $\phi' = \pi/2$ case. Interestingly, the dependence on distortion level is now more complex, with the low distortion case lying between the high and medium cases.

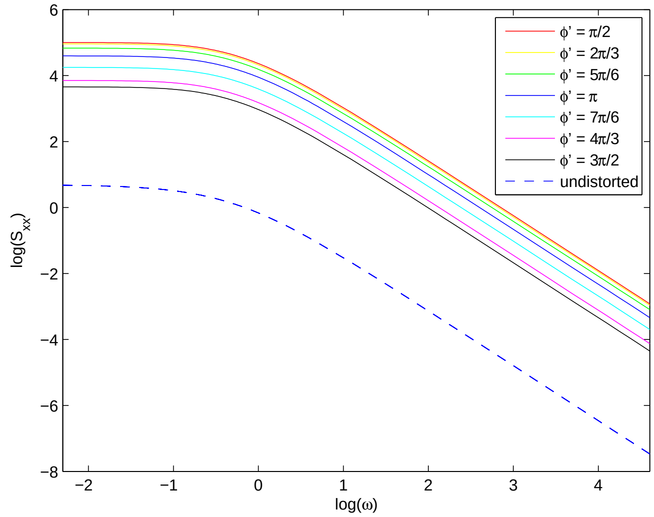

Figure 5.5: Here we have calculated S_{xx} in the high distortion case near the rotor tip ($r'/r_d = 0.9$), at a range of azimuthal positions. We see that the energy level is higher than the undistorted spectrum in all cases. As we move from $\phi' = \pi/2$ (rotor tilted away from -ve x axis) to $\phi' = 3\pi/2$ in equal increments of ϕ', the levels are fairly evenly spaced.

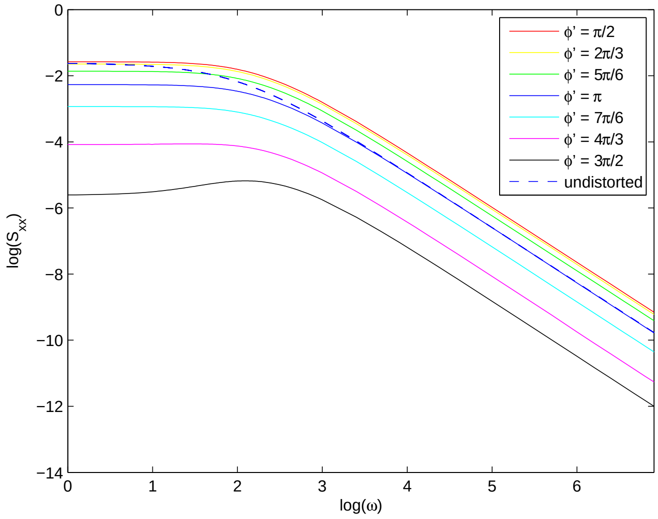

Figure 5.6: Here we show a medium distortion case near the rotor hub ($r'/r_d = 0.4$). The energy level is below that of the undistorted spectrum in most cases, but not all (as was the case for the asymmetric flow in Chapter 4). We also see a peak in the $\phi' = 3\pi/2$ spectrum not present in the other spectra.

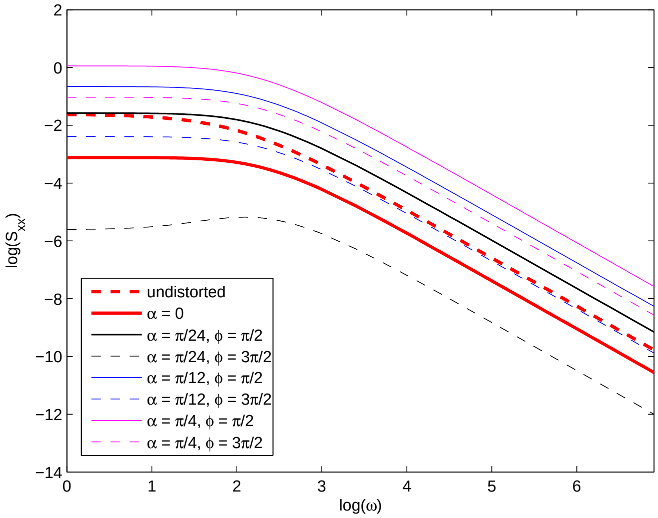

Figure 5.7: Here we have adjusted α, the angle of rotor incidence. We see that as α is increased, the spectral levels increase. However, perhaps surprisingly, the variation with ϕ' decreases.

5.4 Far-field noise calculation

In re-deriving the expression for far-field sound pressure, we must first re-derive the forcing term, before adjusting the appropriate Green's function.

5.4.1 Adjusting the force term

The total force exerted by the rotor on the fluid, $\mathbf{f}$, is simplest to define as a function of the tilted (primed) coordinates. We wish to obtain expressions for the components of $\mathbf{f}$ in the $\hat{\mathbf{e}}_{\mathbf{x}'}$ and $\hat{\mathbf{e}}_{\phi'}$ directions, in order to use both LINSUB and Hanson's form of Green's function. Hanson's analysis is given for a point source representation of blade loading and we extend his theory here by integrating over the full blade planform, finding we are able to perform the integral over the azimuthal source position, ϕ'_s, explicitly.

An upstream gust which impinges upon the leading edge of the rotor blades, with wavevector component $\mathbf{k}$ and constant amplitude $\hat{\mathbf{u}}^\infty$ gives rise to a force on the fluid in the $\hat{\mathbf{e}}_{\mathbf{x}'}$ direction as follows

$$\begin{aligned} f^k_{x'}\left(x', r', \phi', t\right) = &\sum_{b=1}^{B} \rho_0 W \sin\beta(r') \exp\left(-ik_x U_\infty t\right) \sum_{m=-\infty}^{\infty} \Gamma^m_{WW}\left(x', r'; k_x, \chi^m\right) \\ & e^{ik_x X} \sum_{p=-\infty}^{\infty} J_{m-p}\left(r_k R\right) \exp\left(-im\phi_k\right) D'^p_j\left(x_0(r'), r'; k_x, r_k, 0\right) \\ & \hat{u}^\infty_j\left(\mathbf{k}\right) \exp\left(im\left[\phi_0(r') + \frac{2b\pi}{B} + \Omega t\right]\right) \\ & \sum_{s=-\infty}^{\infty} \delta\left[r'\left(\phi' - \Omega t - \phi_0(r') - \frac{2b\pi}{B}\right) - \left(x' - x_0(r')\right)\tan\beta(r') - 2\pi s\right]. \end{aligned} \tag{5.6}$$

In this expression, both the normal to the blade, $\mathbf{N}'$, and the delta function which defines the blades' surfaces are given in the primed coordinate system. The $f^k_{\phi'}$ component is defined similarly, with $\sin\beta(r')$ replaced by $\cos\beta(r')$. (We neglect the radial component of the cross-wind term, $U_\infty \sin\alpha \hat{\mathbf{e}}_{\mathbf{z}'}$, in our calculation of the blade normal for the unleant blades assumed here.)

The distortion amplitude A_{ij} is contained within the quantities D'^p_j, where D'^p_j is based upon C'^p_{ij} in precisely the equivalent way as in Chapter 2 (equation (2.82)). This latter quantity is defined as

$$C'^p_{ij}\left(x', r'; \mathbf{k}\right) = \frac{1}{2\pi}\int_0^{2\pi} A_{ij}\left(x', r'; \mathbf{k}\right) e^{-ip\phi'} d\phi'. \tag{5.7}$$

Note that X, Y and Z within the definition of A_{ij} remain the upstream coordinates in the non-primed system; X', Y' and Z' do not tend to constant values as $x \to -\infty$.

The blade angle β is defined as follows

$$\tan\beta\left(r'\right) = \frac{\Omega r'}{U_\infty \cos\alpha + \frac{U'_d}{2}} = \frac{\Omega r'}{U_\infty \cos\alpha + \frac{U_d}{2\cos\alpha}}. \tag{5.8}$$

We hold the total thrust induced by the actuator disk, T, and the flight speed, U_∞, constant when comparing the axisymmetric and incidence models, which leads to our definition of U'_d in equation (5.5). This model differs from that of Wright (2000) who also considered the case of an angular inflow into a propeller (with no turbulence present) but held the magnitude of the cross-wind component at the rotor face constant instead, given by $U'_d/\cos\alpha$ in our set-up. In Figure 5.8 we have plotted the blade angle β as a function of rotor incidence angle α for a range of U_∞ values, holding $U_f = U_\infty + U_d/2$ constant. We see that for the parameter space of interest to us, small α, the low and high distortion cases behave differently. For the high distortion case β decreases with α, whereas for the low distortion case β increases with α.

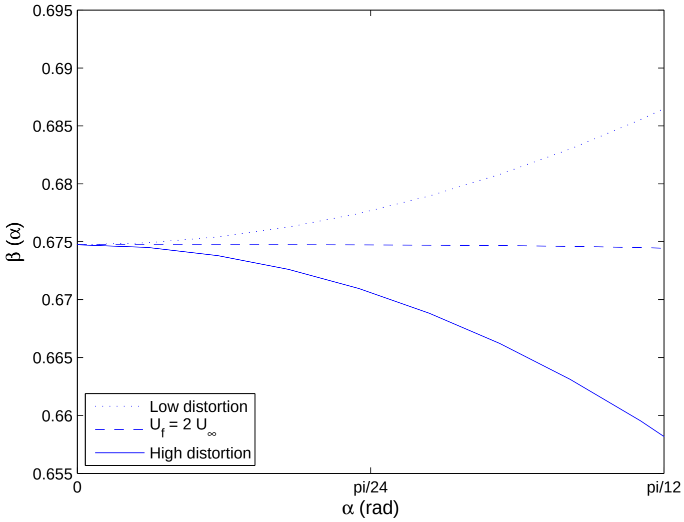

Figure 5.8: Blade angle β plotted as a function of rotor incidence α, for $r'/r_d = 0.4$. When U_f is twice U_∞ we have $U_\infty = U_d/2$, and the two $\cos\alpha$ factors nearly balance each other for a large range of α values (up to around $\alpha = 0.7$ rad).

To obtain the total axial force, $f_{x'}$, we integrate $f^k_{x'}$ over all $\mathbf{k}$. We separate out t and ϕ' dependence explicitly within $f_{x'}$, following the same method as in Chapter 2, to find

$$\begin{aligned} f_{x'}\left(x',r',\phi',t\right) =& \rho_0 W \sin\beta(r') \frac{B}{2\pi r} \sum_{m=-\infty}^{\infty} \frac{1}{(2\pi)^3} \int_{\Re^3} \Gamma^m_{WW}\left(x',r';k_x,\chi^m\right) \exp\left(-ik_x U_\infty t\right) \\ & e^{ik_x X} \sum_{p=-\infty}^{\infty} J_{m-p}\left(r_k R\right) \exp\left\{-im\phi_k\right\} D'^p_j\left(x_0(r'),r';k_x,r_k,0\right) \\ & \left[\int_{\Re^3} u^\infty_k\left(\mathbf{y}\right) \exp\left(-i\mathbf{k}\cdot\mathbf{y}\right) d^3\mathbf{y}\right] d^3\mathbf{k} \\ & \sum_{l=-\infty}^{\infty} \exp\left(i\left(m+lB\right)\left[\frac{\left(x'-x_0(r')\right)\tan\beta(r')}{r'}\right]\right) \exp\left(-ilB\phi_0(r')\right) \\ & \exp\left(-ilB\Omega t\right) \exp\left(i\left[m+lB\right]\phi'\right). \end{aligned} \tag{5.9}$$

5.4.2 Adjusted Green's function

In Chapter 2, when solving the wave equation, we derived the form of Green's function used for a rotor translating in the direction of its axis. Here, we will instead derive the Green's function for a rotor travelling at some non-zero angle of attack to its axis. This was calculated by Hanson (1995) for a point source representation of blade loading, and we give an outline of his analysis here (noting once again that Hanson used the opposite sign convention for the positive x axis) and proceed to cast the Green's function into the equivalent form to that used previously in our analysis.

We recall that in Chapter 2 the wave equation was given in the form

$$\nabla^2 p - \frac{1}{c_0^2}\left(\frac{\partial}{\partial t} + U_\infty \frac{\partial}{\partial x}\right)^2 p = \nabla \cdot \mathbf{f}\left(\mathbf{x}, t\right) = -\sum_{\omega} Q_\omega\left(x, y, z\right) e^{-i\omega t}, \tag{5.10}$$

with solution

$$p\left(x, y, z, t\right) = \sum_{\omega} P_\omega\left(x, y, z\right) e^{-i\omega t}. \tag{5.11}$$

In addition to t dependence, in equation (5.9), we have separated out ϕ' dependence explicitly within $\mathbf{f}$. Thus we have

$$\begin{aligned} Q_\omega\left(x, y, z\right) &= -\sum_{l,m,p=-\infty}^{\infty} \nabla \cdot \left(\mathbf{N}' F^{l,m,p} e^{im\phi'}\right) \\ &= -\sum_{l,m,p=-\infty}^{\infty} \left[\sin\beta(r')\frac{\partial F^{l,m,p}}{\partial x'} + \frac{\cos\beta(r')}{r'} imF^{l,m,p}\right] e^{im\phi'}, \end{aligned} \tag{5.12}$$

where $F^{l,m,p}$ is the appropriate (l, m, p) component of (5.9) and we have applied ∇ directly in (x', y', z') coordinates.

In the tilted system, Hanson finds the following solution

$$\begin{aligned} P_\omega\left(\sigma_0, \theta', \phi'\right) = \frac{e^{\frac{i\omega\sigma_0}{c_0}}}{4\pi\sigma_0\left(1 - M\cos\theta\right)} \int_0^{r_d}\int_{-\infty}^{\infty}\int_{-\pi}^{\pi} Q_\omega\left(x'_s, r'_s, \phi'_s\right) \\ \exp\left[\frac{-i\omega}{c_0\left(1 - M\cos\theta\right)}\left(x'_s\cos\theta' + r'_s\sin\theta'\cos\left(\phi' - \phi'_s\right)\right)\right] r'_s d\phi'_s dx'_s dr'_s, \end{aligned} \tag{5.13}$$

where we integrate over the source coordinates (x'_s, r'_s, ϕ'_s). The changes here from the standard representation of the Green's function are only in the phase term; in the far-field, the amplitude terms are the same to leading order. The form is identical to that found in Chapter 2 with θ' and ϕ' replacing θ and ϕ, except that the non-primed θ appears in the $1/\left(1 - M\cos\theta\right)$ Doppler factors. We can express θ in terms of primed coordinates as follows

$$\cos\theta = \cos\theta'\cos\alpha - \sin\theta'\sin\phi'\sin\alpha. \tag{5.14}$$

We note again that $\theta' \neq \theta + \alpha$ in general, but equality does hold when $\phi' = \pi/2$. The Green's function, as compared to equation (2.126), is therefore given by

$$H'^{l,m}\left(\sigma_0, \theta'; x'_s, r'_s\right) \sim \frac{e^{i\frac{\omega}{c_0}\sigma_0}}{4\pi\sigma_0\left(1 - M\cos\theta\right)}\left(-2\pi\right)J_{m+lB}\left(\gamma'_0 r'_s\right)e^{i\frac{\omega\cos\theta'}{c_0(1-M\cos\theta)}x'_s}e^{-\frac{i(m+lB)\pi}{2}}, \tag{5.15}$$

where $\gamma'_0 = \omega\sin\theta'/c_0\left(1 - M\cos\theta\right)$.

5.4.3 Correlation of far-field pressure

The Power Spectral Density is thus given by

$$\begin{aligned}
\hat{P}^{\text{inc.}}\left(\sigma_0,\theta',\phi',\omega\right) = {} & \rho_0^2 \frac{B^2}{4\pi^2 U_\infty} \frac{1}{4\sigma_0^2\left(1-M\cos\theta\right)^2} \\
& \sum_{l,m,m'} \int_{r'_s,x'_s} \left[J_{m+lB}\left(\gamma'_0 r'_s\right)\right]^* \left[W(r'_s)\Gamma_{WW}^{m}\left(x'_s,r'_s;\omega\right)\right]^* \\
& \left[\frac{i\omega\cos\theta'\sin\beta(r'_s)}{c_0\left(1-M\cos\theta\right)} - \frac{i(m+lB)\cos\beta(r'_s)}{r'_s}\right] \\
& \exp\left\{\frac{-i\omega\cos\theta' x'_s}{c_0\left(1-M\cos\theta\right)} + i(m+lB)\frac{\left[x'_s - x_0(r'_s)\right]\tan\beta(r'_s)}{r'_s} + ilB\phi_0(r'_s)\right\} \\
& \int_{r''_s,x''_s} J_{m'+lB}\left(\gamma'_0 r''_s\right) W(r''_s)\Gamma_{WW}^{m'}\left(x''_s,r''_s;\omega\right) \\
& \left[-\frac{i\omega\cos\theta'\sin\beta(r''_s)}{c_0\left(1-M\cos\theta\right)} + \frac{i(m'+lB)\cos\beta(r''_s)}{r''_s}\right] \\
& \exp\left\{\frac{i\omega\cos\theta' x''_s}{c_0\left(1-M\cos\theta\right)} - i(m'+lB)\frac{\left[x''_s - x_0(r''_s)\right]\tan\beta(r''_s)}{r''_s} - ilB\phi_0(r''_s)\right\} \\
& \sum_{p,p'} \int_{\Re} \widetilde{D}_j^{m,p*}\left(x_0(r'_s),r'_s;k_x,r_k,0\right) \widetilde{D}_k^{m',p'}\left(x_0(r''_s),r''_s;k_x,r_k,0\right) \\
& \left[\int_0^{2\pi} e^{i(m+p-m'-p')\phi_k} S_{kl}^{\infty}\left(\mathbf{k}\right) d\phi_k\right] r_k dr_k dr''_s dx''_s dr'_s dx'_s e^{i(m'-m)\left(\phi'-\frac{\pi}{2}\right)}.
\end{aligned} \tag{5.16}$$

Since ϕ' now appears within θ, the ϕ' integral is no longer straightforward. This increases the time it takes to numerically compute SP for each frequency ω.

5.4.4 SP and SPL plots

In Figure 5.9 we have plotted the SP for a rotor at angle of incidence $\alpha = \pi/12$, compared to the axisymmetric case. We see similar effects as in the asymmetric case considered in Chapter 4, namely a decreased broadband level in the high distortion case and an increased broadband level around 1 BPF in the low distortion case. New effects due to incidence include an increased width peak at 1 BPF in the high distortion case, and a significant increase in peak tonal level in the medium distortion case. As α decreases these effects are found to diminish.

In Figures 5.10, 5.11 and 5.12 we have plotted the directivity. As expected, the level

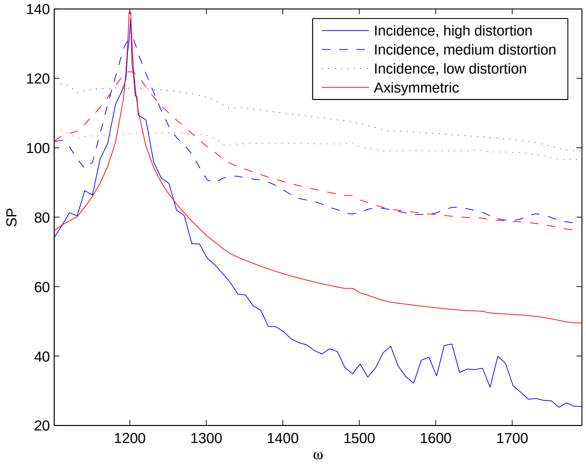

Figure 5.9: In blue are plotted the SP as radiated from a rotor at incidence, for varying distortion levels. Shown in red are the equivalent axisymmetric levels.

is significantly lower away from multiples of BPF in the high distortion case. In Figure 5.11 we see the variation of the directivity as ϕ' changes. This is due to Hanson's adjusted Doppler factors, as well as the effect of non-zero incidence upon the distortion. In Figure 5.12 we see that the variation with α is marginally greater at $\phi' = \pi/2$, that is on the side of the rotor which is tilted away from the flight direction.

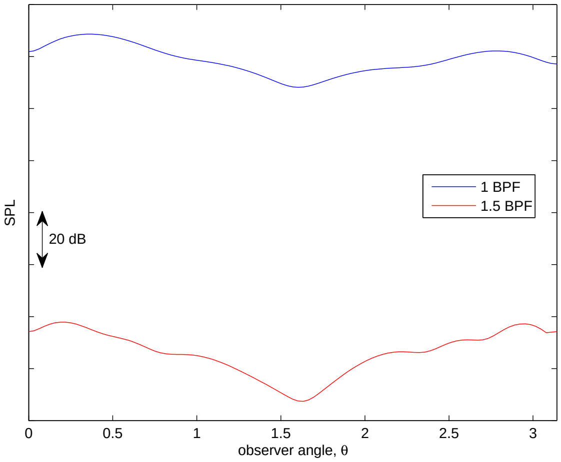

Figure 5.10: Directivity patterns for a rotor at incidence for the high distortion case, at two different frequencies.

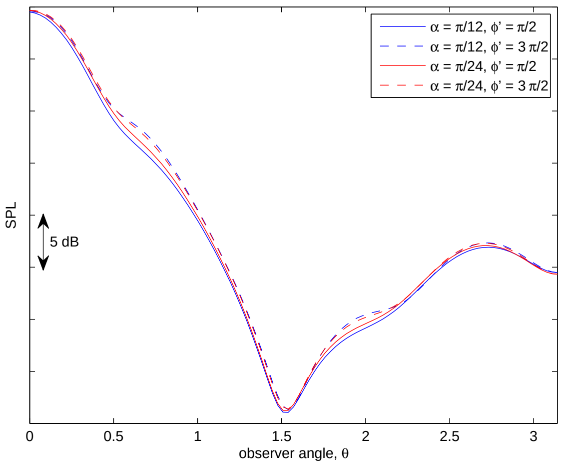

Figure 5.11: Directivity patterns for a rotor at two different angles of incidence, and at two different azimuthal positions, for the frequency $\omega = 1$ BPF.

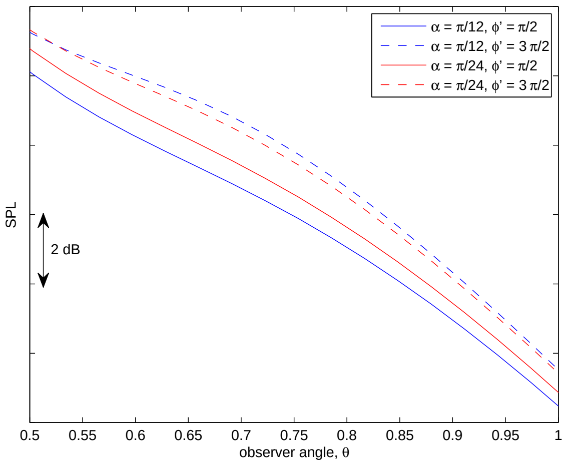

Figure 5.12: Zoomed-in plot of Figure 5.11 above, showing the variation with α at the two extremal azimuthal positions, $\phi' = \pi/2$ and $\phi' = 3\pi/2$. The spectra for $\phi' = 0$ and π will lie between these.

Chapter 6

Summary and Conclusions

6.1 Motivation

We first recall our original motivations for this work. The aim of this Ph.D. project, supported in part through a Rolls-Royce Industrial CASE award, was to further our understanding of Counter Rotating Open Rotor noise, and in particular the phenomenon of Unsteady Distortion Noise. Rolls-Royce is currently running an Advanced Open Rotor development programme, and this Ph.D. took place at the same time as a programme of joint Rolls-Royce/Airbus AOR engine testing. It is believe that UDN will be more significant for AORs than turbofans.

By building on the work of Majumdar and Peake in the mid-1990s we wished to develop a model which could treat the problem of incidence, and other more realistic features of the new generation of open rotors - such as the installation. As detailed in this thesis, the analytic model has now been successfully extended to a non-axisymmetric mean flow system, and applied to two different asymmetric set-ups, including that of incidence. In addition, while undertaking this work certain terms which were neglected in Majumdar's original axisymmetric model were identified and included.

We have implemented several adjustments to the mean flow model to more closely emulate the AOR system: diversion of the inflow around a 'bullet', use of a variable circulation actuator disk model, and analysis of the most appropriate turbulence spectrum and integral lengthscales to use when modelling atmospheric turbulence. At the end of this chapter we list further areas of model development which have been identified but not yet tackled.

6.2 Summary of key results

Here we summarise our findings as detailed in each chapter of this thesis.

6.2.1 Chapter 2 results

Correction to the polar representation of distorted wavevector, l_i, and the distortion amplitude, A_{ij} The quantity $l_i = k_m \partial X_m / \partial x_i$ was first introduced in equation (2.28). We have shown that the l_ϕ component is non-zero, even for axisymmetric mean flows, in which case l_i is given by equation (2.34). This means several A_{ij} terms which were assumed by Majumdar to be zero are in fact non-zero, as can be seen from examination of equations (2.37). These include

$$A_{\phi\phi} = \left(1 - \frac{l_\phi l_\phi}{|\mathbf{l}|^2}\right) \frac{R}{r}.$$

In fact we see that even if l_ϕ is zero, there is still an R/r component of $A_{\phi\phi}$.

Expression derived for the distorted turbulence spectrum S_{ij} which includes all azimuthal orders. An expression for S_{ij}, the Fourier Transform of the correlation between velocities separated in time, was given in equation (2.65). In Majumdar and Peake (1998), only specific azimuthal components were plotted, as given by

$$S_{ij}^m = \frac{2\pi}{U_\infty} \int_{\Re^2} A_{ik}^* (\mathbf{x}, \mathbf{k}) \, J_m^* (r_k R) \, A_{jl} (\mathbf{x}, \mathbf{k}) \, J_m (r_k R) \, S_{kl}^\infty (\mathbf{k}) \, r_k dr_k d\phi_k.$$

If the quantities S_{ij}^m are summed over all m, the two Bessel function terms in fact cancel each other. The motivation for separating S_{ij} into azimuthal components was because S_{xx}^m appeared directly in Majumdar's expression for the spectrum of unsteady blade pressures. However, as discussed in the next point, this is not true for our expression, as we have fully included the azimuthal dependence within the amplitude A_{ij}, not solely that within the phase of the incident velocities.

Numerical results for S_{xx} were given throughout the thesis. The energy level was found to be higher near the tip than the hub of the rotor in all cases considered, due to the sharper change in velocities near the edge of the streamtube contraction. Dependence of S_{xx} upon distortion level is more complex, and depends on the precise mean flow under consideration.

Inclusion of azimuthal dependence within distorted gust amplitude, $A_{ij}\left(\mathbf{x},\mathbf{k}\right)$ For each upstream gust of a particular wavevector $\mathbf{k}$, A_{ij} contains ϕ dependence which should be taken into account when calculating the inter-blade phase angle, χ. This has been implemented within our application of LINSUB to calculate the blade pressure jumps. We have introduced the quantities

$$C_{ij}^{p}\left(x,r;\mathbf{k}\right)=\frac{1}{2\pi}\int_{0}^{2\pi}A_{ij}\left(x,r;\mathbf{k}\right)e^{-ip\phi}d\phi,$$

in order to explicitly bring out the $e^{ip\phi}$ dependence within A_{ij} (equation (2.76)). The quantities D_{j}^{p}, given in equation (2.82), were introduced to facilitate calculation of the normal component of the velocity incident on the leading edge of the blades: $[\sin\beta A_{xi}+\cos\beta A_{\phi i}]$. In Figure 2.6 we showed that D_{j}^{p} decay rapidly with increasing p, and thus we do not need to include very many terms to achieve convergence.

Although their definition is straightforward, the use of these new quantities C and D is one of the most significant aspects to our new model, as this framework allows ready extension to the asymmetric case.

Expressions derived for the spectra of blade pressure and sound pressure. The spectrum of blade pressures, for the axisymmetric case, was given in equation (2.90). In Majumdar and Peake (1998) (equation (2.32)), the blade pressure spectrum was given by

$$\hat{P}_{\text{blade}}\left(\mathbf{x};\omega\right)=\sum_{m=-\infty}^{\infty}\frac{2\pi}{U_{\infty}}\left|\rho_{0}W\Gamma_{WW}^{m}\right|^{2}N_{p}N_{q}S_{pq}^{m}. \tag{6.1}$$

Only the S_{xx}^{m} component appeared in their final expression as all $S_{\phi i}^{m}$ components were assumed to be zero. We have found this not to be the case due to non-zero $A_{\phi i}$, as discussed above.

Similarly, we have now included contributions from $A_{\phi i}$ in our expression for the spectrum of sound pressure (equation (2.133)), rather than solely those which arise from the axial component of the normal vector N_i.

Limiting the r_k integral. Both the spectra of blade pressures and of sound pressures involve an infinite integral over the radial wavevector component, r_k. This arises from neglecting the contribution of the transverse wavenumber to derivatives, for example within ∇^2. When calculating these quantities numerically it is necessary to limit this integral to achieve convergence. We presented a method of doing this in §2.3.3, which involves calculating an 'effective' radial wavenumber k_t and then placing an upper limit upon k_t^2 of ω^2/c_0^2. We have implemented this in our numerical code. A further refinement, using multi-variate stationary phase, is presented in Appendix D.

Numerical results for the blade pressure spectrum and radiated sound obtained. In Figure 2.8 we saw that the blade pressure spectrum contains peaks at multiples of the Rotational Shaft Frequency, and in Figure 2.9 we found that the amplitude of these peaks is reduced when the integral length scale is less than the disk radius ($L < r_d$) but for all $L > r_d$ the heights of the peaks remained approximately constant.

Consistent with previous findings, in Figure 2.11 we found that higher distortion levels lead to a more tonal noise spectrum. For Mach no. = 0.25, and induced velocity at the rotor face 100 m s^{-1}, we found a broadband spectrum of between 100 and 110 dB, with no tonal peaks. Interestingly, as L increases above r_d (Figure 2.12) the spectrum shifts down fairly uniformly at all frequencies, and so we retain tonal peaks for large values of L.

Comparison to Majumdar's results In Figures 2.13 and 2.14 we directly compared our prediction scheme to that of Majumdar. Qualitatively the agreement was excellent, but the inclusion of full ϕ dependence within our model leads to a reduced broadband level in the flight case relative to the tonal peaks of the static testing case.

6.2.2 Chapter 3 results

Implementation of the variable circulation actuator disk model within our framework. The true velocity at the face of an open rotor is more closely modelled by the variable circulation actuator disk than the constant circulation actuator disk. However, in Figure 3.4 we showed that, for a high distortion case, within half a radius of the rotor disk the axial velocity is virtually the same in both cases. Calibration against output from a standard strip theory code showed that using a lower thrust (i.e. a lower value of U_d) in either actuator disk model gives a closer fit. An adjusted velocity profile, where the original Hough and Ordway profile was scaled to lie between r_h and r_d, was also found to approximate the axial velocities better.

Re-derivation of $\partial X_i/\partial x_j$ for the variable circulation flow was detailed in §3.2.5. Increases in $\partial X/\partial x$ and $\partial R/\partial x$ near the tip and decreases near the hub were found when compared to the constant circulation model (see Figure 3.6). Corresponding shifts in the distorted turbulence spectrum, S_{xx}, were shown in Figure 3.7.

Use of the variable circulation model led to a lowered broadband level in the high distortion case, but a raised level in the low distortion case, shown in Figure 3.24. In the medium distortion case the broadband level was lowered but the height of the tonal peak at 1 BPF was raised, shown in Figure 3.25.

Development of an analytic fluid dynamical model to approximate the presence of the 'bullet' upstream of the rotor. In §3.2.3 we introduced a fluid point source upstream of the rotor, simulating the distortion of streamlines around a central engine nacelle. In Figure 3.11 we saw that the addition of this point source raised S_{xx} in the high distortion case at the majority of radial positions, but it was lowered in the medium distortion case near the hub. Full calculation of the derivative of drift for the bullet flow was then given in §3.2.5.

The presence of the bullet was found to lower the noise spectrum marginally, as shown in Figure 3.26.

Inclusion of a secondary actuator disk behind the first, to simulate the presence of the rear blade row. In Figure 3.14 we saw that the addition of a rear actuator disk lowered S_{xx} near the rotor tips in all cases. However, this did not translate to a change in SP, as seen in Figure 3.27.

Investigation of the effect of the form of distortion upon broadband and tonal levels. Through comparison of several different models using 'scaled' and 'unscaled' velocity profiles, we saw in Figures 3.22 and 3.23 that the broadband level is primarily affected by the values of $\partial X_i/\partial x_j$, whereas the tonal peaks are primarily affected by the values of X and R in the phase. Thus the precise form of the distortion seems to affect the broadband UDN level, whereas the magnitude of the overall streamtube contraction affects the UDN tones.

Investigation of the energy distribution of the distorted turbulent eddies. We made an exploratory examination involving the newly defined quantities, $\mathcal{E}_1$ and $\mathcal{E}_2$. The turbulent energy at the blade tip was found to be higher than at the hub in all cases, see for example Figure 3.15. However, we also found that the sum of all diagonal elements of the turbulence distortion tensor, S_{ii}, brings the spectra at hub and tip closer together, as in Figure 3.16.

Throughout Chapter 3 we investigated the role of the fundamental quantities $\partial X_i/\partial x_j$ in determining the distorted turbulence spectrum, for example in the pair of Figures 3.6 and 3.7, and the pair of Figures 3.13 and 3.14. The turbulence spectrum was seen to change directly due to changes in $\partial X_i/\partial x_j$, except for terms where $\partial X_i/\partial x_j \ll 1$, when the δ_{ij} terms of the diagonal elements of A_{ij} dominate.

Investigation of appropriate turbulence models and lengthscales. In Chapter 2 we gave our justification for primarily considering the von Kármán model, as it was found by Wilson et al. (1999) to most closely match true atmospheric spectra (except for the drop-off rate for high wavenumber k), see Figure 2.3. However, to build a model for turbulence shed from the pylon, for example, it was instructive to consider different upstream turbulence models to assess how much S_{ij}^{∞} affected the eventual noise spectrum. In Chapter 3, Figure 3.28, we compared the Liepmann to the von Kármán spectrum. Across different distortion levels, the SP was lowered in the Liepmann case (when L was of the same order as the rotor radius) although the tonal peaks remained similar. The use of the Gaussian spectrum was seen to affect SP very significantly, in Figure 3.29, due to the rapid spectral fall off.

Also in Chapter 3, we discussed the fact that the integral length scale L depends very much on the particular atmospheric conditions, which will vary in space and time. A key element is whether buoyancy or inertia forces are the dominant turbulence generating mechanism. Often measured values of L are higher than those typically used by acousticians, and in Figure 3.30 we calculated results for large values of L. We found that once L was larger than r_d the effect of increasing L simply shifts the spectrum down fairly uniformly, but with the same tonal peaks as occur for $L \sim r_d$.

Finally, we input a range of realistic turbulence parameters (as specified by Simonich et al. (1990)) into our model to produce Figure 3.31. A downward shift in the noise spectrum of around 5 dB was found between 50m and 122m altitude, with a much smaller downward shift seen between 122m and 152m.

6.2.3 Chapter 4 results

Implementation of an asymmetric mean flow model, and calculation of distorted turbulence. Consideration of asymmetric mean flows is of interest to more realistically capture true features of inflow into an AOR and in Chapter 4 we considered a mean flow induced by two actuator disks side by side, separated by distance d. In Figures 4.7 - 4.11 we plotted the distorted turbulence spectrum, and compared these results to the undistorted case, as well as investigating the effect of reducing asymmetry by increasing d.

As in the axisymmetric case, the energy level was found to be higher at the blade tip than the hub in all cases, but dependence of energy level on distortion level was more complex, with the low distortion case lying between the high and medium distortion cases, seen in Figure 4.9. As S_{ij} depends upon ϕ for the asymmetric case we plotted results for a range of ϕ values. The largest difference in spectral level at different radial positions was found to be in the region $\phi = 0$, i.e. closest to the other rotor (see Figure 4.3), where a reduced streamtube contraction is experienced (Figure 4.5). As d increases both the $\phi = 0$ level increases, and the $\phi = \pi$ level decreases, and thus the axisymmetric case lies between the two.

Extension of our UDN model to non-axisymmetric mean flows. In calculating the distorted amplitude, A_{ij}, in the asymmetric case we require both Y and Z (or equivalently R, Φ) in place of R alone in the axisymmetric case. In Chapter 4, the general form for A_{ij} in polar coordinates was derived, see equation (4.22). We note the potential for errors when translating between the cartesian and polar reference frames. The definition of A_{ij} in polars is not intuitively obvious and the derivatives were found to act only on certain terms of the quantities $X_r = R\cos(\Phi - \phi)$, and $X_\phi = R\sin(\Phi - \phi)$.

The key change to the model in the asymmetric case was then in the calculation of a Fourier Series to represent A_{ij}, as now the extra terms $J_n(r_k R)$, $e^{in\Phi}$ and $e^{ik_x X}$ also contain ϕ dependence. New quantities $\widetilde{C}_{ij}^{m,n}$ and $\widetilde{D}_{j}^{m,n}$ were defined. Through substituting these into expressions for the pressure jump across blades, and the total force term, changes were found in the sound pressure spectrum both to the indices which are summed over, and the integral over ϕ_k.

Calculation of the effect of asymmetry upon noise radiated from one rotor. In Figures 4.12, 4.13 and 4.14 we plotted the SP from a single rotor with asymmetric inflow. Key findings are that asymmetry lowers the broadband level, except in the flight (low distortion) case around 1 BPF, where the level is raised by more than 5 dB. The tonal level in the high distortion case is lowered somewhat due to asymmetry, but not as significantly. This agrees with our earlier observation that the precise form of the distortion primarily affects the broadband level.

Calculation of the UDN radiated from two rotors, side by side. Directivity was also calculated in Chapter 4, when we considered the far-field pressure due to two adjacent open rotors. This extension involved substitution of the far-field observer distance from the second rotor into the phase term of the Green's function. Our results, plotted in Figure 4.17, demonstrate that the sound directly beneath the rotors simply adds, whereas out to the sides the sound level is decreased significantly at certain observer positions.

6.2.4 Chapter 5 results

Development of a mean flow model to capture the characteristics of a streamtube contraction into a rotor at incidence. By superposing a tilted actuator disk upon a uniform flow this new velocity field was derived.

Calculation of the effect of incidence upon the distorted turbulence spectrum. In Figures 5.3 - 5.7 several aspects of turbulence distortion at incidence were investigated. The effect of the asymmetry due to incidence was seen to be qualitatively similar to that of two adjacent rotors. Of particular interest is the observation that as the angle of incidence, α, increases, the difference between the distorted spectra at varying azimuthal position in fact diminishes.

Application of Hanson's Green's function to derive an expression for the sound radiated from a rotor at incidence. As shown in Figure 5.9, the effect of incidence upon the radiated sound is similar in certain respects to that of asymmetry due to two adjacent rotors plotted in Figure 4.12. The broadband level in the high distortion case is lowered, and in the low distortion case is raised around 1 BPF. In addition, in the medium distortion case, there is a change to the tonal level in the case of non-zero incidence, which increases and becomes narrower. When the distortion is of an intermediate level, and the flow is neither dominated by the upstream axial flow or a strong actuator disk, the effects of incidence are seen to be most significant. Finally, in Figure 5.11, the greatest differences in directivity at different azimuthal positions were observed to be around $\theta = \pi/4$ and $\theta = 2\pi/3$.

6.3 Overall conclusions

6.3.1 Findings of most relevance to industry

- **Of the various new axisymmetric flow features we have considered, use of the variable circulation actuator disk has the greatest effect.** The bullet's effect appears to be fairly localised near the hub, where the blade travels more slowly, and thus has a less significant effect on noise levels. Inclusion of a rear actuator disk made very little difference to UDN within this model. Scaling the velocity profile to lie between the hub and the tip, rather than using the original actuator disk model, was also a useful technique.

- **Tonal UDN peaks are primarily affected by the total streamtube contraction, whereas broadband level is primarily affected by the form of the distortion.** The form of the distortion, as parametrised by $\partial X_i/\partial x_j$ will be affected by upstream features and asymmetries.

- **The form of the upstream turbulence can have a very significant effect on UDN level.** Further experimental investigation of the spectral form of turbulence shed from installation features would be very useful in the construction of UDN models.

- **Atmospheric turbulence parameters vary widely.** Appropriate values for use within prediction models might be $L \sim 10$ m and $\sqrt{\overline{u_{\infty,1}^2}} \sim 0.25\text{m s}^{-1}$, however the integral lengthscale varies proportionally with height off the ground in reality and turbulence intensity tends to decrease with height. Within our model increasing L above the radius of the rotor is found to shift the noise spectrum down fairly uniformly, so the tonal peaks which are present for $L \sim r_d$ remain.

- **Asymmetries in the mean rotor inflow raise the broadband level for frequencies around 1 BPF, but lower it everywhere else.** In addition, the effect of incidence is most significant when the level of distortion is neither very large nor very small.

- **Our model predicts UDN levels to be around 10 dB lower at approach than at take-off.** In Figure 6.1 we show the results of our model using real industry parameters. As can be seen, the approach level is below that of take-off at all frequencies. The equivalent static result has also been included, demonstrating the formation of tones at high distortion.

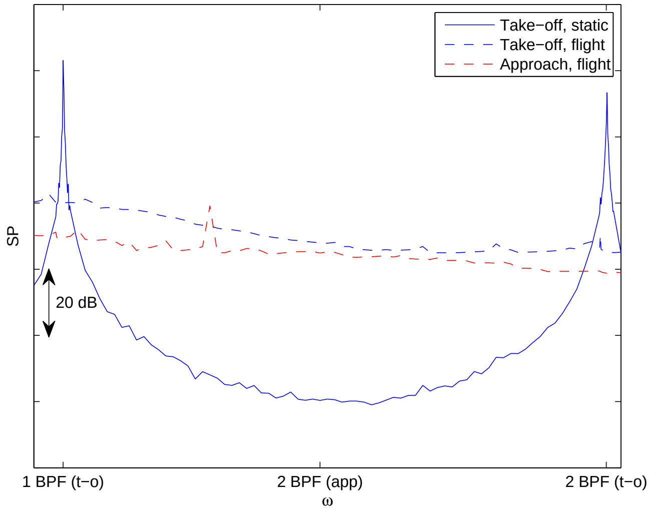

Figure 6.1: Baseline plot, run for realistic open rotor parameters.

6.3.2 Findings of most relevance to theoreticians

- **Overall, the precise form of the distortion does make a few dB difference to peak levels, and can make a significant difference to broadband levels.** However, the magnitude of the streamtube contraction remains the overriding key factor in determining UDN levels.

- **It is essential to limit the integral over transverse wavenumber, r_k, in order to achieve convergence within this model.** A method for doing so has been detailed.

- **Extension to the asymmetric case is possible within this framework, but takes a relatively longer time computationally.** Modal analysis to identify which terms contribute most to expressions, and where to cut off infinite sums, is of importance here.

- **This work has highlighted the non-trivial nature of moving between cartesian and polar reference frames with tensor-like quantities.** Inclusion of all azimuthal terms was seen to affect UDN results.
- **A simple fluid dynamical model for the streamlines induced around the upstream 'bullet' has been presented.**

6.4 Further work

Areas which could now be investigated further, which we did not have time to examine in detail during this Ph.D., include

- Implementation of a full stationary phase argument when determining appropriate limits for the integral over r_k. Some progress has been made towards this, as outlined in Appendix D.
- Use of a more precise isolated blade response model, in place of the LINSUB cascade model.
- Inclusion of entropy fluctuations within the RDT analysis, to simulate the 'hot roots' configuration of AOR, where the engine exhaust interacts with blades.
- Investigation of the effect of different blade leading edge profiles upon UDN.
- Consideration of further turbulence models. For example anisotropic models such as the Batchelor, Karman-Howarth and Birkhoff-Saffman spectra, and the turbulence shed behind a cylinder. We note that it would be a straightforward extension to adjust the Liepmann model, through the use of an exponential correction (Posson and Roger, 2011), to reproduce a faster decay at the top of the inertial range.
- Analysis of how UDN varies during take-off, as flight speed and incidence angle vary with time.
- Improved approximations for the distortion amplitude, A_{ij}.

Appendix A

Legendre functions and actuator disk streamfunction

Legendre functions

The form of Legendre Function used in this thesis is

$$Q_{n-\frac{1}{2}}\left(\omega\right)=\int_{-\frac{\pi}{2}}^{\frac{\pi}{2}}\frac{\cos 2n\alpha}{\left[2\left(\omega-1\right)+4\sin^2\alpha\right]^{\frac{1}{2}}}d\alpha. \tag{A.1}$$

The derivatives with respect to ω, ($Q'_{n-\frac{1}{2}}$ etc.) then follow straightforwardly.

Actuator disk streamfunction

The constant circulation actuator disk velocity streamfunction is given by

$$\Psi^{\text{a.d.}}=\begin{cases}\frac{U_d x}{2\pi}\left(-\frac{E(\kappa)}{\kappa}\sqrt{r_d r}+\frac{\kappa\left(x^2+2r_d^2+2r^2\right)K(\kappa)}{4\sqrt{r_d r}}\right)+\frac{U_d}{4}\left(r^2-\frac{|r_d^2-r^2|\Lambda_0(\beta,\kappa)}{2}\right) & \text{for} \quad r\leq r_d,\\ \frac{U_d x}{2\pi}\left(-\frac{E(\kappa)}{\kappa}\sqrt{r_d r}+\frac{\kappa\left(x^2+2r_d^2+2r^2\right)K(\kappa)}{4\sqrt{r_d r^3}}\right)+\frac{U_d}{4}\left(r_d^2-\frac{|r_d^2-r^2|\Lambda_0(\beta,\kappa)}{2}\right) & \text{for} \quad r>r_d,\end{cases} \tag{A.2}$$

where

$$K(\kappa) = \frac{1}{\kappa} Q_{-\frac{1}{2}}(\omega)\,, \tag{A.3}$$

$$E(\kappa) = \left(1 - \frac{1}{2}\kappa^2\right) K(\kappa) - \frac{\kappa}{2} Q_{\frac{1}{2}}(\omega)\,, \tag{A.4}$$

$$F(\beta, \kappa') = \int_0^\beta \frac{d\theta}{\sqrt{1 - \kappa'^2 \sin^2\theta}}, \tag{A.5}$$

$$E(\beta, \kappa') = \int_0^\beta \sqrt{1 - \kappa'^2 \sin^2\theta}\, d\theta, \tag{A.6}$$

$$\Lambda_0(\beta, \kappa) = \frac{2}{\pi}\left[E(\kappa)F(\beta, \kappa') + K(\kappa)E(\beta, \kappa') - K(\kappa)F(\beta, \kappa')\right]. \tag{A.7}$$

Appendix B

Definition of sound metrics

There are many different metrics used to measure sound. In this appendix we give precise definitions for the metrics used when plotting results for this thesis.

Firstly we note that any quantities we use must include a $\langle , \rangle$-average, so that we can substitute a closed form for the upstream turbulence spectrum (such as the von Kármán spectrum).

Power Spectral Density (PSD)

The Power Spectral Density is defined (Dowling and Ffowcs Williams, 1983) as the Fourier Transform of the autocorrelation of the acoustic pressure

$$\hat{P}\left(\mathbf{x}, \omega\right) = \int_{-\infty}^{\infty} \left\langle \left(p\left(\mathbf{x}, t\right)\right)^{*} p\left(\mathbf{x}, t+\tau\right)\right\rangle e^{i\omega\tau} d\tau. \tag{B.1}$$

The acoustic pressure, p, is a real quantity of course (and thus the complex conjugate is redundant), but $\hat{P}$ will in general be complex. This is one of the quantities for which explicit expressions are given in the main text, see equation (2.133) for example. $\hat{P}$ has dimensions of $\left[\rho^{2}\frac{L^{4}}{T^{3}}\right]$. Energy has dimensions $\left[\rho\frac{L^{5}}{T^{2}}\right]$, and power has dimensions $\left[\rho\frac{L^{5}}{T^{3}}\right]$ (rate of energy).

Power and Power Level (PWL)

Majumdar (1996) then defined the total radiated 'power' in the far-field as

$$P\left(\omega\right)=\int_{\text{sphere of radius }\sigma}\hat{P}\left(\mathbf{x},\omega\right)\sigma^2\sin\theta d\theta d\phi. \tag{B.2}$$

This quantity in fact has dimensions of $\left[\rho^2\frac{L^6}{T^3}\right]$, not power. However, it does give the correct trends of location and height of tones etc. From this, Majumdar defined Power Level (PWL) as

$$\text{PWL}=10\log_{10}\left(\frac{P\left(\omega\right)}{10^{-12}\ \text{ watts}}\right)\text{dB}. \tag{B.3}$$

Since dB are not an absolute unit but a relative one, it would be possible to choose a lengthscale to use in order to give P the correct dimensions for this definition (i.e. dimensions of power). We would simply be changing what the reference level in the denominator refers to.

Sound Pressure Level (SPL)

Again, from Dowling and Ffowcs Williams we have

$$\text{SPL}=20\log_{10}\left(\frac{p'_{rms}}{2\times10^{-5}\text{watts/m}^3\text{Hz}}\right)\text{dB} \tag{B.4}$$

$$=10\log_{10}\left(\frac{\left(p'_{rms}\right)^2}{\left(2\times10^{-5}\text{watts/m}^3\text{Hz}\right)^2}\right)\text{dB}. \tag{B.5}$$

The quantity SPL is used widely. However, it is typically plotted as a function of frequency, rather than time, as would be the case if pressure was used directly, as above. To convert to frequency space, we use the Fourier Transform of pressure, and change the reference quantity in the denominator.

Thus we use the following definition for SPL in this thesis

$$\text{SPL}=10\log_{10}\left(\frac{\left(\text{F.T. of }\ p^2\right)}{\left(2\times10^{-5}\text{watts/m}^3\text{Hz}\right)^2/\text{Hz}}\right)\text{dB} \tag{B.6}$$

$$=10\log_{10}\left(\frac{\hat{P}\left(\mathbf{x},\omega\right)}{\left(2\times10^{-5}\text{watts/m}^3\text{Hz}\right)^2/\text{Hz}}\right)\text{dB}. \tag{B.7}$$

An alternative approach is to ‘undo’ the Fourier Transform of $\hat{P}$ by integrating over frequency, and this is what is done when 1/3 Octave bands are taken. However, 1/3 Octaves have the effect of smoothing the frequency profile, and we would thus lose the tones which are a key characteristic of UDN.

Intensity Level (IL)

We can obtain an expression for Intensity Level per unit frequency using the plane wave result, acoustic intensity $= p'^2/\rho_0 c_0$. Thus, in Robison and Peake (2010) we plot the quantity

$$\mathrm{IL}\left(\mathbf{x},\omega\right) = 10\log_{10}\left(\frac{\hat{P}\left(\mathbf{x},\omega\right)}{\rho_0 c_0\left[10^{-12}\mathrm{watts/m^2Hz}\right]}\right)\mathrm{dB}. \tag{B.8}$$

Again, this is really an ‘intensity level per frequency’.

Appendix C

Sound from non-identical adjacent rotors

Here we give the general expression for the correlation of far-field acoustic pressure due to the UDN generated by two non-identical adjacent rotors.

Within the expression for $\hat{P}$ as given in equation (4.35) the affected quantities are: β, W, ω_Γ (an input to Γ_{WW}) and k_x. In addition, r_d and B appear in several places, and we note that $\phi_0(r)$ and $x_0(r)$ may change as the blade geometry is likely to be altered if the rotation is in a different direction. (We have set $\phi_0(r) = \phi_0 =$ constant and $x_0(r) = x_0 =$ constant throughout our numerical calculations.) Examining the process which led to the form of $\hat{P}$ given in equation (4.35), we see firstly that the statistical average which acts upon the Fourier Transforms of $\mathbf{u}^\infty$ remains the same. The flow upstream of both rotors is the same, and so $\mathbf{u}^\infty$ is of the same form. Thus $k_x = k'_x$ when we perform the $\mathbf{k}'$ integral. Next, the time average now acts on general $\exp(ilB_1\Omega_1 t)$ and $\exp(-il'B_2\Omega_2 t)$ terms, whereby t dependence is removed from the expression, and we require values of l and l' which satisfy

$$lB_1\Omega_1 = l'B_2\Omega_2. \tag{C.1}$$

If $\Omega_1 = -\Omega_2$ and $B_1 = B_2$, we find $l = -l'$. However, for completely general Ω_i and B_i we must have $B_1\Omega_1/B_2\Omega_2 = q/s$ where q, s are integers in order to find any solutions. Finally, the $e^{\frac{i\omega\sigma}{c_0}}$ factors no longer cancel.

Thus we find the most general expression for the cross term of $\hat{P}$ due to the pressure fields of two rotors is

$$
\begin{aligned}
\hat{P}_{\text{cross}}(\sigma,\theta,\phi,\omega) =& \rho_0^2 \frac{B_1 B_2}{4\pi^2 U_\infty} \frac{e^{\frac{-i\omega(\sigma_1-\sigma_2)}{c_0}}}{4\sigma_1\sigma_2(1-M\cos\theta)^2} \\
& \sum_{l,l',m,m'} \int_{r_s,x_s} [J_{m+lB}(\gamma_0 r_s)]^* [W_1(r_s)\Gamma^m_{WW}(x_s,r_s;\omega,\Omega_1)]^* \\
& \left[\frac{i\omega\cos\theta\sin\beta_1(r_s)}{c_0(1-M\cos\theta)} - \frac{i(m+lB)\cos\beta_1(r_s)}{r_s}\right] \\
& \exp\left\{\frac{-i\omega\cos\theta x_s}{c_0(1-M\cos\theta)} + i(m+lB_1)\frac{[x_s - x_{0,1}(r_s)]\tan\beta_1(r_s)}{r_s} + ilB_1\phi_{0,1}(r_s)\right\} \\
& \int_{r'_s,x'_s} J_{m'+lB}(\gamma_0 r'_s)\, W_2(r'_s)\Gamma^{m'}_{WW}(x'_s,r'_s;\omega,\Omega_2) \\
& \left[-\frac{i\omega\cos\theta\sin\beta_2(r'_s)}{c_0(1-M\cos\theta)} + \frac{i(m'+lB)\cos\beta_2(r'_s)}{r'_s}\right] \\
& \exp\left\{\frac{i\omega\cos\theta x'_s}{c_0(1-M\cos\theta)} - i(m'+l'B_2)\frac{[x'_s - x_{0,2}(r'_s)]\tan\beta_1(r'_s)}{r'_s} - il'B_2\phi_{0,2}(r'_s)\right\} \\
& \sum_{p,p'} \int_{\Re} \widetilde{D}^{m,p*}_j(x_{0,1}(r_s),r_s;k_x,r_k,0)\, D^{m',p'}_k(x_{0,2}(r'_s),r'_s;k_x,r_k,0) \\
& \left[\int_0^{2\pi} e^{i(m+p-m'-p')\phi_k} S^\infty_{kl}(\mathbf{k})\, d\phi_k\right] r_k dr_k dr'_s dx'_s dr_s dx_s \\
& e^{i(m'+l'B_2-m-lB_1)\left(\phi-\frac{\pi}{2}\right)} e^{-i(m'-m)\frac{\pi}{2}},
\end{aligned} \tag{C.2}
$$

where $k_x = (\omega - lB\Omega)/U_\infty$. The total Power Spectral Density is then

$$
\hat{P}_{2\text{r}}(\mathbf{x},\omega) = \hat{P}_1(\mathbf{x},\omega) + 2\cos\left(\frac{\omega\sin\theta_1\cos\phi_1}{c_0}\right)\hat{P}_{\text{cross}}(\mathbf{x},\omega) + \hat{P}_2(\mathbf{x},\omega). \tag{C.3}
$$

Appendix D

Stationary phase argument

Finally we detail a more sophisticated argument which could be used when defining the r_k integral limits within $\int_0^{2\pi} \hat{P} d\phi$, but which we did not implement in the numerics.

Within the expression for the pressure spectrum (2.133) we see two integrals of the form

$$I = \int_{r_h}^{r_d} f(r_s) J_\alpha \left(\gamma_0 r_s\right) J_\beta \left(r_k R(r_s)\right) dr_s. \tag{D.1}$$

We can use a multivariate stationary phase argument (as detailed in §9.6 of Jones (1982)) to pick out the key r_s values, given α, β and r_k, which contribute most to this integral. This relationship can then be inverted to allow us to consider a restricted range of r_k values for each pair of r_s and r_s'. Substituting in the exponential definition of the Bessel function

$$J_\alpha \left(\gamma_0 r_s\right) = \int_{-\pi}^{\pi} e^{-i(\alpha\tau - \gamma_0 r_s \sin\tau)} d\tau, \tag{D.2}$$

we find

$$I = \int_{r_h}^{r_d} f(r_s) \left[\int_{-\pi}^{\pi} e^{-i(\alpha\tau - \gamma_0 r_s \sin\tau)} d\tau\right] \left[\int_{-\pi}^{\pi} e^{i(\beta\tau' - r_k R(r_s) \sin\tau')} d\tau'\right] dr_s. \tag{D.3}$$

We have used the complex conjugate of (D.2) when substituting for J_β, which is a real quantity. Now the phase term in three variables is

$$\phi\left(r_s, \tau, \tau'\right) = -\alpha\tau + \gamma_0 r_s \sin\tau + \beta\tau' - r_k R(r_s) \sin\tau'. \tag{D.4}$$

When extending the theory of stationary phase to expressions of more than one variable we seek points of zero gradient of the phase, thus we require

$$\frac{\partial \phi}{\partial r_s} = \gamma_0 \sin\tau - r_k \frac{\partial R}{\partial r_s} \sin\tau' = 0, \tag{D.5}$$

$$\frac{\partial \phi}{\partial \tau} = -\alpha + \gamma_0 r_s \cos\tau = 0, \tag{D.6}$$

$$\frac{\partial \phi}{\partial \tau'} = \beta - r_k R \cos\tau' = 0. \tag{D.7}$$

Using (D.6) and (D.7) to eliminate τ and τ' from (D.5), we find the following condition at points of stationary phase, $r_s = r_s^*$

$$\frac{\sqrt{\gamma_0^2 r_s^{*2} - \alpha^2}}{r_s^*} = \frac{\partial R}{\partial r_s^*} \frac{\sqrt{r_k^2 R(r_s^*)^2 - \beta^2}}{R(r_s^*)}. \tag{D.8}$$

To determine the stationary phase multiplicative factor we calculate the determinant of the Hessian matrix at $r_s = r_s^*$. After some algebra, this is found to be

$$\begin{aligned} \det(\text{Hessian}) = {} & \frac{1}{R}\frac{\partial^2 R}{\partial r_s^2}\left(r_k^2 R^2 - \beta^2\right)\left(\gamma_0^2 r_s^2 - \alpha^2\right)^{\frac{1}{2}} \\ & - \frac{\alpha^2}{r_s^2}\left(r_k^2 R^2 - \beta^2\right)^{\frac{1}{2}} + \left(\frac{\partial R}{\partial r_s}\right)^2 \left(\gamma_0^2 r_s^2 - \alpha^2\right)^{\frac{1}{2}}. \end{aligned} \tag{D.9}$$

The stationary phase result is that, as the phase term gets large,

$$I \sim \sqrt{\frac{(2\pi)^3}{|\det(\text{Hessian})|}} f(r_s^*) e^{-i(\alpha\tau^* - \gamma_0 r_s^* \sin\tau^*) + i(\beta\tau'^* - r_k R(r_s^*)\sin\tau'^*)} e^{-\frac{i\pi}{4}\operatorname{sgn}(\det(\text{Hessian}))}. \tag{D.10}$$

Given m, p and p', we can pick a discrete set of values of r_k which give a range of values of r_s^* and $r_s'^*$ between r_h and r_d. Thus r_k will lie between r_k^h and r_k^d, defined via

$$\gamma_0^2 - \frac{\alpha^2}{r_h^2} = \left(\frac{\partial R}{\partial r_s}\right)^2\Bigg|_{r_s = r_h} \left((r_k^h)^2 - \frac{\beta^2}{(R(r_h))^2}\right), \tag{D.11}$$

$$\gamma_0^2 - \frac{\alpha^2}{r_d^2} = \left(\frac{\partial R}{\partial r_s}\right)^2\Bigg|_{r_s = r_d} \left((r_k^d)^2 - \frac{\beta^2}{(R(r_d))^2}\right). \tag{D.12}$$

This will lead to an increased number of r stations at which $\partial X_i/\partial x_i$ needs to be calculated numerically, which is likely to be time consuming for asymmetric flows.

Nomenclature

A_{ij}	distortion amplitude tensor
α	angle of rotor incidence
b	label for a specific blade
B	total number of blades
β	blade angle
c	blade chord length
c_0	speed of sound
C_{ij}^{p}	p^{th} Fourier coefficient of A_{ij}
$\widetilde{C}_{ij}^{m,n}$	Fourier coefficient of A_{ij} in asymmetric system
d	separation distance between rotors, in asymmetric flow
D_j^{p}	combination of C_{ij}^{p} components
$\widetilde{D}_j^{m,n}$	combination of $\widetilde{C}_{ij}^{m,n}$ components
$\frac{D_0}{Dt}$	material derivative in mean flow
$\frac{D_\infty}{Dt}$	material derivative in uniform upstream flow
δ	Dirac delta function
δ_{ij}	Kronecker delta
Δ	drift function

$\hat{\mathbf{e}}_\mathbf{i}$	basis of unit vectors
E	turbulent energy spectrum
E^G	Gaussian three-dimensional energy spectrum
E^{LM}	Liepmann three-dimensional energy spectrum
$\mathcal{E}_1$	a distorted spectrum energy measure
$\mathcal{E}_2$	a distorted spectrum energy measure
$\boldsymbol{\eta}$	spatial separation vector
$\mathbf{f}$	wave equation forcing term
f_i^k	forcing term due to single upstream wavevector component
$F^{l,m,p}$	component of forcing term
g	axial gap between rotors in co-axial system
g_1	constant used in the von Kármán spectrum
g_2	constant used in the von Kármán spectrum
γ	ratio of specific heats
Γ	blade circulation
Γ_{WW}	non-dimensionalised blade circulation
Γ_{WW}^m	non-dimensionalised blade circulation, for particular azimuthal order
$H^{l,m}$	Green's function
J_n	Bessel function of order n
$\mathbf{k}$	wavenumber vector
k	modulus of wavevector $\mathbf{k}$
k_r	component of wavevector in $\hat{\mathbf{e}}_\mathbf{r}$ direction
k_t	effective radial wavenumber

k_ϕ	component of wavevector in $\hat{\mathbf{e}}_\phi$ direction
K	LINSUB kernel
$\mathbf{l}$	distorted wavenumber vector
l	summation index which arises from sum over blade number
L	integral length scale of free-stream turbulence
λ	reduced frequency
m	azimuthal order
m	strength of point source
M	Mach no. of upstream uniform flow
M_W	Mach no. in chordwise direction
$\hat{\mathbf{n}}$	normal vector on solid body surface (RDT)
n_c	number of chordwise points considered in LINSUB
$\mathbf{N}$	unit blade normal
p	total pressure (mean plus perturbation)
p	far-field sound pressure
p	(superscript) azimuthal order of A_{ij}
p_0	mean pressure
p'	perturbation pressure
$p^{l,m,p}$	component of far-field sound pressure
$\hat{p}^{l,m,p}$	amplitude of component of far-field sound pressure
Δp^b	pressure jump across blade b
P	correlation of far-field pressures
P_{blade}	correlation of blade pressures

$\hat{P}_{\text{blade}}$	spectrum of blade pressures
$\hat{P}$	Fourier transform of far-field pressure spectrum
$\hat{P}_{2\text{r}}$	$\hat{P}$ due to two adjacent rotors
ϕ	azimuthal angle
ϕ'	azimuthal angle in rotating frame
ϕ'	in Chapter 5, azimuthal angle in tilted coordinate system
ϕ_0	azimuthal position of leading edge of blade
ϕ_k	azimuthal component of wavevector
ϕ_s	azimuthal source coordinate
Φ	far upstream azimuthal position
ψ	potential of irrotational component of distorted velocity
ψ'	component of ψ which satisfies the boundary condition on rotor blades
ψ_0	component of ψ which satisfies the inhomogeneous RDT wave equation
Ψ	streamfunction
$\Psi^{\text{a.d}}$	actuator disk streamfunction
Ψ^s	streamfunction due to point source
Q_n	Legendre functions
Q_n'	derivative of Legendre function, with respect to its argument
r	radial coordinate
r_d	rotor radius
r_h	hub radius
r_k	radial component of wavevector
r_s	radial source coordinate

R	far upstream radial position
R_{ij}	distorted velocity correlation tensor
R_{ij}^{∞}	upstream turbulence velocity correlation tensor
ρ	total density (mean plus perturbation)
ρ'	perturbation density
ρ_0	mean density
ρ_∞	constant density of uniform upstream flow
s	blade spacing
S	amplitude radius
S_0	leading order term of S
S_1	first order term of S
S_{ij}	distorted turbulence spectrum
S_{ij}^{G}	Gaussian spectrum tensor
S_{ij}^{LM}	Liepmann spectrum tensor
S_{ij}^{∞}	upstream turbulence spectrum tensor
σ	phase radius
σ_0	distance of observer from rotor, emission coordinate
t	time
T	total propeller thrust
τ	temporal separation vector
θ	polar angle between observer and rotor, emission coordinate
θ'	in Chapter 5, polar angle in tilted coordinate system
Θ_{xx}	one-dimensional turbulent energy spectrum

$\mathbf{u}$	perturbation velocity field (distorted turbulence)
$\mathbf{u}^{\infty}$	turbulence velocity far upstream
u_i^{gust}	distorted velocity due to single upstream gust
$u_i^{\mathrm{rot.}}$	velocity in rotating reference frame
$\mathbf{u}^{\mathrm{vort}}$	vortical component of distorted velocity
$\langle u^2 \rangle$	average of turbulent velocity
$\overline{u_{\infty,1}^2}$	mean square speed of the axial component of turbulent velocity
$\mathbf{U}$	mean flow induced by the rotor
U_{∞}	uniform axial speed far upstream (flight speed)
$U_i^{\mathrm{a.d.}}$	velocity induced by constant circulation actuator disk
$U_i^{\mathrm{bul.}}$	velocity induced by bullet system
$U_i^{\mathrm{co\text{-}ax.}}$	velocity induced by co-axial actuator disks
$U_i^{\mathrm{var.}}$	velocity induced by variable circulation actuator disk
U_d	‘strength’ of the actuator disk
U_f	total axial velocity at disk face
U_r	radial velocity induced by rotor
U_x	axial velocity induced by rotor
U_x^s	axial velocity due to point source
U_{ϕ}	azimuthal velocity induced by rotor
$\mathbf{v}$	total velocity (mean plus perturbation)
w_W	amplitude of velocity perturbation at leading edge of blade
W	mean flow speed in chordwise direction
ω	temporal frequency parameter

ω_Γ	LINSUB temporal frequency
Ω	angular velocity of the rotor
$\mathbf{x}$	position vector
$\mathbf{x}'$	tilted coordinate system, for rotor at incidence
x_0	position of point source
$x_0(r)$	axial position of blade leading edge
x_1	position of stagnation point in point source (bullet) model
x_s	axial source coordinate
X	axial component of distortion vector, $U_\infty \Delta$
X_i	distortion vector
$X_i^{\text{var.}}$	X_i in variable circulation actuator disk case
χ	inter-blade phase angle
Y	far upstream position along y axis
$\hat{z}$	chordwise coordinate
Z	far upstream position along z axis
AOR	advanced open rotor
BPF	blade passing frequency
CAA	computational aeroacoustics
CFD	computational fluid dynamics
dB	decibel
DNS	direct numerical simulation
EPNL	effective perceived noise level
LES	large eddy simulation

LINSUB	‘linearized subsonic’ code
PSD	power spectral density
PWL	power level
RANS	Reynolds averaged Navier-Stokes
RDT	rapid distortion theory
RSF	rotational shaft frequency
SP	spectral power
SPL	sound pressure level
UDF	unducted fan
UDN	unsteady distortion noise

Bibliography

R. K. Amiet. Acoustic radiation from an airfoil in a turbulent stream. *Journal of Sound and Vibration*, 41(4):407–420, 1975.

R. K. Amiet, J. C. Simonich, and R. H. Schlinker. Rotor noise due to atmospheric turbulence ingestion. Part II: Aeroacoustic results. *Journal of Aircraft*, 27(1):15–22, 1990.

K. Anderson, A. Bows, and P. Upham. Growth scenarios for EU & UK aviation: contradictions with climate policy. Working Paper 84, Tyndall Centre for Climate Change Research, 2006.

H. M. Atassi and M. M. Logue. Effect of turbulence structure on broadband fan noise. *Proc. of 14th AIAA/CEAS Aeroacoustics Conference*, (AIAA 2008-2842), 2008.

H. M. Atassi and M. M. Logue. Fan broadband noise in anisotropic turbulence. *Proc. of 15th AIAA/CEAS Aeroacoustics Conference*, (AIAA 2009-3148), 2009.

G. K. Batchelor. *The Theory of Homogeneous Turbulence*. Cambridge University Press, 1953.

G. K. Batchelor and I. Proudman. The effect of rapid distortion of a fluid in turbulent motion. *Quarterly Journal of Mechanics and Applied Mathematics*, 7(1):83–103, 1954.

V. P. Blandeau. *Aerodynamic Broadband Noise from Contra-Rotating Open Rotors*. PhD thesis, University of Southampton, February 2011.

V. P. Blandeau and P. F. Joseph. On the validity of Amiet's model for propeller trailing-edge noise. *Proc. of 16th AIAA/CEAS Aeroacoustics Conference*, (AIAA 2010-3797), 2010.

V. P. Blandeau, P. F. Joseph, and B. J. Tester. Broadband noise prediction from rotor-wake interaction in contra-rotating propfans. *Proc. of 15th AIAA/CEAS Aeroacoustics Conference*, (AIAA 2009-3137), 2009.

R. Boisard, G. Delattre, and F. Falissard. Assessment of aerodynamic and aeroacoustic tools for the open rotor at ONERA. *Proc. of 14th CEAS-ASC Workshop on aeroacoustics of high-speed aircraft propellers and open-rotors*, 2010.

H. H. Brouwer. Analytical method for the computation of the noise from a pusher propeller. *Proc. of 16th AIAA/CEAS Aeroacoustics Conference*, (AIAA 2010-3848), 2010.

P. Busquin et al. European aeronautics: A vision for 2020. Report of the group of personalities, January 2001.

A. M. Cargill. A theory for fan unsteady distortion noise. Theoretical Science Group Report TSG0675, Rolls-Royce plc, 1993.

T. H. Carolus and M. Stremel. Blade surface pressure fluctuations and acoustic radiation from an axial fan rotor due to turbulent inflow. *Acta Acustica united with Acustica*, 88: 472–482, 2002.

C. Cheong, P. Joseph, and S. Lee. High frequency formulation for the acoustic power spectrum due to cascade-turbulence interaction. *Journal of the Acoustical Society of America*, 119(1):108–122, 2006.

A. J. Cooper and N. Peake. Trapped acoustic modes in aeroengine intakes with swirling flow. *Journal of Fluid Mechanics*, 419:151–175, 1999.

N. A. Cumpsty and B. W. Lowrie. The cause of tone generation by aeroengine fans at high subsonic speeds and the effect of forward speed. *Journal of Engineering for Power*, 96(3):228–234, 1974.

P. A. Davidson. *Turbulence: An Introduction for Scientists and Engineers*. Oxford University Press, 2004.

T. Deconinck, P. Hoffer, C. Hirsch, A. De Meulenaere, and J. Bonaccorsi. Prediction of near- and far-field noise generated by contra-rotating open rotors. *Proc. of 16th AIAA/CEAS Aeroacoustics Conference*, (AIAA 2010-3794), 2010.

W. J. Devenport, J. K. Staubs, and S. A. L. Glegg. Sound radiation from real airfoils in turbulence. *Journal of Sound and Vibration*, 329:3470–3483, 2010.

M. Dieste and G. Gabard. Synthetic turbulence applied to broadband interaction noise. *Proc. of 15th AIAA/CEAS Aeroacoustics Conference*, (AIAA 2009-3267), 2009.

A. P. Dowling and J. E. Ffowcs Williams. *Sound and sources of sound.* Ellis Horwood, 1983.

E. Envia. NASA open rotor noise research. *Proc. of 14th CEAS-ASC Workshop on aeroacoustics of high-speed aircraft propellers and open-rotors*, 2010.

I. Evers and N. Peake. On sound generation by the interaction between turbulence and a cascade of airfoils with non-uniform mean flow. *Journal of Fluid Mechanics*, 463:25–52, 2002.

U. W. Ganz. Analytical investigation of fan tone noise due to ingested atmospheric turbulence. NASA Contractor Report 3302 NAS1-15085, Boeing Commercial Airplane Co., 1980.

S. A. L. Glegg and C. Jochault. Broadband self-noise from a ducted fan. *AIAA Journal*, 36(8):1387–1395, 1998.

X. Gloerfelt and J. Berland. Direct computation of turbulent boundary layer noise. *Proc. of 15th AIAA/CEAS Aeroacoustics Conference*, (AIAA 2009-3401), 2009.

M. E. Goldstein. Unsteady vortical and entropic distortions of potential flows round arbitrary obstacles. *Journal of Fluid Mechanics*, 89(3):433–468, 1978.

S. Goldstein. On the vortex theory of screw propellers. *Proceedings of the Royal Society of London. Series A*, 123:440–465, 1929.

R. D. Hager and D. Vrabel. Advanced turboprop project. Technical report, National Aeronautics and Space Administration, Lewis Research Center, 1988.

D. B. Hanson. Spectrum of rotor noise caused by atmospheric turbulence. *Journal of the Acoustical Society of America*, 56(1):110–126, 1974.

D. B. Hanson. Noise of counter-rotation propellers. *Journal of Aircraft*, 22:609–617, 1985.

D. B. Hanson. Sound from a propeller at angle of attack: a new theoretical viewpoint. *Proc. Mathematical and Physical Sciences*, 449(1936):315–328, 1995.

D. B. Hanson. Theory for broadband noise of rotor and stator cascades with inhomogeneous inflow turbulence including effects of lean and sweep. NASA contractor report, United Technologies Corporation, 2001.

D. B. Hanson and K. P. Horan. Turbulence/cascade interaction: spectra of inflow, cascade response, and noise. *Proc. of 4th AIAA/CEAS Aeroacoustics Conference*, (AIAA 98-2319):688–700, 1998.

R. W. Harris and R. D. Cuthbertson. UDF/727 flight test program. *Proc. of 23rd AIAA/SAE/ASME/ASEE Joint Propulsion Conference*, 1987.

G. E. Hoff. Experimental performance and acoustic investigation of modern, counter-rotating blade concepts. NASA Contractor Report 185158 NAS3-24080, GE Aircraft Engines, 1990.

G. F. Homicz and A. R. George. Broadband and discrete frequency radiation from subsonic rotors. *Journal of Sound and Vibration*, 36(2):151–177, 1974.

J. H. Horlock. *Actuator disk theory: discontinuities in thermo-fluid dynamics.* McGraw-Hill, 1978.

G. R. Hough and D. E. Ordway. The generalized actuator disk, in *Developments in Theoretical and Applied Mechanics, Vol. II.* pages 317–336, 1965.

J. C. R. Hunt. A theory of turbulent flow round two-dimensional bluff bodies. *Journal of Fluid Mechanics*, 61(4):625–706, 1973.

D. S. Jones. *The theory of generalised functions.* Cambridge University Press, 1982.

M. Kamruzzaman, T. Lutz, A. Herrig, and E. Krämer. RANS based prediction of airfoil trailing edge far-field noise: impact of isotropic & anisotropic turbulence. *Proc. of 14th AIAA/CEAS Aeroacoustics Conference*, (AIAA 2008-2867), 2008.

E. J. Kerschen and P. R. Gliebe. Noise caused by the interaction of a rotor with anisotropic turbulence. *AIAA Journal*, 19(6):717–723, 1981.

M. J. Kingan and A. McAlpine. Propeller tone scattering. *Proc. of 17th International Congress on Sound and Vibration*, 2010.

M. J. Kingan and R. H. Self. Counter-rotation propeller tip vortex interaction noise. *Proc. of 15th AIAA/CEAS Aeroacoustics Conference*, (AIAA 2009-3135), 2009.

T. J. Kirker. Procurement and testing of a 1/5 scale advanced counter rotating propfan model. *Proc. of 13th AIAA Aeroacoustics Conference*, (AIAA 90-3975), 1990.

L. D. Koch. An experimental study of fan inflow distortion tone noise. *Proc. of 15th AIAA/CEAS Aeroacoustics Conference*, (AIAA 2009-3290), 2009.

R. H. Lange. A review of advanced turboprop transport aircraft. *Progress in Aerospace Sciences*, 23:151–166, 1986.

M. J. Lighthill. Drift. *Journal of Fluid Mechanics*, 1:31–53, 1956.

A. E. D. Lloyd. *Rotor Stator Interaction Noise.* PhD thesis, University of Cambridge, July 2009.

S. J. Majumdar. *Unsteady Distortion Noise*. PhD thesis, University of Cambridge, November 1996.

S. J. Majumdar and N. Peake. Three-dimensional effects in cascade-gust interaction. *Wave Motion*, 23:321–337, 1996.

S. J. Majumdar and N. Peake. Noise generation by the interaction between ingested turbulence and a rotating fan. *Journal of Fluid Mechanics*, 359:181–216, 1998.

R. Mani. Noise due to interaction of inlet turbulence with isolated stators and rotors. *Journal of Sound and Vibration*, 17(2):251–260, 1971.

D. A. McCurdy. Annoyance caused by advanced turboprop aircraft flyover noise. NASA Technical Paper 3027, Langley Research Center, 1990.

D. A. McCurdy. Annoyance caused by aircraft en route noise. NASA Technical Paper 3165, Langley Research Center, 1992.

P. F. Mish and W. J. Devenport. An experimental investigation of unsteady surface pressure on an airfoil in turbulence. Part 1: effects of mean loading. *Journal of Sound and Vibration*, 296:417–446, 2006a.

P. F. Mish and W. J. Devenport. An experimental investigation of unsteady surface pressure on an airfoil in turbulence. Part 2: sources and prediction of mean loading effects. *Journal of Sound and Vibration*, 296:447–460, 2006b.

M. R. Myers and E. J. Kerschen. Influence of incidence angle on sound generation by airfoils interacting with high-frequency gusts. *Journal of Fluid Mechanics*, 292:271–304, 1995.

M. Omaïs and J. Ricouard. Experimental and numerical analysis of the pylon-rotor interaction noise radiated by a contra rotating open rotor. *Proc. of 14th CEAS-ASC Workshop on aeroacoustics of high-speed aircraft propellers and open-rotors*, 2010.

A. Pagano, M. Barbarino, D. Casalino, and L. Federico. Tonal and broadband noise calculations for aeroacoustic optimization of propeller blades in a pusher configuration. *Proc. of 15th AIAA/CEAS Aeroacoustics Conference*, (AIAA 2009-3138), 2009.

A. B. Parry. *Theoretical prediction of counter-rotating propeller noise.* PhD thesis, University of Leeds, February 1988.

A. B. Parry, M. J. Kingan, and B. J. Tester. Relative importance of open rotor tone and broadband noise sources. *Proc. of 17th AIAA/CEAS Aeroacoustics Conference*, (AIAA 2011-2763), 2011.

A. B. Parry and S. Vianello. A project study of open rotor noise. *Proc. of 14th CEAS-ASC Workshop on aeroacoustics of high-speed aircraft propellers and open-rotors*, 2010.

R. W. Paterson and R. K. Amiet. Acoustic radiation and surface pressure characteristics of an airfoil to incident turbulence. NASA Contractor Report CR-2733, 1976.

R. W. Paterson and R. K. Amiet. Noise of a model helicopter rotor due to ingestion of isotropic turbulence. *Journal of Sound and Vibration*, 85(4):551–577, 1982.

N. Peake and D. G. Crighton. Active control of sound. *Annual Review of Fluid Mechanics*, 32:137–164, 2000.

N. Peake and E. J. Kerschen. Influence of mean loading on noise generated by the interaction of gusts with a flat-plate cascade: upstream radiation. *Journal of Fluid Mechanics*, 347:315–346, 1997.

N. Peake and A. B. Parry. Modern challenges facing turbomachinery aeroacoustics. *Annual Review of Fluid Mechanics*, in press, 2012.

H. Posson, S. Moreau, H. Bériot, Y. B. de l'Epine, and C. Schram. Prediction of sound transmission through an annular cascade using an analytical cascade response function. *Proc. of 16th AIAA/CEAS Aeroacoustics Conference*, (AIAA 2010-4030), 2010.

H. Posson and M. Roger. Experimental validation of a cascade response function for fan broadband noise predictions. *AIAA Journal*, 49(9):1907–1918, 2011.

R. A. Reba and E. J. Kerschen. Influence of airfoil angle of attack on unsteady pressure distributions due to high-frequency gust interactions. Report to NASA Langley Research Center, 1996.

D. Redmann, A. Gündel, B. Stritzelberger, and M. Bauer. Engineering approach for a simplified description of rotor-rotor interaction noise of a CROR configuration. *Proc. of 16th AIAA/CEAS Aeroacoustics Conference*, (AIAA 2010-3792), 2010.

J. Ricouard, E. Julliard, M. Omaïs, V. Regnier, A. B. Parry, and S. Baralon. Installation effects on contra-rotating open rotor noise. *Proc. of 16th AIAA/CEAS Aeroacoustics Conference*, (AIAA 2010-3795), 2010.

R. A. V. Robison and N. Peake. Propeller unsteady distortion noise. *Proc. of 16th AIAA/CEAS Aeroacoustics Conference*, (AIAA 2010-3798), 2010.

M. Roger and A. Carazo. Blade-geometry considerations in analytical gust-airfoil interaction noise models. *Proc. of 16th AIAA/CEAS Aeroacoustics Conference*, (AIAA 2010-3799), 2010.

W. Sears. Some aspects of non-stationary airfoil theory and its applications. *Journal of the Aeronautical Sciences*, 8(3):104–108, 1941.

I. J. Sharland. Sources of noise in axial flow fans. *Journal of Sound and Vibration*, 1(3): 302–322, 1964.

J. C. Simonich, R. K. Amiet, R. H. Schlinker, and E. M. Greitzer. Rotor noise due to atmospheric turbulence ingestion. Part I: Fluid mechanics. *Journal of Aircraft*, 27(1): 7–14, 1990.

B. A. Smith. McDonnell Douglas nears commitment to fly propfan on MD-80 testbed. *Aviation Week and Space Technology*, 122(20):32–33, 1985.

S. N. Smith. Discrete frequency sound generation in axial flow turbomachines. Aeronautical Research Council Reports and Memoranda 3709, Ministry of Defence, 1973.

W. H. Snyder. Guideline for fluid modeling of atmospheric diffusion. Technical report, United States Environmental Protection Agency, 1981.

P. R. Spalart, A. K. Travin, M. L. Shur, and M. K. Strelets. Initial noise predictions for open rotors using first principles. *Proc. of 16th AIAA/CEAS Aeroacoustics Conference*, (AIAA 2010-3793), 2010.

J. K. Staubs, W. J. Devenport, and S. A. L. Glegg. Sound radiation from a series of airfoils immersed in grid-generated turbulence. *Proc. of 14th AIAA/CEAS Aeroacoustics Conference*, (AIAA 2008-3018), 2008.

D. B. Stephens, S. C. Morris, and W. K. Blake. Sound generation by a rotor ingesting a casing turbulent boundary layer. *Proc. of 14th AIAA/CEAS Aeroacoustics Conference*, (AIAA 2008-2990), 2008.

A. R. Stuart. Why the UDF? *The Leading Edge all-UDF special issue*, pages 4–9, Fall 1986.

M. Terracol and V. Kopiev. Numerical investigation of the turbulent flow around a truncated cylinder: noise reduction aspects. *Proc. of 14th AIAA/CEAS Aeroacoustics Conference*, (AIAA 2008-2868), 2008.

J. M. Tyler and T. G. Sofrin. Axial flow compressor noise studies. *SAE transactions*, 70: 309–332, 1962.

M. Wang, J. B. Freund, and S. K. Lele. Computational prediction of flow-generated sound. *Annual Review of Fluid Mechanics*, 38:483–512, 2006.

D. S. Whitehead. Classical two-dimensional methods. Manual on Aeroelasticity in Axial-Flow Turbomachinery AGARD-AG-298 Vol. 1, Advisory Group for Aerospace Research and Development, 1987.

C. E. Whitfield, R. Mani, and P. R. Gliebe. High speed turboprop aeroacoustic study (counterrotation). Volume 1: Model development. *Final Report General Electric Co. Advanced Technology Operations*, 1990.

D. K. Wilson, J. G. Brasseur, and K. E. Gilbert. Acoustic scattering and the spectrum of atmospheric turbulence. *The Journal of the Acoustical Society of America*, 105(1): 30–34, 1999.

D. K. Wilson and D. W. Thomson. Acoustic propagation through anisotropic, surface-layer turbulence. *The Journal of the Acoustical Society of America*, 96(2):1080–1095, 1994.

S. A. Wright. *Aspects of unsteady fluid-structure interaction.* PhD thesis, University of Cambridge, April 2000.

J. Yin and A. Stuermer. Noise radiation from installed pusher propeller using coupling of unsteady panel method, actuator disk and FW-H methodology. *Proc. of 16th AIAA/CEAS Aeroacoustics Conference*, (AIAA 2010-3849), 2010.

R. P. Young, J. Tai, B. R. Havrilesko, and D. Mavris. A comparison of community noise metrics for open rotor engine architectures. *Proc. of 16th AIAA/CEAS Aeroacoustics Conference*, (AIAA 2010-4002), 2010.

A. Zachariadis and C. A. Hall. Application of a Navier-Stokes solver to the study of open rotor aerodynamics. *Proc. of ASME Turbo Expo*, (GT2009-59332), 2009.